Vulnerability of Shallow Groundwater
Resources to Deep Sub-surface Energy-
Related Activities -VOGERA

Deliverable 3.2

Characterization of pathways and groundwater vulnerability assessments due to deep energy related activities for the pilot studies

Authors and affiliation:

Willem Zaadnoordijk (TNO-GSN), Ágnes Szalkai (MBFSZ), Cis Slenter (VMM), Koen Beerten (SCK CEN), Marco Bianchi (BGS), Alberto Casillas-Trasvina (SCK CEN), Bart Rogiers (SCK CEN), Andreas Kruisselbrink (TNO-GSN), Tano Kivits (TNO-GSN), Hans Peter Broers (TNO-GSN)

Technical Report 2, WP 3

E-mail of lead author:
willem_jan.zaadnoordijk@tno.nl

Version: final

This report is part of a project that has received funding by the European Union's Horizon 2020 research and innovation programme under grant agreement number 731166.

Deliverable Data		
Deliverable number	D3.2	
Dissemination level	Public	
Deliverable name	Technical report on the characterization of pathways and vulnerability assessments for the pilot studies	
Work package	WP3 Process Understanding	
Lead WP/Deliverable beneficiary	TNO Geological Survey of the Netherlands	
Deliverable status		
Submitted (Author(s))	20/10/2021	Willem Zaadnoordijk (TNO-GSN)
Verified (WP leader)	21/10/2021	Willem Zaadnoordijk (TNO-GSN)
Approved (Coordinator)	22/10/2021	Marco Bianchi (BGS)

GENERAL INTRODUCTION

This report is the second deliverable for Work Package 3 of the VoGERA project (Vulnerability of Shallow Groundwater Resources to Deep Sub-surface Energy Related Activities). This work package seeks to better understand processes and pathways that may be associated with impacts on groundwater resources from energy-related activities in the subsurface. The report introduces the topic and describes the pilot areas that have been used to evaluate possible pathways in detail for several geological settings across Europe. For each pilot area, the results of the data collection and analysis are presented, as well as the vulnerability assessment using the tool that has been developed in Work Package 4 (Conceptual framework for vulnerability characterization) of the VoGERA project.

List of abbreviations & acronyms

BGS	British Geological Survey (part of UKRI)
DINO	National database of information on the shallow Dutch subsurface (available at: http://www.dinoloket.nl)
DMP	Data Management Plan
EGDI	European Geological Data Infrastructure
GSO	Geological Survey Organisation
MBFSZ	Magyar Bányászati és Földtani Szolgálat (Mining and Geological Survey of Hungary)
NLOG	National database of information on the deep Dutch subsurface (available at: http://www.nlog.nl)
SCK CEN	Belgian Nuclear Research Centre
TNO-GSN	Geological Survey of the Netherlands (part of TNO)
VMM	Vlaamse Milieu Maatschappij (Flanders Environment Agency)
VoGERA	Vulnerability of shallow Groundwater resources to deep sub-surface Energy-Related Activities

SUMMARY

This report is the second deliverable for Work Package 3 of the VoGERA project, “Vulnerability of Shallow Groundwater Resources to Deep Sub-surface Energy-related Activities”. This project is part of the Groundwater Theme of the EU’s Horizon 2020 research and innovation programme “GeoERA” project, under grant agreement No 731166. The VoGERA project contributes to societal challenges recognised as part of the Horizon 2020 programme; 3: Secure, clean and efficient energy and 5: Climate action, environment, resource efficiency and raw materials.

The VoGERA project is gathering scientific evidence to investigate the relationship between industrial activity in the deep sub-surface and shallow groundwater resources, in a European context. The project considers the possible impacts on groundwater from a range of sub-surface energy activities (geothermal energy, conventional oil and gas, unconventional oil and gas exploitation, sub-surface energy storage and disposal of energy-related waste such as CO_2) in a consistent manner. An approach to evaluating groundwater vulnerability from sub-surface activities that can be applied across Europe will be developed using this evidence, and the in-depth understanding gained will be used to improve awareness of these issues with decision makers and the public. This will aid better sub-surface spatial planning and policy development for deep sub-surface energy-related activities in relation to groundwater, thus allowing for the simultaneous protection of groundwater for future generations whilst recognizing the need for economic development. A strong link with stakeholders will ensure an approach that is fit for purpose and has maximum impact.

This work package, “process understanding” uses four case study examples to demonstrate and understand particular processes and pathways between deep energy activities and groundwater resources. This report, “Technical report on Characterization of pathways and assessments of groundwater due to deep energy related activities for the pilot studies” is the second technical report for WP3 and includes the results of the pilot studies using existing data, data collected in the VoGERA project, and the tool for vulnerability assessment that has been developed in WP4.

The pilot study areas are: Pannonian Basin (Hungary), Vale of Pickering (UK), Peel Boundary fault near Veghel (the Netherlands), Rauw fault (Belgium). The natural pathways are described using based on the geology and hydrogeology. The risks associated with the pathways are analysed for a specific deep energy activity in each pilot and the results are compared with the outcome of the vulnerability assessment of the WP4 tool, GWV 3D.

The results of the research carried out for the pilots indicated that there is no direct evidence for pathways from the deep subsurface to the groundwater resources, that could lead to deterioration of these pathways in case energy related activities would be started in the deep subsurface. The application of the GWV 3D tool for the pilots confirms this conclusion. However, hotspots with a deep connection have been reported in the literature and the groundwater in the Roer Valley Graben in the Dutch pilot has a 3-Helium over 4-Helium ratio that indicates influence from the mantle.

The risks associated with induced seismicity, contamination from the surface during installation or anthropogenic pathways have not been studied.

TABLE OF CONTENTS

1 Introduction

The overall aim of the VoGERA project is to study the vulnerability of shallow groundwater resources from deep sub-surface energy activities using existing data, information and experience of GeoERA partners and from previous projects. Conceptual models and a vulnerability screening tool have been developed in the project and are validated at a number of pilot study sites.
Understanding and managing hazards and risks associated with potentially harmful activities in order to meet the environmental objectives of the EU Water Framework Directive (2000/60/EC) and Groundwater Directive (2006/118/EC) is a prerequisite for protecting groundwater for future generations. Groundwater protection has traditionally focused on safeguarding water resources from hazards at (or near) the surface. As a result, the risks from near-surface activities are relatively well understood and managed. The controversy surrounding the shale gas industry development in Europe has highlighted the lack of information and systematic practices across the EU for managing a range of hazards to groundwater from energy-related activities in the deep sub-surface.

Work Package 3 “Process understanding” focuses on improving understanding of the potential pathways between deep sub-surface energy activities and shallow groundwater. The scope and a literature survey have been presented in the first technical report (Zaadnoordijk et al., 2019). According to the literature survey the pathways vary strongly in their contribution to the vulnerability of groundwater resources due to deep energy-related activities. Pathways in order of diminishing likeliness of problems are:

- Surface contamination during installation;
- Failing subsurface infrastructure;
- Natural faults;
- Fractures;
- Matrix flow.

The importance of the pathways is larger for energy-related activities, which increase the pressure in the subsurface. It is smaller for activities that only reduce the pressure in the subsurface.

The understanding has been increased further through analysis of hydrogeological, physical, chemical, isotopic, and geophysical information for four pilot sites. The pilots are in different hydrogeological settings across Europe:

- Pannonian Basin (Hungary);
- Vale of Pickering (UK);
- Peel Boundary fault near Veghel and Gilze-Rijen faults near Tilburg (Netherlands);
- Gas and tracer signals in Noord-Brabant (the Netherlands);
- Rauw fault (Belgium).

The pilots have been investigated using existing and newly collected data. Also, they have been used to test the vulnerability tool, which has been developed in Work Package 4 of the VoGERA project (Bianchi et al., 2021), except the Dutch pilots Tilburg and Noord-Brabant. The Tilburg pilot provides insight in the advantage of three-dimensional seismic data (compared to two-dimensional) for the evaluation of fault zones and associated damage zones which may increase permeability. The Noord-Brabant pilot provides a baseline assessment of gas and tracer signals in the shallow groundwater.

This technical report is the second deliverable of Work Package 3 and includes:

- A description of the four pilot areas:

- The analysis of natural pathways and processes relevant for risks for groundwater resources due to specific energy-related activities;
- Conclusions from the pilots and the application of the vulnerability Inventory of data gaps and planning of further data collection.

The pilots are described in the Chapters 2 (Pannonian Basin, Hungary), 3 (Vale of Pickering, United Kingdom), 4 (Veghel and Tilburg with fault along the Roer Valley Graben, the Netherlands), 5 (Noord-Brabant with gas and tracer signals, the Netherlands) and 6 (Rauw fault, Belgium). The report closes with a brief synthesis and outlook in Chapter 7.

2 Pilot Pannonian Basin

2.1 Introduction of the Pannonian basin pilot

The pilot area is situated in the Little Hungarian Plain, which lies between the Eastern Alps and the Transdanubian Range as the western part of the Pannonian Basin. The studied territory is mainly a lowland area of the Kisalföld Basin surrounded by the Eastern Alps in the west and the Transdanubian Range in the east (Figure 2.1).

Figure 2.1 Location of the pilot area in the Pannonian Basin

The Little Hungarian Plain was the target of intensive historical hydrocarbon exploration. The first geophysical measurement campaign was carried out between 1933-1944 and the exploration drilling started in 1935. Several boreholes were drilled, and geophysical measurements were carried out resulting borehole logs, seismic sections and gravitational maps. Despite of the detailed research significant hydrocarbon reservoir were not discovered, but some natural CO_2 gas reservoir (Répcelak, Mihályi, Ölbő) and mixed burnable gas was identified (Figure 2.2).

Due to its positive geothermal anomaly (with heat flow density ranges between 32 and 115 mW/m^2, (mean: 77.6 mW/m^2) and the geothermal gradient between 21 and 55 °C/km (mean: 32.3 °C/km) there are also potential thermal water reservoirs for balneology and geothermal energy utilization (Goetzl et al., 2012, Rotár-Szalkai et al., 2017).

In addition to the nearly 60 boreholes and thermal wells tens of drinking water wells are situated in the region, where drinking water mostly derived from groundwater. Monitoring wells are operated by Mining and Geological Survey of Hungary (MBFSZ) and the West-Transdanubian Water

Directorate observing groundwater heads both of cold and thermal water bodies. Industrial monitoring systems are operated by LINDE, MOL, and Messer.

For testing the developed VoGERA method for vulnerability assessment the Ölbő area CO_2 extraction sites was selected within the pilot area (Figure 2.2). The test target area is a 5 km circle around center of the extraction site.

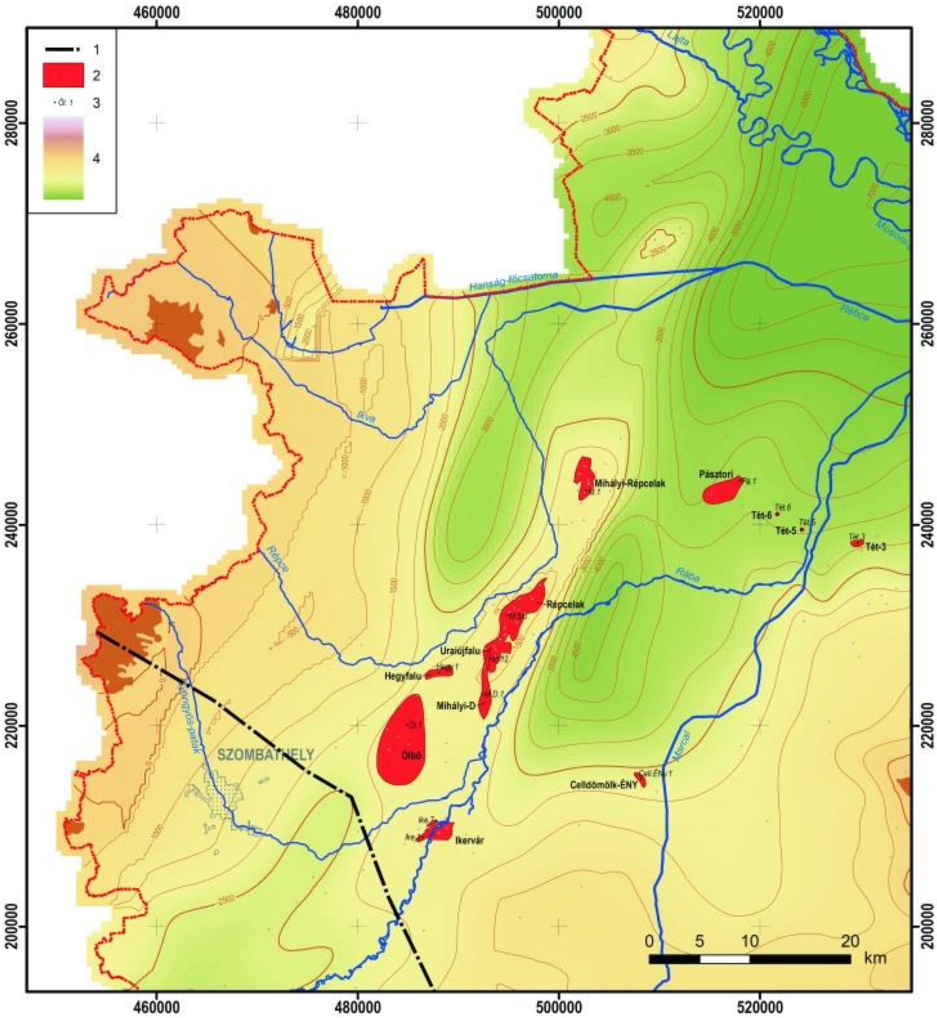

Figure 2.2 Gas reservoirs in the Little Hungarian Plain (Kovács et al., 2018).

Based on the detailed investigations and research of the last decades great deal of information was collected in different institutes and industrial participants. As the result of regional, national and also international projects the detailed geological maps, cross-sections and models exist in different scales and resolutions. The developed borehole and well databases contain geological profiles, hydrogeological, geophysical and geochemical information. 3D geological map (Maros et al., 2012) and 3D regional hydrogeological flow model (Tóth et al., 2016) were developed. Testing the new novel methodology was based on the integrated evaluation of some outdated borehole geological profile, geophysical measurements and basic data.

2.2 Geology and hydrogeology of the Pannonian Basin pilot

2.2.1 Geological settings

The studied area belongs to the ALCAPA major tectonic unit (East Alpine-Central Western Carpathian-North Pannonian lithospheric segment). The basement comprises of Palaeo- and Mesozoic crystalline and sedimentary sequences belong to the Lower to Upper Austroalpine nappe units and the Penninic unit. The ALCAPA nappe system contains oceanic crust series and Adria derived far travelled nappe systems, overthrusted onto each other predominantly of south eastern vergency. The Austroalpine nappes are composed by far-travelled crystalline sequences, with multiphase, medium grade amphibolite facies metamorfites and Palaeozoic-Mesozoic cover on them – are overthrusted the Penninic structure zone (Figure 2.3).

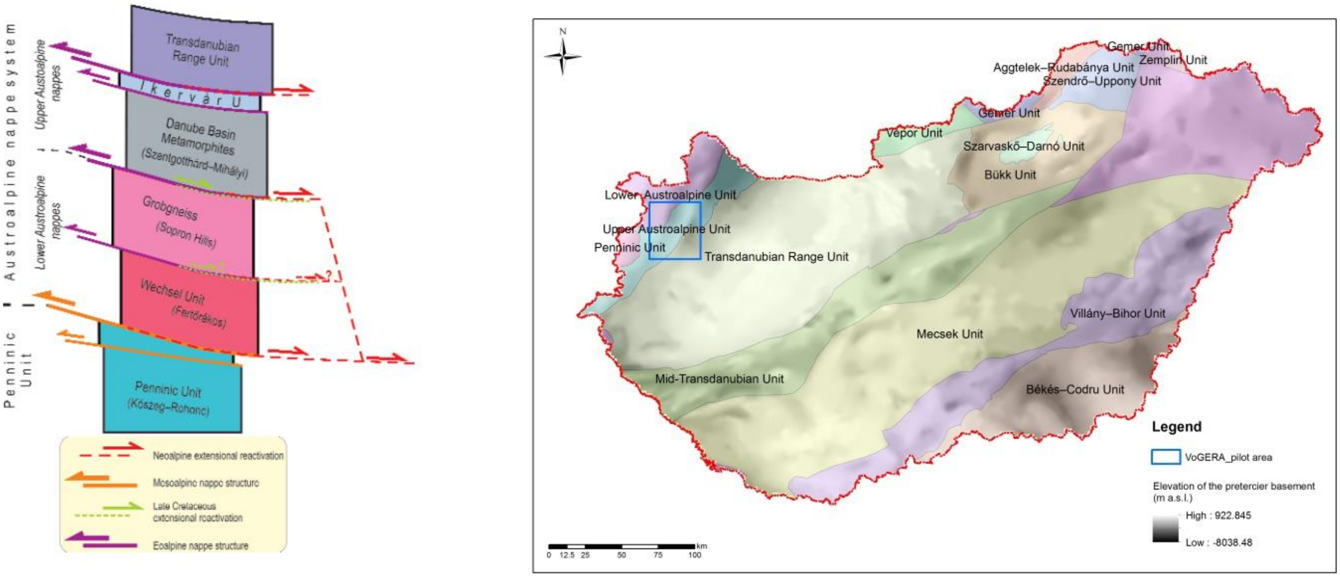

Figure 2.3 Tectonic model of the Pre-Cenozoic structural units of North Transdanubia (Haas and Budai 2014).

Therefore the basement of the western part of the Pannonian basin is extremely diverse and shows a complex structure, built up of various metamorphic and non-metamorphic Palaeo- and Mesozoic crystalline and sedimentary rocks that formation was associated with the Alpine-Carpathian orogene (Csontos and Vörös, 2004, Schmid et al., 2008, Haas et al., 2010, Haas and Budai, 2014). They have a composite structural pattern, arranged into nappes along thrust sheets, dissected by strike-slip and normal faults, associated with the multi-phase tectonic development of the basin (Fodor et al., 1999, Horváth et al., 2006, Haas et al., 2012) (Figure 2.4). These rocks also form some outcropping mountain regions, so called “inselbergs” (e.g. Transdanubian Range). The pre-Neogene basement is composed of various Palaeozoic metamorphic rocks, Mesozoic carbonates and siliciclastics (Figure 2.3 and Figure 2.4).

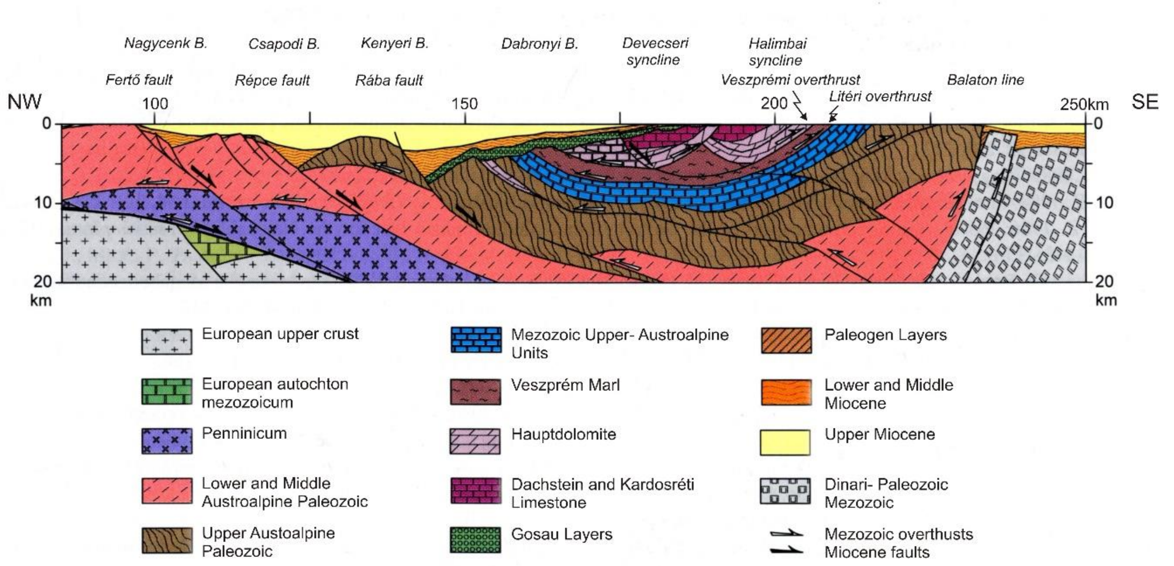

Figure 2.4 Deep geological cross-section across the Kisalföld Basin and the Transdanubian Range (modified after Tari and Horvath, 2010).

The basin fill consists of Neogene sediments. The Miocene sedimentation started with the Eggenburgian transgression: littoral gravel and sand covered by offshore sandy clay were dominant. During the Ottnangian and Karpatian terrestrial–fluvial–limnic successions were formed in the basin (Ligeterdő Formation). Locally thin coal seams and eastward rhyolite tuff interbeddings are known.

The subsidence of the Kisalföld Basin commenced at the end of the Early and the beginning of Middle Miocene. Due to early Badenian tectonic movements the basin was segmented resulting very different sedimentation environments and sedimentary facies. Badenian successions started with abrasion basal breccia and conglomerate, locally with calcareous matrix (Pusztamiske Formation). In the depocenter off-shore, deepmarine siliciclastic sediments (sandy silt, silt, silty clay marl) were accumulated (Baden Formation). The near shore facies are sand-sandstone, the offshore deep-basin facies are represented by fine sandy silt, silty clay marl with sandstone intercalations and sandy-silty claymarl (Szilágy Formation). In shallow marine facies it is overlain by corallinacean limestone (Lajta Formation). On the top of the lower Badenian gypsum and dolomite laminae can appear with some tuff intercalations. During the upper Badenian calcareous clays, siltstones and sandstones with volcanoclastics and biogenic limestones in the margins were settled in the area. In the onset of the Sarmatian biogenic calcareous sediments of shoreline and fine-siliciclastic sediments (clay, clay marl, calcareous marl, siltstones and sands) of shallow-marine facies (Kozárd Formation) were deposited in brackish environment. In nearshore areas conglomerates, sandstones, limestones can be found (Tinnye Formation), locally with lignites and tuffs.

The Pannonian (Late Miocene and Pliocene) geo-history is characterized by the presence of Lake Pannon. This “Lake” got isolated from Paratethys and was infilled by sediments of large thickness transported by rivers, originating in the surrounding uplifting Alpine and Carpathian mountain belts. The resulting siliciclastic sequences can be as thick as several thousand meters in the deepest sub-basins (Figure 2.5). The shelf-slope system is prograded from NW to SE. During the Lower Pannonian coarse sediments – abrasional conglomerates – were deposited along the shorelines (Békés Formation). The prograding shelf sedimentation was characterized by alluvial deltas which were formed along the feet of mountain ranges. The most prevalent deposits of this time were the pelagic marls (marls and calcareous marls) of the 'starving' basin (Endrőd Formation). As the shelf-slope system prograded turbidites started to deposit (Szolnok Formation) in the foreground and the shelf slopes. On the slope mainly silt was deposited (Algyő Formation), coarser sediments settled only in turbidites. During the earliest Upper Pannonian delta front sediments accumulated on the sedimentary shelf were formed (Újfalu Formation). In the central regions of the basin the sedimentation resulted in wide and thick sheets of sand with relatively good connectivity. After that a deltaic plain, than an alluvial plain was formed with large amount of floodplain silt and mud, and isolated channel sand bodies (Zagyva Formation.). During the Early Pliocene fluvial sedimentation systems became dominant.

By the end of the Late Miocene, rivers running down from the neighbouring mountains filled up the basin, and a continental terrain came into being in the area of the former basin.

In the Quaternary fluvial sedimentary environment was dominant in the region. Rivers form alluvial fans in different size while in areas flooded with stagnant water were characterized with lake and marsh sedimentation.

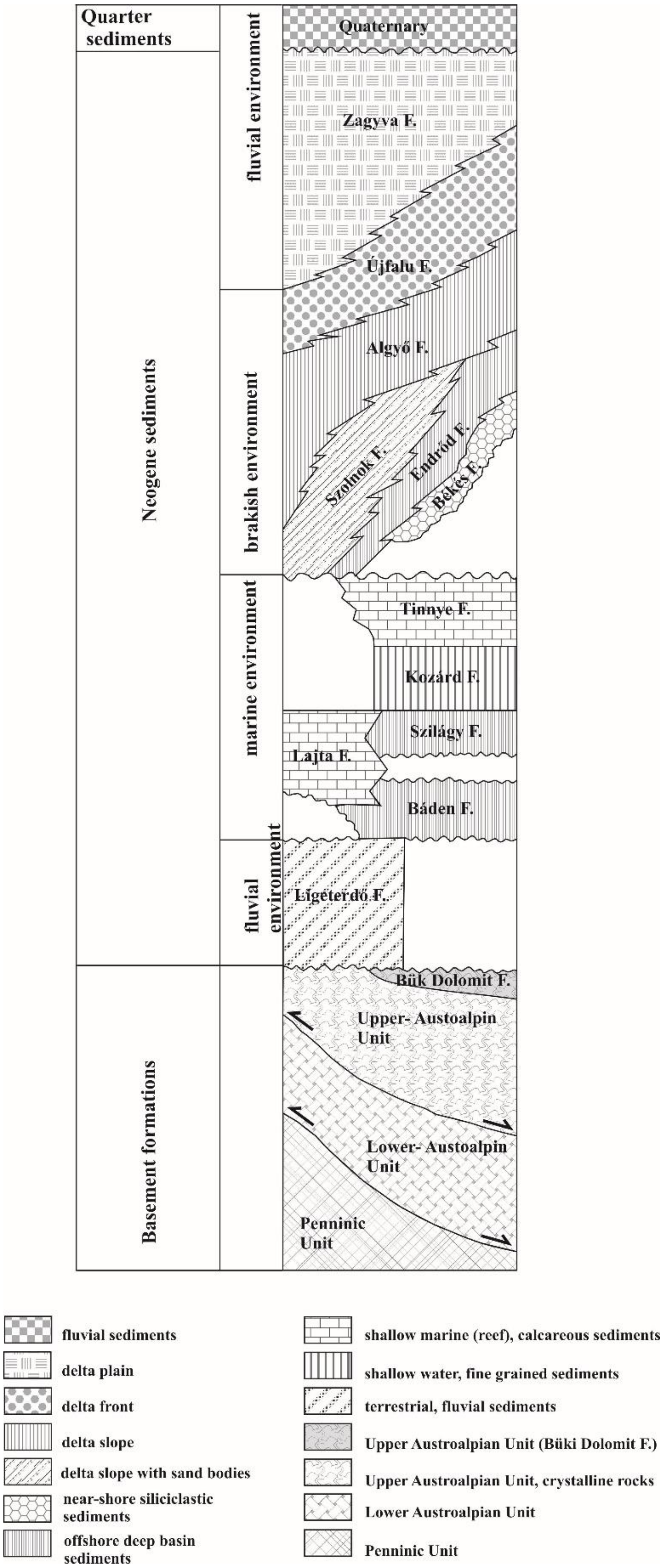

Figure 2.5 Theoretical succession in the pilot area.

2.2.2 Hydrogeologic conditions

The groundwater flow system of the pilot area is controlled by the considerable hydraulic potential between the recharge and discharge areas (i.e. surrounding mountain chains and low-lying basin), sufficient recharge (precipitation) and extensive deep lying permeable formations outrcrop on the margins. These basic conditions are provided by the geological buildup of the basin. The mountain regions situated at the edges of the western part of the Pannonian Basin (mostly outside of the national border) representing the natural boundaries of the flow system. These regions having high relief (Alps, Male Karpaty, Carpathians, Transdanubian Midmountains) serve as the main recharge areas, where the basement rocks (crystalline, or carbonate) outcrop. Part of the infiltrated precipitation returns to the surface in the form of cold water springs at the basin margins, or within the mountain area after a short path forming local simple gravity driven flow systems. The other part is moving toward the deeper layers and forms the regional flow system. At bigger depths, along the deeper flowpaths groundwater warms up, and changes its chemical character due to water-rock interactions. The regional flow systems either terminate at springs at the margins of the mountain regions, or continue in the depth below the lowlands, in the deep sinking basement units. In some places, where the basement is connected to the porous sediment formations filling the Neogene basins, the groundwater of the basement aquifers pass over to the porous layers, forming the flow system of the sedimentary basins. In these cases thermal groundwater also feeds the overlying shallow subsurface freshwater Quaternary and Plio-Quaternary aquifers. Otherwise, the flow system of the basement is separated from the above described flow system of the porous aquifers, and the main discharges of the basement system are only the springs at the margins of the mountains. The other major type of the basement aquifers includes those deep carbonate rock bodies with fairly stagnant thermal groundwater reserves that do not have direct hydraulic connection (supply) with the surface systems. They normally contain thermal groundwater with high temperature and high NaCl type salinity (fossil waters) and may have a restricted recharge from the overlying porous aquifers. When the geometry (vertical or subvertical permeable zone of the closed basement aquifers, i.e. conduit channels along larger fault zones) makes it possible, a closed thermal convection (free convection) may develop. For example, where the Middle Miocene aquifers (abrasional and shore sands, gravels, reef carbonates, etc.) directly overly on the basement rocks and form a joint hydraulic unit.

The groundwater flow system of the Neogene sub-basins is divided to an upper gravitational part and a deeper part, where the density and heat difference driven flow is added to the gravitational system. The two regional sub-systems are separated by thick Upper Miocene-Pliocene aquitards, which form the lower part (delta slope facies) of the Pannonian basin fill sedimentary succession (Tóth et al., 2012). Below this regional aquitard layer and in areas far away from the gravitational flow systems stagnant or very slow flows operate. These groundwaters are partly supposed to originate from the sea-water of the last transgression of the geological evolution of the area (i.e. they are fossil confined groundwaters), but according to new results the high TDS content can derive from evaporate dissolution as well (Rotár-Szalkai et al., 2018).

In the deep part of the basin areas the presence of the former or recent overpressured zones has to be taken into consideration. These are generally formed on areas where thick clays and clayey marls are present (‘Miocene’-‘Pannonian’ clayey marls); mainly compactional and/or tectonic, diagenetic processes may take part in their formation. The slow fluid migration induced by cross-flows from the overpressured zones towards the basement, or to the upper aquifers are important from hydrogeochemical point of view. The amount of water deriving from these units is generally less than the water budget of the main aquifers, but the high dissolved solids content of the overpressured zone's water significantly contributes to the hydrogeochemical character of the exploited thermal waters and often determines their balneological/medicinal value.

The gravitational flow systems of the upper porous aquifers in basin areas can be divided into regional, intermediate and local systems. The deepest regional flow system penetrates till the delta-front and the delta-plain sands of the Upper Pannonian sedimentary sequence. The sedimentary and post-depositional erosion processes may significantly modify the stratification of these units, and as a result the forced flow paths and recharge/discharge conditions, too. Under favourable conditions the sandy aquifer units are outcropping, or are in direct contact with Quaternary aquifers on the hilly areas with a higher hydraulic potential, therefore providing a fairly quick and direct recharge. Due to frequent alternation of the sand-silt-clay layers the flow system has a significant anisotropy but the entire sedimentary succession forms a single hydro-stratigraphic unit. The intermediate flow systems encompass the multi-level sandy aquifers of the Upper Pannonian delta-plain sedimentary sequence. They also play a role in the recharge of the deeper porous and the basement aquifers. The shallowest groundwater (local) flow system can be divided into two main types. On the hilly areas the precipitation percolating through the pre-Quaternary weathered, or coarse- grained sediments feeds the Quaternary (mostly Holocene) alluviums. Here this local flow often meets the intermediate and regional flow systems. The larger streams and deeper and larger alluvial aquifers form another type of alluvium, which is a discharge of the deeper flow systems. The conceptual model of groundwater flow systems are shown in Figure 2.6.

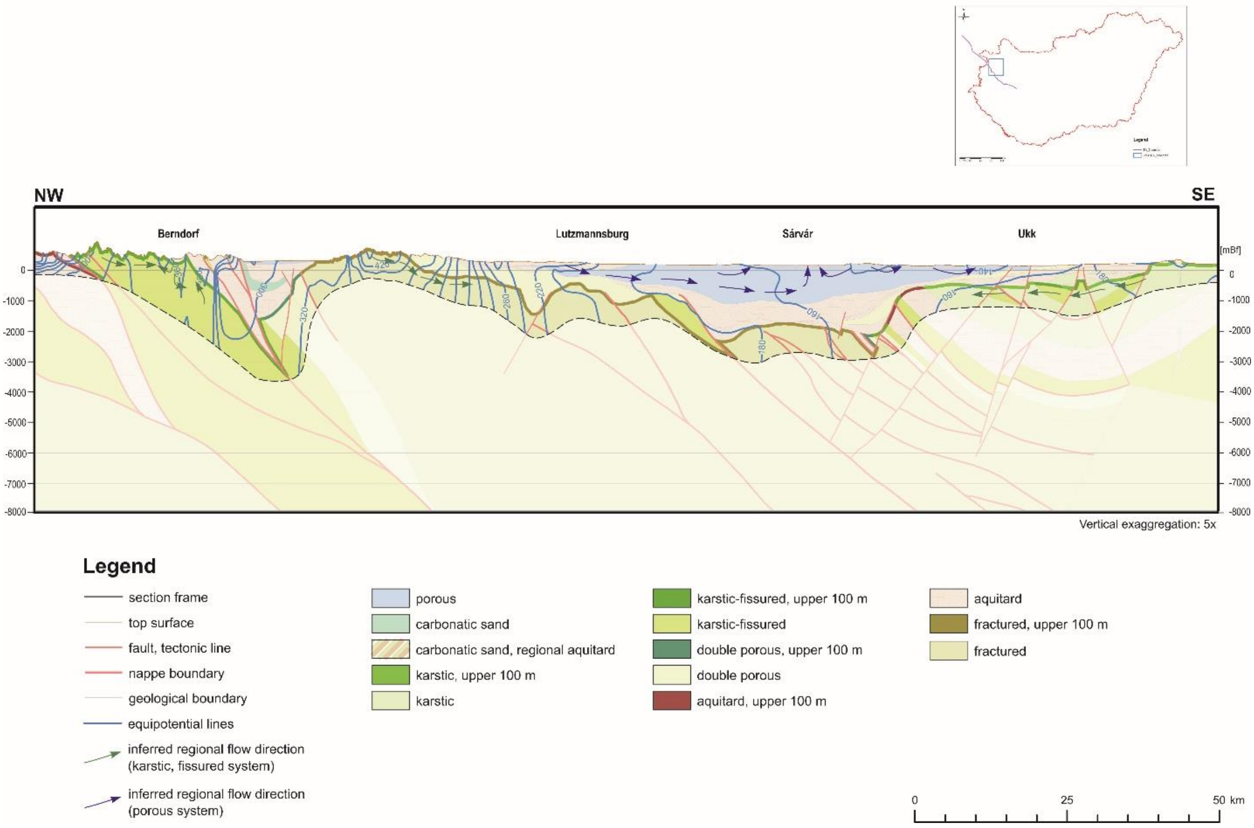

Figure 2.6 Schematic hydrogeological cross-section at the western part of Pannonian Basin (Rotár-Szalkai et al., 2013).

The Pannonian delta sediment series are covered by thin (0-200 m) Quaternary layers. These fluvial sediments represent the important drinking water aquifers of the regions. Due to the lack of regional aquitard layers, hydraulic connection exists between the Quaternary formations and the Upper Miocene-Pliocene sediment series.

2.3 Integrated results of the Ölbő area

2.3.1 Geological characterization of the Ölbő area

The Ölbő area has been explored by 10 boreholes (depth exceeds 1000 m), 2D seismic profiles, and nearly 20 wells illustrated on Figure 2.7.
As the result of intensive geophysical research performed in the frame of the earlier hydrocarbon exploration several geophysical maps (magnetotelluric, telluric, deep geoelectric, gravitational and magnetic) are available too. The applied geological model was determined by geological sequences of stratigrafical units based on well-log interpretations and evaluation of seismic profiles. The 3D geological model developed in the frame of TRANSENERGY project (Maros et al., 2012) was also considered.

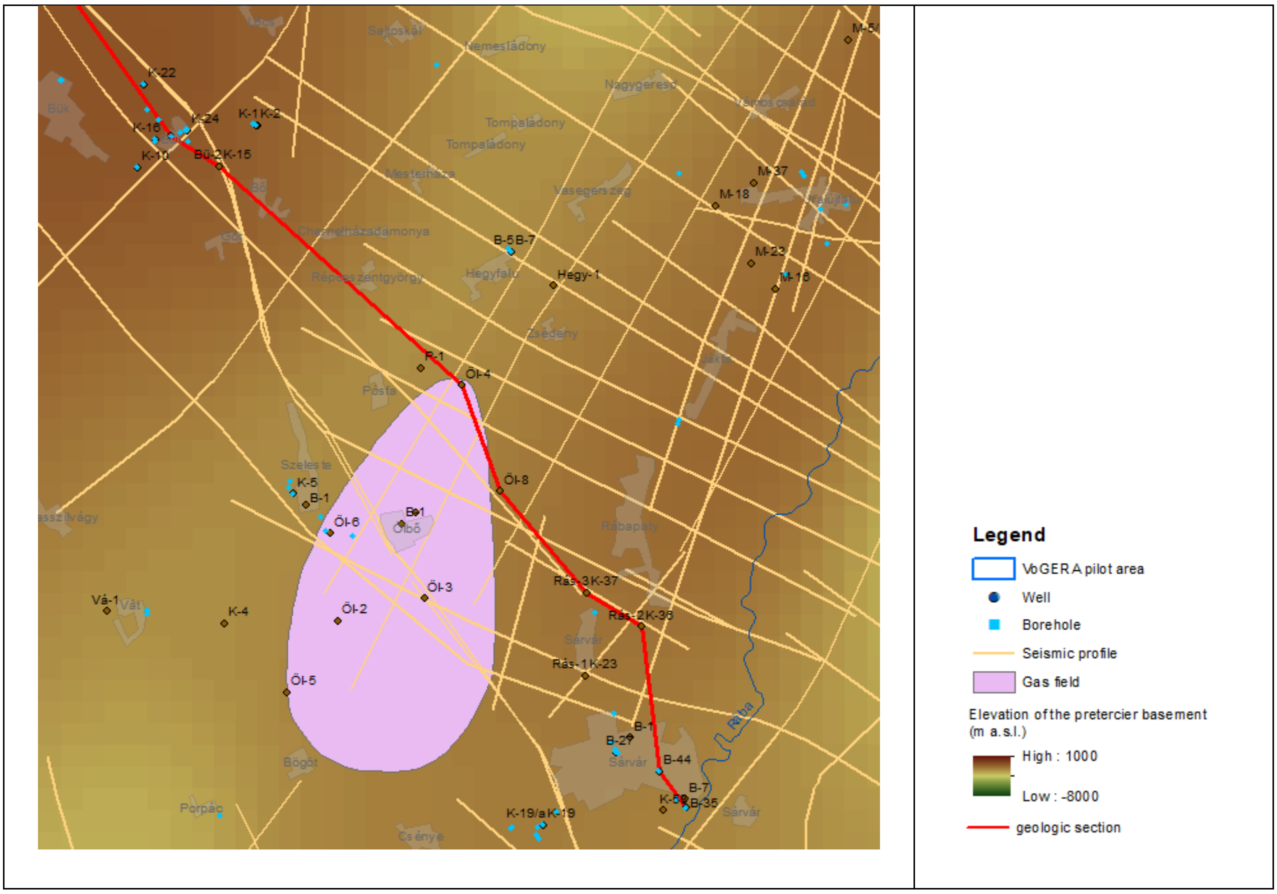

Figure 2.7 Boreholes, wells and seismic profiles in the Ölbő area (Red line illustrates location of the constructed geological section)

The surface of the Pre-Cenozoic basement of the area was determined by the tectonic movements of the Mesozoic and the extensional deformations during the Miocene (Figure 2.8). Some of the tectonic structures of the basement reactivated and can be followed in the Pannonian sediments too. Relief of the basement is characterized by the NNE–WSW striking ridge called Mihályi High is followed by almost parallel deep sub-basins, the Csapod Trough on the west and Kenyeri Trough on the east, The Ölbő area is situated as far as the NNE margin of the Mihályi ridge.

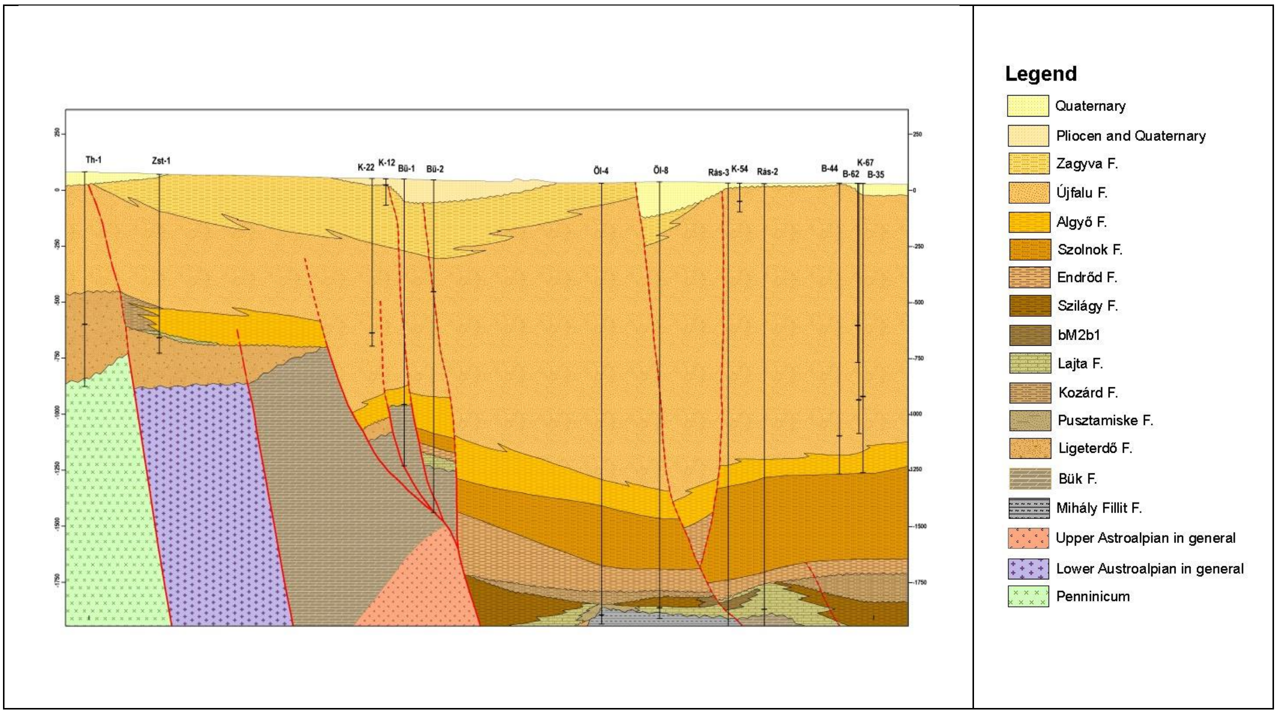

Figure 2.8 Geological section of the Ölbő area (for location see Figure 2.7).

The basement consists mainly of metamorphosed crystalline rocks of the Upper Austro-Alpine nappe system. The tectonically relocated unit built up from the Rábamente Metamorphic Complex. The low-grade (Szentgotthárd Phyllite, Mihály Phyllite, Bük Dolomite, Ölbö Carbonate Phyllite) and very low-grade (Nemeskolta Sandstone schist, Sótony Metabasalt) metamorphic formations were interpreted as the result of an Early Palaeozoic sedimentary cycle (Fülöp 1990). The dominant basement formation within Ölbő area is the Mihály Phyllite. The several hundred meters thick formation consists of phyillite, calcareous phyllite and quartz phyllite. Bük Dolomite can be identified in a small tectonic block within the Ölbő area. The maximum thickness of the low grade Devonian Dolomite is about 280 m.

The Neogene porous sediment series have been directly deposited on the tectonically preformed surface of the basement rocks. This results very heterogenic lithology of the Miocene sediments deposited in different environment. The maximum thickness of the Miocene- Pannonian porous sediment series is 2000 m in the target area.

In the Ölbő area the Miocene sediments start with Karpatian to lower Badenian age Ligeterdő Formation, which is made up mainly of fluvial, subordinately brackish water gravel, conglomerate, sand and marl. The lower part of the lower Badenian is missing all over the area due to early Badenian tectonic movements and erosion. Badenian successions start with the upper part of the lower Badenian with abrasional basal breccia and conglomerate, locally with calcareous matrix. In marginal, shallow marine facies it is overlain by corallinacean limestone (Lajta Formation). It occurs in smaller patches with the thickness of some tens of meters. Nearshore facies are characterized by grey, greenish-grey sand-sandstone (Pusztamiske Formation). Offshore deep-basin (shallow bathyal) facies are represented by fine siliciclastic sediments: sandy silt, silty clay marl with sandstone intercalations and sandy-silty claymarl. In the Upper Badenian siliciclastic sediments were deposited (Szilágy Clay Marl Formation) due to the renewed flooding. With the onset of the Sarmatian a significant change occurred, which was triggered by the restriction of the open sea connections of the Central Paratethys. Biogenic calcareous sediments (mollusca bearing limestone, and oolithic limestone, Cerithium limestone) of shoreline facies (Tinnye Formation) and fine-siliciclastic sediments (grey, greenish-grey clay marl, sand, silty clay marl) of shallow-marine facies (Kozárd Formation) were deposited (Figure 2.8 and Figure 2.9).

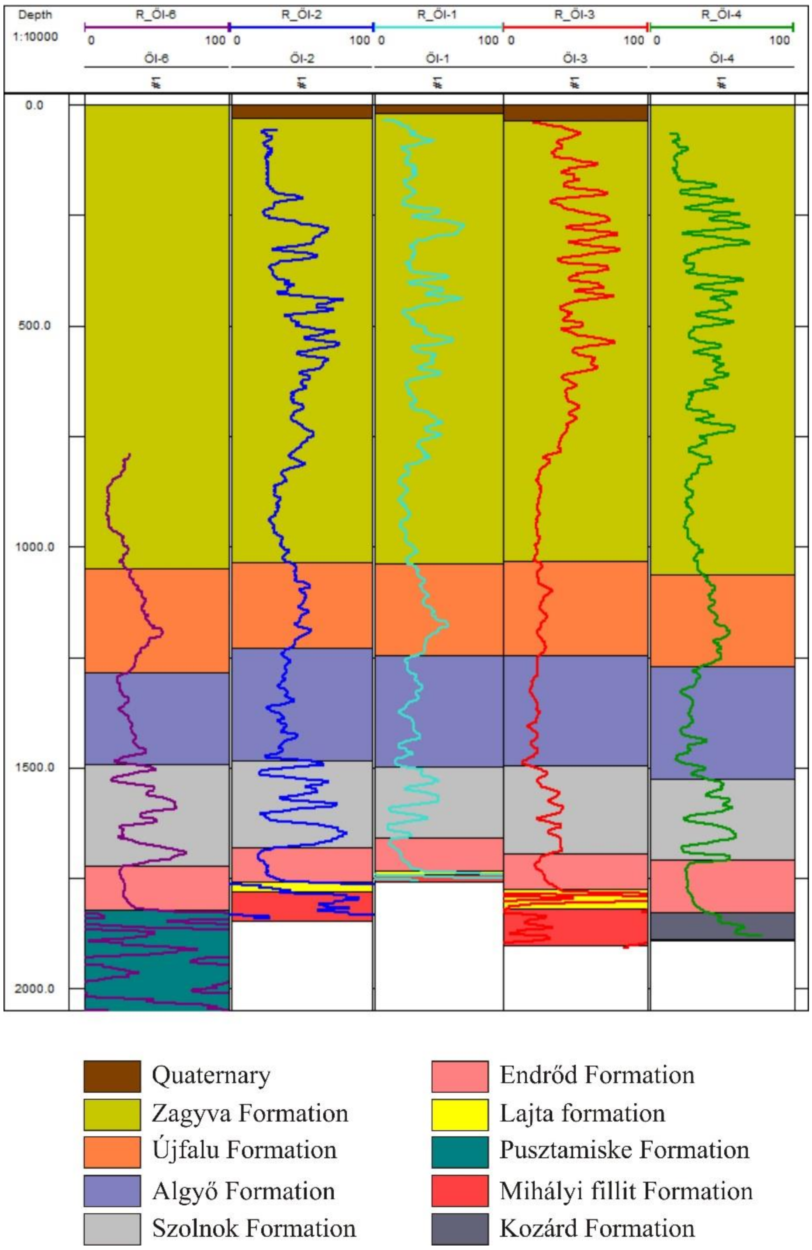

Figure 2.9 Interpretation of the Neogene formations based on the borehole logs in Ölbő area.

The Pannonian sequence deposited in the shelf-slope system which may have been started in the late Sarmatian and deposited during the Upper Miocene. The fine siliciclastic sequences of different facies are represented as the Endrőd Formation. It is made up homogeneous pelitic deposits. Distal turbidites are represented by separate sand bodies of the Szolnok Formation. Underwater slope (delta slope and basin slope) sediments are represented predominantly by dark grey clay marl as coarser sediments were carried further toward the basin to be deposited as turbidites (Algyő Formation). The mentioned Lower Pannonian sediments covering the Ölbő High block are represented with restricted thickness comparing the surrounding deeper basins.

The Lower Pannonian formations are overlain by 1200-1400 m thick Upper Pannonian sediment series. Sand bodies occurring along the fluvial delta fronts belong to the Újfalu Formation. Deposits of the alluvial plain are represented by the frequent alternation of fluvial and lacustrine fine grained sand, silt, clay and clay marl beds locally with lignite strips (Zagyva Formation). By the end of the Late Miocene, rivers running down from the neighbouring mountains filled up the basin, and a continental terrain came into being in the area of the former basin (Figure 2.8 and Figure 2.9).

Boreholes explored significant CO_2 gas field in the Badenian Lythottamnious limestone, but the tests of Öl-2 and Öl-3 boreholes indicate some gas in the Palaeozoic basement too.

The basement built from Devonian Dolomite of the Bük Formation. It is covered by the Miocene series which mainly consists of sediments deposited in the Badenian.

2.3.2 *Hydrogeology of the Ölbő area*

The Ölbő area is situated in the central part of the deep basin, far from the regional recharge and natural discharge areas. This region is the territory of the previously described intermediate and regional flow systems.

The Crystalline Basement Formations represent fractured aquifers, usually with low permeability. Nevertheless, in structural zones and the upper weathered zone their permeability can be higher, and can act as thermal water or CO_2 gas reservoirs. Due to its deep basinal position little information available about their hydrogeological characteristics and the locations of basement reservoirs. In general they can be characterized by intensive heterogeneity, decreasing fissure aperture closing downwards with depth, causing the decreasing of permeability. Due to tectonic effects hydraulic conductivity can be increased locally.

The Devonian Dolomite Formation is a special type of basement aquifers. It can be characterized as a fractured aquifer, with high permeability, which originates from multiple tectonic stresses, the reactivation of structural elements, and possible karstification during exposed periods. The aquifer comprises two separate blocks, at more than 1000 m depth. These blocks have different hydraulic connection with adjacent units, which results in varying hydrochemical characteristics. The block located in the Bük region has indirect recharge, with low (4000-14000 mg/l) TDS concentration. The block near Ölbő-Sárvár forms closed structure without any significant recharge, and this stagnant water has high total dissolved content (exceeds 30000 mg/l).

The Lower- and Middle Miocene layers have hydrogeological importance only in basin marginal position, or where they are deposited directly on the basement where they represent connected reservoirs with basement rocks. They are represented by Badenian or Sarmatian sands and limestones and can be characterized by double porosity and high permeability. These layers can be considered as porous reservoirs, with often direct hydraulic connection to the basement reservoirs. The widespread thin permeable layers of Badenian and Sarmatian shallow-marine clastic carbonates are usually surrounded by low permeability marl and clay, which results restricted recharge of the aquifers. The low grade of groundwater flow results extremely high TDS values. The thickness of the Badenian units varies between 10-60 meters, while the Sarmatian ones vary between 50-120 meters.

Within the several thousand meters thick Middle- and Upper Miocene-Pliocene basin fill complex the deep basin sediments and lower delta slope sequences mainly consist of clay, or sandy clay therefore act as regional aquicludes. They separate the flow system of the basement from the deep (usually thermal water) flow system of the porous formations of the Pannonian reservoir. The isolated permeable sand bodies derived from turbidites has no connections with other aquifer layers, therefore they have restricted hydrogeological importance.

On contrary the delta front and delta plain sedimentary succession is built up of alternating sand and sandy clay layers, large lenses reflecting the former shelf front, shelf and alluvial plain sedimentary environment. The Upper Pannonian sandy layers belong to the most important aquifers, as they supply both cold drinking water and thermal water.

The aquifer layers of the central part outcrop at the edges of the depression. Towards the interior part of the basin, the number of the sandstone aquifer layers increases, and simultaneously thickens, while porosity and permeability decrease as a result of sediment compaction within the young sedimentary basin. In general, the up to 10 meters thick sand bodies are lens-shaped and cannot be followed laterally for long distances. The sandy aquifer layers vary with aquitard clay and sandy clay layers. The vertical and lateral extent of the aquifer layers are varying quickly. Alternating sandy and silty layers cause that the permeability varies within wide range. These sediments are characterized by a strong anisotropy (Kh/Kv often higher than 5000 (Tóth et al., 2016) at a regional scale due to the frequent alternation of the sand, silt and clay layers. Although the permeability of the clayey-marly strata is 1–2 magnitude lower than that of the sandy units, this is still enough to provide hydraulic connection between the sand layers, thus make the entire Upper Pannonian sedimentary succession one hydro-stratigraphic unit characterized by an almost uniform hydrostatic pressure. This reservoir has good hydraulic connections and low total dissolved content (below 2000 mg/l).

The Quaternary sediments are important only in river alluvial formations. Their thickness does not exceed 100 m in Ölbő area.

2.3.3 Hydro-geochemical character of groundwater in the Ölbő area

The different hydro-stratigraphical units can be characterized by specific hydro-geochemical composition.

Groundwater of Quaternary formations usually is Ca-Mg-HCO_3 water type. The TDS values are between 500-800 mg/l. The dominant anion is HCO_3– (370-600 mg/l), the main cations are the Ca^{2+} (60-11 mg/l) and Mg^{2+} (20-50 mg/l), while Na+ content is between 10-40 mg/l.

Chemical composition of groundwater in the thick Upper Pannonian sediment series shows some differences in the depth intervals. This variance is caused by distinctive water-rock interactions along their different length pathways. The cold groundwater (depth until 500 m) has TDS values between 450-700 mg/l. This value is further increasing with depth and at the interval between 700-1300 m varies between 700-5000 mg/l. While the Ca-Mg-Na-HCO_3, Na-Ca-Mg-HCO_3 type water is the dominant in the upper part, the deeper thermal water can be characterized mostly by Na-Ca-HCO_3, Na-HCO_3 type water. The increasing Na/Ca ratio is due to the ion exchange process. Although HCO_3^- is the dominant anion (1300-4700 mg/l), in the deeper part the Cl^- content (70-1080 mg/l) is increasing too. This groundwater can be characterised by significant NH_4^+ and gas content as well.

The chemical composition of the Lower Pannonian water is known only from the wider region, and represents the aquifers with restricted hydraulic connection. The TDS values are high, between 5900-45900 mg/l, and the water types are $NaHCO_3$, Na-Cl-HCO_3 and Na-Cl.

The Miocene aquifers also can be characterized with high TDS values (6500-31700 mg/l). The chemical composition of groundwater is represented by Na-HCO_3, Na-HCO_3-Cl and Na-Cl types.

The groundwater of the basement formations are characterized by extremely high TDS values with Na-Cl water type. The Bük Dolomite was explored only by Rás-1 and Rás-2 boreholes, where TDS varies between 38000-71000 mg/l, while the Ölbő-2 and Ölbő-3 boreholes exploring Mihály Phyllite the TDS of groundwater is between 30000-113500 mg/l.

In general, we can conclude that due to water-rock interaction and longer pathways, about 500 m depth there is a significant change in the chemical composition of groundwater and in the case of almost every component. The TDS and Cl– concentration is increasing with depth, and in the lower flow system (below the regional aquitard) it can characterized high, in the basement extreme high values. The HCO_3– concentration is increasing with depth too, but at below the depth of about 1200 m there is no significant change in its value. It is important to point out, that with depth the amount of data is decreasing, which results increasing uncertainty in the data evaluation.

2.4 Application of Tool to the Pannonian Basin

The 3D Groundwater Vulnerability tool was tested in the Ölbő area in 5 km around the site centre. The distinguished geological units are listed in Table 2.1 (compare Figure 2.5).

Table 2.1. Identified geological units

Unit number	Formation	Lithology	Sedimentation environment
Unit 1	Quaternary	Sand, gravel, silt and clay	Fluvial environment
Unit 2	Zagyva F.	Altering thin layers of sandstone, silt and clay	Alluvial plain- along the shore of Lake Pannon
Unit 3	Újfalu F.	Cyclic repetition of sand, silts, clays,	Progradation of deltaic lobes on the shallow shelf of Lake Pannon
Unit 4	Algyő F.	Clay, marl, siltstone with sandy intercalations	Shelf margin slope
Unit 5	Szolnok F.	Alteration of fine to very fine standstone and siltstones/marls, with the dominance of sandstone	Turbidite lobes situated in the deep basin
Unit 6	Endrőd F.	Calcareous marl, silty marl	Several hundred deep bottom of Lake Pannon
Unit 7	Kozárd F.	Caly, claymarl, calcareous marl, sand	Near-shore, shallow marine environment
Unit 8	Pusztamiske F.	Gravel, conglomerate, calcareous silt	Near-shore, shallow marine environment
Unit 9	Lajta Limestone F.	Lythotamnious limestone, calcareous sand	Sallow marine (reef) environment
Unit 10	Bük Dolomite F.	Dolomite, dolomite breccia	
Unit 11	Mihály F.	Low grade metamorph phyllite, calcareous phyllite, quartz phyllite	

2.4.1 *Potential receptors*

Different types of potential receptors were determined in Ölbő area. The most important receptors are the Quaternary and Upper Pannonian (Zagyva Formation) drinking water aquifers (Aquifer of primary importance as a groundwater resource; receptor type „A”). Thermal aquifers are also considered (Aquifer of secondary importance; receptor type „B”). The depth of the drinking water aquifers varies between 50-250 m below surface, while the thermal aquifers are situated at the depth interval of 800-2500 m. The most important Upper Pannonian thermal water aquifer is represented by the Újfalu Formation.

The potential receptors were also classified based on the type of the water utilization, TDS content and depth. The applied classification is shown in Table 2.2. In this context Endrőd and Mihály Phyllite Formations are considered as not a groundwater resource receptor type “D”). The Lajta Limestone and the Büki Dolomite Formations can be characterized as important thermal aquifer in the wider region too, but due to their isolated settings at Ölbő area they were listed as “Aquifer of minor importance as a groundwater resource” (receptor type “C”) together with other less important Lower Pannonian thermal aquifers.

Table 2.2. Classification of receptors

GEOLOGICAL UNIT	RECEPTOR CLASSIFICATION
Quaternary	A
Zagyva	B
Újfalu	B
Algyő	C
Szolnok	C
Endrőd	D
Kozárd	C
Pusztamiske	C
Lajta Limestone	C
Mihály Phyllite	D
Bük Dolomite	C

2.4.2 *Hazards*

Regarding hazards characterisation fluid release mechanism was determined as “No permeability enhancement (passive) for conventional oil and gas”. There is no injection of fluid to maintain reservoir pressure.

2.4.3 *Intrinsic vulnerability*

The intrinsic vulnerability is a function of the geological setting (geometrical relationships and hydrogeological properties) and the hydrogeological conditions. It includes:

- the vertical and horizontal distance between source and receptor,
- amount of clay/mudstone in intervening units,
- type of flow in the intervening units,
- the presence of faults cross-cutting the intervening units and thus directly connecting the source and the receptor,

- solution features,
- anthropogenic features.

2.4.3.1 *Vertical and horizontal distance*

In the frame of analysing intrinsic vulnerability the value of the vertical separation distance between source and base of receptor varies in wide range as receptors are situated both in the shallow and deeper depth intervals. Location of source is considered at the depth of 1800 m below surface while drinking water aquifers are located between 50-250 m, geothermal aquifer layers (having secondary importance) are situated 800-2500 m. In some cases the location of the thermal water aquifers are deeper than the source or they are situated at the similar depth (Kozárd F., Pusztamiske F., Mihály Phyllite F., Bük Dolomite F.).

Lateral separation distance between source and receptor was considered the minimum value, due to presence of both the primary and secondary receptors direct in the under- and overlaying geological units.

2.4.3.2 *Amount of clay*

Due to the sedimentation environments most of the formations consist of altering sandy and clayey layers. Based on the geological sequences of the boreholes and wells the thickness of the total mudstones and clays in intervening units between source and receptor were established by simple addition. The total mudstone and clay thickness shows increasing trend from the source to the surface, although in the Upper Pannonian and younger formations (Újfalu F., Zagyva F., Quaternary sequences) don't form regional aquitard layers. Most of the Lower Pannonian formations (Algyő F., Szolnok F., Endrőd F.) dominated by clay layers. While the higher sand content layers of Algyő and Endrőd Formations appear in sporadical lenses the sand content of the Szolnok Formation form individual bodies separated by fine grained sediments due to the turbidit origin.

2.4.3.3 *Type of flow*

Potentential for groundwater flow within receptors was characterised based on permeability (Tóth et al., 2016). Low potential was dedicated to aquifers class A to C receptor, which are not fractured or consisting of > 50% of low permeability unconsolidated sediments (Algyő F:, Szolnok F., Kozárd F., Pusztamiske F.). Aquifers, class A to C receptors characterized by fractured (low connectivity of the fracture network) or consisting of > 50% medium permeability unconsolidated material are dedicated as medium potential category (Zagyva F., Újfalu F.). High potential was signed to class A to C receptor which extesively fractured (the Lajta Limestone with double porosity, the Büki Dolomite with highly connected fracture network) or consisting of > 50% of highly permeable unconsolidated sediments (Quaternary sediments).

Head gradient driving flow was identified as "Head gradient from source to receptor or head gradient unknown". According to the groundwater head data derived from borehole measurements there is significant head gradient from the source to the receptor in Upper Pannonian (Újfalu F., Zagyva F.) and Quaternary formations. The head gradient values are lower in the Lower Pannonian formations (Endrőd F., Szolnok F., Algyő F.). There is no significant head gradient from the source to the receptors in the case of some deep thermal water aquifers (Kozárd F., Pusztamiske F., Lajta Limestone F., Mihály Phyllite F., Bük Dolomite F.). In latter layers the density driven flow mechanism is the dominant instead of gravity driven flow.

2.4.3.4 *The presence of faults*

The region of the Kisalföld Basin is structurally divided by several faults and a nappe system. Even though groundwater flow is not influenced by tectonics and individual structures within the Ölbő area, while it determines the regional flow system in larger scale. Most of the structures are Pre-Pannonian, only a few reactivated and manifested in the Upper Pannonian sediments.

2.4.3.5 *Solution features*

There are no formations present in the region where dissolution of rock or karstification has created pathways by altering the porosity or hydraulic conductivity.

2.4.3.6 *Anthropogenic features*

Anthropogenic features-are represented only by the previously drilled boreholes. Since, these boreholes were created in the 60s and 70s with older technology, they have to considered as potential risk for contaminant transport or CO_2 leakage (Figure 2.10).

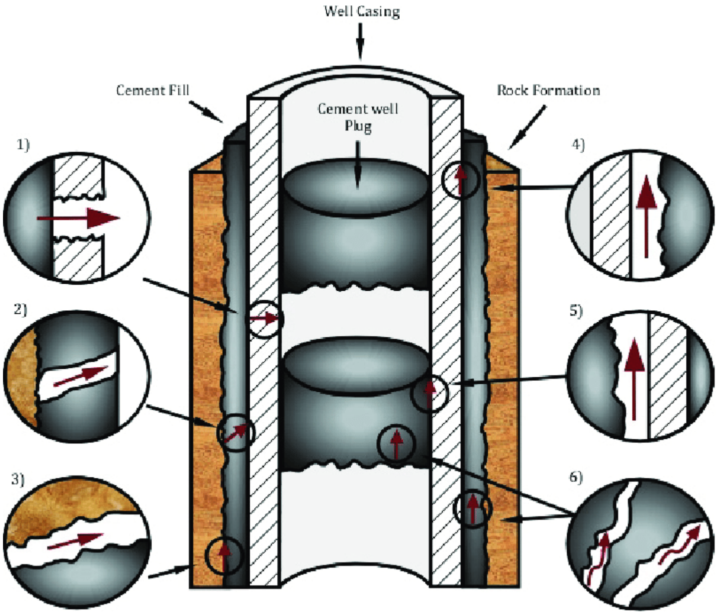

Figure 2.10 Overview of potential leakage pathways along an existing wellbore: 1) through the casing, 2) through fractures on the cement wall, 3) between the cement wall and formation rock, 4) between cement fill and casing, 5) between cement plug and casing, and 6) through the cement plugs (Recasens et al., 2017).

2.5 Discussion of the Pannonian Basin pilot

The vulnerability of the shallow aquifers takes into account the receptor importance, intrinsic vulnerability, hazards and the specific vulnerability to produce a classification of either low, medium-low, medium-high or high.

Performing the vulnerability analysis based on the common methodology developed in the frame of VoGERA project the summary table of the Ölbő area is shown in Table 2.3.

Table 2.3. Calculation of the specific vulnerability

Geological unit	Receptor classification	Intrinsic Vulnerability Score (IntV)	Hazard Score (H1xH2)	Specific Vulnerability Score (SpecV)	Risk group
Unit 1 (Quaternary)	A	30.5	2	61	Medium/Low
Unit 2 (Zagyva F.)	A	29.5	2	59	Medium/Low
Unit 3 (Újfalu F.)	B	31.5	2	63	Low
Unit 4 (Algyő F.)	C	37	1	37	Low
Unit 5 (Szolnok F.)	C	44.5	1	44.5	Low
Unit 6 (Endrőd F.)	D	47	1	47	Low
Unit 7 (Kozárd F.)	C	53.5	1	53.5	Low
Unit 8 (Pusztamiske F.)	C	57	1	57	Low
Unit 9 (Lajta Limestone F.)	C	63	1	63	Low
Unit 10 (Mihály Phyllite F.)	D	54	1	54	Low
Unit 11 (Bük Dolomite F.)	C	63	1	63	Low
CONFIDENCE		Low	High	Low	

Based on the “Specific Vulnerability Score” of the analysis (Table 2.3) the Ölbő area can be characterized Medium/Low vulnerability for the aquifer of primary importance as a groundwater resource and Low for the aquifer of secondary importance (mostly geothermal aquifers). This final indicator was calculated multiplying the Intrinsic Vulnerability Score and the Hazard Score.

Due to the geological settings, especially the high ratio of mudstone the Intrinsic Vulnerability Score is represented by relative low values. Since the pilot area is situated in a great sedimentary basin the properties of the porous basin fill sediments have decisive role and the tectonical structures have minor impact on vulnerability.

Lack of Mining activity in the Ölbő area this anthropogenic features does not endanger vulnerability. In contrast, wells and boreholes close to site of interest mean a potential risk for the aquifers, as they can shortcut the flowpaths. This is the most significant source of risk in the aquifers in Ölbő area, where large number of boreholes are situated due to the previous intensive hydrocarbon explorations.

The common methodology provides a preliminary estimation of the vulnerability, but in the case of any planned deep activity further detailed analysis is required.

3 Pilot Vale of Pickering

3.1 Introduction of Vale of Pickering pilot

The Vale of Pickering is located in Yorkshire, northeast England (Figure 3.1). This relatively flat, east-west oriented basin surrounded by higher grounds (i.e. the North York Moors in the north, Howardian and Hambleton Hills in the west, and Yorkshire Wolds in the southeast) has been considered for exploration for shale gas extraction. The area of interest covers approximately 20 km north to south, and 60 km east to west and it is part of the catchment of the River Derwent. The land use is primarily arable farming, while Scarborough, Pickering and Malton are the main urban centres.

In response to proposals of shale gas exploration, the BGS and Public Health England, an executive agency of the Department of Health and Social Care (DHSC), in collaboration with several UK public universities (Birmingham, Bristol, Manchester and York), conducted hydrogeological investigations in the area to establish the environmental baseline of groundwater composition (Bearcock et al., 2015; Bell et al., 2017; Smedley et al., 2015, 2017). As part of the research activities, 3D geological models of the superficial and bedrock geology were developed (Ford et al., 2015; Newell et al., 2015), as well as the collection of extensive data sets of surface and groundwater composition, seismicity, ground motion, air quality, radon and soil gas (Ward et al., 2017, 2018). The location of the boreholes included in the monitoring network is shown in Figure 3.2.

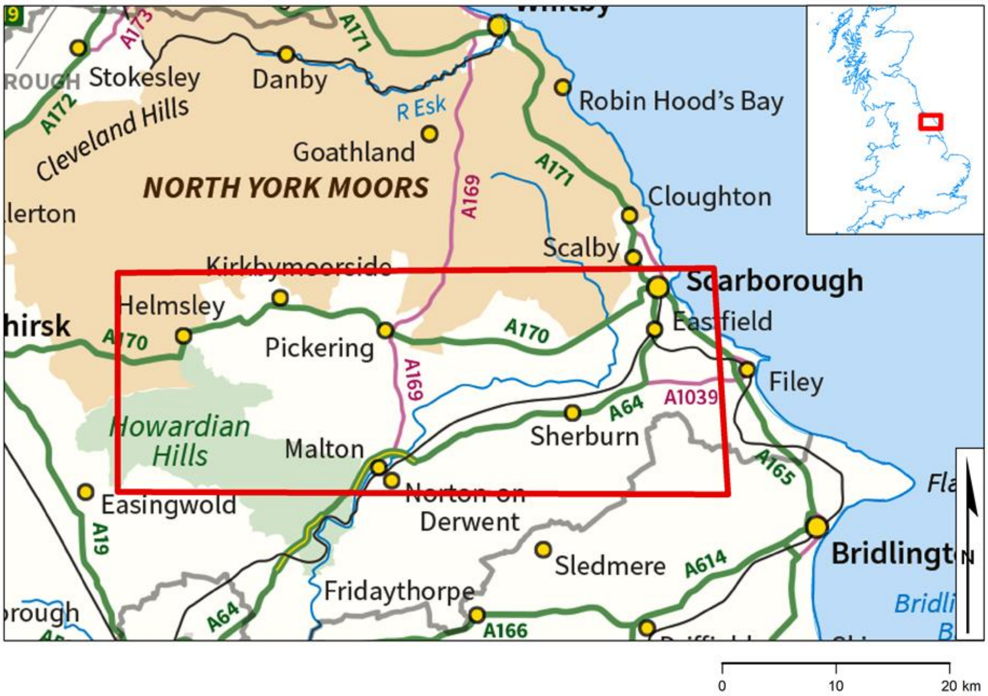

Figure 3.1 Vale of Pickering Pickering pilot area. © Crown Copyright and/or database right 2021. Licence number 100021290 EUL.

3.2 Geology and hydrogeology of the Vale of Pickering

3.2.1 Geo-hydrological setting

The Vale of Pickering is an extensional sedimentary basin (Cleveland Basin) filled by a sequence of Permian to Quaternary geological units (Figure 3.2). The potential target for shale gas extraction is the Bowland Shale formation (Andrews, 2013), which lays at a depth of around 2000 m below sea level. The geological units above the Bowland Shale include two aquifers containing important groundwater resources. The shallowest aquifer consists of Quaternary sediments, of mainly glaciolacustrine origin with marginal alluvial fan deposits. Borehole logs show that these sediments have variable thickness up to 40 m, although generally thinner or absent near the north and western margins of the basin and around the town of Kirby Misperton in the centre of the Vale.

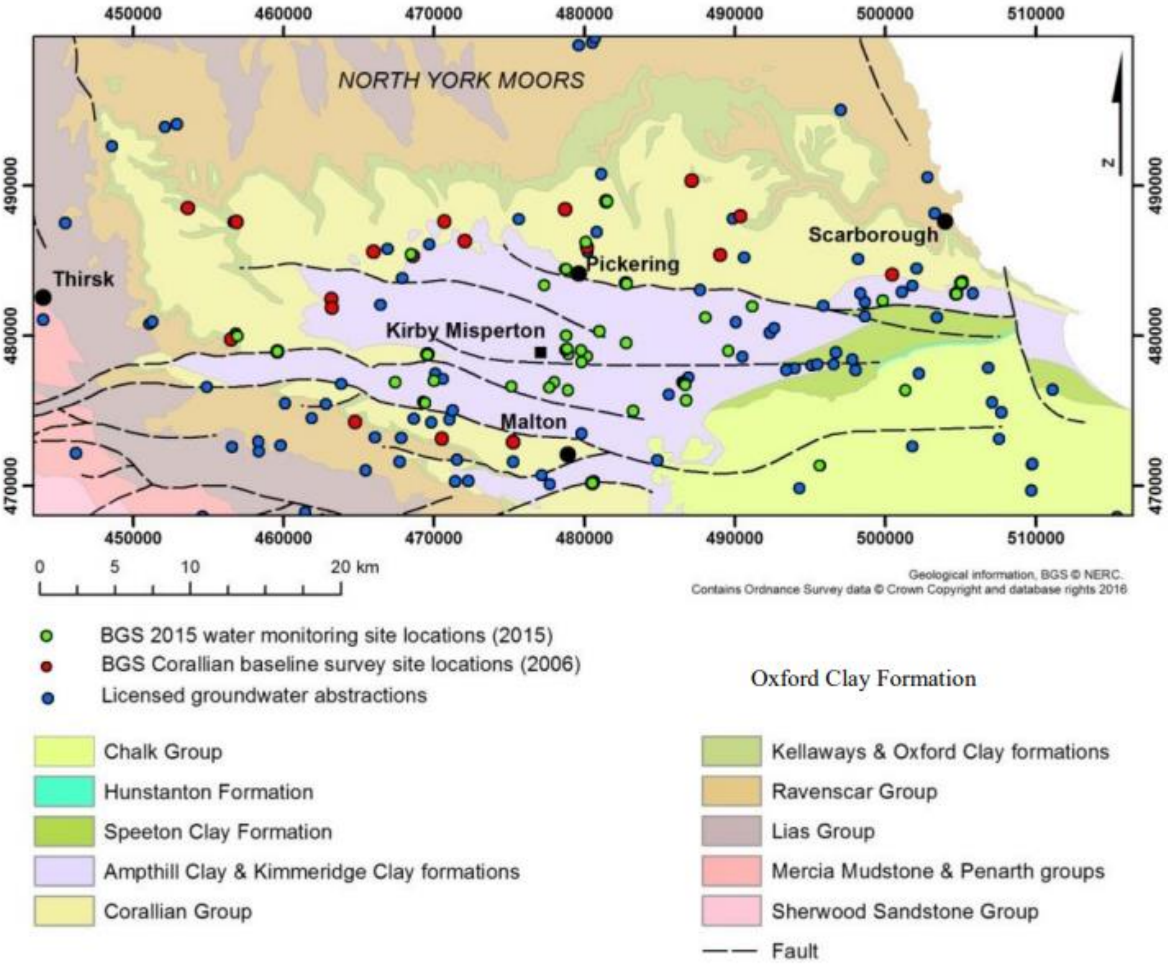

Figure 3.2 Regional bedrock geology map of the Vale of Pickering, showing water abstraction boreholes and past groundwater investigations (from Ward et al., 2017). Geological information, BGS @ NERC. Contains Ordnance Survey data © Crown Copyright and database rights 2016.

The Quaternary deposits overlie the Jurassic Ampthill & Kimmeridge Clay formations which consists of a series of mudstone and siltstone with occasional sandstone horizons (Reeves et al., 1978). Sandy horizons and the weathered upper sections of the less permeable deposits can contain locally important amounts of groundwater. For this reason, both the Quaternary deposits and the upper weathered Ampthill/Kimmeridge formations have been included into the so called "Superficial" aquifer system (Ward et al., 2017).

The main aquifer in the Vale of Pickering is the Jurassic Corallian (Limestone) Group, which consists of a 100 m – 150 m thick sequence of calcareous sandstones and limestones. This unit is designated as a Principal Aquifer[1] according to the Environment Agency of the United Kingdom government's Department for Environment, Food and Rural Affairs (DEFRA), and it used for both public and private supply. As shown in the geological map of Figure 3, this formation crops out forming the northern and southern margins of the Vale. Here the aquifer is unconfined and the saturated zone is generally thin (Foley et al., 2012). A number of springs along the margins of the Kimmeridge Clay discharge groundwater from the unconfined aquifer (Smedley et al., 2017). In the Vale, the Corallian Limestone underlies the less permeable Ampthill/Kimmeridge Clay formations, and therefore the aquifer is confined. The confined Corallian Limestone aquifer at the centre of the Vale is not exploited because of its depth (typically >200 m) and elevated salinity of groundwater. The main source of groundwater recharge in the Corallian aquifer is direct infiltration of rainfall at the outcropping areas along margins of the Vale of Pickering. The upper reaches of the River Derwent in the northeast also provide recharge to the aquifer (in the order of 35 ML day^{-1}, Foley et al., 2012) while further downstream the river is groundwater fed (Carey & Chadha, 1998). The distribution of groundwater head in the Corallian indicates that flow is from the elevated outcropping areas towards the confined section of the aquifer in the centre of the Vale. Transmissivity values estimated from pumping tests are very variable ranging from 35 m^2 day^{-1} up to 40,000 m^2 day^{-1} (Allen et al., 1997). As confirmed by the results of tracer tests (Foley et al., 2012), this variability is linked to the presence of dissolution features and karstic fissures embedded in a network of much smaller fractures (<1 mm in aperture), which are responsible for a significant portion of the total flow. Consequentially, groundwater flow behaviour in the Corallian aquifer is that typical of a dual permeability aquifer

The base of the Corallian aquifer correspond to the upper surface of the Jurassic Oxford Clay formation. In the Cleveland Basin, this formation consists mainly of calcareous mudstones. Below, the geology in the basin becomes progressively older, consisting of Jurassic (Ravenscar Group and Lias Group), Triassic, Permian (Sherwood Sandstone Formation, Roxby Formation, Zechstein Group), and Carboniferous units. A geological cross section is shown in Figure 3.3. The Bowland Shale formation, of the Craven Group, is considered a potential target for shale gas extraction in the Vale of Pickering as well as in other areas in England (Andrews, 2013). The lithology is mostly characterised by organic-rich marine shale deposits of Carboniferous Age. In the Vale, the depth of upper surface ranges between 1700 m and 2200 m, at the contact with the overlying Millstone Grit Group. There is uncertainty regarding the thickness of the Bowland Shale in the Vale of Pickering due to the absence of sufficiently deep borehole data. Conventional gas is extracted from the Permian Zechstein group above, which has an upper surface between 1400 m (north) and 1000 m (south) below ground level, and a total thickness of approximately 350 m (Loveless et al., 2018).

---

[1] Principal Aquifer – "These are layers of rock or drift deposits that have high intergranular and/or fracture permeability - meaning they usually provide a high level of water storage. They may support water supply and/or river base flow on a strategic scale. In most cases, principal aquifers are aquifers previously designated as major aquifer." – (Environment Agency, 2017)

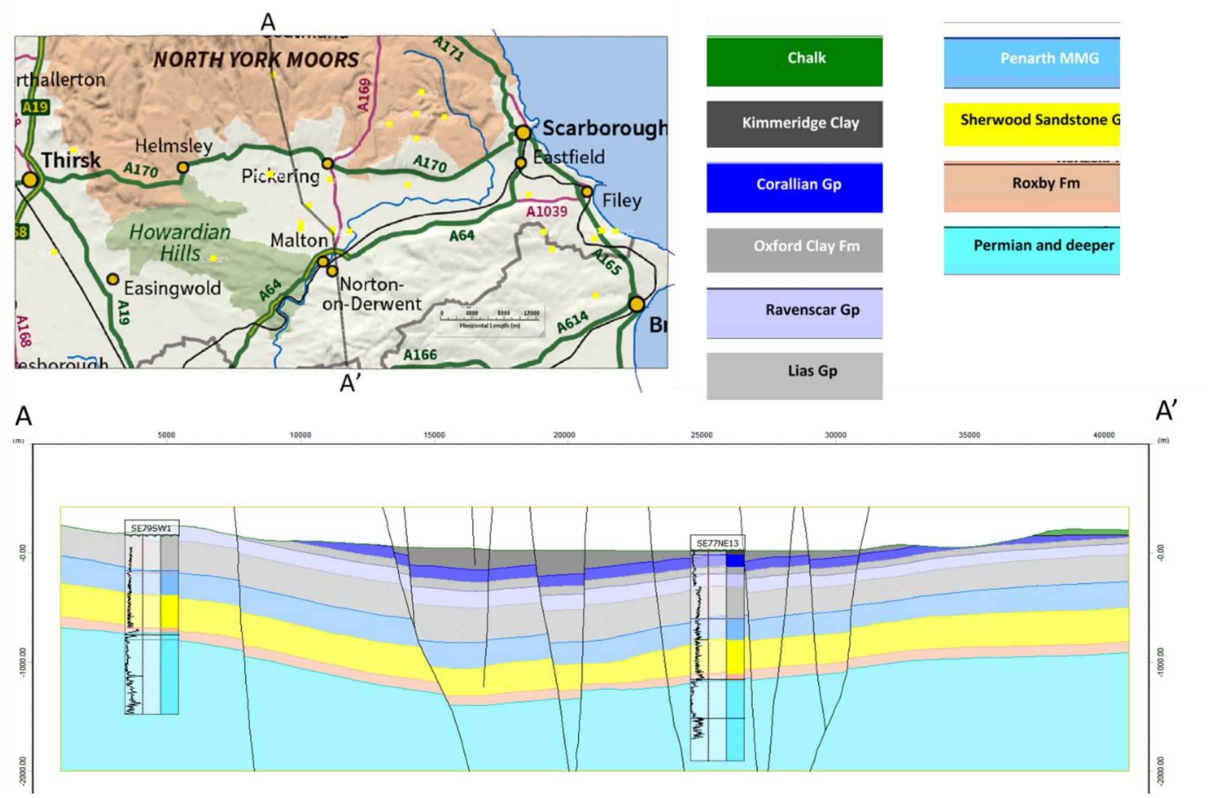

Figure 3.3 Geological cross section of Vale of Pickering (modified from Newell et al., 2015).

3.2.2 Hydrogeochemistry

Hydrochemical characterisation of groundwater samples from the Superficial and Corallian aquifers have been performed as part of the baseline monitoring program (Bearcock et al., 2015; Smedley et al., 2017; Ward et al., 2017). Summarising the main findings, groundwater from the Superficial aquifer has a very variable composition, with a range from $CaHCO_3$ to $Na\text{-}HCO_3$ types, and it is anoxic in character. Groundwater in the unconfined Corallian is mainly $Ca\text{-}HCO_3$ dominated, while the confined Corallian in the central part of the vale is $Na\text{-}HCO_3$ dominated. Confined groundwater has also high concentrations of dissolved methane, which is most likely of biogenic rather than thermogenic origin. Further sampling and geochemical characterisation of the Corallian aquifer (Bell et al., 2016, 2017) revealed methane concentrations above detection limit, although not as high as to exceed the lower explosion limit (1600 µg/l).

3.2.3 Structural control on groundwater flow and presence of faults

A geological model of the Vale of Pickering including the post-Permian units was developed by Newell et al. (2015). The model highlights the strong structural control on the geometry of the Corallian aquifer and adjacent strata (Figure 3.4). In particular, it shows that the continuity of the Corallian Limestone is interrupted by a system of faults, with a predominately E-W strike. Although hydrogeological data are missing, it is likely that faulting affects groundwater flow in the confined sections of the aquifer, resulting in a compartmentalisation of the aquifer. The level of hydraulic separation between the different blocks is not understood as well as whether the faults are listric (i.e. they flatten out with depth) within the Zechstein/Permian or through-going. The answer to this question has implications for delineating potential pathways from the Bowland Sahel to the Corallian aquifer.

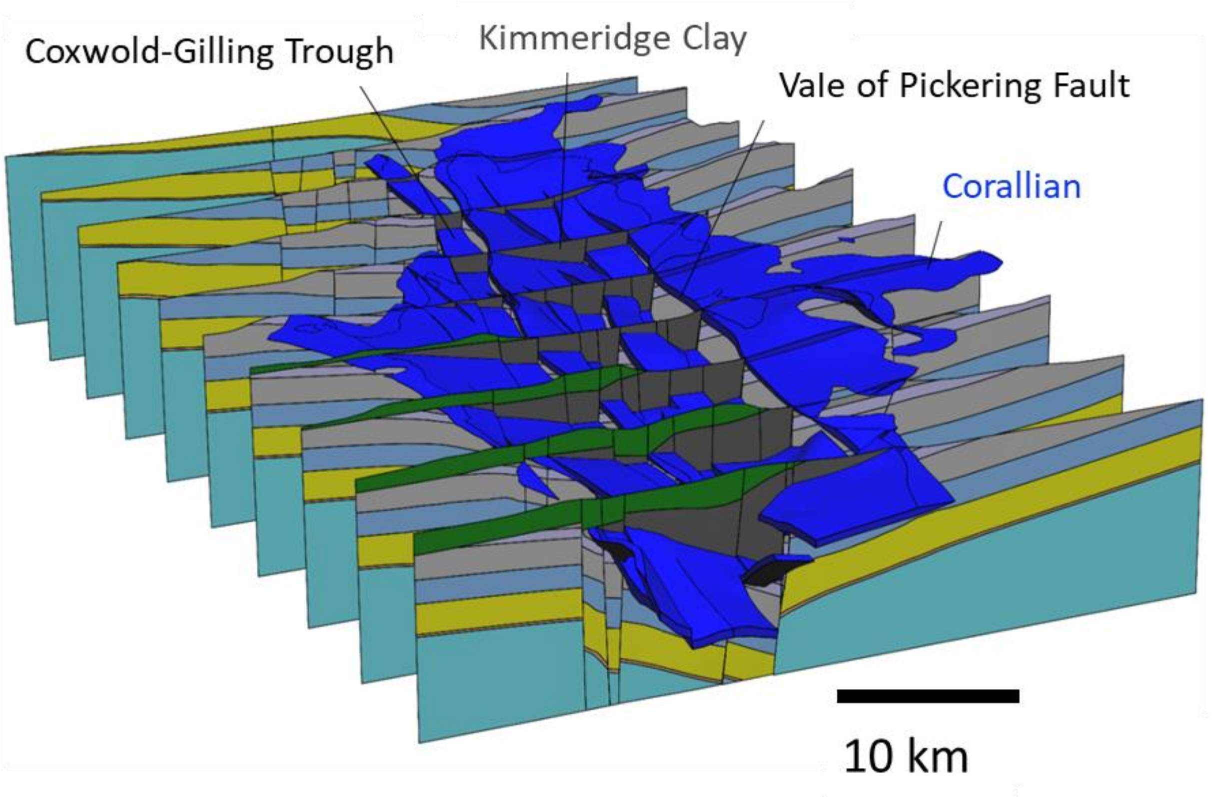

Figure 3.4 Geological modelling of the Vale of Pickering (from Newell et al., 2015).

3.3 Results for the Vale of Pickering

The Vale of Pickering has a number of conventional oil and gas wells, along with an exploratory shale gas well in the centre of the site. The shale gas well was drilled in 2013, and permission to hydraulically fracture was granted in 2016. However, no hydraulic fracturing activity has taken place to date. In this section, we present the results of the application of the screening approach GWV 3D (see VoGERA deliverable WP4, 4.2) to estimate the vulnerability of potential groundwater receptors to a hypothetical extraction activity of shale gas from the Bowland Shale (Craven Group) in the Vale of Pickering. The area of interest for the vulnerability assessment is assumed to be located just south of the Kirby Misperton village (Figure 4.1) and to have a radius of 2000 m around a shale gas well pad. The extraction well is assumed to reach the target shale unit at an approximate depth of 2000 m and has a lateral extension of 1000 m within the target unit. A phase of high-volume hydraulic fracturing to enhance the permeability of the shale rock is also assumed to be part of the planned activities.

Screening results (intrinsic vulnerability, specific vulnerability and risk group) are shown in Table 3.1. In relation to shale gas extraction activities in the Bowland Shale, the intrinsic vulnerability scores for the receptors vary from 26.5 to 51. The minimum intrinsic vulnerability score was calculated for a receptor in the Oxford Clay Formation. The maximum score corresponds to the Millstone Grit Formation which directly overlies the Bowland Shale. The specific vulnerability scores consider the hazard associated with shale gas extraction activities such as the implementation of high-volume hydraulic fracturing. This technique could potentially generate preferential pathways and overpressures in the subsurface driving potential contaminants from deep to shallower receptors. The level of confidence of the specific vulnerability scores is low due to the uncertainties associated with the direction of the head gradients. A risk group was assigned to each receptor by combining the specific vulnerability score and the receptor class (see Table 2 in VoGERA WP4, D4.2).

The final risk classification reflects the value of the groundwater resource within each geological unit (i.e. the receptor classification). In fact, the Corallian aquifer is classified in the medium/high risk for shale gas extraction, while the Millstone Grit Formation is classified as low risk despite having the highest specific vulnerability score. Similarly, the Kimmeridge Clay, Ravenscar and Sherwood Sandstone, which are class "B" receptors, are classified as medium/low risk in relation to shale gas extraction, while the remaining potential receptors (class "C" and "D") are in the low receptor risk group. By lowering the receptor class of the Sherwood Sandstone from "B" to "C", which could be justified by the poor quality of the groundwater resource due extremely high salinity reduces the final estimated risk from medium/low to low.

Table 3.1 Scores for the vulnerability screening for a hypothetical shale gas extraction activity in the Vale of Pickering. The Bowland Shale is the target formation.

Geological unit	Receptor classification	Intrinsic Vulnerability Score (IntV)	Hazard Score (H1xH2)	Specific Vulnerability Score (SpecV)	Risk group
Kimmeridge Clay Fm.	B	33.5	8	268	Medium/Low
Corallian Group	A	41	8	328	Medium/High
Oxford Clay Fm.	D	26.5	8	212	Low
Ravenscar Fm.	B	33.5	8	268	Medium/Low
Lias Group	C	31.5	8	252	Low
Mercia Mudstone Group	C	37	8	296	Low
Sherwood Sandstone Group	B	42	8	336	Medium/Low
Zachstein Group	D	38	8	304	Low
Millstone Grit Group	D	51	8	408	Low
Bowland Shale					
CONFIDENCE		Low	Low	Low	

3.4 Application of Tool for the Vale of Pickering

In this section we present the assumptions and the data behind the rating of the factors considered by the GWV 3D screening tool, which resulted in the results presented in Table 3.1.

3.4.1 *Geological sequence*

The representative geological sequence for the area of interest was derived from the National Geological Model UK3D ((Waters et al., 2016), which is a national-scale 3D geological model representing the geology of Great Britain from ground surface up to 6.5 km in depth. E-W and N-S cross sections of the 3D model across the area of interest were used to understand the lateral and vertical geometry and to estimate the depths of the top and the base of the geological units (Table 3.2). Published data and interpretations regarding the geology of the Vale were also considered for the development of the conceptual geological model of the area of interest (Ford et al., 2015; Newell et al., 2015). Lithological descriptions of the units were taken from the memoir of the 1:50000 geological sheet n. 52 (Powell et al., 1992) and the official BGS Lexicon (https://www.bgs.ac.uk/technologies/the-bgs-lexicon-of-named-rock-units/). In particular, the information regarding the volumetric fraction of mudstone and clay was used to estimate a cumulative thickness of these low-permeability layers within each unit.

Table 3.2 Geological sequence for the area of interest in the Vale of Pickering, with relative receptor and flow potential classifications of the receptors.

Geological unit	Lithology	Depth top (m)	Dept base (m)	Receptor Classification	Flow potential
Kimmeridge Clay Fm.	Shale/claystone (100%)	0	-178	B	Medium
Corallian Group	Limestone (0%)	-178	-285	A	High
Oxford Clay Fm.	Shale, siltstone and sandstone (33%)	-285	-363	D	Not an aquifer
Ravenscar Fm.	Sandstone, some shale (33%)	-363	-633	B	Medium
Lias Group	Shale (100 %)	-633	-868	C	Low
Mercia Mudstone Group	Mudstone (100 %)	-868	-1072	C	Low
Sherwood Sandstone Group	Sandstone (0%)	-1072	-1246	B	Medium
Zachstein Group	Anhydrite and dolomite	-1246	-1620	D	Not an aquifer
Millstone Grit Group	50 % mudstone and sandstone (50%)	-1620	-1988	D	Not an aquifer
Bowland Shale	Shale	-1988	-2219		

The classification of the receptors in terms of value of the groundwater resource was initially based on aquifer designations obtained from the metadata integrated into the UK3D model as well as from aquifer designations form the UK Environment Agency. In particular, the Kimmeridge Clay was designed as “B” receptor given the number of boreholes abstracting groundwater of potable quality at moderate yields (~ 5 L/s). The Corallian Group was assigned to highest value class “A” being the unit a principal aquifer in England according to the Environment Agency. The Sherwood Sandstone is also designated as a principal aquifer. However, in the area of interest, this unit is very deep and groundwater sampling from a deep borehole in the area showed extremely high TDS values ranging from about 58,000 mg/L up to 142,700 mg/L (for reference TDS of seawater is around 35,000 mg/l). For this reason, this unit was ranked as a “B” receptor. Known unproductive formations (Oxford Clay) or formations were water quality data indicated extremely poor water quality due to very extreme were salinity classified as “D” (Zechstein and Millstone Grit Groups). The Ravenscar Formation is a secondary aquifer in certain parts of England and therefore was classified as a potential “B” receptor. Similarly, the Mercia Mudstone and the Lias Group are designated as secondary aquifers by the EA. However, groundwater resources within these units in the area of interest is likely to be of very poor quality given the depth. Therefore, they were both classified as potential “C” receptors.

In terms of flow potential, all the units are expected to have a mixture of intragranular and fracture flow. However, there is very high uncertainty regarding the permeability of the matrix and the connectivity of fractures due to lack of hydraulic testing data, especially for the deeper units. For the Sherwood Sandstone, BGS conducted hydraulic testing of a deep borehole (max depth of 500 m) in the area, which indicated a hydraulic conductivity in the order of 0.1 m/day. The dolomitized and fractured carbonates of Zechstein Group has porosity of around 0.12 and a permeability of 0.5–1.5 mD according to Harrison et al. (2020). Flow potential is assumed to be high in the Corallian aquifer given the high transmissivity resulting from the presence of well-connected fractures and dissolution features (Foley et al., 2012; Reeves et al., 1978). A medium flow potential is assumed for the Ravenscar Group and Kimmeridge Clay Formation although the confidence on these attributions is low.

3.4.2 Intrinsic Vulnerability scoring

The ratings assigned to the factors considered for estimating the intrinsic vulnerability of the potential receptors are presented in Table 3.3.

In the area of interest the Bowland Shale which can be potentially targeted for shale gas extraction occurs at a depth of about 2 km. Therefore, the calculated vertical separation between the target formation and the Corallian aquifer is more than 1700 m. Without considering any other vulnerability factor, Such vertical separation can be considered very safe in terms of risk of contamination of the aquifer from deep shale gas extraction, hence the rating of 1 for a potential receptor in this formation. Similar considerations apply for the uppermost units in the geological sequence. The highest rating (highest intrinsic vulnerability) was assigned to the Millstone Grit Group since this unit directly overlies the target shale formation. A uniform zero rating was assigned for the lateral separation since no unit is adjacent to the target formation. The level of confidence of these ranking is medium.

The geological sequence in the area of interest is characterised by the presence of relatively thick layers of low permeability mudstones acting as barriers to the transport of potential contaminants from depth towards shallow receptors. In particular, 50% of the Millstone Grit unit is assumed to consist of mudstone, resulting in a cumulative thickness of 184 m. The Mercia Mudstone and the Lias Group are also thick (> 200 m) mudstone units. Accordingly, the ratings of the intrinsic vulnerability factor considering the presence of low-permeability sediments in the intervening units between target unit and the receptor (except for the Millstone Grit) are generally very low to low, with values ranging from 1 to 2 with a medium level of confidence.

The rating of the factor for the groundwater flow potential (GFP in Table 3.3) ranges from 0 (Receptors of class "D") to 3 ("High flow potential"). The rationale for this rating is discussed in Section 3.4.1 as well as the assigned low confidence level.

Table 3.3 Rating of the intrinsic vulnerability factors for the Vale of Pickering Pilot study.

Geological Unit	VS	LS	MIU	GFP	F	SF	M	BH
Kimmeridge Clay Fm.	1	0	1	2	3	0	0	2
Corallian Group	1	0	1	3	3	2	0	2
Oxford Clay Fm.	1	0	1	0	3	0	0	2
Ravenscar Fm.	1	0	1	2	3	0	0	2
Lias Group	2	0	1	1	3	0	0	2
Mercia Mudstone Group	2	0	2	1	3	1	0	2
Sherwood Sandstone Group	3	0	2	2	3	1	0	2
Zachstein Group	5	0	2	0	3	1	0	2
Millstone Grit Group	8	0	5	0	3	0	0	2
Confidence level	*M*	*M*	*M*	*L*	*M*	*H*	*H*	*H*

VS: Vertical separation between target unit and the base of the receptor; LS: Lateral separation between target unit and the base of the receptor; MIU: Mudstones and clays in intervening units between target unit and the receptor; GFP: Groundwater flow potential; F: Faults cutting intervening units and receptor; SF: Solution features in intervening units and receptor; SF: Solution features in intervening units and receptor; M: Anthropogenic features-mines close to site of interest; BH: Anthropogenic features-boreholes close to site of interest.

As shown in Figure 3.4, the subsurface below the area of interest is likely to be heavily faulted. Several important large-scale faults are also marked in the geological map of the area (Figure 3.3). According to the geological interpretation presented by Newell et al. (2015), these faults offset the post-Permian bedrock units. However, there is no data to confirm whether the fault planes cut through the Carboniferous units or they become listric in the more-ductile anhydrite units of the Zechstein Group. For the vulnerability assessment, a worst-case assumption was made and the faults are assumed to cut the pre-Permian units as well as those below. With this assumption, a rating equal to 3 (out of 4) was assigned to all the units. The confidence level of this rating is medium given the lack of data regarding the hydrogeological properties of the fault zones.

The presence of solution features in the Corallian Limestone is attested from direct observations such as sinking rivers and borehole inspections and from the interpretation of tracer and pumping tests (Allen et al., 1997; Carey & Chadha, 1998; Foley et al., 2012). Therefore a rating equal to 2 was assigned to the vulnerability factor considering solution features in intervening units and receptor (*SF* in Table 3.3). The lithology of some geological units may also suggest the presence of solution features. In particular, anhydrite and dolomite strata are known to be present in the Zechstein Group, while anhydrite and gypsum rich layers in the Sherwood Sandstone and Mercia

Mudstone units have been documented in the logs of boreholes in the Vale. A rating of 1 and a medium confidence level were assigned to these units.

No historic or present-day mining activities are known in the area of interest, and therefore a zero rating was assigned to the factor considering the proximity mines (*M* in Table 3). However, other antropic features that could represent preferential flow paths for the movement of potential contaminants are present within the area of interest. These are a number of wells extracting gas from the Zechstein Group (Harrison et al., 2020). A rating equal to 2 was therefore assigned to all the geological units for this factor (i.e. BH in Table 3)

3.4.3 *Specific Vulnerability scoring*

The hazard assessment for the estimation of the specific vulnerability score is shown in Table 3.4. The rating assigned to the realise mechanism hazard (H_1) considers the permeability enhancement of the target formation by means of high-volume hydraulic fracturing, which is commonly done in the initial phase of a shale gas extraction operation. The overpressurisation of the subsurface to induce the fracturing of the shale rocks could potentially create a driving hydraulic gradient towards shallow receptors. However, pressure data are not available to clearly identify the direction of the hydraulic gradient in all different units. In the absence of data, the GWV 3D approach assumes that there is an upward head gradient from the target formation to the receptor (i.e. the worst-case scenario) in accordance with the precautionary principle (H_2 = 2). The confidence for this hazard is low except for the Kimmeridge Clay and Corallian Group where artesian conditions have been observed.

Table 3.4 Hazard worksheet for the Vale of Pickering in GWV 3D.

Geological unit	**Release mechanism hazard (H_1)**		**Head gradient driving flow (H_2)**		**Hazard score**	**Confidence**
	Rating	**Confidence**	**Rating**	**Confidence**		
Kimmeridge Clay Fm.	4	High	2	Medium	8	Medium
Corallian Group			2	Medium	8	Medium
Oxford Clay Fm.			2	Low	8	Low
Ravenscar Fm.			2	Low	8	Low
Lias Group			2	Low	8	Low
Mercia Mudstone Group			2	Low	8	Low
Sherwood Sandstone Group			2	Low	8	Low
Zachstein Group			2	Low	8	Low
Millstone Grit Group			2	Low	8	Low
Bowland Shale						

3.5 Discussion of the Vale of Pickering

The application of the GWV 3D tool provided an assessment of the vulnerability of groundwater resources as well as of the risks associated with shale gas extraction activities in the Vale of Pickering.

Intrinsic vulnerability scores generally decrease with the vertical separation from the target Bowland Shale formation. The slightly higher scores estimated for the Corallian Group and Kimmeridge Clay are the result of higher vulnerability of these two units in relation to higher flow potential compared to deeper units and to the presence of known solution features in the Corallian Group. For the estimation of the intrinsic vulnerability, it has been assumed that multiple faults could provide potential pathways for all of the units within the area of interest. This assumption is quite speculative at the moment and it was made according to a worst-case scenario approach. To increase the confidence in the assessment, additional data are required to improve the understanding of the geometry and extension of the faults and of their hydraulic properties. Similarly, a characterisation of the hydraulic head or pressure field in the deeper formations would increase the confidence regarding the direction and magnitude of the hydraulic head gradient, which in the vulnerability assessment was assumed to drive potential contaminants from the deep towards the shallow subsurface. This assumption was also made in favour of safety.

With the assumptions made for the intrinsic vulnerability assessment, the estimated risk for the considered receptors ranges from medium/high to low, with the highest identified risk group estimated for the Corallian Limestone aquifer. The classification of the receptors is a fundamental step in the risk analysis. For instance, downgrading of the potential receptor class of the Sherwood Sandstone and the Ravenscar Group from “B” to “C” would lower the risk group of these two units from medium/low to low, which is potentially a more realistic scenario given the very low quality of the groundwater resources within these two formations in the area of interest.

4 Roer Valley Graben Fault structures from seismic data for the Veghel and Tilburg pilots, the Netherlands

4.1 Introduction of Dutch pilot areas

The Peel boundary fault and Gilze-Rijen faults are part of a major fault system in the Netherlands separating western Noord-Brabant, the Roer valley Graben in the center and the Peel Block in the east (Figure 4.1). We chose the Peel Boundary Fault near Veghel as our main Dutch pilot site for VOGERA for which 2D seismic data is available. Additional to the Veghel pilot, we used 3D seismic data for the area around Tilburg, to demonstrate the additional value of such measurements for fault characterization (see section 4.4.4 for details). The area around Tilburg is known for complex fault patterns around the Gilze-Rijen Fault zone (Figure 4.1). The Veghel pilot is located on the Northeastern edge of the Roer Valley Graben, whereas the Tilburg pilot and the Belgian Rauw fault pilot are located on the opposite side of the Graben (compare Figure 6.1). In a third Dutch pilot, the shallow groundwater composition in the entire province of Noord-Brabant has been investigated for influences from the deep subsurface.
All three pilots lie within the area of the cross boundary demonstration project H3O-PLUS, which is part of the GeoERA project RESOURCE, also within the Groundwater theme. The faults are included in the fault database that has been created in the GeoERA project HIKE, part of the Energy theme (Van Gessel et al., 2021).

Chapter 4 of this report describes the Veghel and Tilburg pilots which focus on the structural tectonic setting as well as the structure of the fault zones and the associated damage zones. Chapter 5 covers the hydrogeochemical and tracer studies that were carried out in the Noord-Brabant pilot.

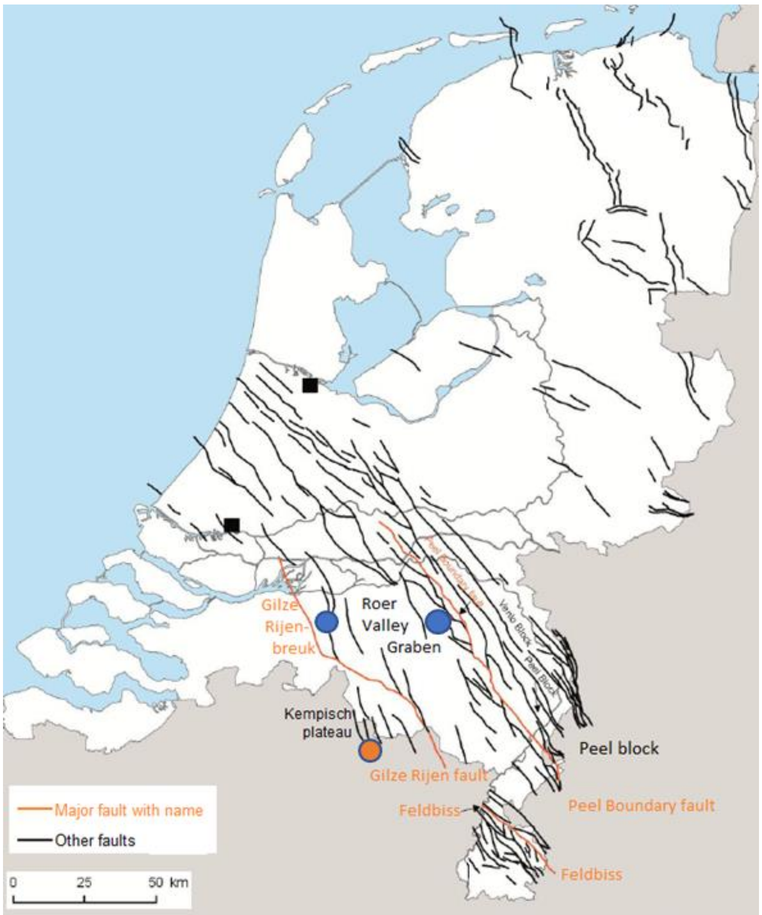

Figure 4.1 Faults in the Netherlands with the Peel Boundary Fault as major fault in the fault system on the Northeastern edge of the Roer Valley Graben (Dutch pilots marked with blue symbol, Rauw fault Belgium in orange symbol)

4.1.1 The Veghel Fault

Currently, there are no deep energy-related activities near the fault, but the groundwater abstraction BW27 of water company Brabant Water is located nearby. The rationale for the choice of the Veghel area as pilot is that the decrease of the groundwater heads due to the pumping will induce upward transport along the fault from the deep subsurface if there is a hydraulic connection.

In the shallow subsurface, there are abstraction wells for the production of drinking water and groundwater monitoring wells, from a local dedicated monitoring network and the provincial groundwater monitoring network. Both groundwater heads and groundwater quality are monitored. The quality of the abstracted water is also monitored. Groundwater is also abstracted for agricultural purposes in the area.

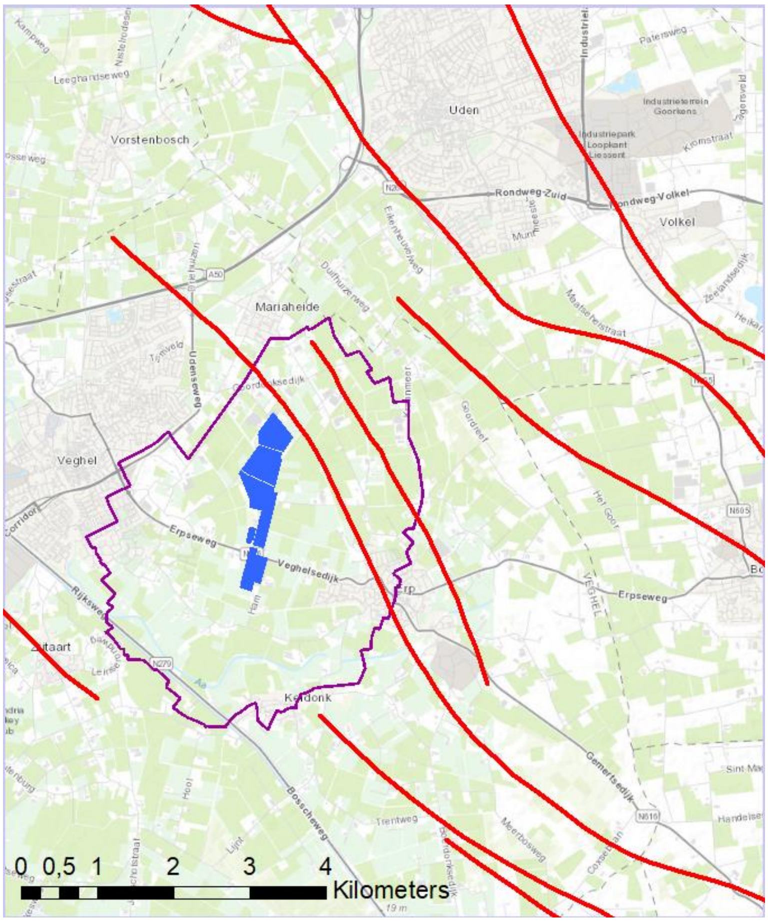

Figure 4.2 Topographical map with faults (red lines), drinking water abstraction BW27 (blue) and its groundwater procection area (purple).

Within the pilot area, there is a single abandoned oil exploration well which gives information of the geological buildup in this region. The well is specified in the database of oil, gas and geothermal energy exploration and production in the Netherlands and the Dutch sector of the North Sea continental shelf (http://www.nlog.nl). This well, KDK-01, was drilled in 1992 to a depth of 2.2 kilometers (Figure 4.3). No further activities have been employed and no hydrocarbon field has been identified.

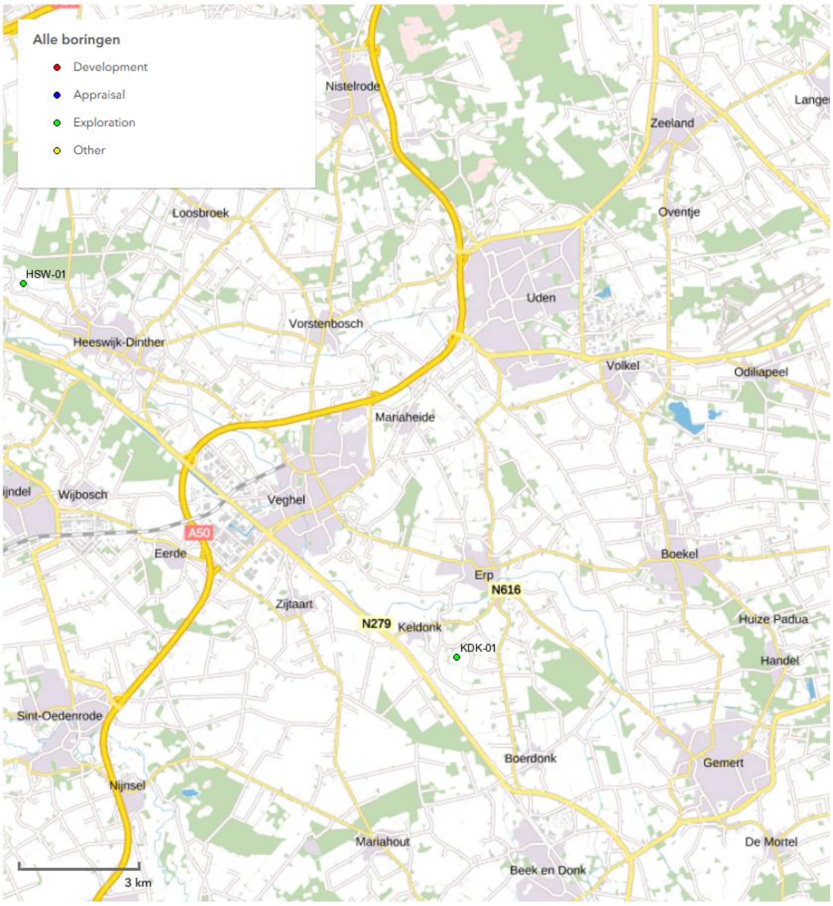

Figure 4.3 Abandoned hydrocarbon exploration well KDK-01 located in pilot area

For the Veghel pilot, possible geologic connections between the deep subsurface and the groundwater resources in the upper hundreds of meters have been evaluated using data on the gas composition and – isotopes in the groundwater and analysis of the fault structures. The structural tectonic aspects are described in the current chapter, the tracer study is described in Chapter 5.

4.1.2 The Gilze-Rijen Fault Zone near Tilburg

The pilot area of the Gilze-Rijen Fault near Tilburg is shown in Figure 4.4. For this region, there is additional information about the fault structures due to the combined extent of two 3D seismic surveys: Tilburg_L3CLY2001A and Waalwijk_L3CLY1992A (available at https://www.nlog.nl). We assess how the 3D information may help us to unravel the position of damage zones which may indicate possible connections between the deeper and shallower subsurface.

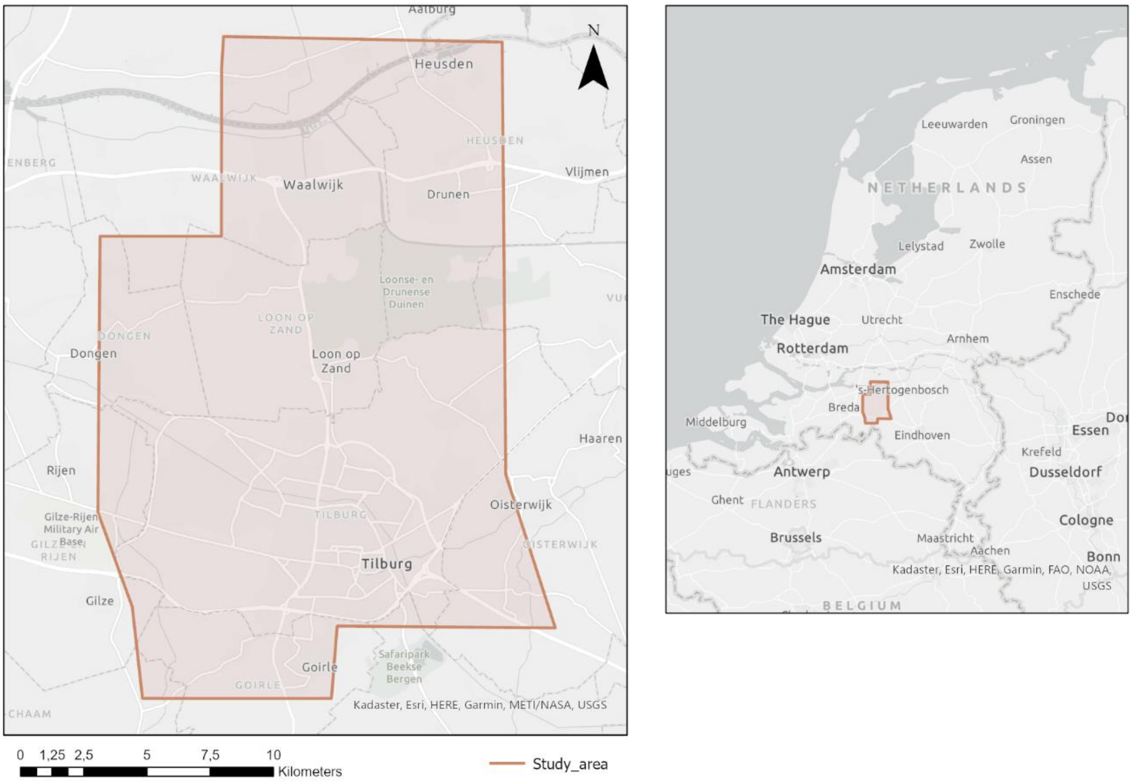

Figure 4.4 Location of studied 3D seismic surveys in the Gilze-Rijen Fault zone near Tilburg.

4.2 Geology and hydrogeology near Veghel and Tilburg

4.2.1 Geology around the Veghel pilot

The geological setting of the Veghel pilot is characterized by an east-northeast dipping alternation of clay and sand layers with north-northwest to south-southeast striking normal faults. It is located in the Roer Vally Graben, near the Eastern flank of the graben. REGIS II is a model of the regional hydrogeology of the part of the subsurface relevant for the groundwater resources (available at http://www.dinoloket.nl). Figure 4.5 shows a W-E cross section from REGIS for the Veghel pilot.

The subsurface has been modelled to a greater depth in the geological model DGMdiep (see Figure 4.6). Some 2D seismic surveys have been carried out in the area (see http://www.nlog.nl) (Figure Figure 4.7).

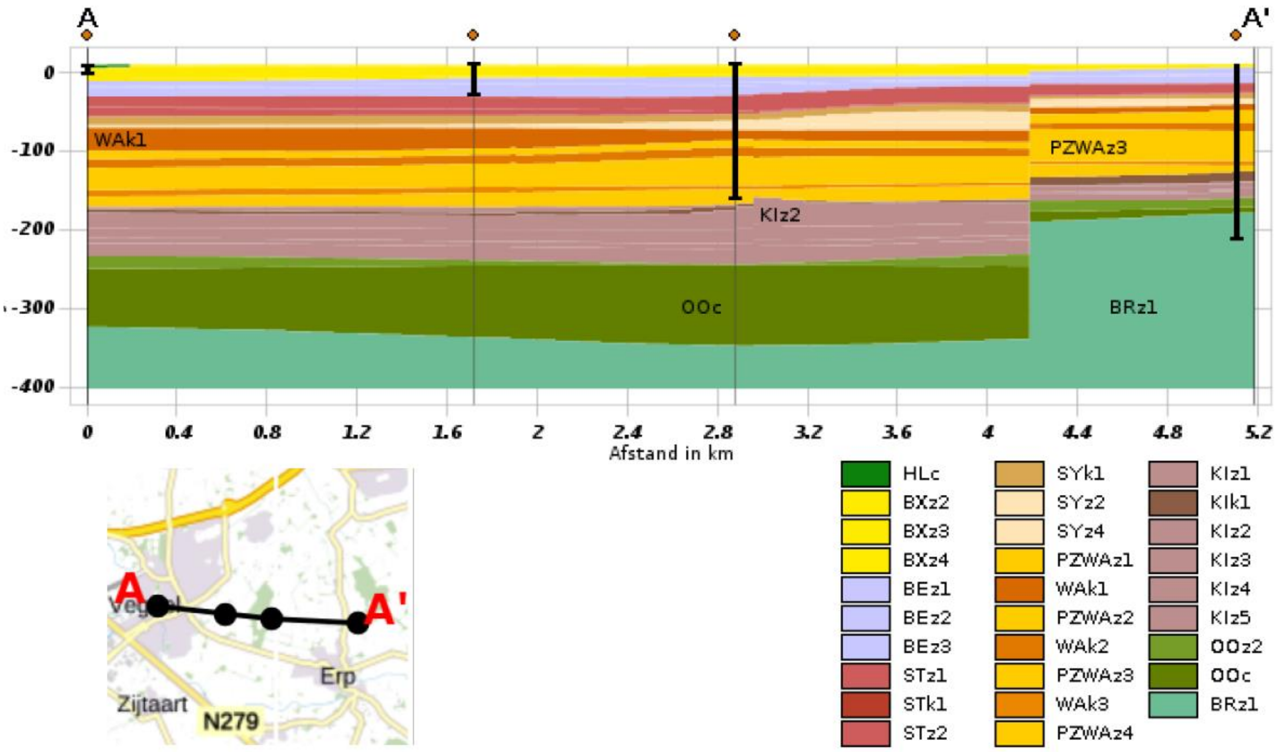

Figure 4.5 REGIS II hydrogeological cross section with Formation (first 2 letters of codes) and hydrogeological units ('z' for aquifer, 'k' for aquitard)

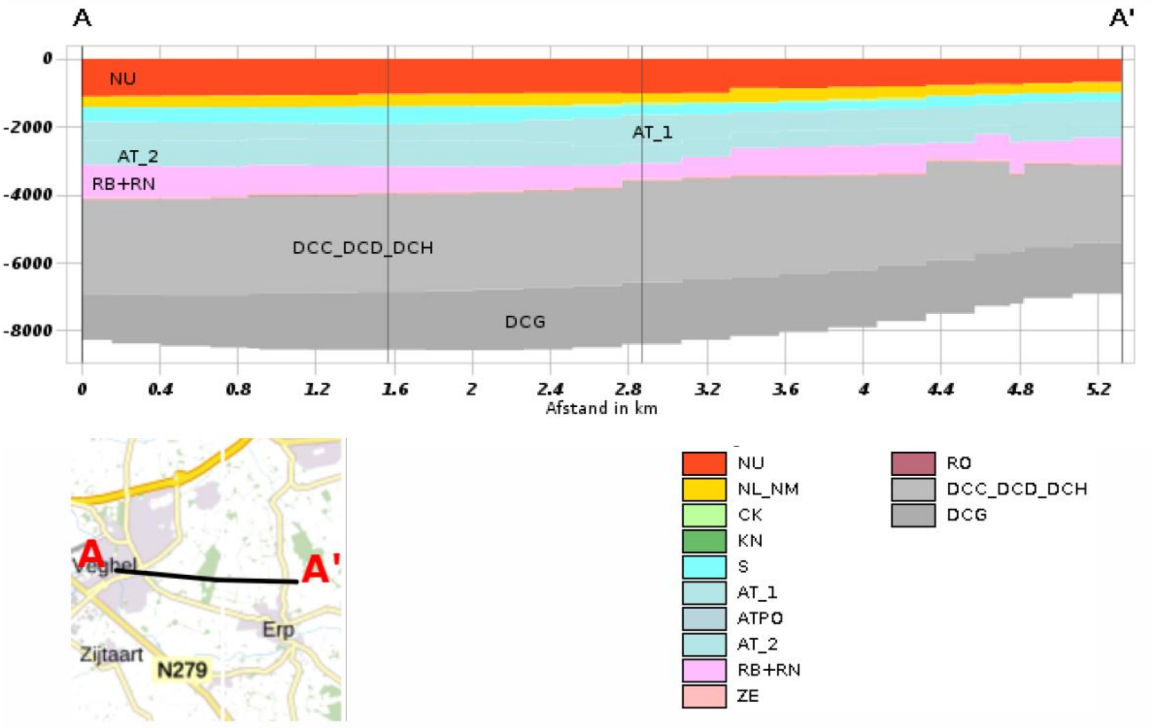

Figure 4.6 Geological cross section from the deep Digital Geological Model of the Netherlands (DGMdiep) with geological groups (N = North Sea, C=Chalk, ZE=Zechstein, see further https://www.dinoloket.nl/nomenclature-deep)

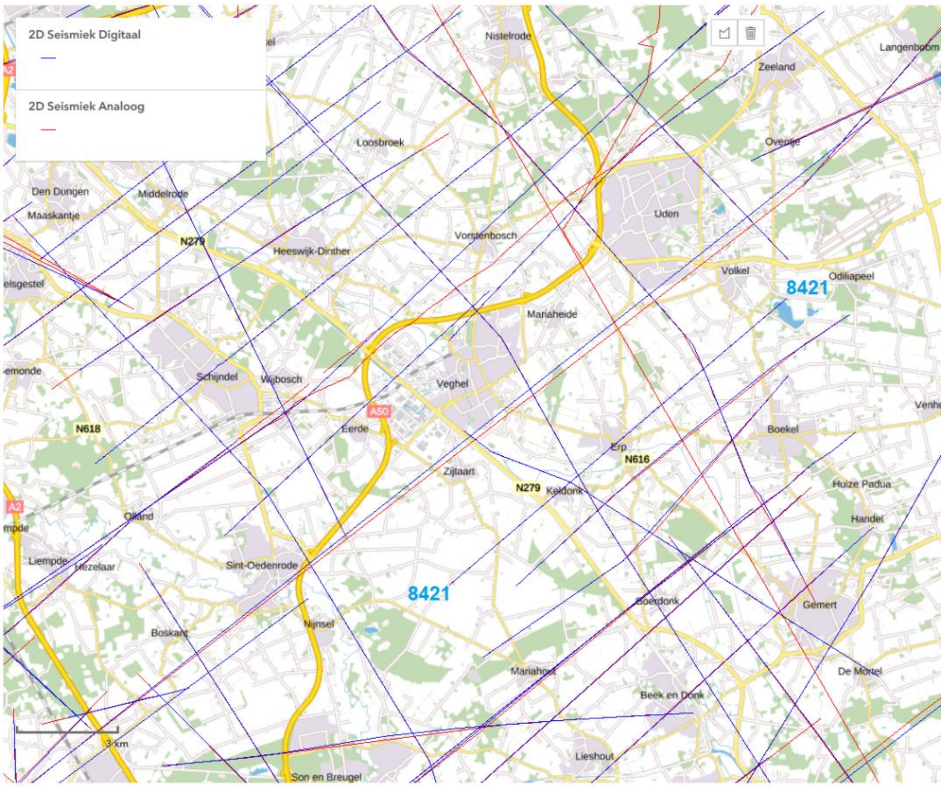

Figure 4.7 Seismic surveys in NLOG around the Veghel pilot

Figure 4.8 shows the seismic line crossing the strike of the Peel Boundary Fault which is indicated in Figure 4.7. It is unclear how much of the structure of the Peel Boundary Fault and its damage zone can be detected from the available seismic data.

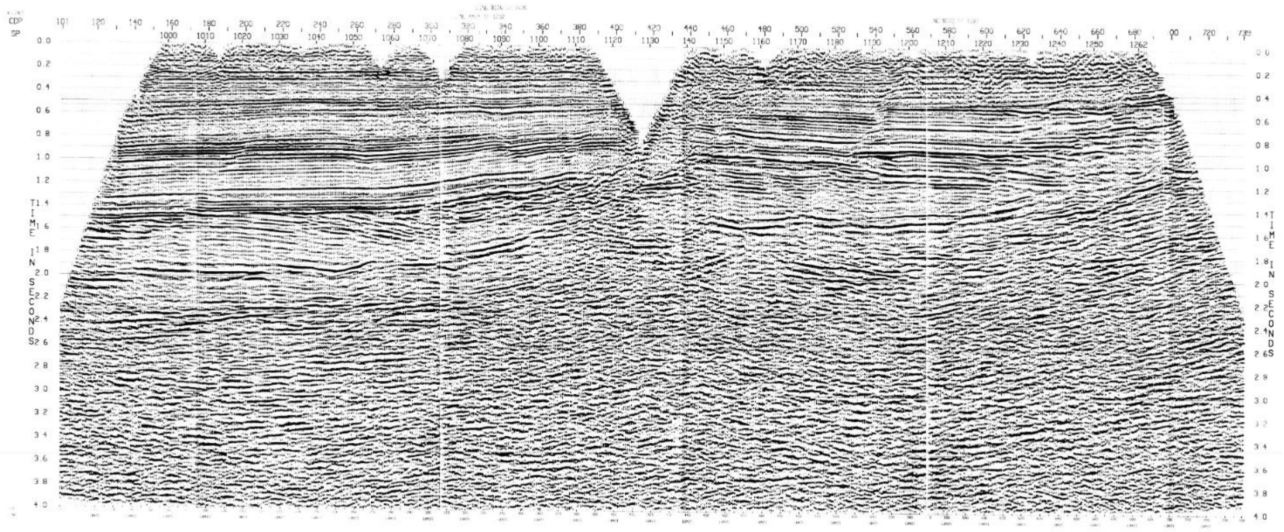

Figure 4.8 Seismic survey 8421 from NLOG (for location see Figure 4.7)

In the shallow subsurface, the Peel Boundary Fault has a large resistance to flow across the fault. This has been mentioned in many publications (e.g. de Ridder et al., 1967; van den Berg et al., 2002). Much less attention has been paid to the vertical hydraulic conductivity in the damage zone along the fault, although it has been suggested this may be an important pathway for vertical groundwater flow (Bense et al., 2003).

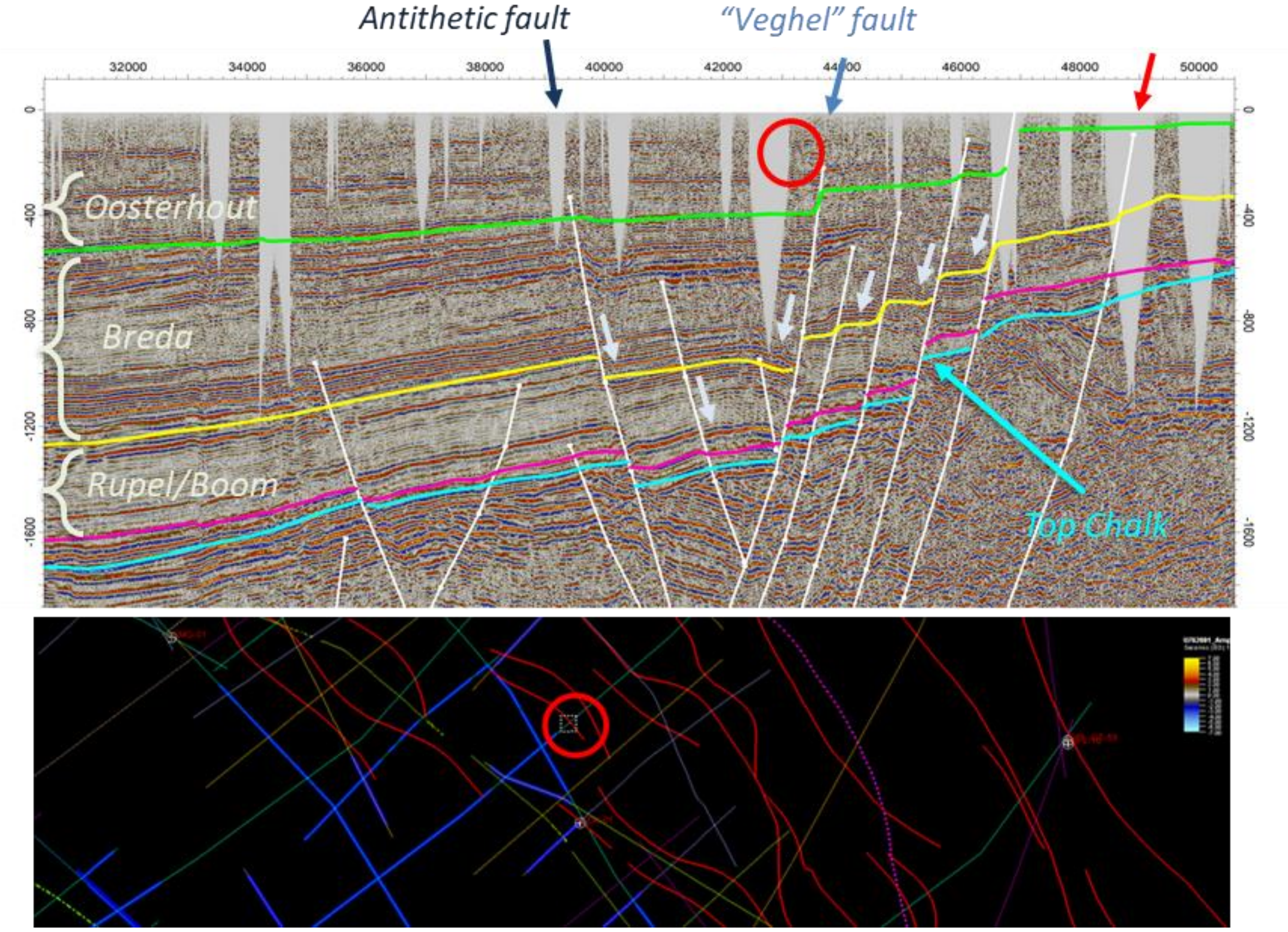

Figure 4.9 Interpreted seismic survey 8119 with location of well field BW27 (red circle).

Figure 4.9 illustrates the position of the BW27 public supply well field relative to the tectonic structure of the Roer Valley Graben. The well field is located close to a secondary fault of the Peel Boundary Fault system which borders the Roer Valley Graben at the eastern side. An antithetic fault to the west of the well field (also visible in Figure 4.9) borders a smaller, graben like structure between the BW27 secondary fault and the antithetic fault to the west. A previous study showed that this “*marginal through*” accommodates a body of paleowater of water that was partly recharged before the Last Glacial Maximum (Broers et al., 2021). Table 4.1 summarizes the hydrogeological units and corresponding lithologies which are present in the Veghel pilot region.

Table 4.1 Stratigraphic layers at the Veghel pilot site which are used in the fault model in section 4.4 (data from the H3O Roerdalslenk-Noordwest" project).

Analysis-code	**Unit**	**Hydrogeological code**	**Lithology**
1	Holocene	HLc	Sand
2	Boxtel sand 1	BXz2	Sand
3	Boxtel sand 2	BXz3	Sand
4	Boxtel sand 3	BXz4	Sand
5	Beegden sand 2	BEz2	Sand
6	Beegden sand 3	BEz3	Sand
7	Sterksel sand 1	STz1	Sand
8	*Sterksel clay 1*	*STk1*	*Clay*
9	Sterksel sand 2	STz2	Sand
10	*Stramproy clay 1*	*SYk1*	*Clay*
11	Stramproy sand 2	SYz2	Sand
12	Stramproy sand 3	SYz3	Sand
13	*Waalre clay 1*	*WAk1*	*Clay*
14	Peize sand 2	PZWAz2	Sand
15	*Waalre clay 2*	*WAk2*	*Clay*
16	Peize sand 3	PZWAz3	Sand
17	*Waalre clay 3*	*WAk3*	*Clay*
18	Peize sand 4	PZWAz4	Sand
19	Kiezelooliet sand 1	KIz1	Sand
20	*Kiezelooliet clay 1*	*KIk1*	*Clay*
21	Kiezelooliet sand 2	KIz2	Sand
22	Kiezelooliet sand 3	KIz3	Sand
23	Kiezelooliet sand 4	KIz4	Sand
24	*Oosterhout clay 1*	*OOk1*	*Clay*
25	Oosterhout sand 2	OOz2	Sand
26	*Oosterhout complex*	*OOc*	*Clay*
27	Breda sand 1	BRz1	Sand
28	Breda sand 2	BRz2	Sand
29	Breda sand 3	BRz3	Sand
30	*Veldhoven*	*VEWIk1*	*Clay*
31	Voort	VEVOc	Sand
32	*Rupel*	*RUBOK1*	*Clay*
33	*Landen*	*HAc*	*Clay*
34	Heers	HSc	Sand

4.2.2 Geology around the Tilburg pilot

Table 4.2 summarizes the hydrogeological units and corresponding lithologies which are present in the Tilburg pilot region which are drawn from the “H3O-Roerdalslenk-Noordwest” project.The H3O project area shows an overlap with the 3D seismic survey area (Figure 4.10). The H3O-Roerdalslenk-Noordwest project delivered a hydrogeological model of the Tertiary interval of a section of the Roervalley graben area. From this project, 35 layers that are present within the study area have been included in the juxtaposition analysis in section 4.4.4. The stratigraphy in the area is characterized by a frequent alternation between sand and clay layers.

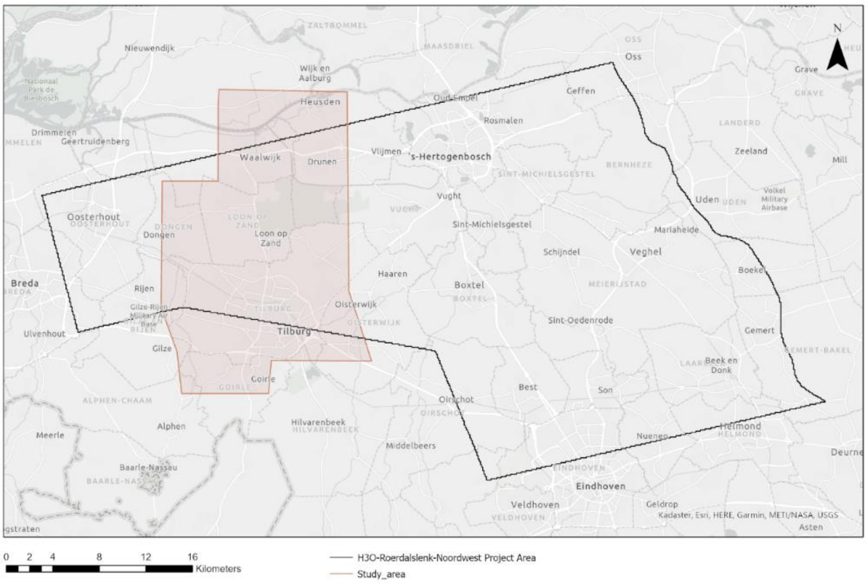

Figure 4.10 Overlap of 3D seismic data with project area H3O Roerdalslenk Noordwest.

Table 4.2 Stratigraphic column in the 3D seismic survey area (showing only the H3O stratigraphic layers present in this area).

Juxta-analysis-code	**Unit**	**Hydrogeological code**	**Lithology**	**Age**
1	Boxtel sand 2	BXz2	Sand	Mid-Pleistocene-Holocene
2	*Boxtel-Liempde*	*BXLMk-1*	*Clay*	Mid-Pleistocene-Holocene
3	Boxtel sand 3	BXz3	Sand	Mid-Pleistocene-Holocene
4	Boxtel sand 4	BXz4	Sand	Mid-Pleistocene-Holocene
5	*Sterksel clay 1*	*STk1*	*Clay*	Early-Mid Pleistocene
6	Sterksel sand 1	STz1	Sand	Early-Mid Pleistocene
7	Sterksel sand 2	STz2	Sand	Early-Mid Pleistocene
8	*Stramproy clay 1*	*SYk1*	*Clay*	Early-Mid Pleistocene
9	Stramproy sand 2	SYz2	Sand	Early-Mid Pleistocene
10	Stramproy sand 3	SYz3	Sand	Early-Mid Pleistocene
11	Peize sand 1	PZWAz1	Sand	Early Pleistocene
12	*Waalre clay 1*	*WAk1*	*Clay*	Early Pleistocene
13	Peize sand 2	PZWAz2	Sand	Early Pleistocene
14	*Waalre clay 2*	*WAk2*	*Clay*	Early Pleistocene
15	Peize sand 3	PZWAz3	Sand	Early Pleistocene
16	Peize sand 4	PZWAz4	Sand	Early Pleistocene
17	*Maassluis clay 1*	*MSk1*	*Clay*	Early Pleistocene
18	Maassluis sand 2	MSz2	Sand	Early Pleistocene
19	*Maassluis clay 2*	*MSk2*	*Clay*	Early Pleistocene
20	Maassluis sand 3	MSz3	Sand	Early Pleistocene
21	*Oosterhout clay 1*	*OOk1*	*Clay*	*Late Miocene - Pliocene*
22	Oosterhout sand 2	OOz2	Sand	*Late Miocene - Pliocene*
23	*Oosterhout complex*	*Ooc*	*Clay*	*Late Miocene - Pliocene*
24	Breda I	BRz1	Sand	Early Miocene
25	Breda II	BRz2	Sand	Early Miocene
26	Breda III	BRz3	Sand	Early Miocene
27	Someren	VESO-c	Sand	Early Miocene
28	*Veldhoven*	*VEWIk1*	*Clay*	*Late Oligocene*
29	Voort	VEVO-c	Sand	Late Oligocene
30	*Rupel*	*RUBOk1*	*Clay*	*Early Oligocene*
31	Brussel	DOz2	Sand	Early -Mid Eocene
32	*Ieper*	*DOIEk1*	*Clay*	*Early Eocene*
33	Dongen Basal Sand	DOz4	Sand	Early Eocene
34	*Landen*	*HAc*	*Clay*	*Late Paleocene*
35	Heers	HCs	Sand	Late Paleocene

4.3 Using 3D seismic data to assess fault characteristics and damage zones

4.3.1 Fault dimensions and displacement

A typical fault, with length (L) and height (H), has an elliptical shape. The maximum amount of cumulative displacement (d_{max}) is located at the center of the ellipse and decreases with distance away from the center (color gradient in Figure 4.11a). The edge of the fault plane, where cumulative displacement has decreased to zero, is referred to as the fault tip (Tip loop in Figure 4.11a).

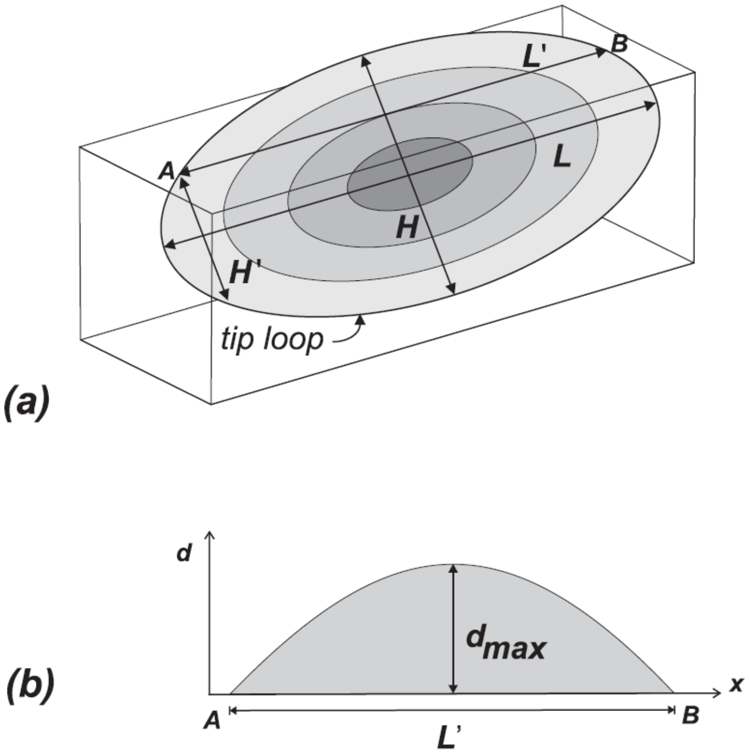

Figure 4.11 Fault shape (Kim & Sanderson, 2005)

Figure 4.11b shows a d_{max}/L plot; the length of a line across the fault plane (L) been plotted on the X-axis with amount of cumulative displacement (d_{max}) plotted on the Y-axis.
There is a strong relationship between a fault's dimensions (L or H) and the maximum displacement at the center (d_{max}), given by the d_{max}/L ratio. This relationship is often assumed to be scale-invariant, meaning that this applies to both small fractures (<1m) and large faults (>100m).
Values for the d_{max}/L ratio may vary slighty depending on material properties, fault type (normal fault, strike-slip fault or a combination of these), fault evolution (linkage) and reactivation. Despite these variations, multiple studies have shown a consistent relationship between maximum displacement (d_{max}) and length (L) (Figure 4.12).

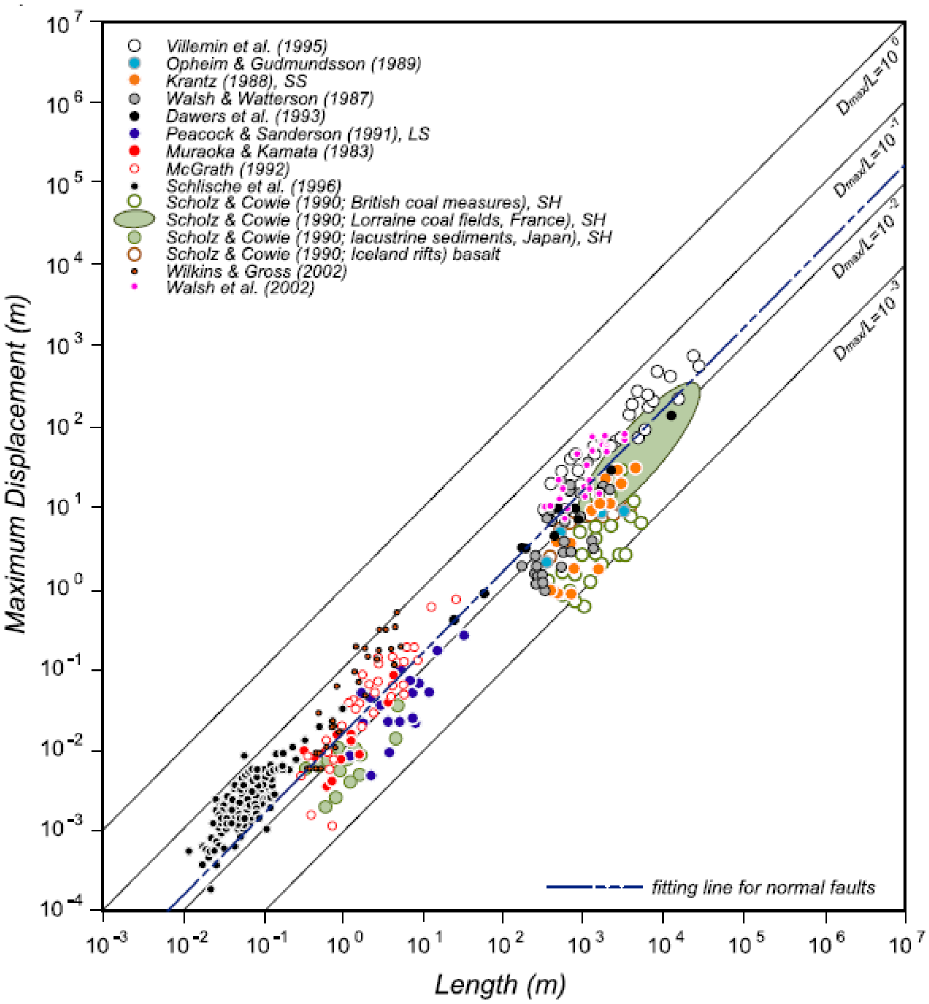

Figure 4.12 Plots of maximum displacement (d_{max}) against fault length (L) (from: Kim & Sanderson, 2005).

The displacement at the outermost parts of a fault is below the resolution of the seismic data and can therefore not be observed. However, the d_{max}/L ratio can be used to estimate the total length of a fault based on the observed maximum displacement of modelled stratigraphic layers.

When an interpreted fault is based on 2D seismic data only, the total length of the fault and the maximum amount of displacement is uncertain because the interpretations of both faults and stratigraphic layers are limited by the availability and spacing of 2D seismic lines. Therefore 3D seismic data yield far better and accurate interpretations and subsequent analysis results as will be shown for the Tilburg pilot site in section 4.4.4.

4.3.2 Fault linkage

With the accumulation of displacement a fault's dimensions expand. Over time faults in an "en-echelon" pattern (Figure 4.13, stage 1) can extend far enough to create a lateral overlap (Figure 4.13, stage 2). This is called soft linking of segments and the structure in between the two fault plane is called a relay ramp. With further accumulation of displacement this relay ramp can eventually be breached, effectively connecting the two overlapping faults planes in what is referred to as hard-linking of fault segments (Figure 4.13, stage 3).

Due to the elliptical shape fault planes, a relay ramp can be breached at the center-depths of overlapping fault planes but still be intact at deeper and more shallow depths. This is illustrated by

Figure 4.14; this figure shows a top view of seismic data (a variance map) at different time-depths (in milliseconds), showing an intact and breached relay ramp at different depths.

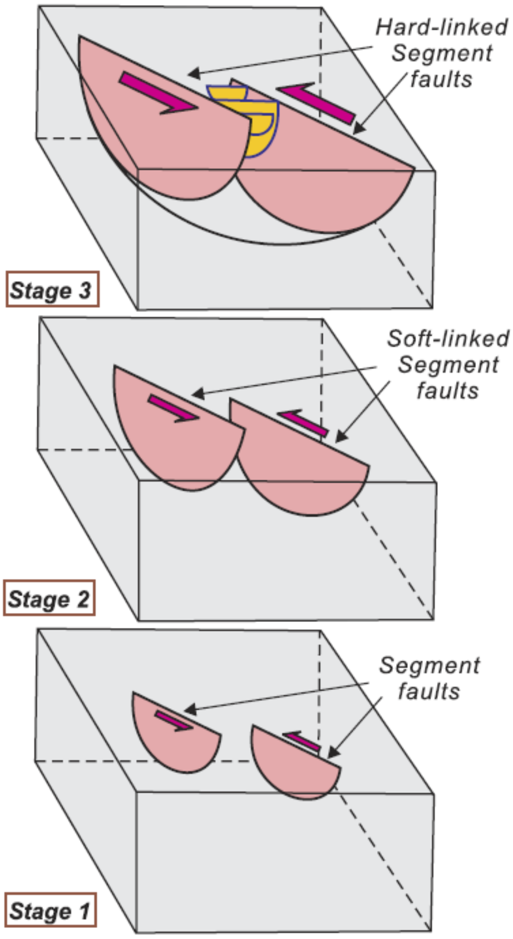

Figure 4.13 Three stages of fault linkage (from Kim & Sanserson, 2005).

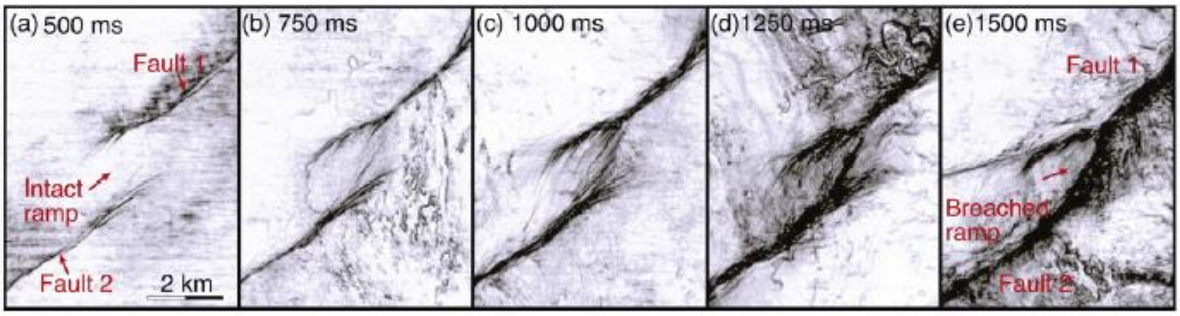

Figure 4.14 Seismic data (variance timeslices) showing two overlapping faults forming a relay ramp (a) that becomes breached at depth. At 1500 ms (two-way time) the ramp is completely breached (hard-linked) (from Fossen & Rotevatn, 2016).

4.3.3 Fault displacement of segmented faults

As a result of linkage of fault segments into a larger fault plane, the displacement on this larger fault plane is not distributed as indicated in Figure 4.11, with the maximum displacement located in the center of the plane. Instead, two areas of high displacement and thus the original, pre-linkage fault-segments can be identified after running a fault displacement analysis on these fault planes. Figure 4.15 illustrates the merging of two distinct d_{max}/L plots into a single d_{max}/L plot with two peaks (stage 3).

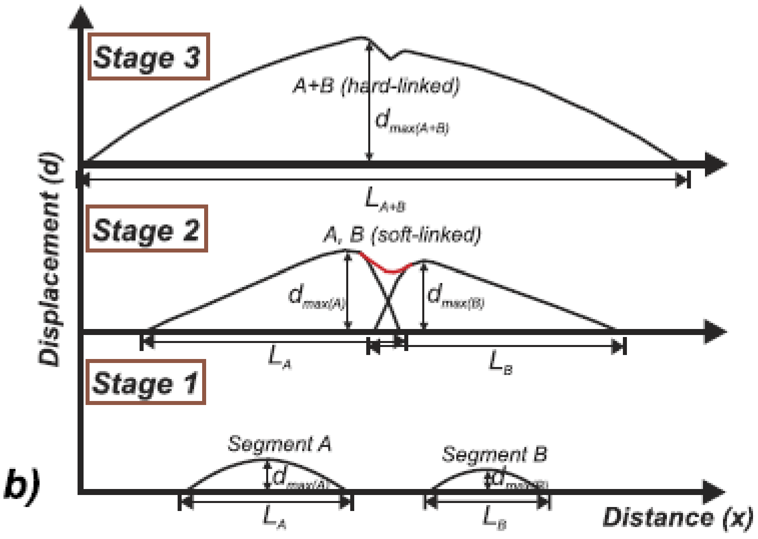

Figure 4.15 Displacement graphs of linkage of two fault segments (Kim & Sanderson, 2005).

4.3.4 Damage zones

The volume of deformed, fractured rock in a certain radius around a fault plane is called a damage zone. These damage zones are the result of the initiation, propagation, interaction and build-up of slip along faults (Kim et al., 2004). It is worth noting that faults in the subsurface are not discrete features. Even though faults in subsurface models are modelled as flat planes with zero thickness, in reality they are complex zones of deformation with a certain thickness depending on the aforementioned fault characteristics.

Three main types of damage zones are defined (Figure 4.16) and these types occur depending on the direction of movement of the fault. Normal faults and reverse faults (mode III) show movement in the vertical direction and strike-slip faults (mode II) show movement in the horizontal direction. Oblique faults show a combination of vertical and horizontal movement.

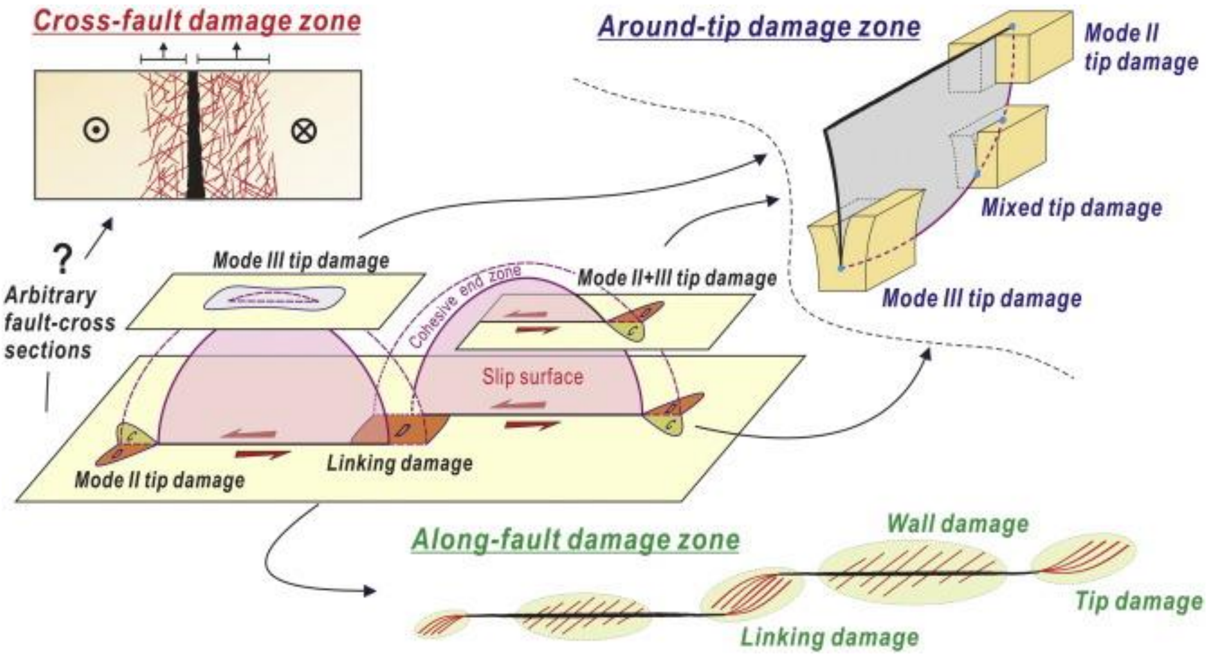

Figure 4.16 Different types of damage zones. (Choi, Edwards, Ko, & Kim, 2016)

4.3.4.1 Tip damage zones

Tip damage zones appear at the tip loop of a fault plane. These damage zones occur at mode II and III faults. The tip damage area is correlated to the fault length (Figure 4.17) and show different fracture patterns depending on the mixture of mode II and III movement and the place of the fault in the context of the geological structure (synthetic- or antithetic fault, branch fault or no branch fault).

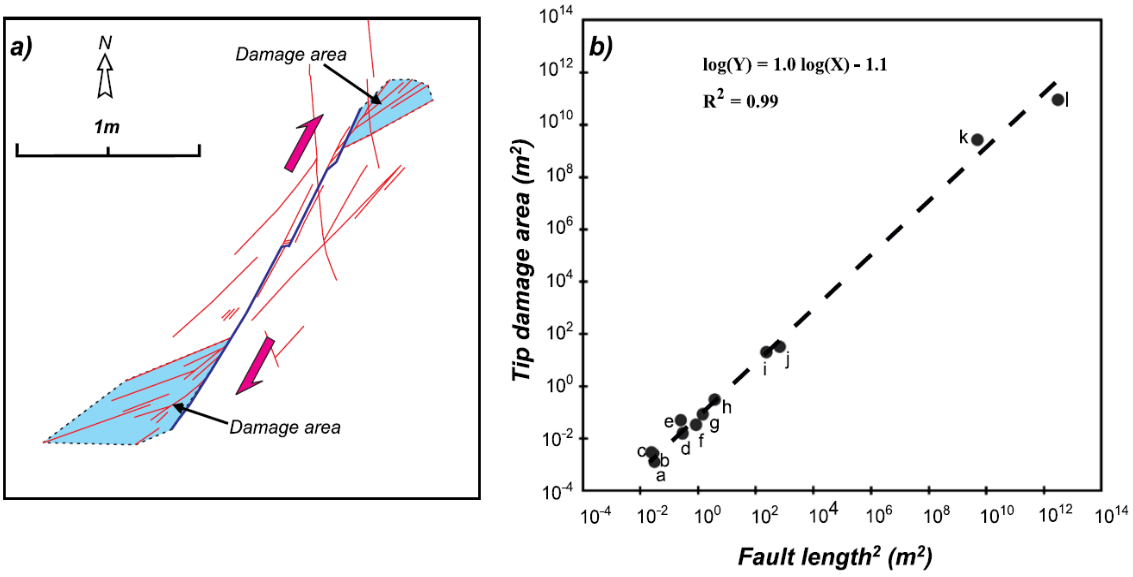

Figure 4.17 Correlation between tip damage area and fault length ((Kim & Sanderson, 2005))

4.3.4.2 Wall damage zones

Wall damage zones, also referred to as cross-fault or along-fault damage zones, are zones of broken-up or fractured material on both sides of a fault plane. The amount of damage (fractures per volume) decreases away from the fault plane (Figure 4.18). At the edge of the damage zone the host rock is undeformed. The dimensions of a wall damage zone, like the thickness perpendicular to the fault plane, are correlated to the displacement of the fault (Figure 4.19).

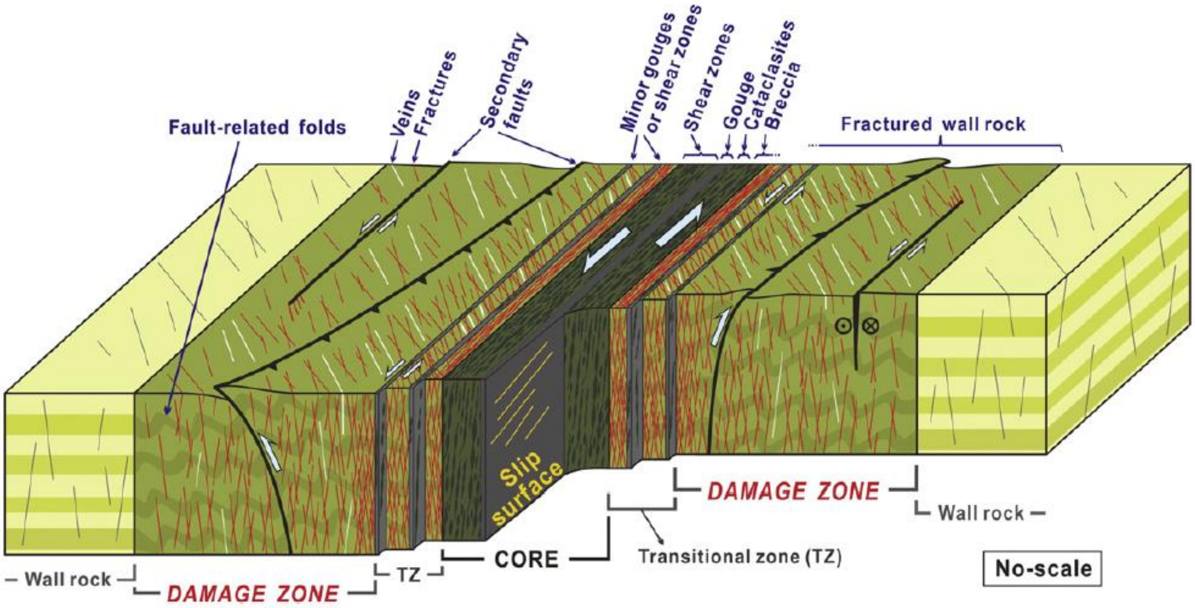

Figure 4.18 Illustration of a wall damage zone (Choi, Edwards, Ko, & Kim, 2016)

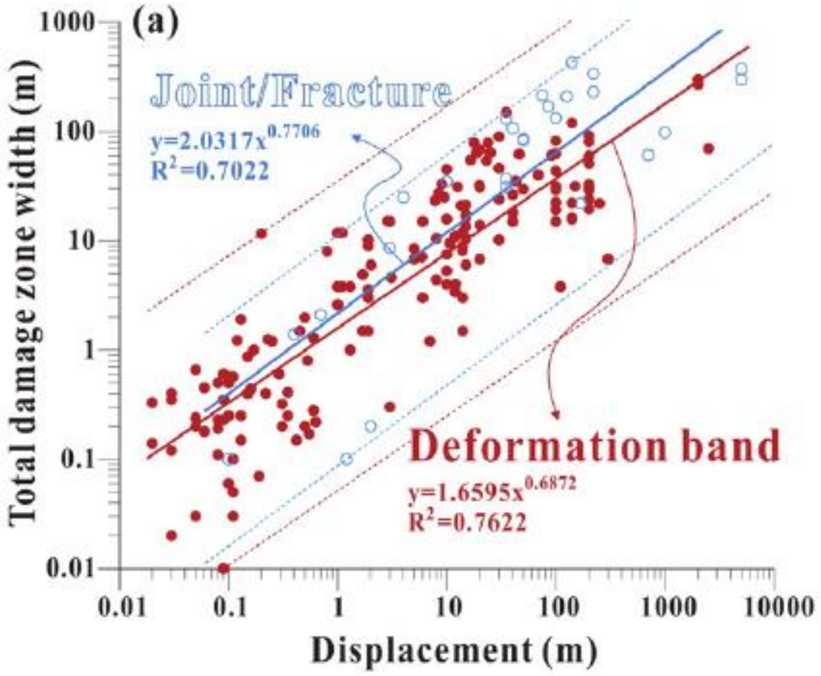

Figure 4.19 Example of a log–log plots of damage zone width against displacement (Choi, Edwards, Ko, & Kim, 2016)

4.3.4.3 Linking damage zones

Relay ramps, the structure in between two overlapping fault planes, are structurally complex due to the large amount of smaller fractures with varying orientations. A relay ramp represents a type of damage zone referred to as a linking damage zone. This is irrespective of whether the fault-segments have been hard- or soft-linked.

These areas of fault-linkage play an important role in groundwater dynamics around faults, even in mature and advanced faults, due to relay-enhanced fault permeability.

A damaged but intact relay ramp (soft-linking) may increase lateral flow of fluid, or bed-parallel flow, due to the increased fracture density. A breached relay ramp (hard-linking) of fault segments reduces this lateral flow due to the occurrence of low-permeable deformation bands. However, the fractured damage zone still offers a conduit for vertical migration of fluids. Figure 4.20 illustrates the vertical migration of fluids along the fault surface in the context of a sealing fault with an intact relay ramp.

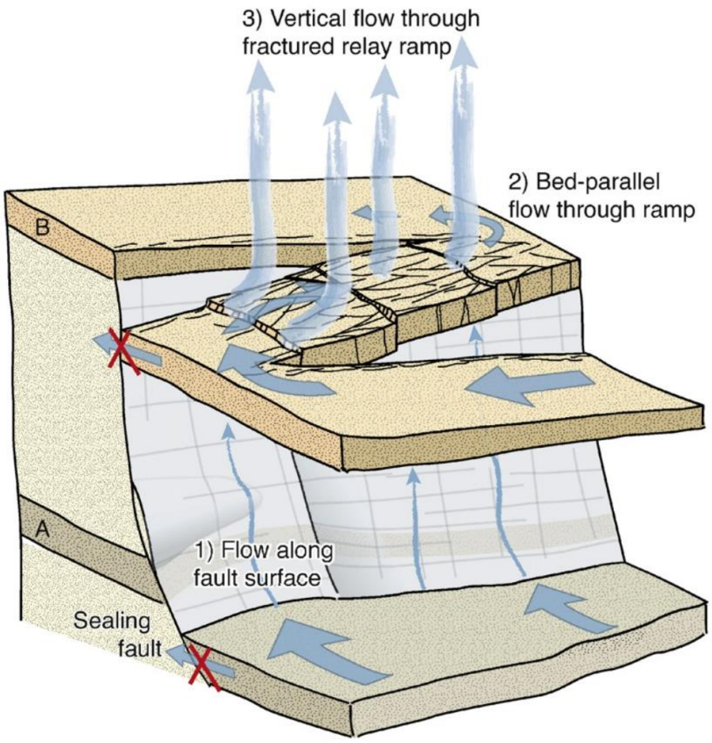

Figure 4.20 Illustration of vertical flow through a fractured relay ramp (Fossen & Rotevatn, 2016).

4.3.5 *Juxtaposition analysis*

The purpose of a juxtaposition analysis is to gain insight into connections of different stratigraphic layers, or zones, at fault planes and the implications for groundwater flow based on the lithology of the layers involved. Connections of zones can be visualized with a matrix-scheme with zones in the footwall plotted on the Y-axis and zones in the hanging-wall plotted on the X-axis. Figure 4.21 and its accompanying matrix-scheme show a pre-deformation state in which each footwall-zone only connects to its hanging-wall equivalent. After deformation, zones in the footwall are juxtaposed to different zones in the hanging wall (Figure 4.22).

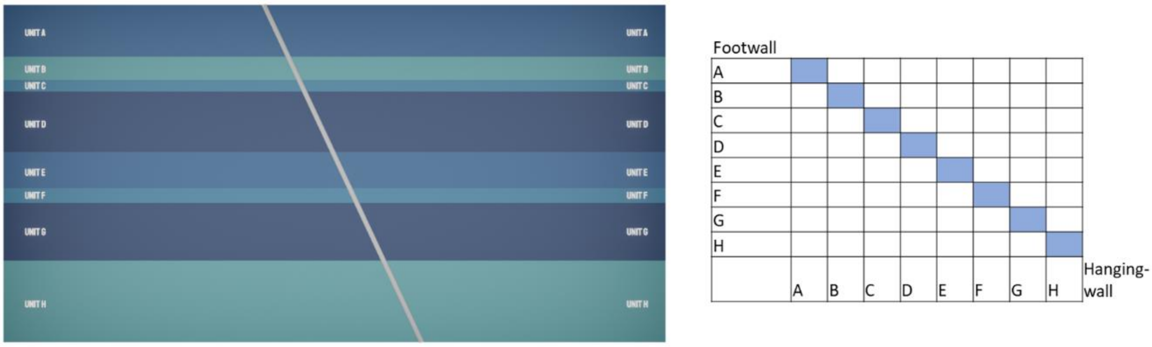

	A	B	C	D	E	F	G	H
A	🟦							
B		🟦						
C			🟦					
D				🟦				
E					🟦			
F						🟦		
G							🟦	
H								🟦

Figure 4.21 Pre-deformation situation with the future fault as grey line (left). There are no lateral connections of zones to other zones as depicted by the matrix-scheme (right).

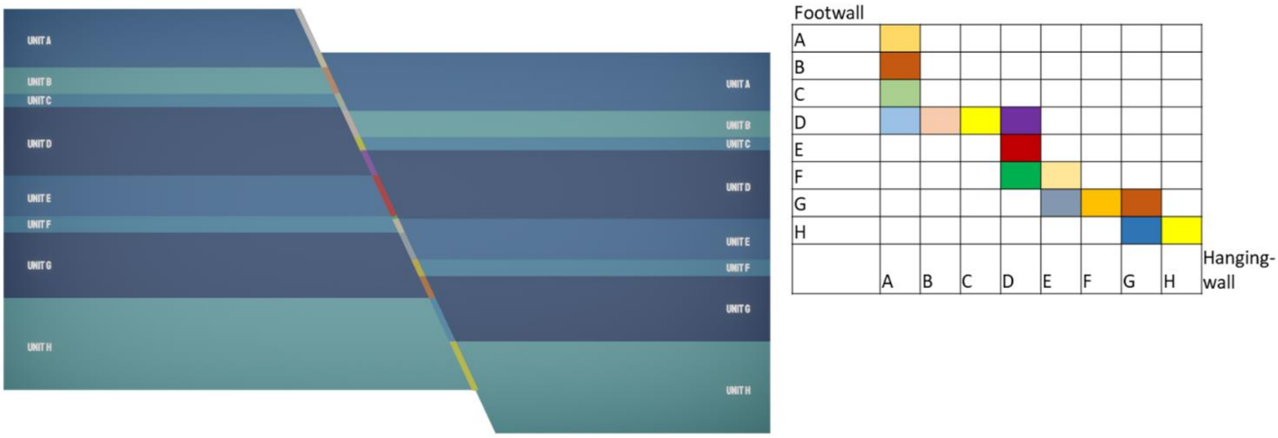

	A	B	C	D	E	F	G	H
A	🟨							
B	🟧							
C	🟩							
D	🟦	🟧	🟨	🟪				
E				🟥				
F				🟩	🟨			
G					🟦	🟧	🟫	
H							🟦	🟨

Figure 4.22 Post-deformation: The front-sides of the zones in the footwall now connect across the fault to different zones in the hanging wall (left). The matrix scheme (right) shows which zones are now juxtaposed (e.g. A in the hanging-wall side is juxtaposed to A,B,C and D in the footwall).

When combined with lithological information, a juxtaposition analysis can be used to identify possible migration paths for groundwater flow (Figure 4.23). With 35 zones, such as available for the Tilburg pilot, a total of 630 different combinations of zone-to-zone contact are theoretically possible. The two simplified lithologies in this study can result in three different combinations: sand-on-sand, clay-on-sand, clay-on-clay. On the fault plane the different combinations of zone-to-zone and lithology-to-lithology contacts can be visualized.

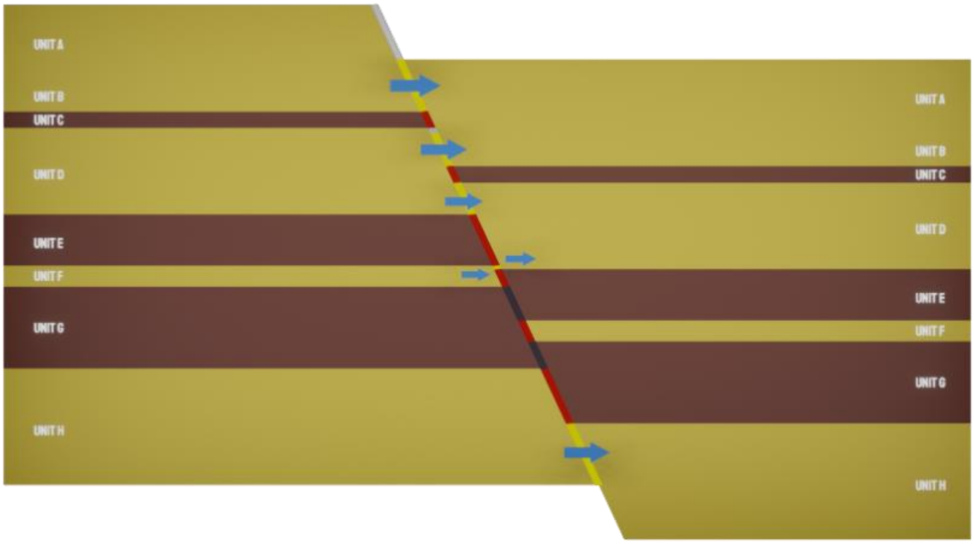

Figure 4.23: Post-deformation: lithology. The juxtaposition results can be combined with lithological information in order to identify possible migration pathways for groundwater and/or gas.

4.3.6 Clay smear

The permeability of a fault can be reduced significantly by clay-rich fault gouge. Clay-rich fault gauge can appear when clay-rich strata is “smeared” across the fault-plane during displacement of the fault (Figure 4.24). A thin, clay-rich barrier may thus be present in the fault-zone, even at sand-on-sand contacts, hindering flow of groundwater or gas.

The possible presence of clay smear has not been taken into account in this pilot-study. A thorough study, including clay smear, requires more detailed lithological information for each zone. This would also include simulations of clay-sand distributions within each zone.

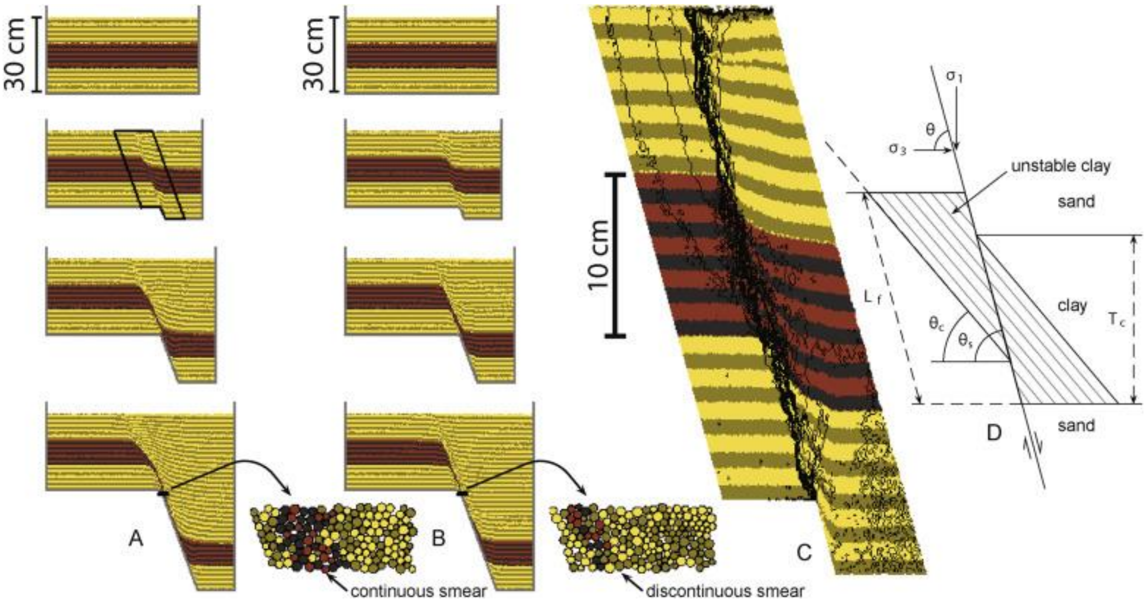

Figure 4.24 An illustration of clay smear in a fault-zone

4.4 Results for fault zones near Veghel and Tilburg

4.4.1 Fault displacement at the Veghel fault

This section presents a visualization of various aspects of the Veghel Fault (Figure 4.25 compare with Figure 4.2).

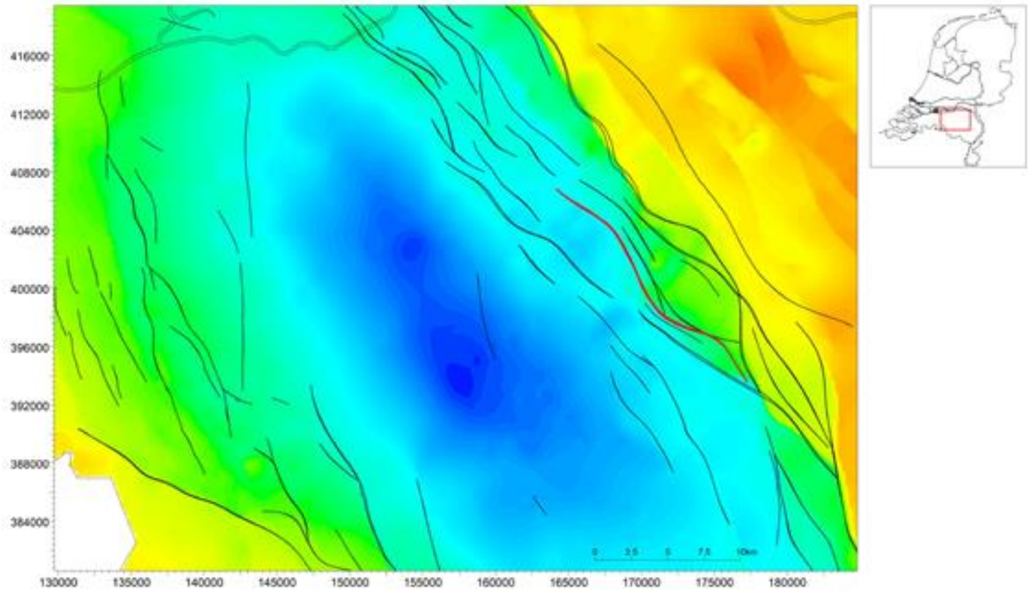

Figure 4.25 Location of Veghel Fault (red) within the Peel Boundary Fault zone. Colours denote the depth of the base of the Tertiary

The fault plane and horizons have been derived from the “H3O- Roerdalslenk-Noordwest” project. This is a hydrogeological model of the tertiary interval of a section of the Roervalley graben area. From this project, 34 layers that are present within the study area have been included (see Table 4.1). The pillar-grid voxel model allows for an analysis of the displacement of the fault. The results of this analysis can be visualized on the fault-plane and extracted, comparable to the juxtaposition analysis. The results of the displacement analysis at the Veghel pilot show that the majority of the displacement occurred in the center of the fault plane as was expected from Figure 4.11 (compared Figure 4.11 with Figure 4.26). However, there is also a substantial amount of displacement on the left side and, in a lesser amount, on the right side of the fault plane. This can be explained by the evolution of the fault-plane which involves the linkage of different fault segments (see section 4.3.2).

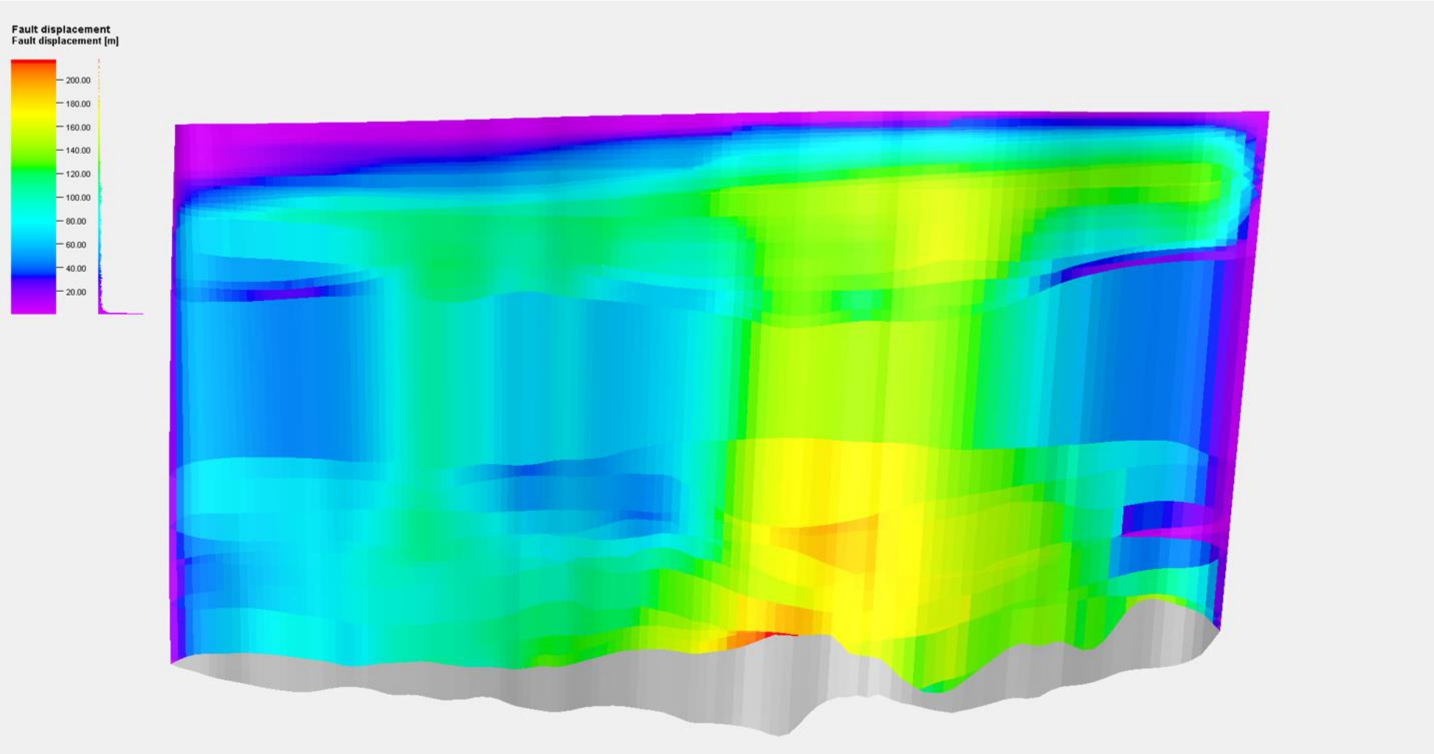

Figure 4.26 Fault displacement Veghel fault based on geological model.

In the area of the Veghel pilot only two-dimensional seismic surveys are available. Therefore, this visualization of the Veghel fault was derived from a geological model in which the position of the fault and the elevation of the layers have been estimated based on the seismic results and other available data. This also means no accurate description of the fault to large depths is possible.
The next section shows the additional information that can be derived from results of a three dimensional seismic survey.

4.4.2 Juxtaposition analysis at the Veghel fault

For the juxtaposition analyses, the modelled stratigraphic layers are taken from the “H3O-Roerdalslenk-Noordwest” project (seeTable 4.1). It is common for these layers to have a certain sand-to-clay ratio (i.e. 90% sand, 10% clay) but for the sake of simplicity a binary approach has been used and the layers have been assumed to be 100% sand or 100% clay.

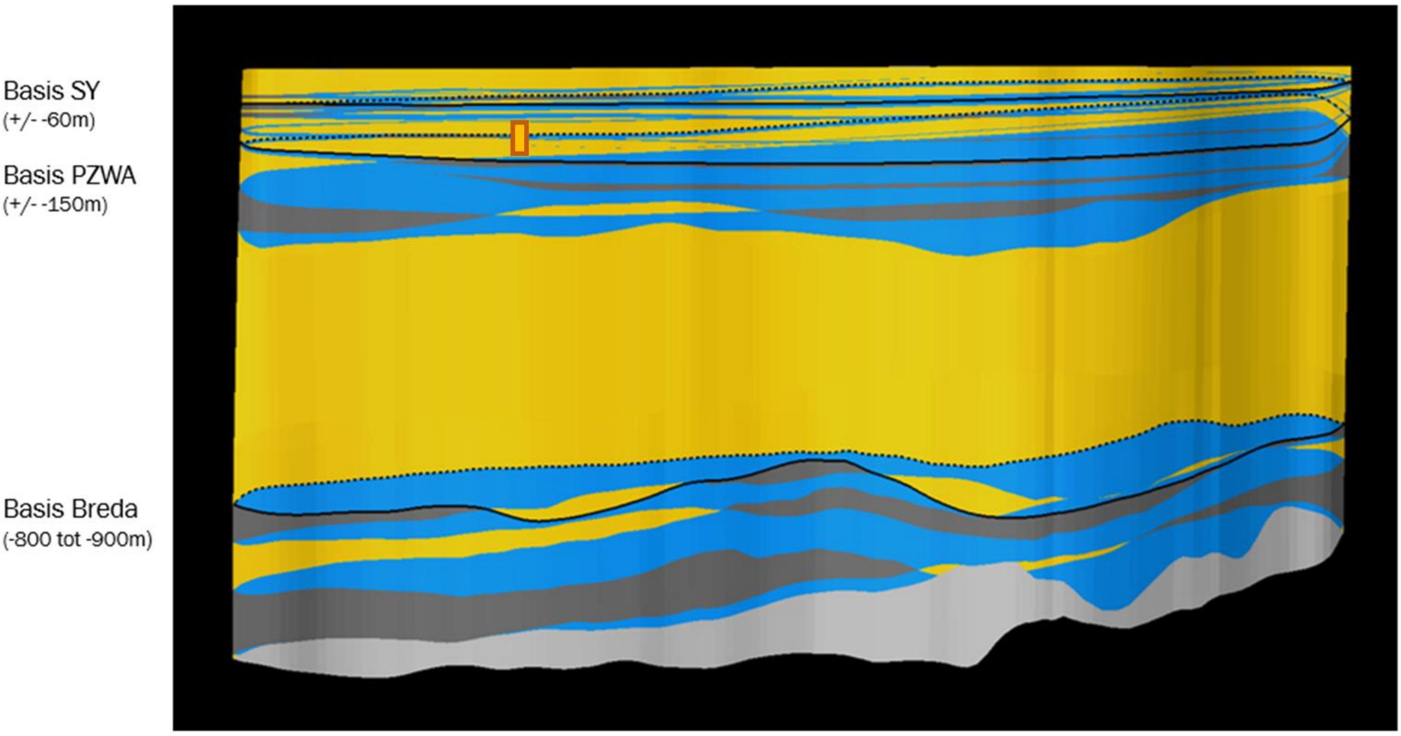

Figure 4.27 Results for the juxtapostion analyses for the Veghel Fault in the longitudinal direction of the fault. The rectangle represents the approximate position of the BW27 well field (see Chapter 5). Yellow = sand-sand contact, blue = sand-clay contact, grey = clay-clay contact.

The juxtaposition analyses for the Veghel fault faults return a roughly similar distribution pattern of the three lithological contact combinations (Figure 4.27). The colours on the fault planes correspond to the following contact types:

- Yellow: Sand-to-sand contact
- Blue: Clay-to-sand contact or vice versa
- Grey: Clay-to-clay contact.

The figure indicates a sequence of clay-clay and sand-sand contacts in the upper part of the profile which is most relevant for the shallow activities such as drinking water production. Caly-clay contacts are dominant between 150 and 200 m depth and below 700 m depth. The sand-sand contact over large parts of the Brede Formation between 300 and 700 m depth might be overestimated by the choice of 100% sand in the juxtaposition analysis because the Breda Formation is known to contains quite some intercalated clay layers. Moreover, clay smear is very posssible in the top part of the profile and in the depth range of the Breda Formation (see also section 4.3.6)

Figure 4.28 shows a perpendicular section of the Cenozoic Formations and lithrologies showing the fault displacement. For the shallower depth range, that is above the Breda units (green in the left part of the Figure), the faults are characterized by an alternation between sand-to-sand contacts, sand-to-clay contacts and clay-to-clay contacts. Below the Breda units, the Veldhoven clay, Rupel clay, Ieper clay and Landen clay units are thicker than the intermediate sand layers. This, combined with substantial fault displacement, results in predominantly clay-to-clay- and sand-to-clay contacts. From Figure 4.28, it is not immediately clear whether the Veghel fault forms an important barrier to lateral groundwater flow, or would rather be very permeable. The 2D seismic information does not enable to draw further conclusions for the Veghel Fault. That is why we also examined the Tilburg pilot, where 3D information helps to identify damage zones in the deeper subsurface, which may lead to vertical connections between the deeper and shallower subsurface.

As indicated, clay smear along the fault transect may induced stronger sealing conditions in lateral direction, as clay smear is very posssible in the top part of the profile where many intercalated clay layers are visible in Figure 4.28 as well as in the depth range of the Breda Formation which is known to contain clay intercalations (see also section 4.3.6)

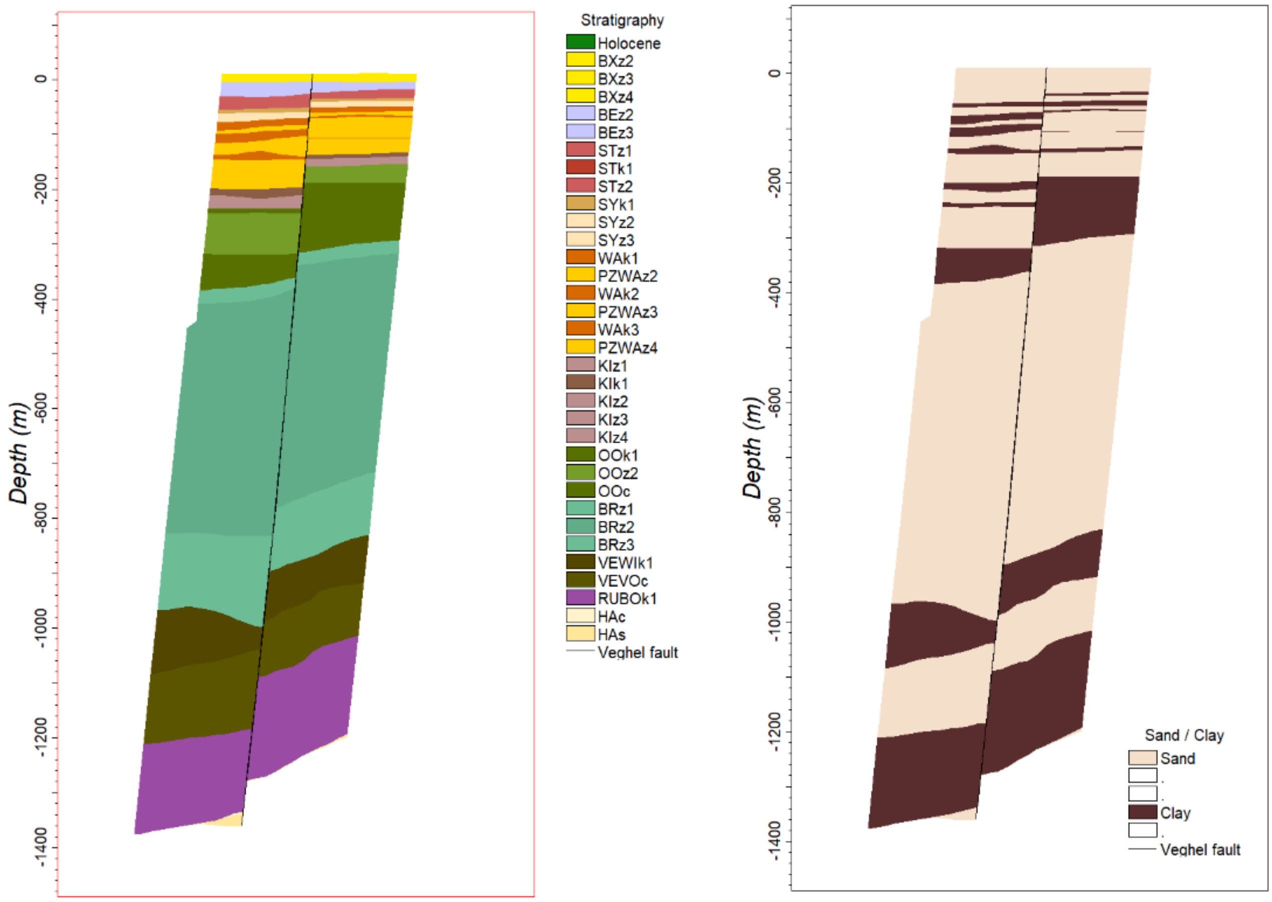

Figure 4.28 Cross-section of the Cenozoic interval across a fault near Veghel, showing the thickness of the Breda units (teal colors)

4.4.3 Consequences for shallow aquifers around Veghel

The displacements along the Peel Boundary fault near Veghel have been derived from a subsurface model based on the 2D seismic data and borelogs in the area. This means that the structure of the fault is not known in between the intersections with the seismic lines and a direct assessment is not possible of large damage zones forming potential vertical pathways. Chapter 5 deals with potential contaminant migration pathways and controls on fluid flow/transport in the surroundings of the Veghel fault by means of the characterization of gas compositions and tracer measurements. The reader is referred to section 5.3.2 for further details.

4.4.4 Fault structure from 3D seismic data in the Tilburg area

Faults and fault-zones play an important role in the permeability of stratigraphic layers and the movement of fluids and gases in the subsurface. In the absence of 3D seismic data and availability of solely 2D seismic data it is difficult to obtain a clear picture of faults and fault-zones in terms of traces, dimensions and displacements.

This section explains the added value of 3D seismic data over 2D seismic data by:

- Looking at physical principles concerning fault dimensions and displacements and, given a highly detailed fault model paired with a highly detailed stratigraphic model, how dimensions can be derived from displacements (and vice-versa);
- Discussing 3D seismic derivatives (variance maps) that allow for top-down visualization of faults. These variance maps can give insight into fault traces, lengths, fault evolution and linkage of fault segments, and damage zones;
- Discussing subsequent analyses regarding fault-permeability (juxtaposition analyses).

For the Tilburg pilot four faults have been used for the displacement- and juxtaposition analyses (Figure 4.29). These faults are also taken from the H3O Roerdalslenk-Noordwest project and have been refined in order to obtain more detailed results.

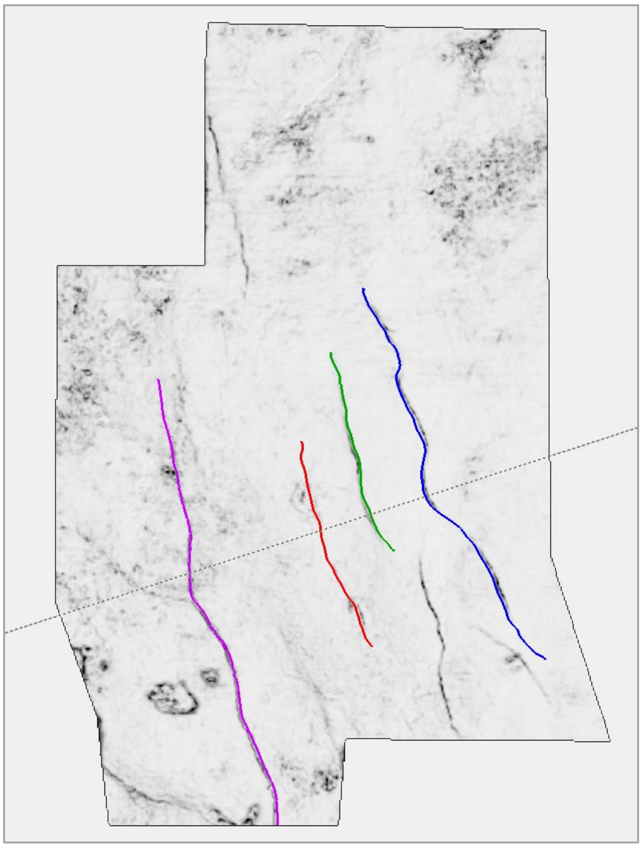

Figure 4.29 Modelled faults; from West to East: Fault 1 (purple), Fault 2 (red), Fault 3 (green), Fault 4 (blue); dotted line is location of seismic cross-section.

4.4.4.1 Fault patterns

The faults in the Tertiary interval of the Tilburg pilot show a north-northwest to south-southeast trend. The underlying Chalk group from the Cretaceous era includes faults with a northwest-southeast strike (Figure 4.30). These faults extend upwards into the lowermost layers of the Tertiary interval (Figure 4.31). The amount of faults extending into the more shallow stratigraphic layers decreases with in upward direction.

Figure 4.30 Fault pattern of the base of the Oosterhout Formation (from H3O-Roerdalslenk Noordwest). Clearly, less faults are visible relative to the deeper plane of the top of the Chalk (Figure 4.31)

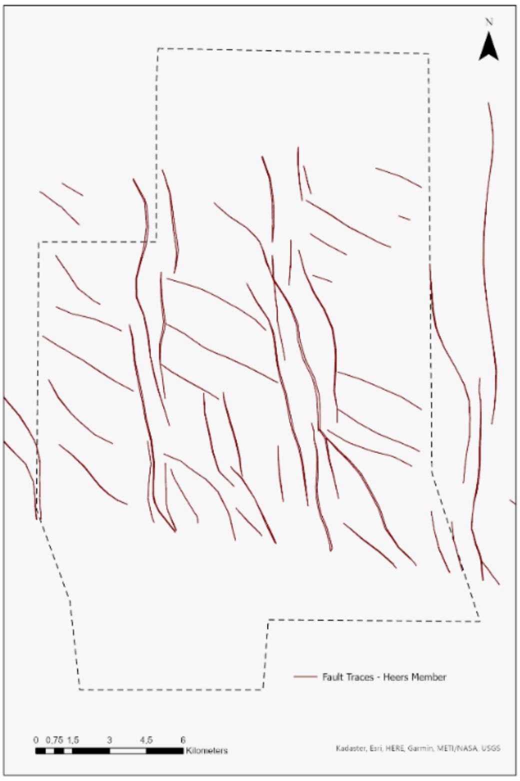

Figure 4.31 Fault pattern of the base of the Heers Formation, corresponding to the top of the Chalk (from H3O-Roerdalslenk Noordwest).

Figure 4.32 shows a seismic profile across the selected faults. The seismic section shows the interpreted horizons of a reflector in the Breda Formation (pink), the base of the Veldhoven clay (green), the near base of the Brussel sand and the base of the Heers sand.

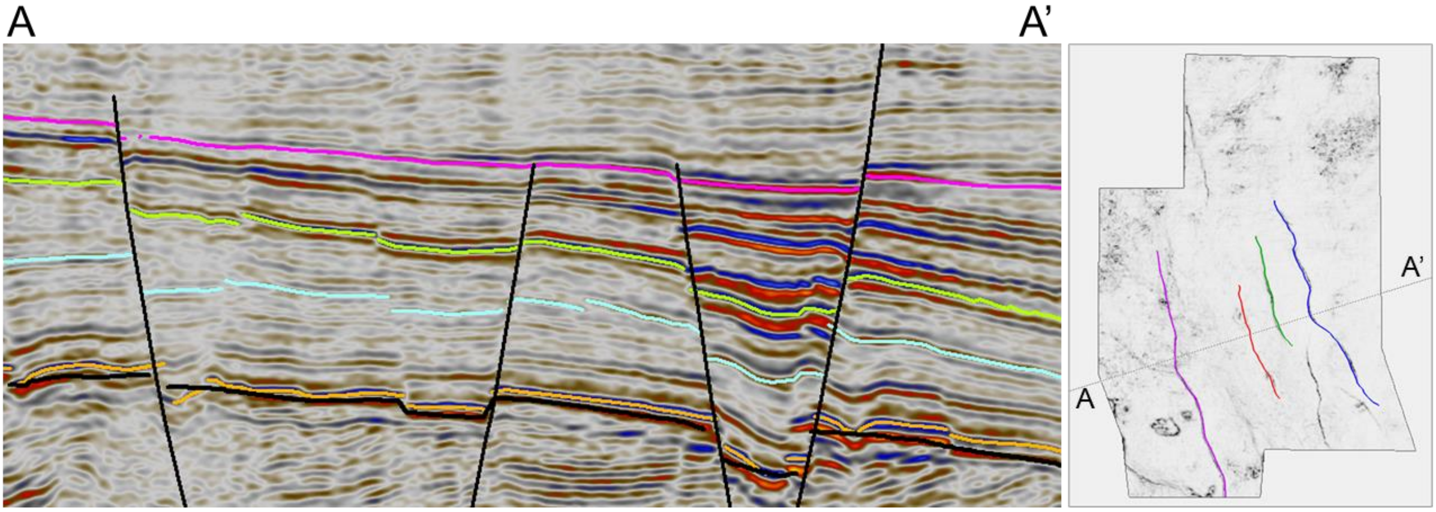

Figure 4.32. Seismic section from west (left) to east (right), showing the interpreted horizons within the fault framework. from top to bottom: intra-Breda (pink), base Veldhoven clay (green), near base Brussel sand (blue), base Heers sand (orange).

4.4.4.2 Fault displacement at the Tilburg faults

The results of the displacement analyses are visualized on the fault-planes (Figure 4.33: fault 1, Figure 4.34: fault 2 and 3 and Figure 4.35: fault 4; see Figure 4.29 for location of the faults).

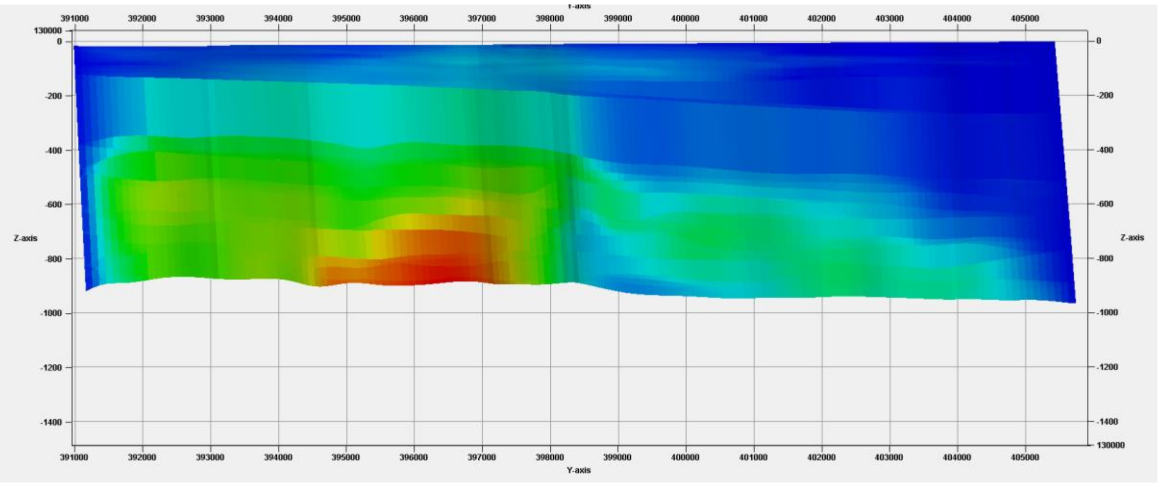

Figure 4.33 Displacement analysis of fault 1 visualized on the fault plane.

Figure 4.33 shows the distribution of displacement on the fault plane of fault 1 (modelled length: 15389 meters). The maximum amount of displacement (red area) is not located at the center of the plane but slightly to the left at the bottom of the fault plane. It also shows a low amount of displacement at the center and another local high amount of displacement on the right of the center. This indicates two fault segments with a relay ramp at the center. At the top of the fault plane, affecting the youngest stratigraphic layers, this displacement signature is no longer present. Instead, albeit with low amounts of displacement, the center of displacement is located at the center of the fault. This indicates that the two previous segments have been hard-linked and that the resulting larger fault now behaves as a single fault.

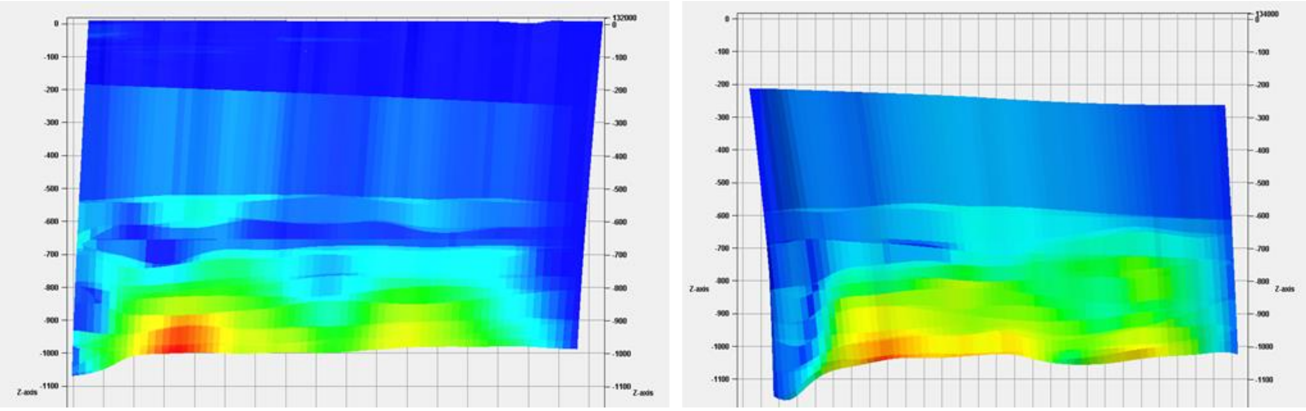

Figure 4.34 Displacement analysis of faults 2 and 3 visualized on the fault plane

Figure 4.34 shows the distribution of displacement on the fault plane of faults 2 and fault 3 (modelled length: 7824 meters and 7190 m, respectively). For fault 2, it shows a text-book example of a displacement graph for two linked fault segments: two clear peaks of high displacement left and right of the center of the fault. Unlike fault 1, there are no signs that this signature has changes in the top-most stratigraphic layers. For fault 3, also two local displacement highs left and right of the center are visible. Although this fault does not penetrate into stratigraphic units above the Breda unit, it does show relocation of the maximum amount of displacement to the center of the fault plane in the Breda unit.

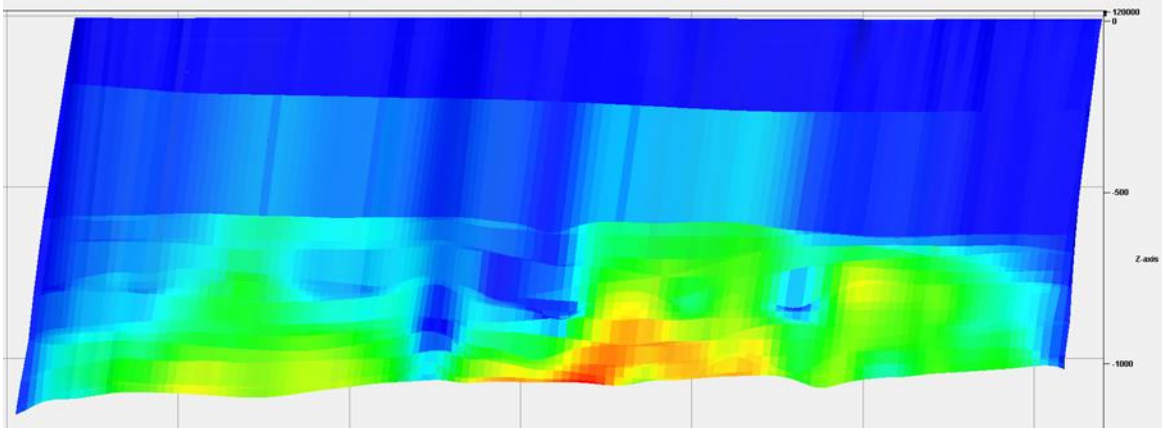

Figure 4.35 Displacement analysis of fault 4 visualized on the fault plane

Figure 4.35 shows the distribution of displacement on the fault plane of fault 4 (modelled length: 15258 meters). This fault is comparable to fault 2 in the sense that there are no signs of movement of this fault as a single fault. Noteworthy however is the possibility of three fault-segments. Besides the obvious segment on the left, the local high at the right side of the red-shaded area might indicate a third segment.

In summary, it is apparent from displacement analyses for the four faults in the area that these faults are an aggregate of linked fault-segments. It may mean that these linkages have associated “linking damage zones” (see section 4.3.2), which may involve a reduction of lateral flow due to the occurrence of low-permeable deformation bands or the possibility of more permeable conduits for vertical migration of fluids (see Figure 4.20).

4.4.4.3 Variance maps at the Tilburg pilot

Further insights into faults and fault-patterns can be obtained by derivatives of the seismic signal of a 3D seismic survey, also referred to as seismic attributes. One such attribute is the Coherence attribute, with variance being a coherence method. A coherence attribute allows for visualizations of sudden changes, or discontinuities, in the seismic signal. A fault is a feature that affects the seismic signal and thus can be visualized by using the variance values of a seismic survey.
The variance of a seismic survey can be plotted on stratigraphic horizons to create variance maps for these horizons. With variance maps the exact traces and lengths of faults at different depth levels can be ascertained and therefore aide in the interpretations of faults, especially in areas with a high fault density.

Variance maps have been made for four horizons for the top-down visualization of fault-traces at different depths. Four strong reflectors have been chosen for quick and continuous 3D auto-tracking interpretations for these horizons (Figure 4.32). The corresponding horizons have been indicated in this cross-section with a color: an intra-Breda formation reflector (pink), the base of the Veldhoven clay (green), a near base Brussel reflector (blue) and the base of the Heers sand member, which equals the top of the Chalk (orange).

Figure 4.36 shows areas where linkage of fault segments have resulted in a larger, continuous fault plane (areas A, B and C). The four variance maps of the 4 selected horizons give insight into the state of the relay ramps at different depth levels; non-existent, soft-linked or hard-linked (see section 4.3.4.3 . These relay ramps are the structure in between two overlapping fault planes, which may represent linking damage zones.

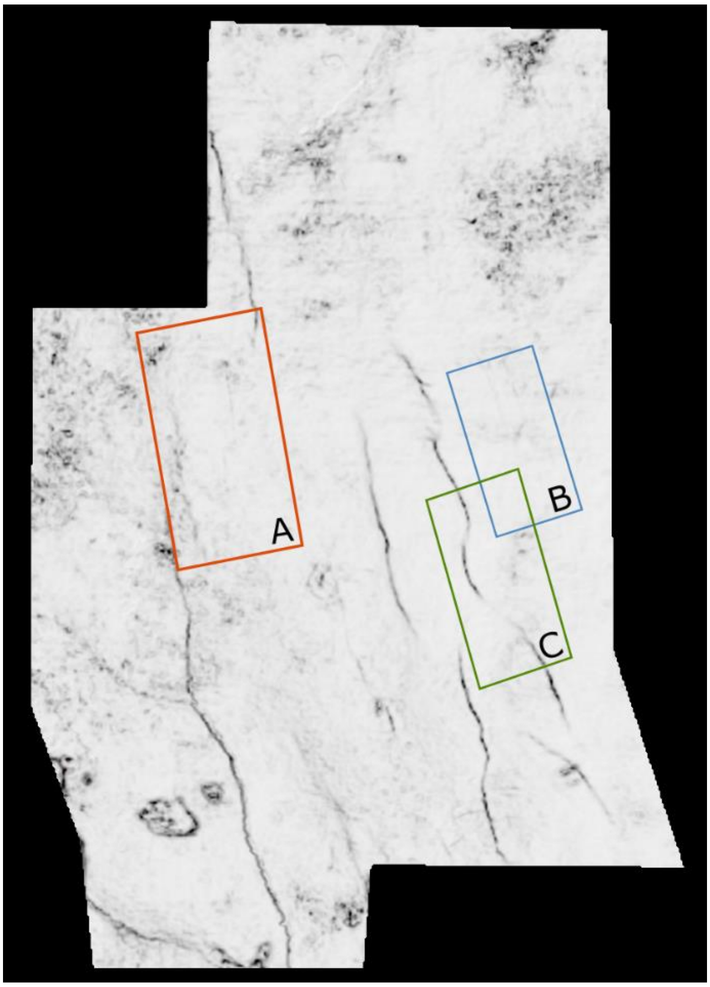

Figure 4.36 Areas showing linkage of faults into larger fault planes.

Area A

No faults are visible in this area on the variance map of the intra Breda reflector. On the variance map of the base Veldhoven clay multiple faults appear. Two of these faults are arranged in an en-echelon pattern and are part of a graben structure. These faults appear to have been linked on the variance maps of the deeper reflectors (blue and orange maps). Also, a connection with a fault north of Area A becomes apparent. On the variance map of the base Heers sand, it becomes harder to distinguish between fault traces due to the dipping of faults on both sides of the graben in opposite direction.

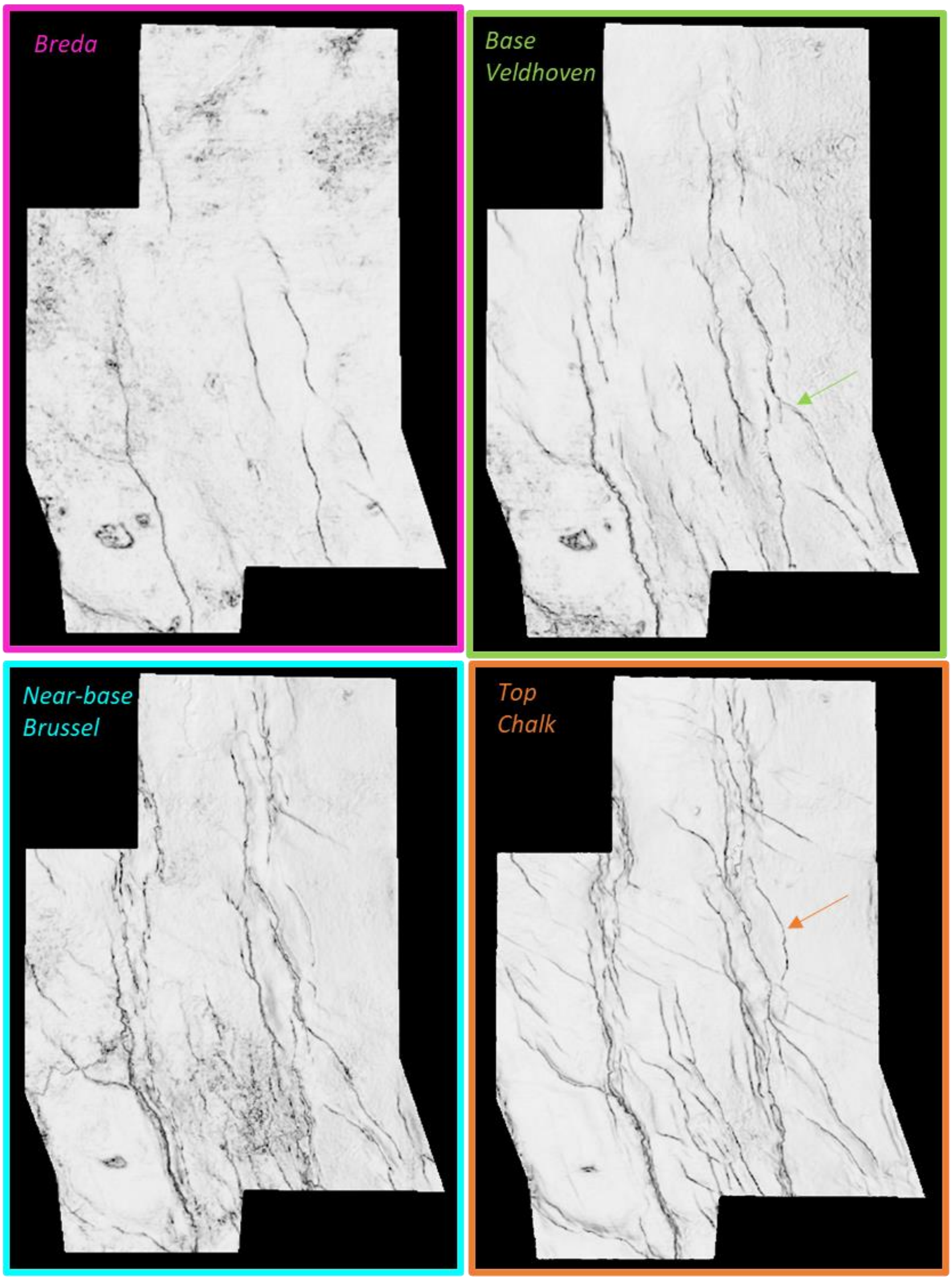

Figure 4.37 Variance maps at 4 horizons which are shown in Figure 4.32 from shallow to deep: an intra Breda formation strong reflector (pink), the base Veldhoven(green), the near-base Brussel (blue) and the base Heers/ top Chalk (orange).

Area B

This shows a good example of the elliptical shape of a fault plane. There is no fault visible on the variance map for the intra Breda reflector. A small fault becomes visible on the Veldhoven clay variance map which extends slightly on each successive variance map. The increase in length decreases with depth and because of the roughly equal spacing of the stratigraphic surfaces in depth, an elliptical shape can be deduced (Figure 4.38 and arrow in Figure 4.37).

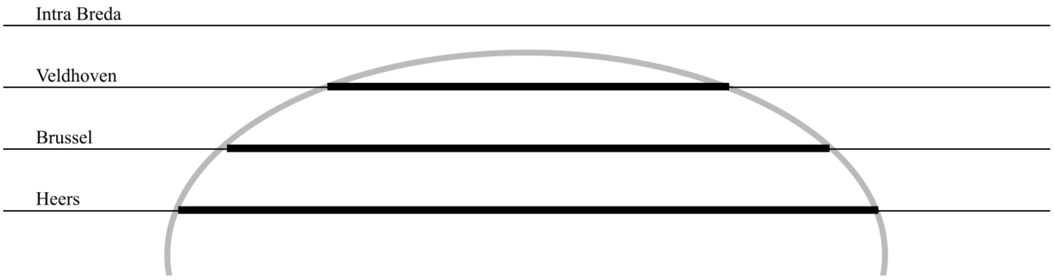

Figure 4.38 Deduced elliptical shape of a fault in Area B. Dark lines on the reflectors show the trace of the fault on the variance map and the grey circle indicates the deduced fault plane.

Area C

Area C shows the linking of two fault segments and a breach of the relay ramp. The variance map of the intra Breda reflector shows two separate faults. The area in between, the relay ramp, already appears to have been affected at this level. The variance map of the Veldhoven clay shows a continuous trace across the relay ramp. On the variance maps of the deeper reflectors the two original segments are no longer identifiable by trace.

4.4.5 Juxtaposition analysis at the Tilburg pilot

The juxtaposition analyses for the four modelled faults return a roughly similar distribution pattern of the three lithological contact combinations (Figure 4.39). The colours on the fault planes correspond to the following contact types:

- Yellow: Sand-to-sand contact
- Blue: Clay-to-sand contact or vice versa
- Grey: Clay-to-clay contact

For the shallower depth range, that is above the Breda units which is indicated for Fault 4, the faults 2 and 4 show an alternation between sand-to-sand contacts, and clay-to-clay contacts. Contrary for fault 1, an alternation exists mainly between sand-to-sand and clay-to-sand contacts. Fault 3 does not penetrate into the units above the Breda units, so no conclusions may be drawn here..

The combined Breda units account for roughly half (40%-50%) of the total thickness of the Cenozoic interval (Figure 4.39). This results in a large portion of the fault planes consisting of sand-to-sand contact types.

As the main aquifers used for drinking water production are above the Breda Formation, especially fault 1 on the western side seems to form a barrier against lateral groundwater flow.

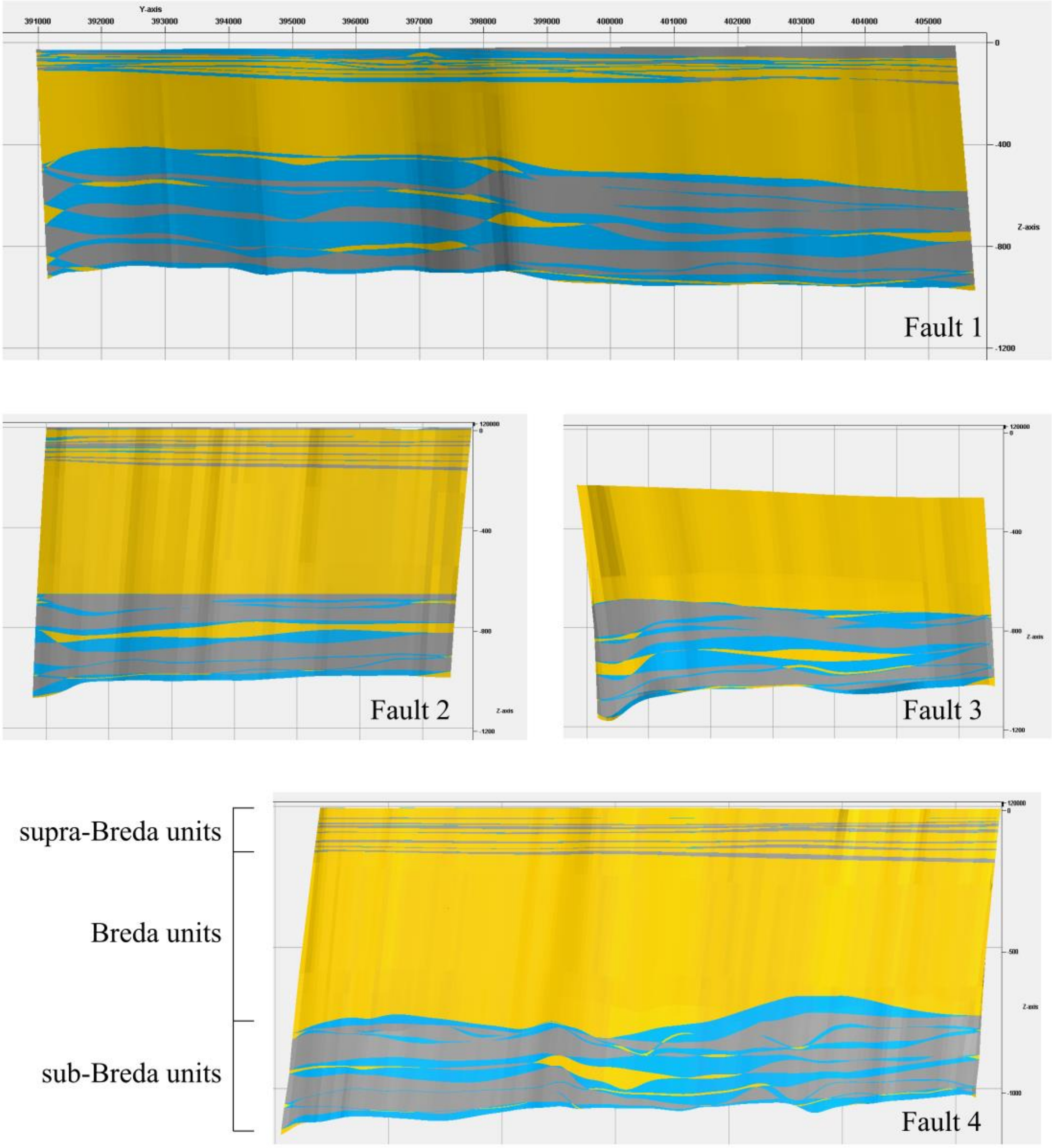

Figure 4.39 Results for the juxtapostion analyses for the four faults.

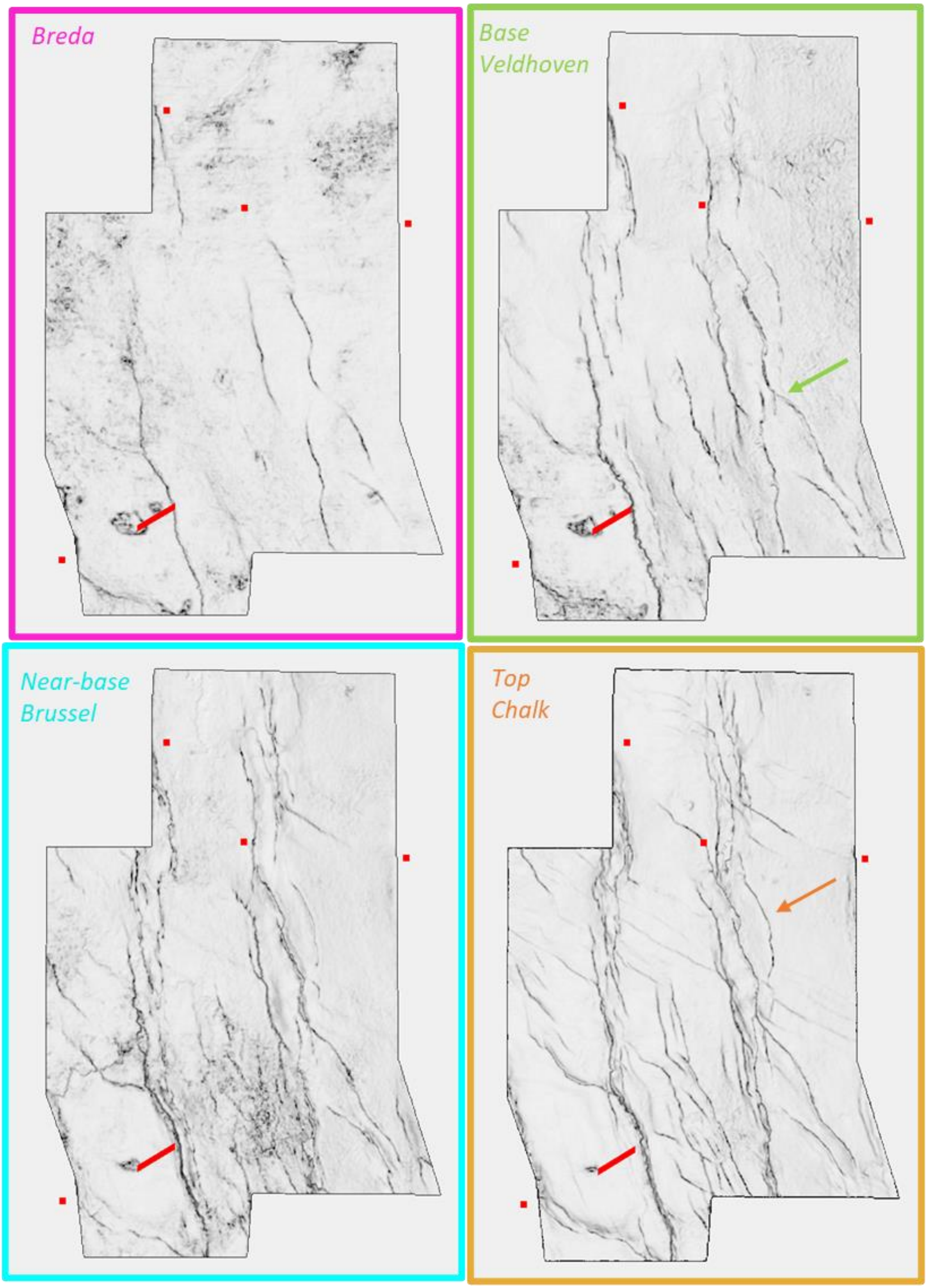

Figure 4.40 Confrontation of the fault variance maps and the shallow aquifer used for drinking water production. Red symbols at approximate locations represent 5 water works in the area with varying pumping depths between ~ 50 and 150 m. The most southerly water production sites are known to be very close to fault 1 and pumps between 40 and 180 m depth.

4.4.6 Consequences for shallow aquifers around Tilburg

The shallow aquifers around Tilburg are intensively used for drinking water production and other water demands such as irrigation for agricultural purposes. It is interesting to see how these faults may influence the water works. One of the water works (red line = BW 19) is very close to the shallow location of fault 1 (Figure 4.40). From the juxtaposition analysis, it seems reasonable to assume that fault 1 should induce a horizontal hydraulic resistance which is confirmed by earlier work of Bense et al. (2003). Fault 1 is clearly present is the shallower 50 m of the subsurface with lateral discontinuities of layers visible up to very shallow sediment layers (Van Uum et al., 2003). The figure also shows that faults are no vertical structures; the dip with depth. This can be clearly see near well field BW19 (red line): the fault plane has a more easterly location than the same fault at shallow depth.

Whether the faults form more permaeable conduits between the deeper subsurface and these shallower aquifers is yet unknown. Helium-4 and Helium-3 measurements of the the mixed raw water at well field BW19 did not give indications for such a connection (Broers et al. 2021), other than having a small mantle signal which is present in most of the Roer Valley Graben water works (see Chapter 5 and Broers et al. 2021a). For the current VOGERA study, no further work on the characterization of these well fields has been performed. But Chapter 5 deals with tracer studies to identify deep-shallow connections by means of gas compositions and tracers for the Roer Valley Graben and well field BW27 in particular.

4.5 Application of Tool for the Veghel pilot

The GWV 3D tool has been applied using the information of section4.2.1. Figure 4.41 shows the geological units as distinguished in the deep Digital Geological Model of the Netherlands (DGMdiep available at https://www.dinoloket.nl/en; see Figure 4.6). The lithology and the clay (mudstone) thicknes per layer have been based on the borelog of the hydrocarbon exploration well KDK-01 (see Figure 4.3 for location).

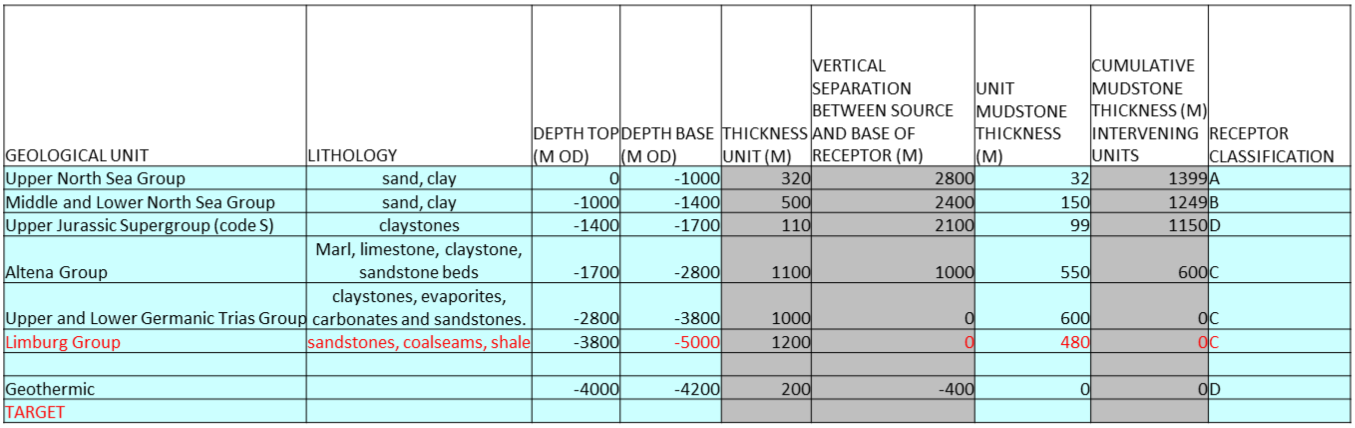

GEOLOGICAL UNIT	LITHOLOGY	DEPTH TOP (M OD)	DEPTH BASE (M OD)	THICKNESS UNIT (M)	VERTICAL SEPARATION BETWEEN SOURCE AND BASE OF RECEPTOR (M)	UNIT MUDSTONE THICKNESS (M)	CUMULATIVE MUDSTONE THICKNESS (M) INTERVENING UNITS	RECEPTOR CLASSIFICATION
Upper North Sea Group	sand, clay	0	-1000	320	2800	32	1399	A
Middle and Lower North Sea Group	sand, clay	-1000	-1400	500	2400	150	1249	B
Upper Jurassic Supergroup (code S)	claystones	-1400	-1700	110	2100	99	1150	D
Altena Group	Marl, limestone, claystone, sandstone beds	-1700	-2800	1100	1000	550	600	C
Upper and Lower Germanic Trias Group	claystones, evaporites, carbonates and sandstones.	-2800	-3800	1000	0	600	0	C
Limburg Group	sandstones, coalseams, shale	-3800	-5000	1200	0	480	0	C
Geothermic		-4000	-4200	200	-400	0	0	D
TARGET								

Figure 4.41 Veghel pilot in GWV 3D: Geological sequence.

The content of the “geological sequence” worksheet (Figure 4.41) is carried over to the next sheet “Hazard assessment” which has been completed with ratings and confidences to determine the hazard scores (Figure 4.42).

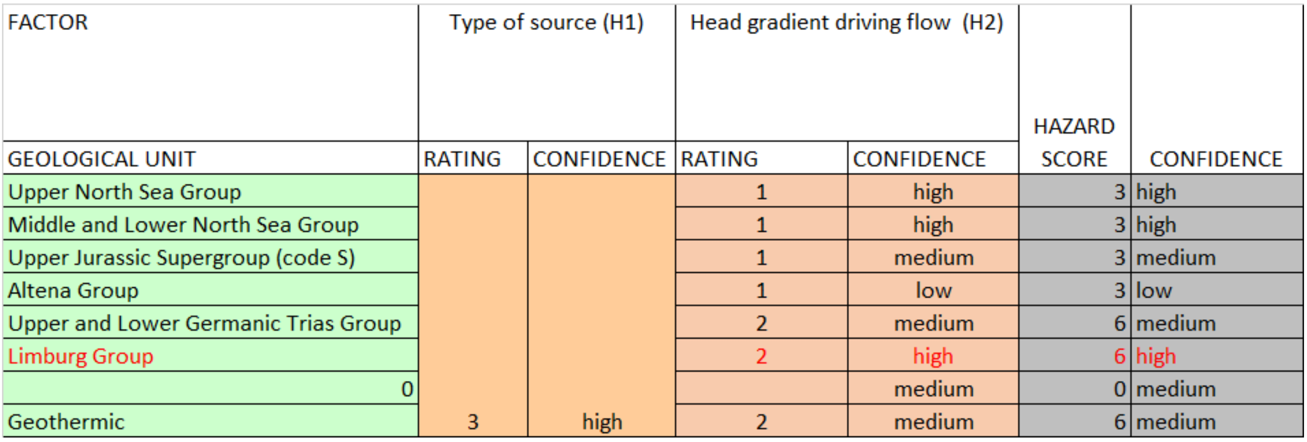

FACTOR	Type of source (H1)		Head gradient driving flow (H2)		HAZARD SCORE	CONFIDENCE
GEOLOGICAL UNIT	RATING	CONFIDENCE	RATING	CONFIDENCE		
Upper North Sea Group			1	high	3	high
Middle and Lower North Sea Group			1	high	3	high
Upper Jurassic Supergroup (code S)			1	medium	3	medium
Altena Group			1	low	3	low
Upper and Lower Germanic Trias Group			2	medium	6	medium
Limburg Group			2	high	6	high
0				medium	0	medium
Geothermic	3	high	2	medium	6	medium

Figure 4.42 Veghel pilot in GWV 3D: Hazard assessment.

In the next step, the separation distances and amount of clay between the geothermic activity and the geological units are specified (Figure 4.43). The information for the intrinsic vulnerability is completed by filling in the columns for the flow mechanism and presence of features that could provide preferential pathways (Figure 4.44).

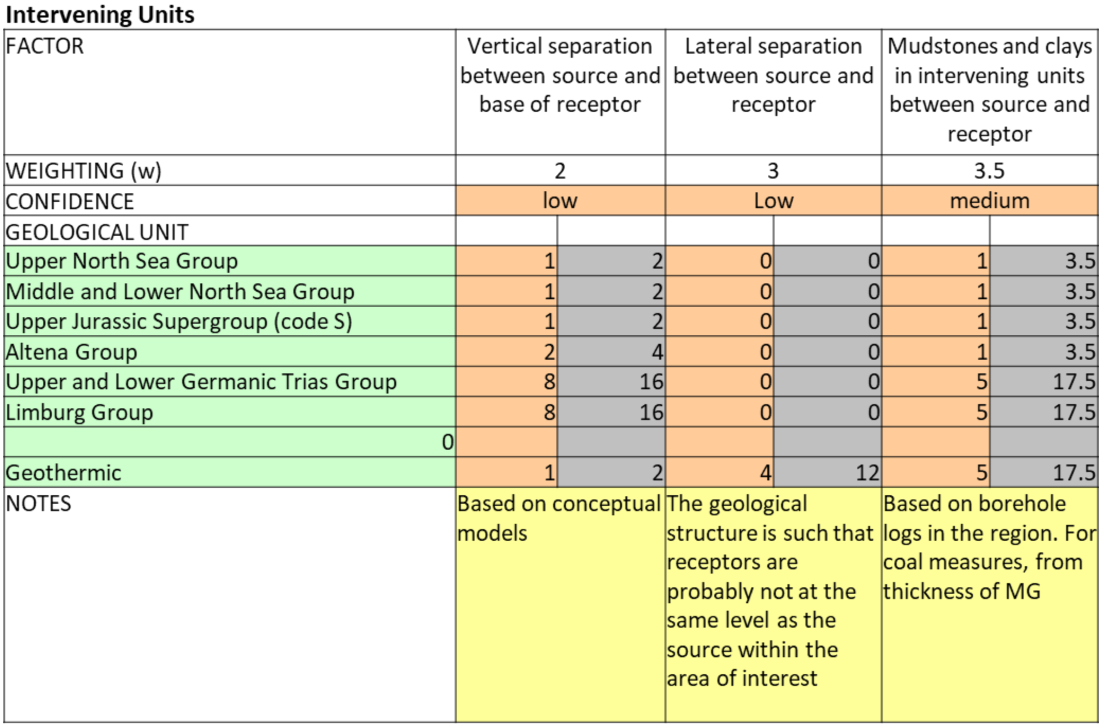

Intervening Units

FACTOR	Vertical separation between source and base of receptor		Lateral separation between source and receptor		Mudstones and clays in intervening units between source and receptor	
WEIGHTING (w)	2		3		3.5	
CONFIDENCE	low		Low		medium	
GEOLOGICAL UNIT						
Upper North Sea Group	1	2	0	0	1	3.5
Middle and Lower North Sea Group	1	2	0	0	1	3.5
Upper Jurassic Supergroup (code S)	1	2	0	0	1	3.5
Altena Group	2	4	0	0	1	3.5
Upper and Lower Germanic Trias Group	8	16	0	0	5	17.5
Limburg Group	8	16	0	0	5	17.5
0						
Geothermic	1	2	4	12	5	17.5
NOTES	Based on conceptual models		The geological structure is such that receptors are probably not at the same level as the source within the area of interest		Based on borehole logs in the region. For coal measures, from thickness of MG	

Figure 4.43 Veghel pilot in GWV 3D: Intervening units of intrinsic vulnerability sheet.

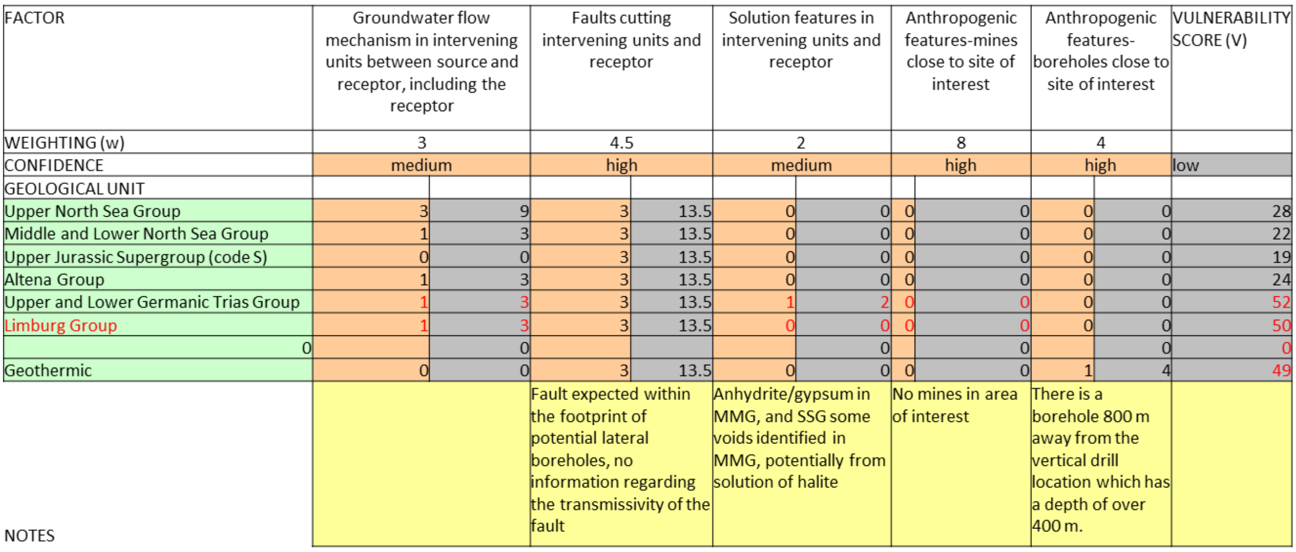

FACTOR	Groundwater flow mechanism in intervening units between source and receptor, including the receptor		Faults cutting intervening units and receptor		Solution features in intervening units and receptor		Anthropogenic features-mines close to site of interest		Anthropogenic features-boreholes close to site of interest		VULNERABILITY SCORE (V)
WEIGHTING (w)	3		4.5		2		8		4		
CONFIDENCE	medium		high		medium		high		high		low
GEOLOGICAL UNIT											
Upper North Sea Group	3	9	3	13.5	0	0	0	0	0	0	28
Middle and Lower North Sea Group	1	3	3	13.5	0	0	0	0	0	0	22
Upper Jurassic Supergroup (code S)	0	0	3	13.5	0	0	0	0	0	0	19
Altena Group	1	3	3	13.5	0	0	0	0	0	0	24
Upper and Lower Germanic Trias Group	1	3	3	13.5	1	2	0	0	0	0	52
Limburg Group	1	3	3	13.5	0	0	0	0	0	0	50
0		0				0		0		0	0
Geothermic	0	0	3	13.5	0	0	0	0	1	4	49
NOTES			Fault expected within the footprint of potential lateral boreholes, no information regarding the transmissivity of the fault		Anhydrite/gypsum in MMG, and SSG some voids identified in MMG, potentially from solution of halite		No mines in area of interest		There is a borehole 800 m away from the vertical drill location which has a depth of over 400 m.		

Figure 4.44 Veghel pilot in GWV 3D: additional features for intrinsic vulnerability.

The resulting vulnerabilities (Figure 4.45) are all in the lowest class for the assigned receptor classes. For class A receptors the minimum risk group is “Medium/low”, indicating that further analysis should always be carried out for important groundwater resources when considering a deep energy-related activity.

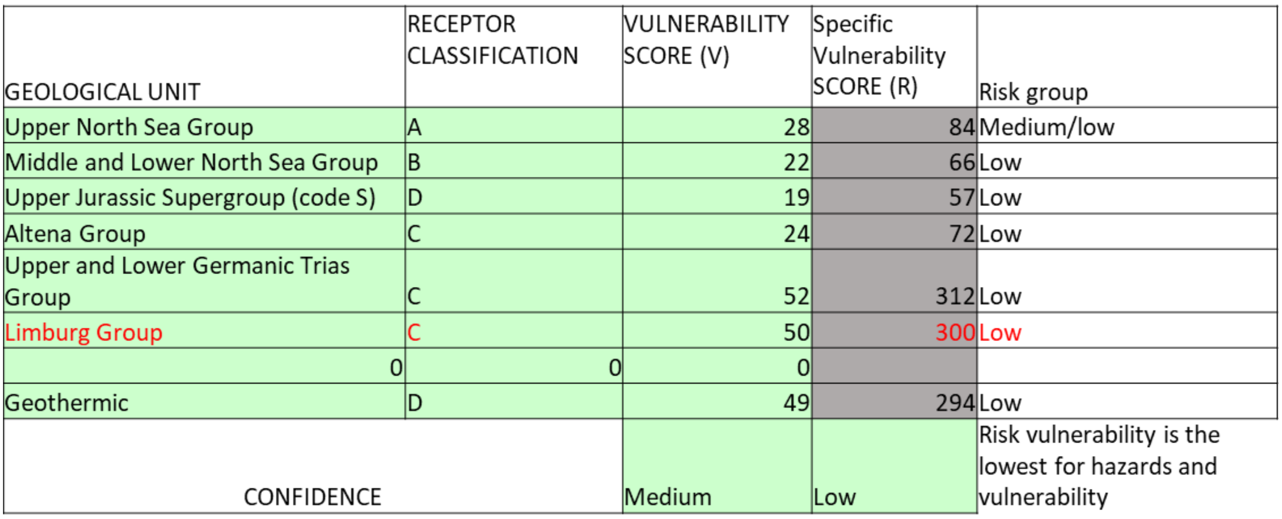

GEOLOGICAL UNIT	RECEPTOR CLASSIFICATION	VULNERABILITY SCORE (V)	Specific Vulnerability SCORE (R)	Risk group
Upper North Sea Group	A	28	84	Medium/low
Middle and Lower North Sea Group	B	22	66	Low
Upper Jurassic Supergroup (code S)	D	19	57	Low
Altena Group	C	24	72	Low
Upper and Lower Germanic Trias Group	C	52	312	Low
Limburg Group	C	50	300	Low
0	0	0		
Geothermic	D	49	294	Low
CONFIDENCE		Medium	Low	Risk vulnerability is the lowest for hazards and vulnerability

Figure 4.45 Veghel pilot in GWV 3D: resulting vulnerabilities.

The risk groups are the lowest available for each unit. The value of 84 for the Upper North Sea Group is well below the upper value of the range from 0 to 250 for the score of “Medium/low” for the class A selector.

4.6 Discussion for fault zones near Veghel and Tilburg

In this chapter, we investigated the possibilities of 2D and 3D seismic data for the identification and evaluation of potential contaminant migration pathways and controls on fluid flow/transport behaviour that would indicate a connection between the deeper and shallow subsurface with the ultimate aim to assess the vulnerability of aquifers which produce fresh groundwater for human uses.

We used a subsurface model based on 2D seismic data and borelogs for the evaluation of the fault zone near Veghel. This provided only an indication of the fault segments that were linked by the fault evolution. The linking zones may induce vertical connections as “linking damage” may enhance vertical connectivity. This is especially true if these damage zones are apparent in the deeper consolidated deposits, which may enhance permeability and the flow of liquids or gas through those consolidated deposits in the direction of the unconsolidated deposits higher in the profile. Indications for these kind of pathways are present near Veghel, but a further analysis would require the use of 3D seismic data.
The application of the GWV 3D tool indicates a vulnerability in the lowest risk group for each receptor. However, the presence of an important groundwater resource (class A receptor) asks for more detailed investigation.

Juxtaposition analysis at the Veghel Fault indicates a sequence of clay-clay and sand-sand contacts in the upper part of the profile which is most relevant for the shallow activities such as drinking water production. The juxtaposition analysis was done with a quite rough assumption of 100% sand in sand layers and 100% clay in clay layers. This may overestimate the potentially permeable sand-sand contacts and possibly underestimate the effects of clay smear at the fault plane. We would recommended to do a subsequent analysis with a more detailed geological model to investigate the possible effects of clay smearing, for example using geostatistical realisations with different architectures of clay and sand mixes and different proportions of clay and sand in the sandy formations. We think that clay smear is very possible in the top part of the profile and in the depth range of the Breda Formation (see also section 4.3.6, and Figure 4.46)

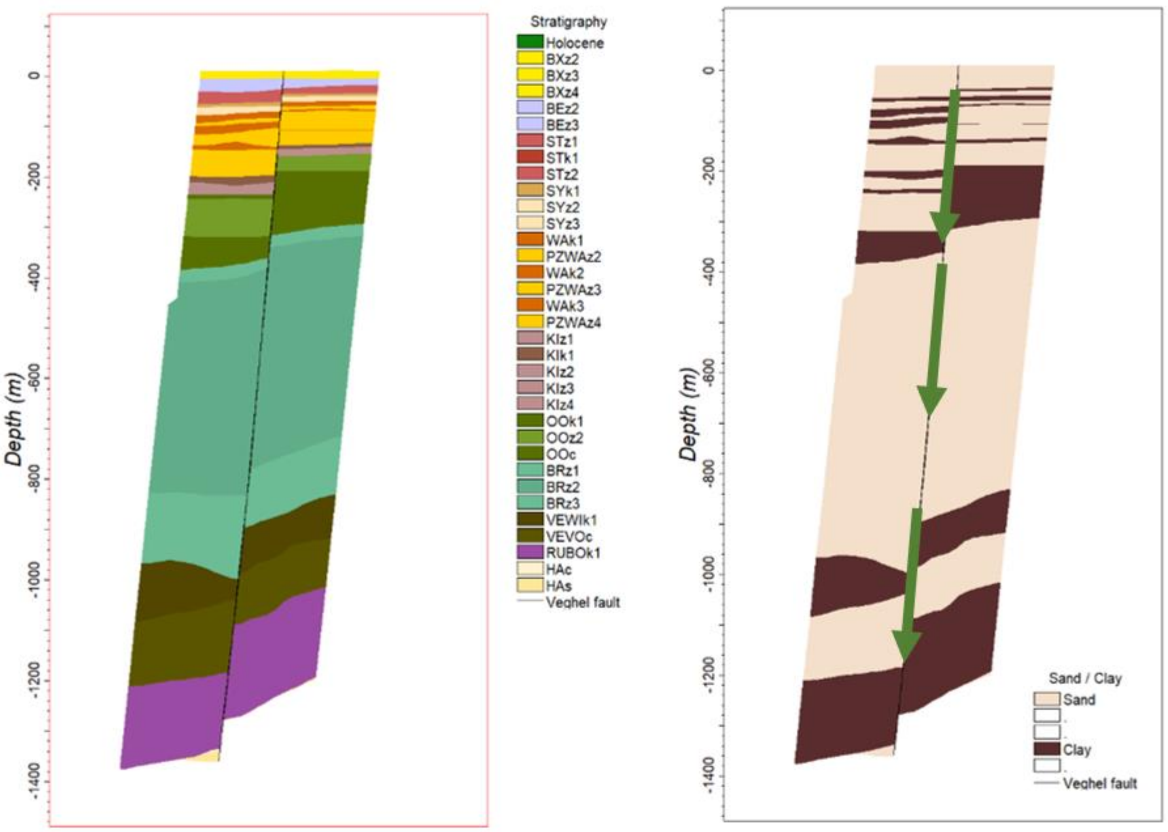

Figure 4.46 Possible effects of clay smear along the Veghel Fault as clay contents in the sediments may be higher than estimated in the current setup of the study. Arrows denote parts of the profile where clay smear is conceivable.

The 3D seismic study near the Gilze-Rijen Fault zone at Tilburg reveals the opportunities to further characterize damage zones around faults. The analysis clearly showed the 3D structure of the faults and the increase of linkage between fault segments in the deeper subsurface which cannot be seen in the more shallow horizons. Especially the deepest plan at the top of the Chalk reveals the presence of intensive faulting and suggest that damage zones are quite broad and abundantly present. These damage zones at larger depth in consolidated deposits may result in enhanced vertical permeability of the fault zone which may induce upward flow of fluids and gases.

We made a first attempt to a risk or probability map for the presence of linking damage zones which illustrates the potential hotspots for vertical connections (Figure 4.47). This risk map for potential vertical migration was made from the top Chalk horizon als permeability changes in damage zones are more apparent in consolidated rocks and not so much in the unconsolidated sediments above it. Importantly, because of the 3D structure of faults, these hotspots may not be located at the exact location of a fault in the upper Formations as the position of the fault zone varies with depth because of the fault plane dip. Whether the upwards migration of gases or fluids is hampered by lithological variations in the upper unconsolidated deposits has not been studied here, but the ample presence of clay layers between the deeper hard rock and the shallower aquifers that are used for drinking water production may limit the actual vertical exchange of fluids and gases. It is interesting though, that a signal for 2.5% of mantle contribution for the ^{4}He and 96% contribution for the ^{3}He is present in almost all the the water works in the Roer Valley Graben which has been linked to the Graben to be a important rift zone with substantial tectonic movement in the past (Broers et al. 2021a, see also Chapter 5).

Figure 4.47 Top Chalk variance map with locations of linking-damage zones which may present risks for vertical connections through the consolidated desposits towards shallower layers

5 Gas and tracer signals in the Pilot Noord-Brabant, the Netherlands

5.1 Introduction of the analysis for the province of Noord-Brabant

5.1.1 Overall aims

In the Netherlands, the Noord-Brabant region was chosen to identify potential pathways between the deep and shallow subsurface, including fault zones and high permeability zones, and to assess the groundwater vulnerability of shallow groundwater relative to deep subsurface activities. Three pilots were distinguished:

- Peel Boundary fault near Veghel;
- Gilze-Rijen faults near Tilburg;
- Gas and tracer signals in the shallow groundwater.

The first two pilots have been reported in Chapter 4 of this report. The current chapter presents the third pilot which aims to investigate relations between the deep and shallow subsurface in the pilot region, using a range of physico-chemical data including stable isotope, dating/residence time indicators, temperature and hydraulic head/flow data in combination with geophysical methods where possible. Tracer techniques that were used include noble gas composition, methane and methane isotopes, ^{3}He and ^{4}He, and age tracers such as ^{14}C. We combined this information with information about the hydrogeological build-up of the region and regional hydraulic head gradients, to evaluate whether or not there is evidence for localized hydraulic perturbation caused by the identified pathways that would affect groundwater vulnerability. The work was complemented by a baseline characterization of the gas composition in the shallow groundwater.

5.1.2 Research topics in the pilot Noord-Brabant

The pilot site of the Netherlands is the province of Noord-Brabant. Within this province, three subtopics were investigated which are explained in more detail below. These subtopics are:

1. Baseline monitoring of gases in shallow groundwater. We used new gas measurements that were carried out in the provincial groundwater quality monitoring network to investigate the gas composition of shallow groundwater and the isotope composition of methane as a proxy for thermogenic or biogenic sources;
2. Connections between the deep subsurface and shallow groundwater: fault hydrology in the surroundings of the public supply well field of Veghel. We characterized the water samples from the pumping wells to investigate whether the position relative to the nearby fault zone would influence the tracer and gas composition;
3. Connections between deep and shallow: regional groundwater discharge near the city of ‘s-Hertogenbosch. The baseline monitoring of methane and methane isotopes gave an indication for the upward seepage of groundwater with a thermogenic methane signal. We characterized the gas composition and assessed the groundwater ages in a 250 m deep multi-level observation well in order to better understand the local influence from the deep subsurface.

Results of the work at the three cases are described in the sections 5.3.1, 5.3.2, and 5.3.3, respectively.

5.2 Geology and hydrogeology of the province of Noord-Brabant

The province of Noord-Brabant is part of the Dutch lowlands an represents a comparatively flat area with altitudes ranging from mean sea level (MSL) in the north and west to 30 m above MSL in the southeast. Water tables are typically shallow, mostly within 1–5 m below the surface. Geologically, we distinguish 3 zones with a different hydrogeological setting; the western part, the Roer Valley Graben (RVG) in the center and the higher Peel Block in the east (Figure 5.1). The Roer Valley Graben is a tectonic structure that has a NW-SE orientation and is part of an old rift system that extends from the Rhone Valley in France, through the Rhine Valley Graben in Germany, through the Roer Valley Rift System into the North Sea basin. The Roer Valley Graben hosts a thick series Tertiary and Quaternary sediments and contains a large resource of fresh groundwater. The Peel Block which has been uplifted relative to the Graben supports an aquifer with a thickness of approximately 50 meters, whereas fresh aquifers in western Brabant have a thickness of 100-200 meters.

Fluvial and estuarine gravel and sand deposits of the Rhine-Meuse system form the main aquifers for groundwater abstraction in the Roer Valley Graben, especially the Pliocene Kieseloolite (KI) and Late Pliocene / Early Pleistocene Waalre (WA) Formations are used for water supply purposes. Especially the upper part of the Waalre Formation forms a major aquitard that confines the deeper groundwater which is pumped for drinking water supply. This is also true for well field BW27 which is located close to the Peel Boundary fault system (Figure 5.1, also see sections 4.1.1 and 4.2.1).

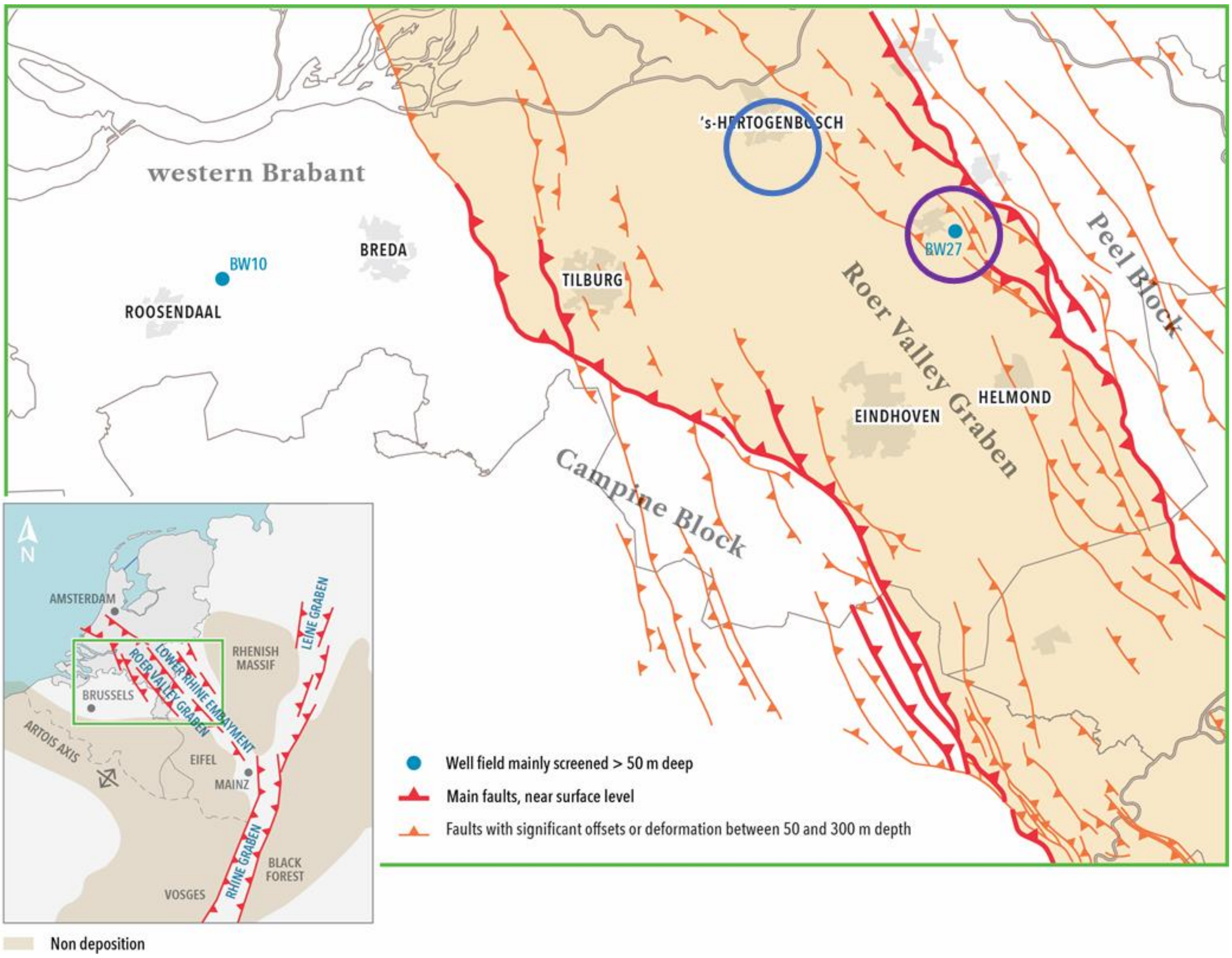

Figure 5.1 Map of the province of Noord-Brabant. The orange and red lines indicate the fault zones, the red bold lines indicate the main fault zones that border the Roer Valley Graben: the Peel Boundary fault zone in the east and the Feldbiss fault zone in the west. Purple circle indicates the BW27 well field. Blue circle represents the 's-Hertogenbosch pilot site.

The aquitard at the top of the Waalre Formation is partly overlain by periglacial and fluvial deposits form the Early Pleistocene Stramproy Formation (SY) and coarse fluvial sands and gravels of the Middle Pleistocene Sterksel Formation (ST). The Sterksel Formation forms the main first aquifer in the Graben. The prime aquifers in western Brabant outside the Roer Valley Graben are made up of the sediments of the Pleistocene Waalre and Stramproy Formations and the underlying marine Maassluis and Oosterhout Formations. On the Peel Block, the upper thin aquifers consists of sediments from the Kieseloolite Formation and the gravels from the Meuse river that are distinguished as the Beegden Formation. On top of most of the Study area, the Boxtel Formation is present, which consists of fine sands and loam from periglacial and eolian origin.

Shallow multi-level monitoring wells of the provincial monitoring network of Noord-Brabant were used to gain information about the composition of shallow gases in the region. This is the first pilot described in this chapter. The observation wells of the monitoring network are typically screened at 10 and 25 m depth, in the shallow geological units that were described previously: the Boxtel and Sterksel Formations in the Roer Valley Graben, the Boxtel and Beegden Formations at the Peel Block and the Boxtel and Upper Waalre Formation in western Noord-Brabant.

We paid special attention to a well in the Roer Valley Graben near the city of ‘s-Hertogenbosch. The 250 m deep multi-level well that we sampled, contains the whole range of shallow geological formations: starting at depth in the Oosterhout Formation and subsequently the Kieseloolite Formation, Waalre Formation, Sterksel Formation and the Boxtel Formation at the top of the profile.

Figure 5.2 shows how the Veghel pilot around Brabant Water well field BW27 and ‘s-Hertogenbosch are situated relative to the faults of the Peel Boundary fault system. Well field BW27 lies close to a secondary fault of the Peel Boundary zone which was described in detail in Chapter 4. The ‘s-Hertogenbosch site is situated in one of the deeper parts of the Roer Valley Graben outside of the direct influence of the bordering faults. The ‘s-Hertogenbosch region was chosen because it represents a regional groundwater discharge area; the city of ‘s-Hertogenbosch is situated where several brooks join, including the Dommel river, before these brooks drain into the more northerly Meuse river.

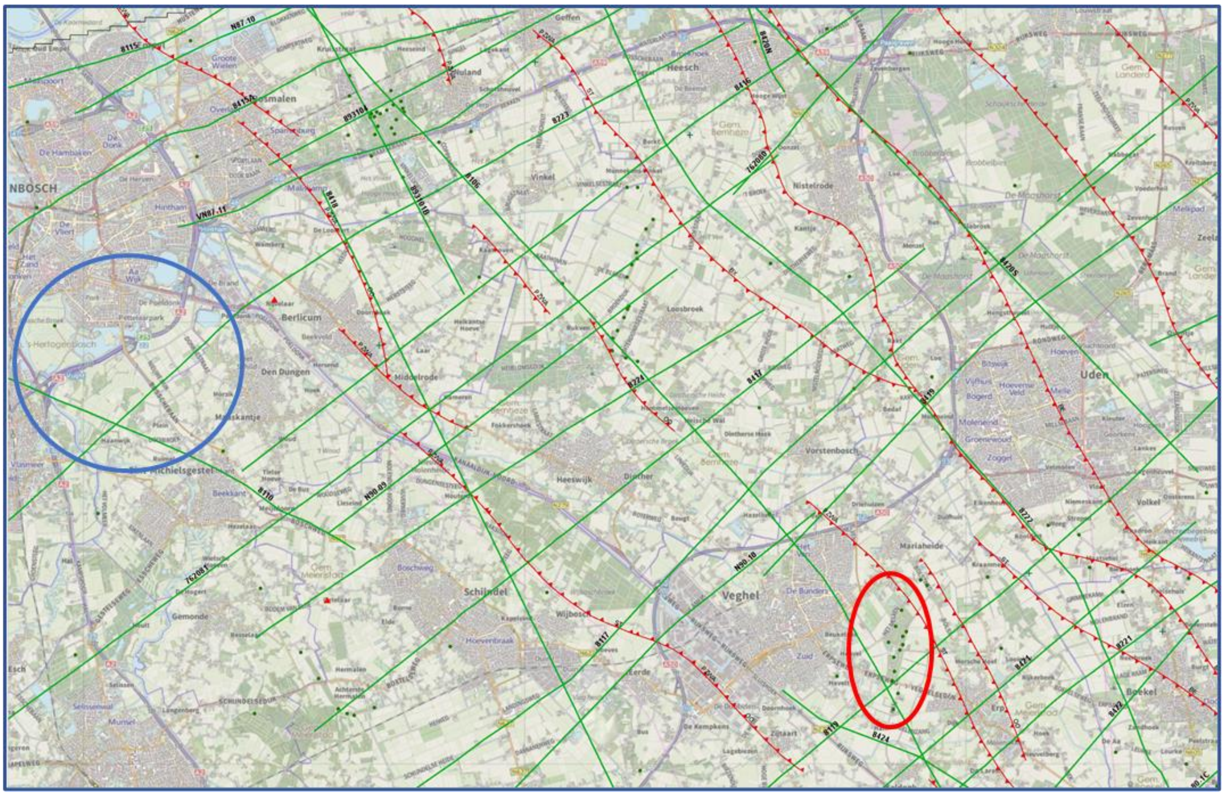

Figure 5.2 Setting of the Veghel pilot with the BW27 well field (red) and the ‘s-Hertogenbosch area (blue) relative to the faults of Peel Boundary fault system (northeastern border of the Roer Valley Graben).

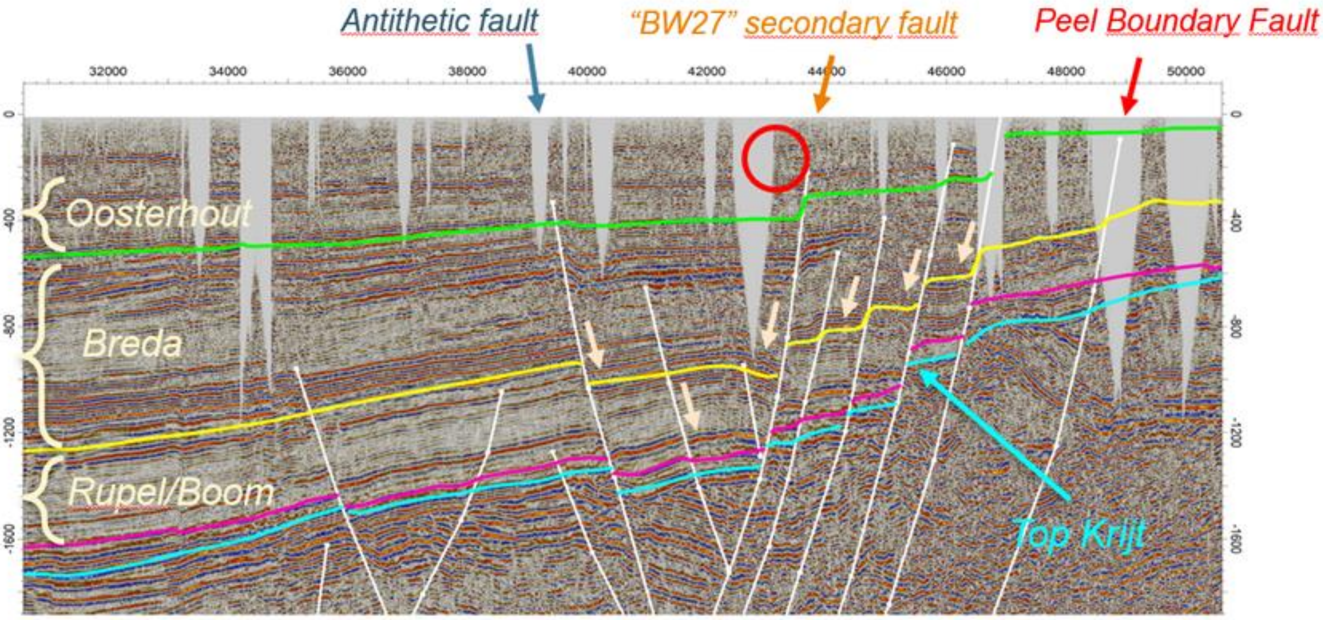

Figure 5.3 Situation of the BW27 well field in a seismic cross-section perpendicular to the Roer Valley Graben tectonic structure. The green line represents the lowe boundary of the marine Oosterhout Formation. The red circle shows the approximate position of the BW27 well field of the Veghel pilot.

Figure 5.3 illustrates the position of the BW27 public supply well field relative to the tectonic structure of the Peel Boundary fault system which borders the Roer Valley Graben at the eastern side. The well field is located close to a secondary fault of the Peel Boundary Fault system (compare Figure 4.2). An antithetic fault to the west of the well field (also visible in Figure 5.2) borders a smaller, graben like structure between the BW27 secondary fault and the antithetic fault to the west. A previous study showed that this "*marginal through*" accommodates a body of paleowater of water that was partly recharged before the Last Glacial Maximum (Broers et al., 2021).

5.3 Results for the province of Noord-Brabant

5.3.1 Baseline monitoring gases in shallow groundwater in Noord-Brabant

This section describes the baseline monitoring of gases in the provincial groundwater quality monitoring network (PMG) of the province of Noord-Brabant. The network consists of over 120 multi-level observation wells throughout the province. Typically, these wells consist of filters at standardized depths of 10, 15 and 25 meters below surface level with screen lengths of 1 or 2 meters. The monitoring network is used for compliance and surveillance monitoring for the EU Water Framework Directive in addition to the provincial groundwater management tasks.

The wells of the provincial monitoring network have been sampled by TNO Geological Survey of the Netherlands for age dating by $^{3}H/^{3}He$ during campaigns in 2001, 2008/2009 (Visser et al, 2007) and recently in 2017/2018 (Kivits et al, 2019). During this last sampling campaign, additional samples were taken for the characterization of gas composition and methane isotopes. The locations of this sampling campaign are shown on the map in Figure 5.4. The results of this sampling campaign give a baseline of gas composition of the shallow groundwater in the province of Noord-Brabant, which can be used to investigate the effects of possible future (energy related) activities in the deep subsurface to the shallow groundwater.

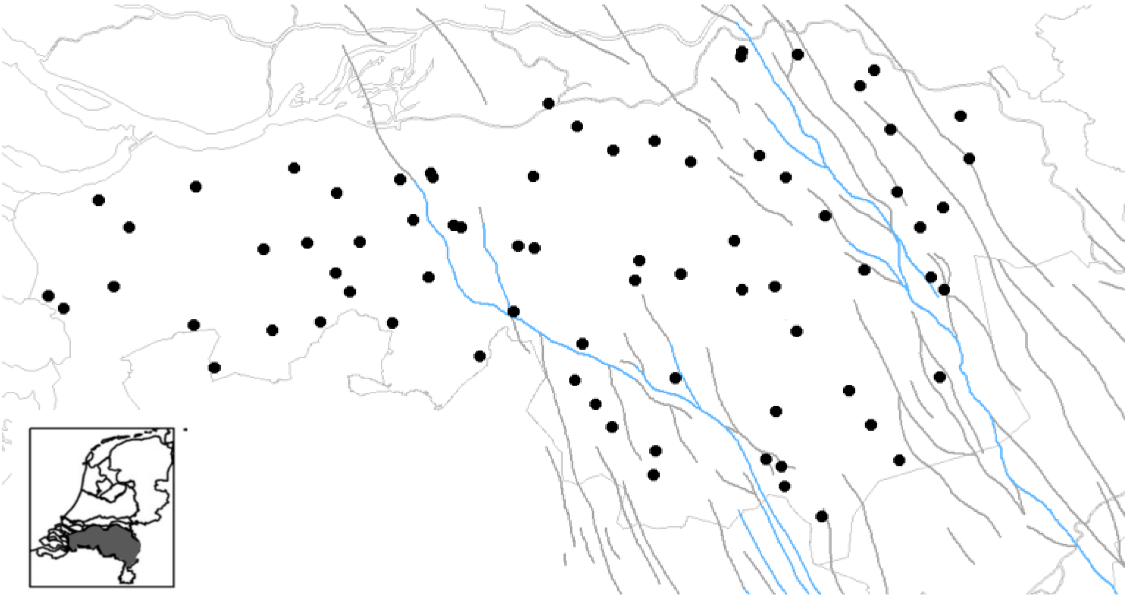

Figure 5.4 Map showing the locations of the wells of the provincial groundwater quality monitoring network of Noord-Brabant which have been sampled for gas composition and methane isotopes.

Figure 5.5 Sampling for dissolved gases in groundwater using Isoflasks

Gas samples were taken by using Isoflasks^{TM} (Isotech). These are vacuum sealed bags in which groundwater can be collected leaving headspace above the water sample (see Figure 5.5). Isolab B.V. in Neerijnen in the Netherlands performed the analyses. This included the determination of the composition of the headspace gas and the carbon and deuterium isotope fraction of methane ($\delta^{13}C$-CH_4 and $\delta^{2}H$-CH_4). The gas composition was reported as an absolute concentration in mole fraction for methane (and alkanes with a longer carbon chain) and N_2, CO_2, Ar and O_2. The isoflasks were allowed to equilibrate with the temperature and pressure inside the lab, and the volume of water inside the isoflask was calculated by weighing the sample and substracting the empty weight of an isoflask. The temperature and pressure gave a value for Henry's Law constant, which was used to calculate the concentration of gas within the aqueous fase of the sample. This was added to the concentration of gas in the headspace to arrive at the original concentration of the dissolved gas in the groundwater sample. $\delta^{13}C$-CH_4 and $\delta^{2}H$-CH_4 were only measured if enough gas was available after the measurements for the gas composition. Out of a total of 157 samples, 142 could be analysed for $\delta^{13}C$-CH_4 and 88 for $\delta^{2}H$-CH_4.

5.3.1.1 *Methane in shallow groundwater*

Figure 5.6 shows the methane concentrations that were measured in the wells of the provincial groundwater quality monitoring network. In this network, generally the 1st and 3rd filters are sampled, corresponding to depths of approximately 10 and 25 meters below surface. In case of overlapping points on the map of Figure 5.6, the shallow filter is displayed north of the deeper filter. Methane is found in all but one filter, where no gas could be extracted from the isoflask. Methane concentrations are generally quite low with a median concentration of 0.03 mg/l (10-percentile to 90-percentile range: 0.0005 and 1.58 mg/l). The average concentratio of 1.54 mg/l is strongly influenced by a number of outliers with concentrations over 10 mg/l. Over 55% of all samples have methane concentrations of <0.1 mg/l, while only 14% is higher than 1 mg/l. These higher concentrations can mostly be found in the central area of the Roer Valley graben and in the northwestern area of the province, which is characterized by low-lying sea clay with brackish water close to the surface.

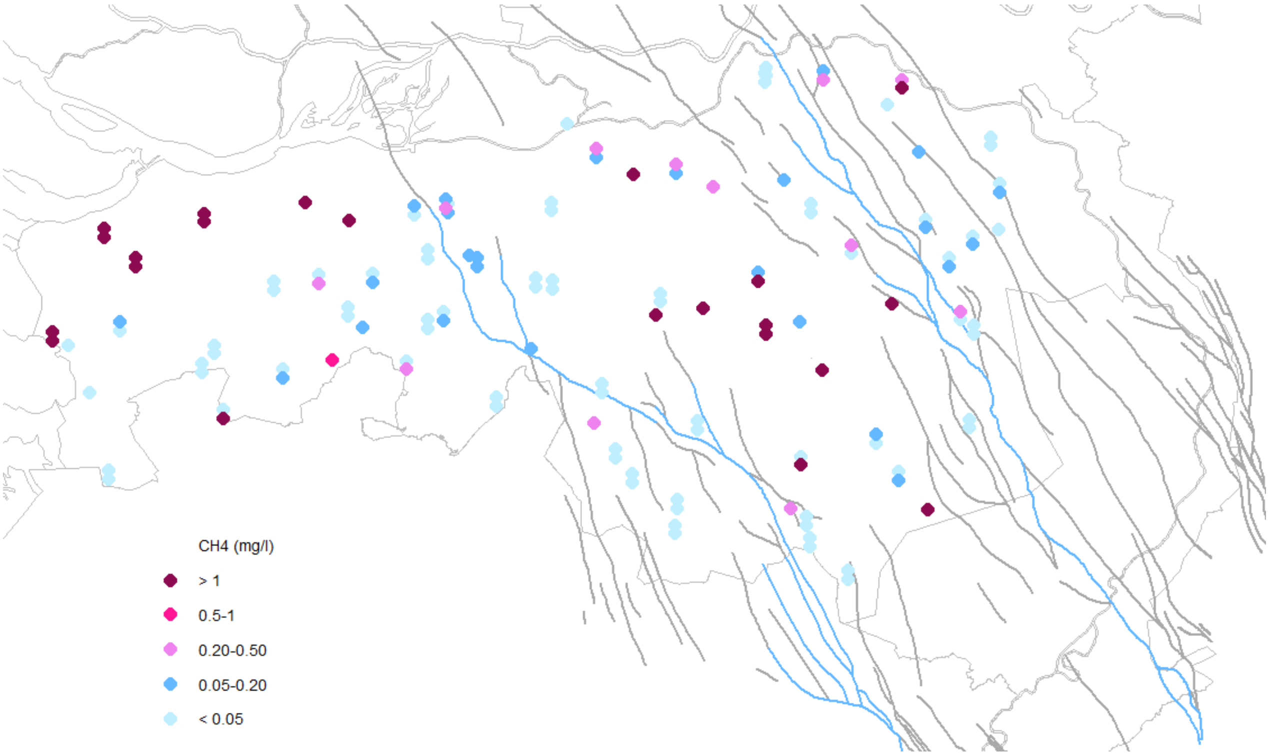

Figure 5.6. Map showing methane concentrations (in mg/l) in the wells of the provincial groundwater quality monitoring network. Shallow filters are displayed just north of the deeper filters.

The methane that is present in the groundwater has been formed by the decomposition of organic substances and it can be separated into two types: biogenic and thermogenic. In shallow formations, methane is generally formed by microorganism-mediated decomposition of organic matter through several redox-related processes (see Pinson et al. 2020 for more information on the redox classification of the sampled wells). This type of methane is also known as biogenic methane. In deeper formations, hydrocarbon gases are formed by the thermal cracking of organic substances due to increased temperatures and pressures, and the methane that is formed there is known as thermogenic methane. The presence of thermogenic methane in shallow groundwater gives an indication for possible pathways from the deep subsurface to the shallow groundwater, since thermogenic methane is only formed in deeper formations.

5.3.1.2 Indications for thermogenic methane

Both the methane concentration and the isotopic composition of methane provide insight in the origin of the methane. Hydrocarbon gases in groundwater can be differentiated based on the chemical composition of the gas and the isotopic signatures of carbon and deuterium. Thermogenic gas is generally composed of methane (C1), with significant amounts of ethane (C2) and propane (C3). The ratio of C1 over C2 and C3 (C1/(C2+C3)), also known as the “wetness”, can be used to determine the origin of the gas. Generally a ratio C1/(C2+C3) of less than 100 gives an indication for thermogenic gas. Biogenic gas usually contains at most trace amounts of ethane and higher alkanes (<0.05%) resulting in a dryness ratio of over 1000 (see Figure 5.7).

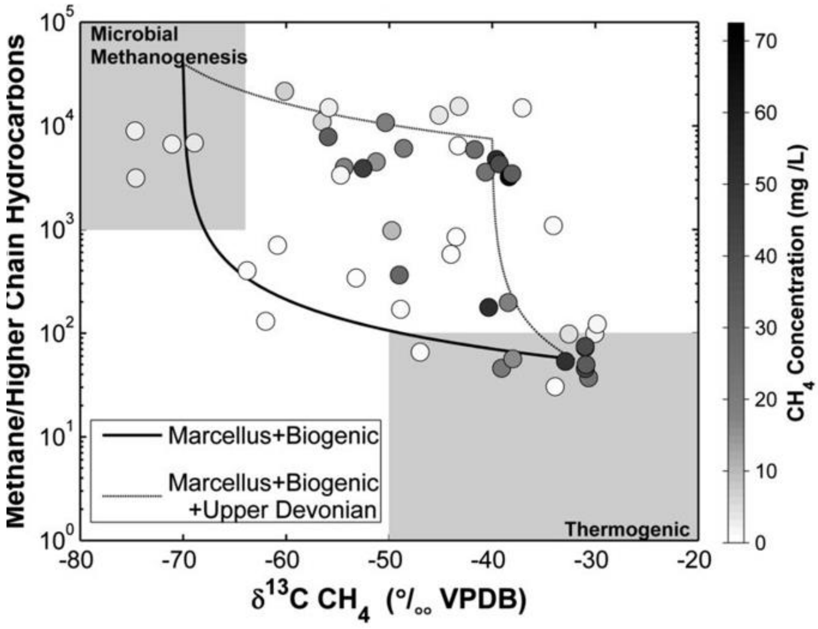

Figure 5.7. Plot of $\delta^{13}C-CH_4$ (in ‰ Vienna Pee Dee Belemnite) against the ratio of methane versus methane and propane (C1/(C2+C3)), also known as a Bernard diagram, indicating the different regions for biogenic and thermogenic gas. Figure taken from Jackson et al. (2013).

Another indication for thermogenic versus biogenic gas is the isotope signature of carbon and deuterium present in methane, represented as the $\delta^{13}C-CH_4$ (in ‰ VPDB, short for Vienna Pee Dee Belemnite, Assonov et al., 2020) and $\delta^{2}H-CH_4$ (in ‰ VSMOW or Vienna Standard Mean Ocean Water). Carbon isotope ratios ranging from -120‰ to approximately -60‰ generally indicate biogenic gas, while $\delta^{13}C-CH_4$ ratios greater than -55‰ indicate methane with a thermogenic origin (Jackson et al., 2013, Humez et al., 2019, Schloemer et al., 2018). The isotope ratio of deuterium ($\delta^{2}H-CH_4$) is also representative for the origin of methane, although in a lesser extent than the $\delta^{13}C-CH_4$. Ratios of $\delta^{2}H-CH_4$ from -400‰ to -150‰ are indicative of methane with a biogenic origin, while ratios of -275‰ to -100‰ indicate thermogenic methane (see Figure 5.8).

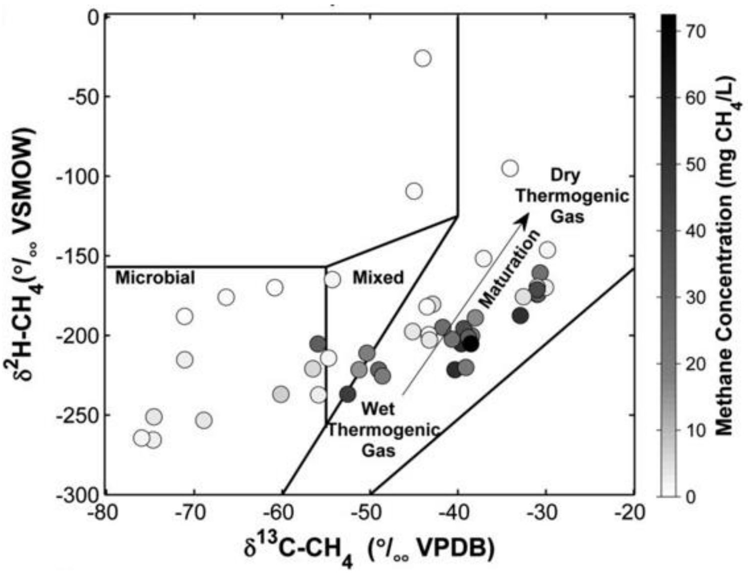

Figure 5.8 Plot of δ^{13}C-CH$_4$ (in ‰ Vienna Pee Dee Belemnite) against δ^2H-CH4 (in ‰ VSMOW), also known as a Schoell diagram, with indicative ranges for biogenic (microbial) and thermal gas. Figure is taken from Jackson et al,. 2013.

The map in Figure 5.9 shows the δ^{13}C-CH4 values for the wells in the provincial monitoring network. In 109 out of the 142 filters where δ^{13}C-CH4 could be measured (77%) the values are low (δ^{13}C-CH4 <-50‰ VSMOW), indicating methane from biogenic origin in most places. In some locations higher values are observed (δ^{13}C-CH4 >-50‰ Vienna Standard Mean Ocean Water), most notably in a number of wells in the northern part of the central Roer Valley Graben.

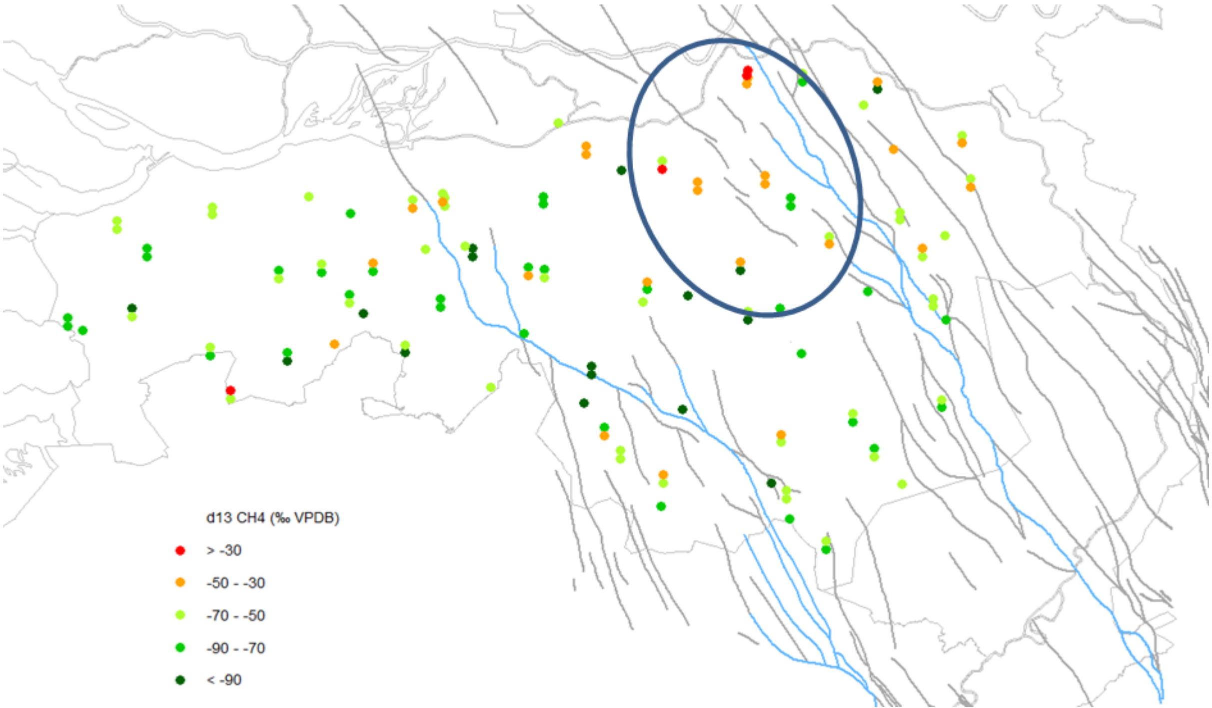

Figure 5.9. Map showing δ^{13}C-CH4 values (in ‰ Vienna Pee Dee Belemnite) of the measured wells in the provincial groundwater quality monitoring network. In general, low values (green) indicate methane with a biogenic origin, and high values (red) indicate methane with a suspected thermogenic origin.

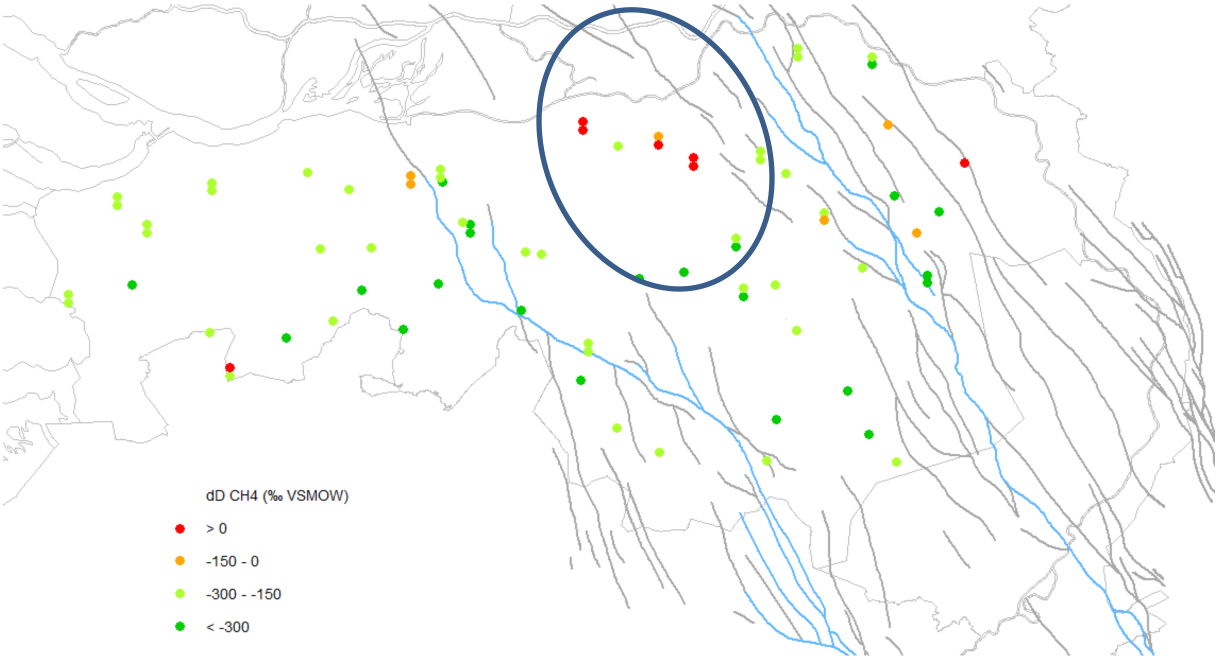

Figure 5.10. Map showing δ^{2}H-CH4 values for methane(in ‰ Vienna Standard Mean Ocean Water) of the measured wells in the provincial groundwater quality monitoring network.

The northern part of the Roer Valley Graben also shows enriched values for δ^{2}H-CH$_4$ (see Figure 5.10). Although enriched values for δ^{2}H-CH$_4$ generally are a less clear indication for thermogenic methane than enriched values of δ^{13}C-CH$_4$, it is still indicative that it occurs in the same region. But again, most δ^2H-CH$_4$ values indicate methane with a biogenic origin. Since the methane samples were collected during an age-dating campaign using ^{3}H/^{3}He, there is also information on the ^{4}He concentrations in the wells of the provincial monitoring network (see Figure 5.11). Radiogenic ^{4}He is produced in the earth's crust, and is typically found in higher concentrations in deeper subsurface layers. Elevated concentration in shallow groundwater could indicate a possible flow path for deeper groundwater into shallow layers (Banks et al. 2019, Gardner et al. 2011, Gumm et al. 2016). The blue zones in Figure 5.11 indicate discharge areas where it is known that upward seepage occurs toward the shallow groundwater layers. This explains the elevated radiogenic ^{4}He concentrations that are found in some of these areas. Elevated concentrations are also found in clay areas (green zone), most notably in the north-western part of the province. In these clay areas, groundwater flow is complicated due to the many aquitards that are present in the subsurface, and upward groundwater flow apparently also causes increased radiogenic ^{4}He concentrations in these areas. The same region which shows enriched δ^{13}C-CH4 and δ^2H-CH4 values also has increased radiogenic ^{4}He concentrations (indicated by the blue circle), strengthening the case for a possible upward groundwater flow in this region. The northern part of the Roer Valley Graben is known as a regional discharge area where older groundwater seeps up into shallower layers, so there is a possibility for the presence of thermogenic methane in this region. The presence of possible thermogenic methane and elevated radiogenic ^{4}He concentrations let to a further investigation into this region near the city of 's-Hertogenbosch, which is presented in section 5.3.3.

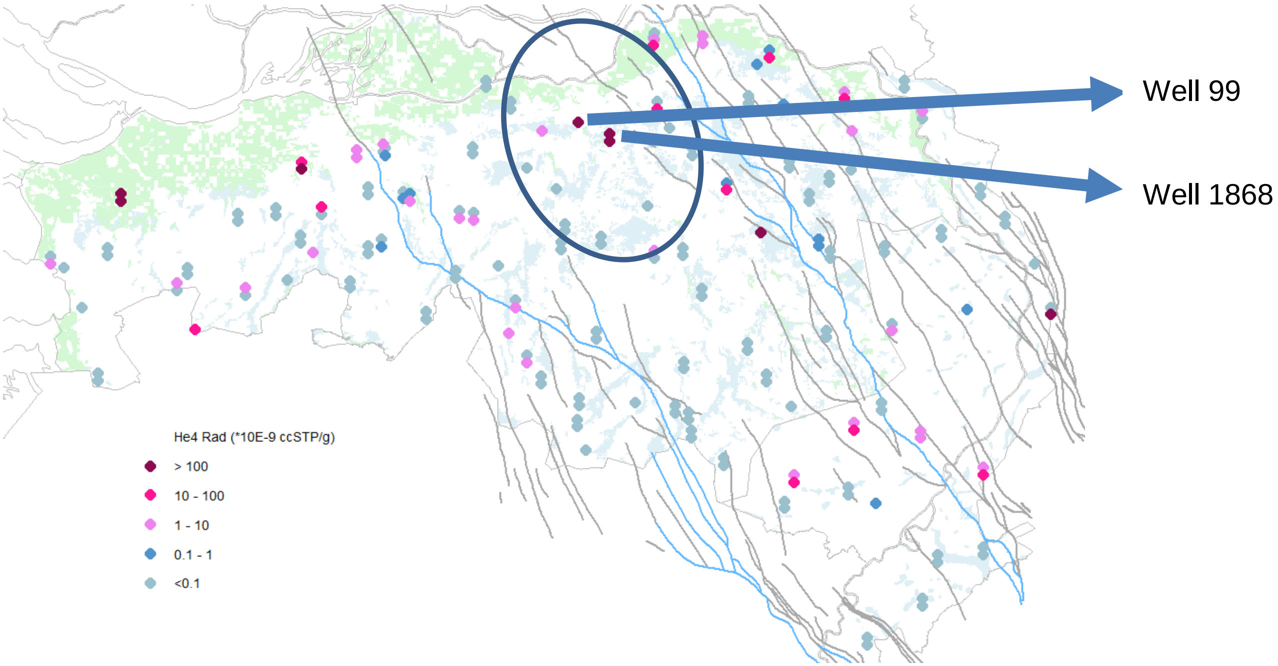

Figure 5.11 Map of radiogenic ^{4}He concentrations (10^{-9} ccSTP/g) in the wells of the provincial monitoring network. The blue zones in the map indicate regional discharge areas and the green zones indicate clay area.*

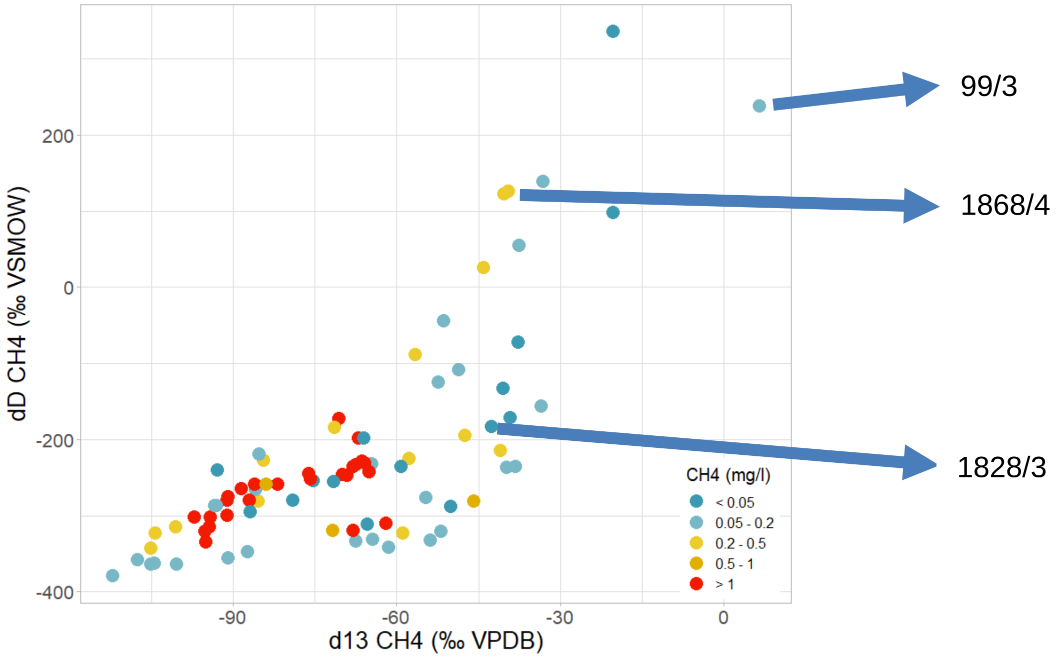

Figure 5.12 Schoell diagram ($\delta^{13}C$-CH_4 versus $\delta^{2}H$-CH_4) after the example of Figure 5.8 of the samples of the provincial monitoring network. The methane concentrations of the samples are indicated by the colours.

Figure 5.12 shows the $\delta^{13}C$-CH_4 against the $\delta^{2}H$-CH_4 values for the sampled filters. Taking the reference from Figure 5.8, most values fall within the microbial or biogenic methane range ($\delta^{13}C$-CH_4 < -50‰ VPDB and $\delta^{2}H$-CH_4 < -150‰ VSMOW). There are a number of points which have $\delta^{13}C$-CH_4 values of over -50‰ and also have enriched $\delta^{2}H$-CH_4 ratios, which could indicate thermogenic methane. However, the figure also shows the methane concentrations for these wells, and it is quite clear that all filters with higher methane concentrations (> 1 mg/l) are of biogenic origin.

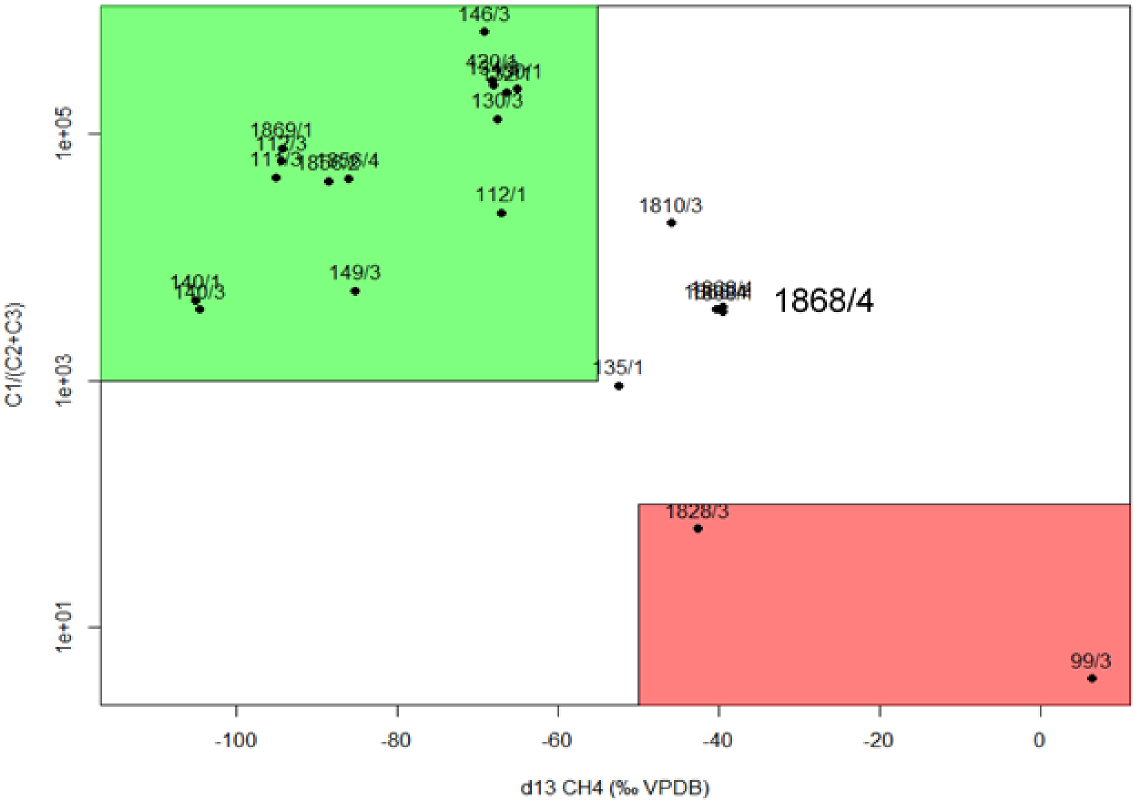

Figure 5.13 Bernard diagram (δ^{13}C-CH$_4$ versus the C1/(C2+C3) ratio) after the example of Figure 5.7 for the samples of the provincial monitoring network, with labelled filter names. The green zone indicates biogenic methane, and the red zone indicates methane with a thermogenic origin.

The plot in Figure 5.13 of δ^{13}C-CH$_4$ versus the ratio of methane (C1) over the sum of ethane (C2) and propane (C3) clearly shows that the majority of measurements fall within the biogenic zone (green zone). Only a limited number of filters show significant concentrations of ethane and propane, most notable filters 1828/3 and 99/3 (red zone). Co-occurrence of ethane and propane as a byproduct of methanogenesis have been reported as a common process in seawater and lake sediments, so the presence of trace amounts of ethane and propane does not conclusively indate the gas to be of thermogenic origin (Schloemer et al, 2018). For the vast majority of the samples (136 out of 157) no ethane or propane was detected at all, which would indicate that these samples are most likely all of biogenic origin. Most samples that did show the presence of ethane and propane (21 filters) have very low concentrations of ethane and propane, which would still indicate biogenic methane. This poses the question if the enriched δ^{13}C-CH$_4$ found for the samples in Figure 5.12 are really indicative of thermogenic methane, or if another process is causing an enrichment of isotope values.

There are certain conditions thinkable where groundwater with methane of biogenic origin would mix with groundwater with significant sulfate concentrations. Anaerobic oxidation of methane, coupled with bacterial sulfate reduction, is known to enrich the δ^{13}C-CH$_4$ ratio (Barker and Fritz, 1981), which could lead to falsely labelling biogenic methane samples as thermogenic. This could occur in regional discharge areas where deeper groundwater containing biogenic methane flows upward into groundwater with significant concentrations of sulfate. The other way around is also possible, where sulfate containing waters, possibly stemming from agriculture or urban areas, are introduced into layers with older methanogenic groundwater, a process which could be strenghtened by decreasing groundwater heads in deeper layers due to pumping (see also section 5.3.3).

This hypothesis is more or less confirmed by looking at the plot of methane versus sulfate concentrations (Figure 5.14). The plot shows a clear relation between methane and sulfate, with high methane concentrations only occurring in sulfate-reduced waters with sulfate concentrations below 5 mg/l and vice-versa. It also becomes clear that enriched $\delta^{13}C-CH_4$ values (orange and red symbols) are only found in groundwaters with significant sulfate concentrations. This points to the process of anaerobic methane oxidation, leading to an enrichment in $\delta^{13}C-CH_4$ of biogenically formed methane. This, coupled with the fact that for most samples only trace amount of ethane and propane have been found, would indicate that we find no indications for the presence of thermogenic methane in shallow groundwater.

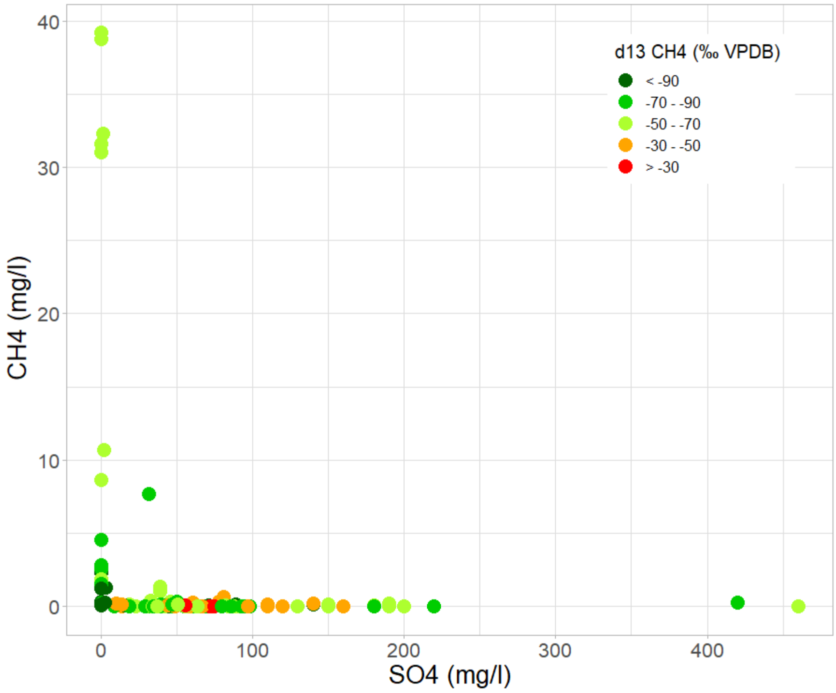

Figure 5.14 Plot showing the sulfate concentrations versus the methane concentrations (both in mg/l) for the wells of the provincial monitoring network. The $\delta^{13}C-CH4$ ratios of the samples are indicated by the colour of the points.

Humez et al. (2016) propose a classification into 4 classes to distinguish if methane in groundwater is generated in situ, or whether the geochemical situation indicates that the methane has migrated into the aquifer and that isotope fractions possibly have been altered by methane oxidation. The first category indicate the *in situ generation of biogenic methane* indicated by samples with $\delta^{13}C-CH_4$ <-55‰ and a dryness parameter (C1/(C2+C3)) >1000, and suitable methanogenic conditions (no nitrate and negligible sulfate concentrations). This category accounts for 67 out of 157 samples in our case (43%).

The second category also consist of samples with $\delta^{13}C-CH_4$ < -55‰ and a dryness parameter >1000, but also with higher sulfate concentrations. Humez et al. (2016) reports significant sulfate concentrations as higher than 1 mM, or 96 mg/l. These conditions are inconsistent with in situ methanogenesis, thus suggesting that *biogenic methane has migrated* into sections of the aquifer with more oxidizing conditions. Apparently the methane has not yet been oxidized in a process coupled to sulfate reduction; so $\delta^{13}C-CH_4$ values are not enriched. There are 17 filters which comply with these characteristics (or about 11%).

The third category contains the apparent or *pseudo-thermogenic methane groundwater*. These samples consist of $\delta^{13}C-CH_4$ >-55‰, but still with the absent of higher alkanes (wetness parameter of > 1000). Such high $\delta^{13}C-CH_4$ values usually indicate thermogenic methane, but can also be caused by methane oxidation. This group consists of 39 filters in our case (25% of all samples). The average methane concentration of this group is low at 0.09 mg/l while the sulfate concentration is significant at an average of 84 mg/l. The low methane concentrations and absence of higher alkanes do not suggest an upward flow of groundwater containing thermogenic methane, so the enriched $\delta^{13}C-CH_4$ must come from *anaerobic methane oxidation coupled with sulfate reduction*. Thus, for his group, we exclude the possibility of a thermogenic origin.

The last category consists of samples with both enriched $\delta^{13}C-CH_4$ values (>-55‰) and also a significant wetness parameter (<500). There are only 2 samples out of the 157 filters which comply with these parameters, namely filter 1828/3 and 99/3. Although both the enriched $\delta^{13}C-CH_4$ and wetness parameter point to thermogenic methane, it is questionable if this is the case for these 2 filters. The methane concentrations are low (0.04 and 0.11 mg/l for 1828/3 and 99/3 respectively) and sulfate concentrations are high (110 and 56 mg/l respectively), thus suggesting that the enriched $\delta^{13}C-CH_4$ values could be due to anaerobic methane oxidation. This seems especially likely for filter 99/3 since it has a very enriched $\delta^{13}C-CH4$ value of +6.5‰ (the only sample we found with positive $\delta^{13}C-CH_4$). The tritium concentrations in both of these filters are also relatively high: 5.85 TU for 1828/3 and 3.71 TU for 99/3, which are typically indicative of a mixture with recent water (Visser et al., 2007; Kivits et al., 2019). Both of these wells are also located in urban areas, thus making pollution from above also a possibility for the higher ethane and propane concentrations. For example, for filter 99/3 there is a known vinylchloride pollution plume at approximately 1 km south of the well, which has spread to a known depth of 36 m below surface. This is close to the filterdepth of 99/3 (30.6 m below surface) and the plume is known to spread north (GS Noord-Brabant, 2012), so ethane and propane pollution is definitely a possibility here. Due to the very low methane concentrations of these filters, coupled with the high sulfate and tritium concentrations, we believe a biogenic origin of the methane to be most likely, but a possible mix with thermogenic methane cannot be excluded.

5.3.1.3 Conclusions from methane in the provincial groundwater quality monitoring network

The gathering of methane samples during a groundwater age-dating campaign made it possible to perform a baseline monitoring for dissolved gases in the shallow groundwater in the province of Noord-Brabant. The gas composition and carbon and deuterium isotopes were measured to distinguish between biogenic and thermogenic methane, to see if there are any possible pathways between deeper layers and the shallow groundwater. We conclude that the majority of detected methane is of biogenic origin, formed from methogenisis through the microorganism-mediated decomposition of organic matter. Enriched $\delta^{13}C-CH_4$ were found for a number of filters, but most of these enriched values are coupled with an absence of higher alkanes and a presence of high sulfate concentrations, pointing to anaerobic methane oxidation which is known to enrich $\delta^{13}C-CH_4$ values leading to a “pseudo-thermogenic” methane signal. In these cases there is most likely a mixing of biogenic methane from deeper layers with sulfate-rich groundwater from shallower layers, coming from agricultural or urban areas. Only in two filters is the methane signal inconclusive: enriched $\delta^{13}C\text{-}CH_4$ values and the presence of ethane and propane point to the presence of thermogenic methane, but low methane concentrations and high sulfate concentrations make a biogenic origin more likely. Nonetheless we conclude that for the vast majority of samples no thermogenic methane was found, thus making natural pathways of deeper groundwater wich would transport thermogenic methane into the shallow subsurface unlikely.

5.3.2 Connections between deep and shallow: fault hydrology at the well field BW27

5.3.2.1 Hydrogeological setting of the well field

The well field BW27 is located close to a secondary fault of the Peel Boundary Fault (see also section 4.4.1). The well field consists of a number of 25 individual pumping wells which are screened between 100 and 160 m depth. The pumping screen lengths vary between 29 and 57 m.

Figure 5.15 shows the position of the well field relative to the secondary fault of the Peel Boundary Fault zone and a cross-section illustrating the hydrogeological buildup. The pumping wells draw water from the Waalre Formation, mainly from the layers PZWAz3 en PZWAz4. Figure 5.3 shows the position of the well field relative to the Peel Boundary Fault zone at a smaller spatial scale in a seismic section.

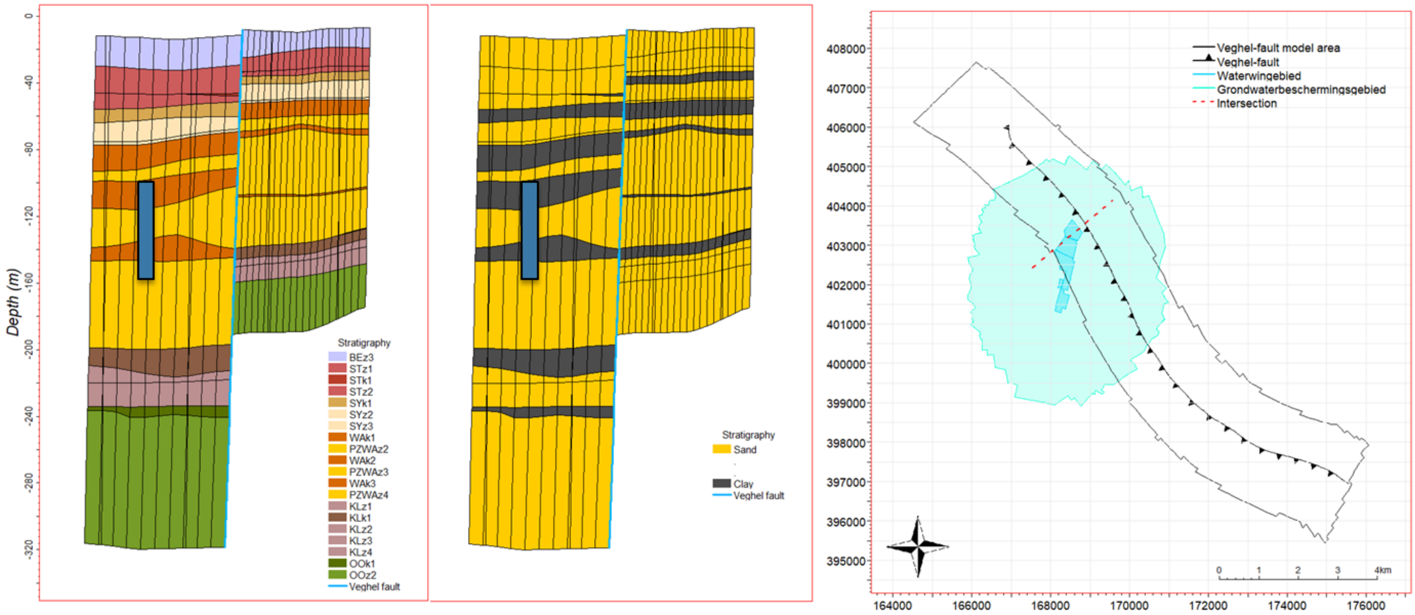

Figure 5.15 Cross-section perpendiular to the secondary fault near BW27. Blue block represents the average depth of pumping. Left: REGIS hydrogeological units. Center: distinction between clay and sand layers. Right: poisition of the well field relative to the fault.

The Peel Boundary Fault zone, and the main Peel Boundary Fault (see Figure 5.3) is considered to represent an obstruction for lateral flow due to the seemingly sealed properties of the fault. A number of papers (Bense et al. 2003, Bense et al. 2013, Bense and Person, 2006, Lapperre et al. 2019, Houtgast et al. 2000) confirm this hypothesis. However, it is unclear whether the fault zone may act as a more permeable tectonic structure in the vertical direction (Bense et al. 2003, 2013).

In the current study, we tried to obtain more information about the vertical connections through gas and tracer characterization.

5.3.2.2 Existing information

The well field BW27 pumps fresh water. A few of the pumping wells have somewhat elevated chloride concentrations, especially the eastern and northerly wells (Figure 5.16). A previous modelling study (Van Baar et al. 2013) hypothesizes that these wells receive a larger proportion of deeper water from more brackish layers, due to the sealed nature of the fault, which prevent the easterly lateral supply of fresh water from shallower layers. They also postulate the option that vertical flow through the vertically permeable fault zone could be responsible for the elevated chloride concentrations. However, they agree that the precise reason for the observed salinization of the wells remains unknown.

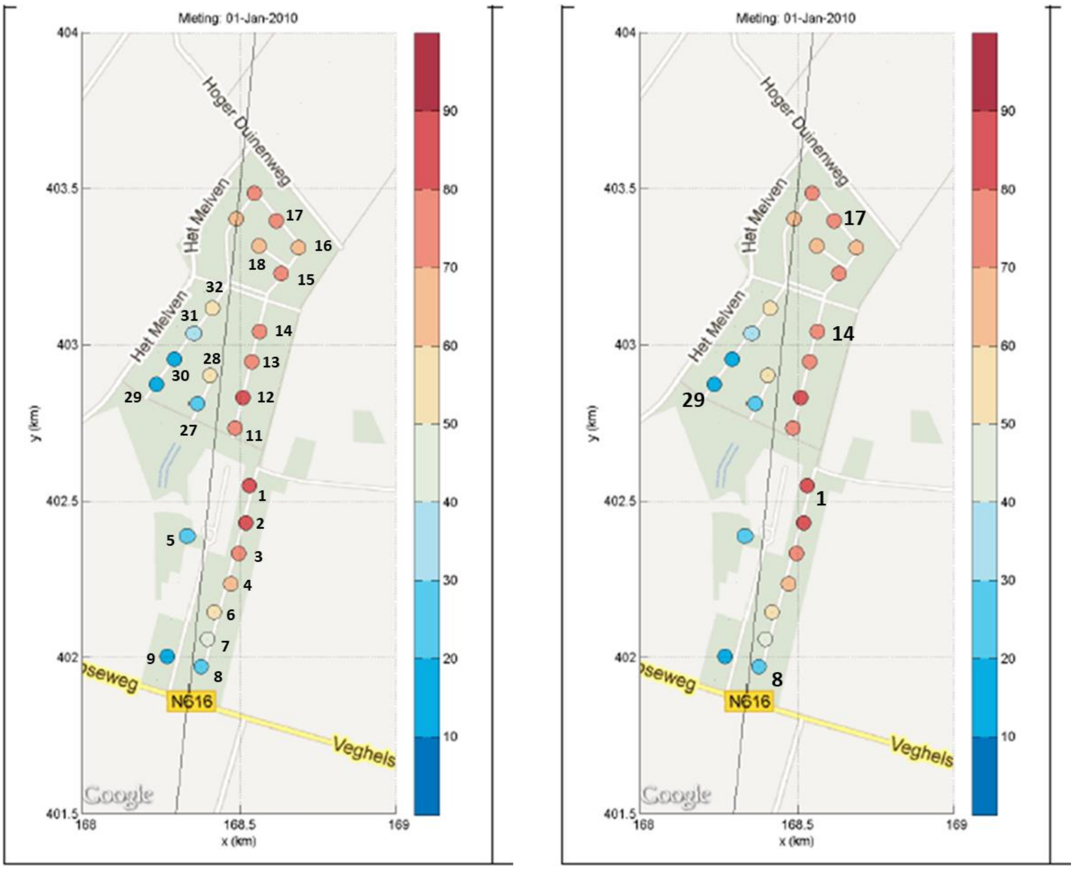

Figure 5.16 Well numbers and chloride concentrations (colour scale) in the 25 active pumping wells in 2010 (source: Van Baar et al. 2013) Left: numbers of all active wells. Right: numbers of the wells sampled again for this study in 2019.

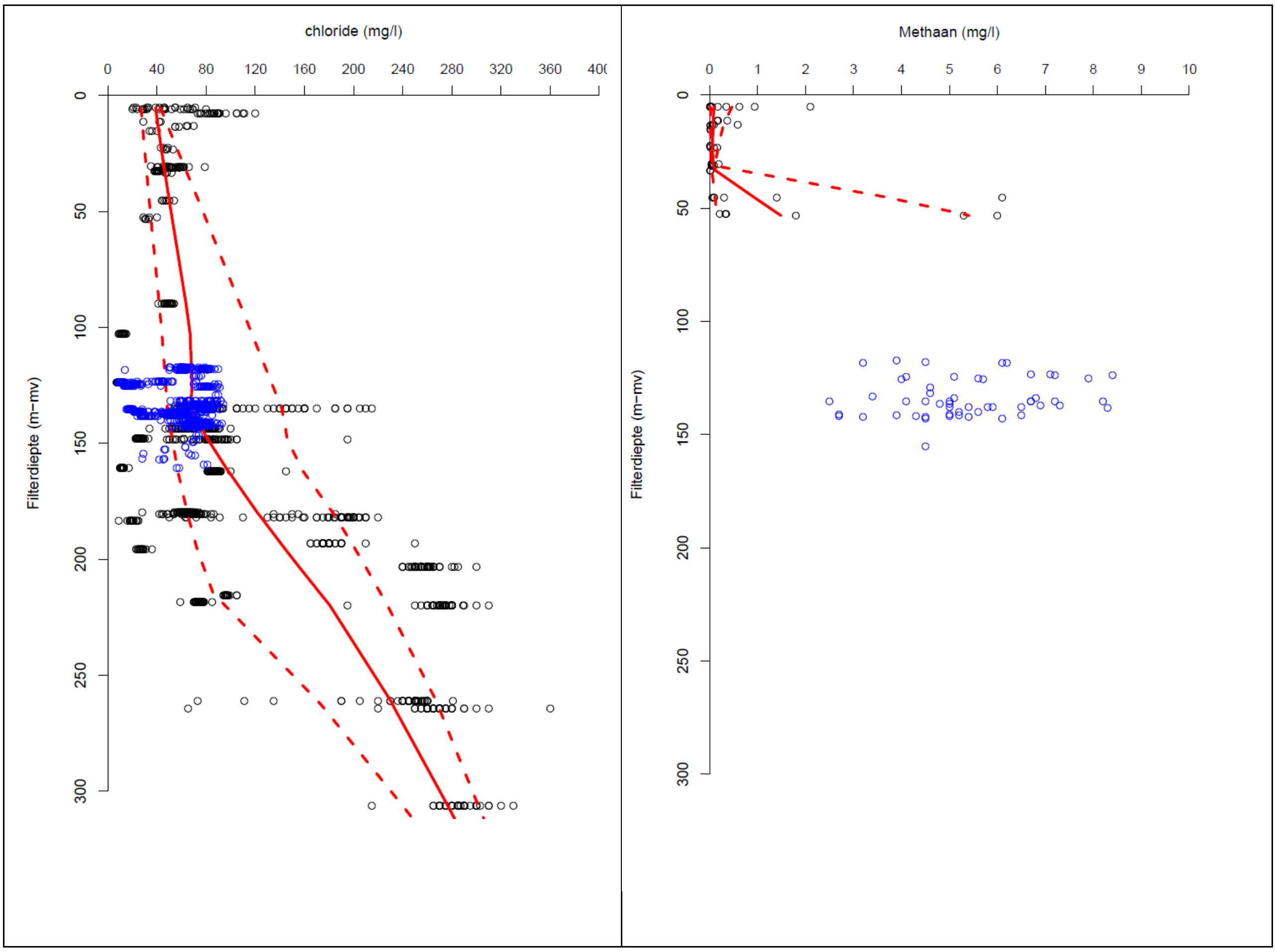

Figure 5.17 Concentration-depth profiles for methane and chloride for the surroundings of well field BW27 near Veghel. Black open dots represent measurements in short-screened multi-level observation wells around the well field. Blue open dots represent measurements of the pumped water in the 25 pumping wells.

The concentration-depth profiles of Figure 5.17 confirm the elevated chloride concentrations in the deeper subsurface of BW27 and show that the pumping wells draw substantial concentrations of methane. In a previous study, Broers & de Weert (2015) investigated the methane isotopic composition and found a $\delta^{13}C\text{-}CH_4$ value of -85.1‰ which points to a biogenic source of the methane (see also section 5.3.1).

5.3.2.3 Data acquisition for GeoERA VOGERA

In 2019, we sampled the mixed water from the pumping wells PP1 to PP9 (“VO1-raw”) and the water from the individual pumpings wells PP1, PP8, PP14, PP17 and PP29. The samples were analysed for major chemistry, methane and methane isotopes and ^{18}O. Furthermore, we collected samples for age dating, including ^{3}H, $^{14}C_{DIC}$, $^{13}C_{DIC}$. Additionally, we sampled for ^{39}Ar of the mixed water and the pumping wells PP1 and PP8 (Broers et al., 2021b).

The acquired data is listed in Table 5.1 and Table 5.2. The new sample for the mixed raw water (“VO1-raw”) is very similar to the previous sample taken from the mixed water of all pumping wells (“BW27-raw”; Broers & de Weert, 2015) for most of the tracers and gas compositions.

Table 5.1 Measurements of age tracers and estimated ^{14}C apparent age for well field BW27 (for a detailed assessment of the age distributions, see Deliverable D6.4 of GeoERA HOVER)

BWNR	NGT °C	^{3}H (TU)	$^{4}He_{rad}$ cc STP g-1	pH	$^{14}C_{DIC}$ pmC	$\delta^{13}C$ ‰	^{39}Ar pmAr	CH_4 mg/l	Cl mg/l	SO_4 mg/l	HCO_3 mg/l	Mean age of the mix from DTTDM model (years)
BW27-raw		0.02 ± 0.01	1.67E-06	7.16	15.0	-8.5	-	6.1	51.3	< 5	350	
VO1-raw	4.1± 0.3	0.09 ± 0.05	1.61E-06	7.15	13.9	-9.1	9 ± 5	5.4	49	< 5	350	13,000
VO2-PP1	1.7± 0.3	0.10 ± 0.05	1.75E-06	7.19	10.1	-10.6	-	4	75	< 5	370	17,000
VO3-PP8	7.2± 0.3	0.12 ± 0.05	7.15E-07	7.23	21.3	-5.3	-	7.7	29	< 5	340	7,000
VO4-PP14	4.8 ± 0.3	0.02 ± 0.05	1.70E-06	7.29	-	-	-	4.6	68	< 5	360	-
VO5-PP17	5.9± 0.3	0.01 ± 0.05	2.15E-06	7.3	15.6	-9.7	-	5.3	59	< 5	350	11,000
VO6-PP29	5.3± 0.3	0.01± 0.05	6.51E-07	7.28	13.8	-8.1	-	4.1	11	< 5	370	11,000

Table 5.2 Measurements of indicators for connections between the deeper and shallow subsurface

BWNR	CH_4 mg/l	$\delta^{13}C_{CH4}$ ‰	$\delta^{2}H_{CH4}$ ‰	^{18}O ‰$_{VSMOW}$	^{2}H ‰$_{VSMOW}$	Ne/He ratio	$^{3}He/^{4}He$ ratio	$^{3}He/^{4}He$ Relative to R_a
BW27-raw	6.1	-83.5	-	-7.5	-50.8	0.50	4.28E-07	$0.21R_a$
VO1-raw	5.4	-87.0	-275	-7.7	-52.0	0.19	3.38E-07	$0.21R_a$
VO2-PP1	4	-88.6	-280	-8.2	-55.4	0.13	3.38E-07	$0.22R_a$
VO3-PP8	7.7	-84.7	-268	-7.1	-47.7	0.27	3.52E-07	$0.21R_a$
VO4-PP14	4.6	-86.3	-275	-8.0	-53.6	0.14	3.30E-07	$0.21R_a$
VO5-PP17	5.3	-84.1	-269	-7.4	-50.2	0.12	2.45E-07	$0.15R_a$
VO6-PP29	4.1	-89.2	-280	-7.7	-52.3	0.55	4.65E-07	$0.24R_a$

5.3.2.4 Age distributions of the individual pumping well and the resulting mix

The age distributions of the Veghel well field BW27 have been explored in GeoERA HOVER (Broers et al., 2021b). Figure 5.18 shows the main outcomes; the age distributions which classify the proportions of pumped water from the age classes <100 years, 100-300 years, 300-1,000 years, 1,000-10,000 years, 10,000-25,000 years and > 25,000 years.

From the Figure, it becomes clear that the fraction from the Pleistocene 10,000—25,000 years age class is dominant (67% ± 6%). In the age grouping that was applied in the Broers et al. (2021a) paper this would classify the well field as age group “MO”. The ^{39}Ar measurement which is available for the mixed water from the pumping wells PP1 to PP9 (“VO1-raw”) seems to imply that a fraction of either 100-300 or 300-1,000 years old water is present in the mixture. The uncertainty of these fractions is rather high, 10 ± 10% and 8 ± 5% respectively, thus varying between 0 and maximum 20%.

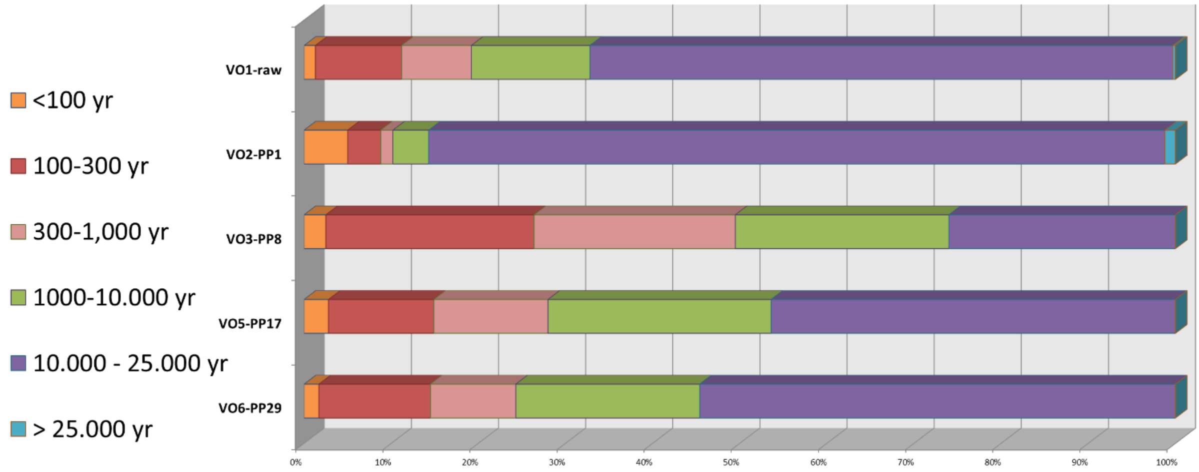

Figure 5.18 Visualisation of the age distributions for the samples VO1 (mixed water from the pumping wells PP1 to PP9: "VO1-raw"), VO2 (pumping well PP1), VO3 (pumping well PP8), VO5 (pumping well PP17) and V06 (pumping well PP29).

Figure 5.18 also implies that pumping well 1 ("VO2-PP1") shows the overall oldest water with a prominent peak in the 10,000-25,000 years age range (85% ± 6%), with possible small fractions of the 1,000-10,000 and/or > 25,000 years age ranges. These fractions could, however, also be 0% each. Thus, pumping well 1 pumps the oldest water from a limited age window.

Contrary, pumping well 8 ("VO3-PP8") covers a much broader age range, but with high uncertainty for the fractions 100-300 years, 300-1,000 years and 1,000-10,000 years. The age distribution will definitely be better constrained when the ^{39}Ar results come available. But clearly, pumping well 8 pumps the relatively youngest water from the 5 investigated pumping wells at the Veghel well field BW27. The other pumping wells 17 ("VO5-PP17") and 29 ("VO6-PP29") show intermediate age distributions with a clear peak in the 10,000-25,000 years age range.

Overall, these age distributions are within the range of expectations from the Broers et al. (2021a) study. Interesting is the measurable ^{39}Ar concentration in the mixed water from the pumping wells 1-9 ("VO1-raw"). It might imply that water from shallower aquifers is approaching the pumped wells, presumably concentrated in the corners of the well field at pumping well 8 and pumping well 29. The ^{39}Ar data for pumping well 8 will be revealing once it becomes available.

5.3.2.5 Links between age indicators and chloride

There is a clear link between chloride and the ages of the water; pumping well 1 pumps the oldest water and has the highest chloride concentrations. The relationships between the tracers and chloride is further investigated in Figure 5.19. The figure indicates a clear positive relation between $^{14}C_{DIC}$ and ^{18}O indicating that older water with lower ^{14}C activities is also depleted in ^{18}O, which is related to depleted ^{18}O indicating colder past recharge temperatures in the Pleistocene era. Pumping well 1 ("VO2-PP1"), which pumps the largest proportion of old Pleistocene water, is low in ^{14}C and low in ^{18}O and exhibits the highest chloride concentrations. Pumping well 8 ("VO2-PP8") is situated in the other extreme of the spectrum: relatively high ^{18}O, $^{14}C_{DIC}$ activity and low chloride concentrations. Somehow, pumping well 29 ("VO6-PP29") does not fit really well for chloride; the well pumps the lowest chloride but has intermediate ^{14}C and ^{18}O. However, pumping well 8 ("VO2-

PP8") and 29 ("VO6-PP29") are both low in $^4He_{rad}$ which support the hypothesis that pumping well 29 has a significant proportion of older water.

From the tracers considered, $^4He_{rad}$ seems to capture the chloride pattern best, with pumping wells 1, 14 and 17 showing the highest $^4He_{rad}$ and the highest chloride and pumping wells 8 and 29 the lowest $^4He_{rad}$ and the lowest chloride. The mixed water lies at the center of the scatter, which would be expected if all wells would contribute the same proportion of the total abstraction. The overall results seems to imply that the high chloride water is drawn from deeper layers which also show elevated $^4He_{rad}$.

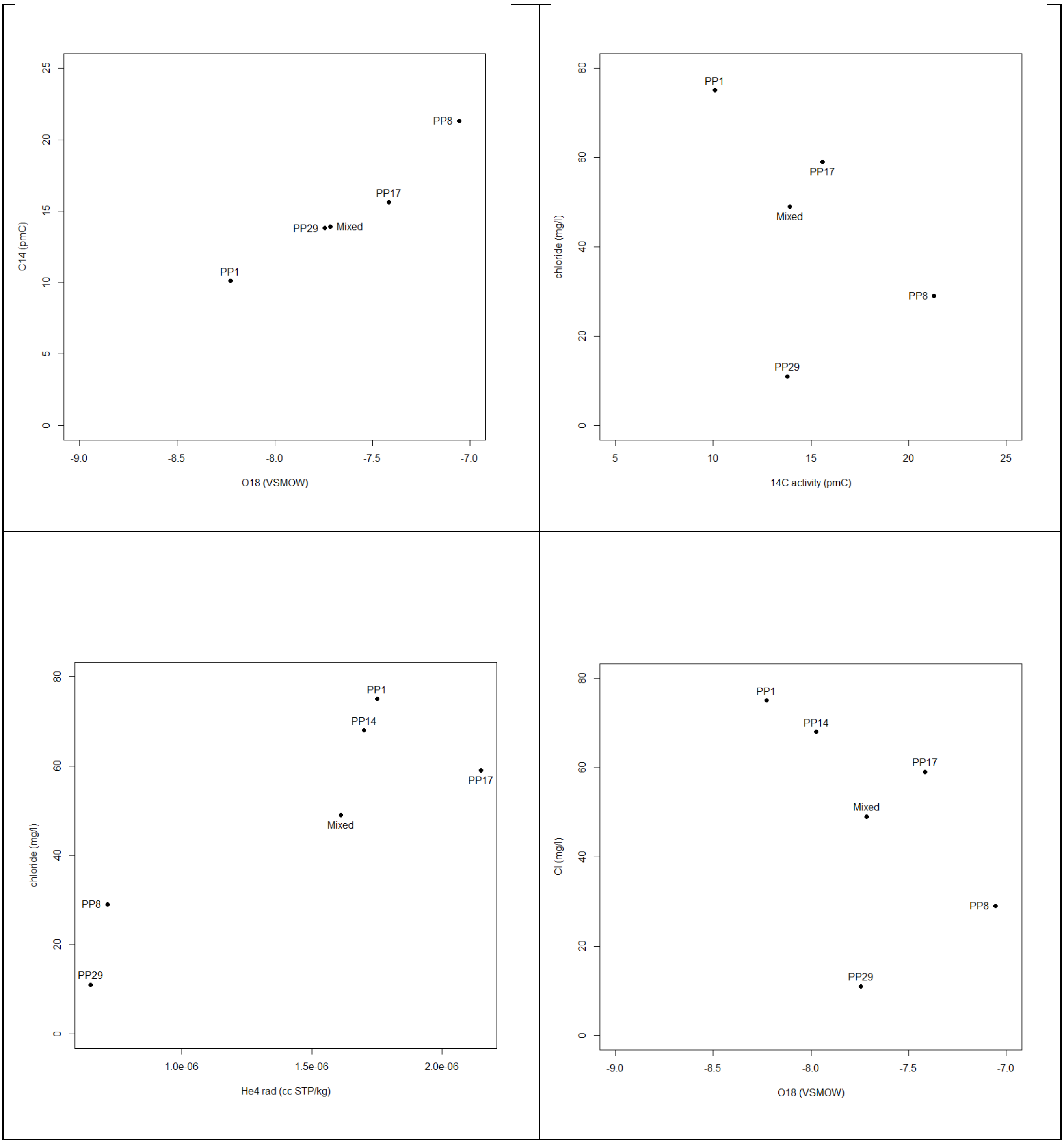

Figure 5.19 Relations between chloride and the tracers $^{14}C_{DIC}$, $^{4}He_{rad}$ and ^{18}O.

5.3.2.6 Indications for deep-shallow connections

For the Veghel well field BW27, we explored whether the water of the well field has characteristics that point to upwelling of fluid or gas from the deep subsurface, which would indicate that the fault zone would form a connection between the deeper subsurface and the shallower aquifers. It builds on studies as by Freundt (2017) and Gumm et al. (2016) who aimed to identify a suite of hydrological and isotope system tracers which are able to point to highly permeable reservoirs in great depths, using measurements in the better accessible shallow aquifers located well above the geothermal target aquifers. Freundt hypothesized that the upwelling of fluids from the target aquifer along fault zones would imprint the shallow aquifers with characteristic signals. They especially tested ^{3}He/^{4}He, and other hydrological tracers like tritium, ^{14}C and radon to find out if they would offer valuable information to identify those imprints (Freundt, 2017). Their ultimate aims were to lower the exploration risks and costs associated with the placement and construction of new geothermal power plants, by developing a tracer analysis of shallow groundwater at relatively low costs, which could narrow the search for beneficial locations. Our current study aims to try a similar set of tracers to see whether they would help to estimate the risks of deep fluids and gases to deteriorate water quality in the shallow aquifers that are used for drinking water supply.

Figure 5.20 shows a result from the Freundt (2017) study. He found evidence for a ^{3}He hotspot of mantle origin near a fault zone in the Upper Rhine Graben. As such, the author proved the opportunities of the tracer technique to identify potential geothermal resources. However, the study also reveals that the region affected by the elevated ^{3}He concentrations could be rather limited spatially, so that the effects can be very local. In that sense, it is interesting to explore the Veghel well field which is close to a secondary fault of the Roer Valley Graben and has a line of pumping wells perpendicular to the fault strike direction.

.

Hydrogeological Setting

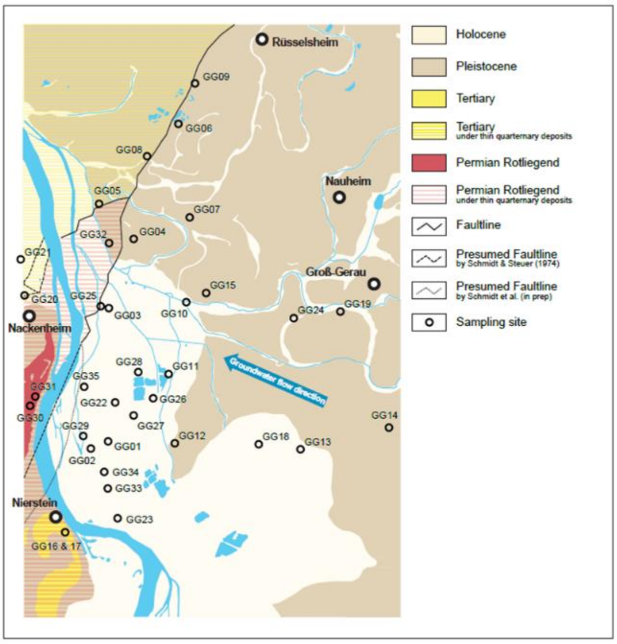

^{3}He concentrations

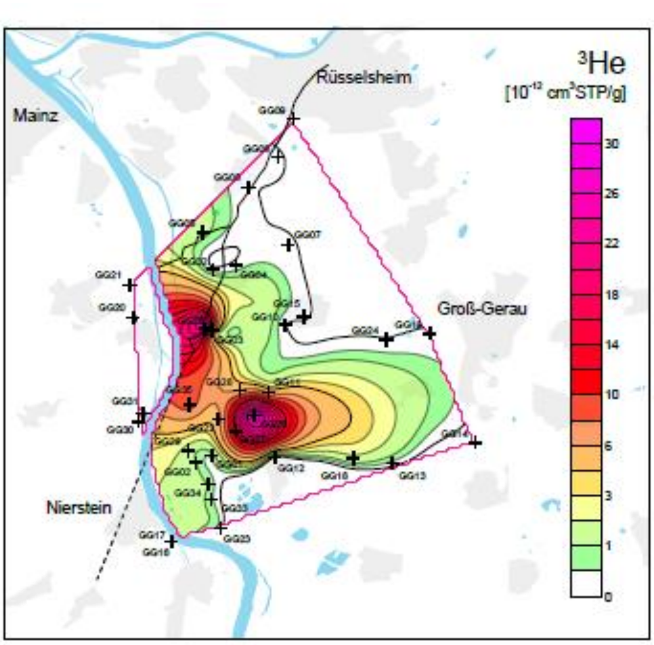

Figure 5.20 Example of elevated ^{3}He concentrations (right) that are related to a mantle contribution around a fault zone in the Groß Gerau region after Freundt (2017). The main fault in the region separates the the Upper Rhine Graben on the east from the Mainzer Becken and the risen Niersteiner Horst, which is an upthrow block of the fault, outcropping the Permian Rotliegend. The ^{3}He concentrations in 10^{-12} cc STP/g indicate 2 hotspots.

We used two sets of tracers to check whether there are indications of a deep source of fluids or gases at and around the Veghel well field BW27:

1. The ^{3}He and ^{4}He concentrations that could reveal a mantle influence;
2. The concentrations and isotopic composition of methane, which could reveal a thermogenic methane source at depth.

^{3}He and ^{4}He analysis

An influence of mantle fluids can be investigated using a plot similar to Figure 5.21. It helps to interpret the noble gas composition, as it describes the mixing from 3 reservoirs: water which is equilibrated with the atmosphere (blue point), water which is determined by the radiogenic production of ^{4}He in the earth crust (orange point) and water which is determined by a flux from the earths mantle (dark red). Typically, precipitation water that infiltrates into an aquifer starts at the blue point and picks up ^{4}He during aging of the water due to decay reactions from the U/Th decay series. This aging history will proceed along the orange mixing line. Deviations from the line are possible due to mixing with a mantle derived component, which typically occurs in volcanic regions and may occur in tectonic active regions where a fault zone may induce increased vertical permeability and possible gas connections between the deeper and shallower subsurface. Analyzing such data, one has to correct for possible disturbance by ^{3}He which is produced from the decay reaction of tritium (olive green), but this can probably be neglected in our study of the Veghel well field BW27 as the tritium concentrations are very low (Table 5.1).

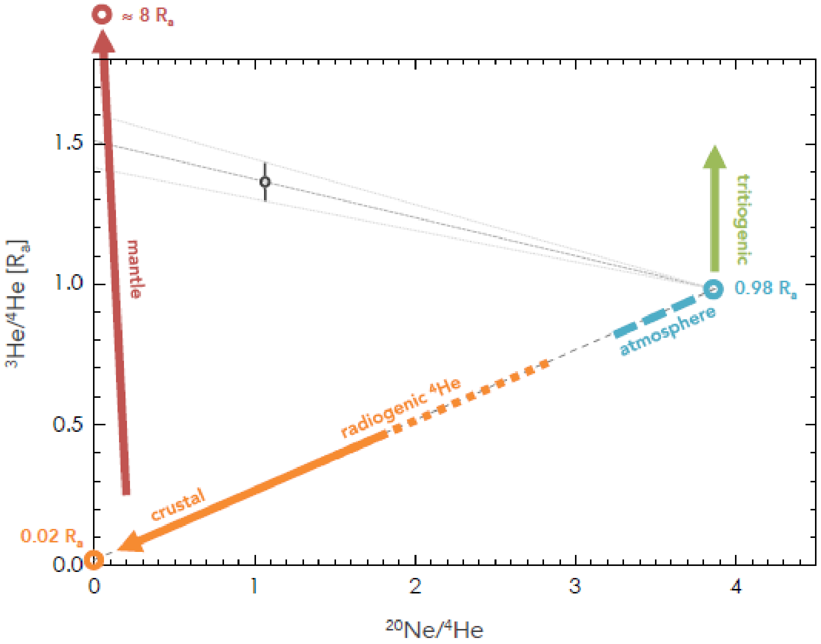

Figure 5.21 Separation of the different ^{3}He/^{4}He reservoirs by using the three-isotope-plot introduced by Pyle (1993), plotting ^{3}He/^{4}He over ^{20}Ne/^{4}He. A mantle component (dark red) would increase the ^{3}He/^{4}He ratio relative to the crustal ^{4}He production line (orange), but care should be taken that no tritiogenic ^{3}He is present in the mixture as this would also increase the ratio (green), shifting the ratios upwards (figure from Freundt, 2020).

We created a similar plot for the ^{3}He and ^{4}He ratio of the mixed water from the pumping wells 1-9 and of the water from the individual pumping wells at the Veghel well field (Figure 5.22). Clearly, the samples plot in the lower left corner close to the crustal end point, but above the crustal radiogenic mixing line (dotted line). Instead, the samples plot close to a line with a somewhat higher ^{3}He/^{4}He ratio of 0.18*R$_A$ which was found to be representative for many samples in the Brabant region (Broers et al. 2021a).

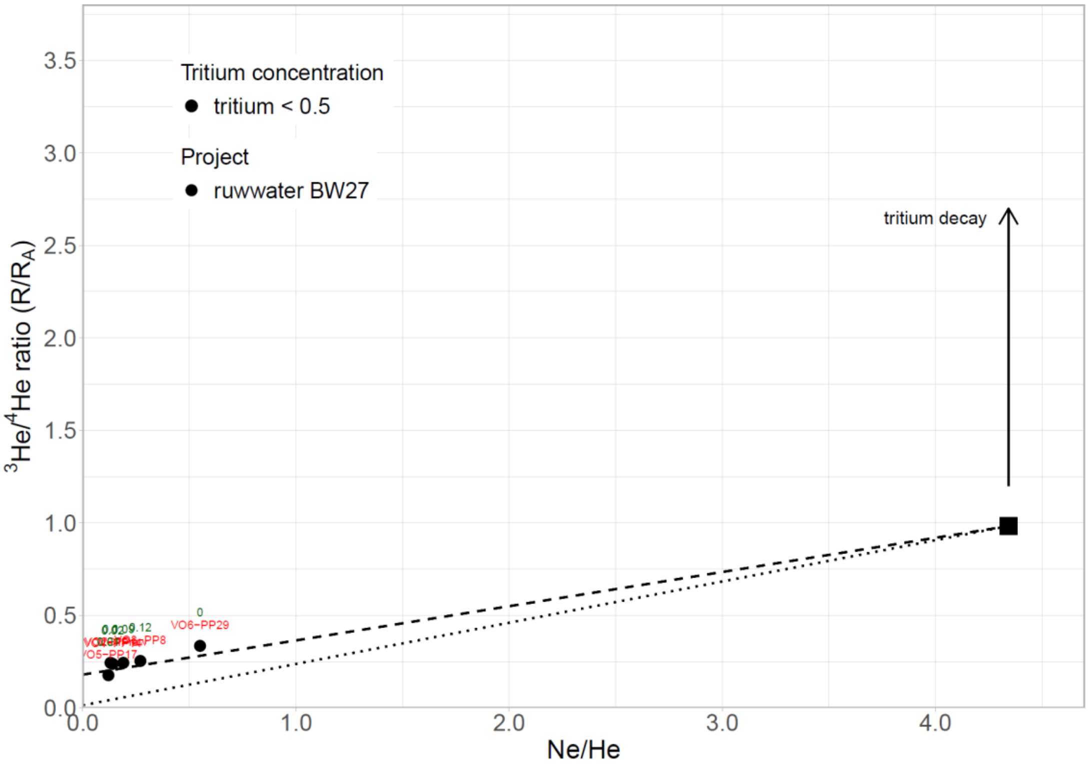

Figure 5.22 Ne/He ratio vs ^{3}He/^{4}He ratio for the 6 individual pumping wells and the mixed raw water of well field BW27. Green labels denote the ^{3}H concentrations. Samples VO2-PP8 and VO6-PP29 plot to the right of the rest of the group. All samples plot far from the atmospheric equilibrium point and close to the Mantle/Crust mixing line of the Broers et al. (2021a) study.

A more detailed graph was made to estimate the ^{3}He/^{4}He ratio relative to the atmospheric ratio (Figure 5.23). The estimations for the ^{3}He/^{4}He ratio that are listed in Table 5.2 are based on the extrapolation that was made in this figure. The samples from pumping well 14 (“VO4-PP14”), 1 (“VO2-PP1”) and 8 (“VO2-PP8”) plot close to the orange line of 0.21 R$_{A}$. Pumping well 1 plots just above it (0.22 R$_{A}$) and 17 and 29 plot at the 0.15R$_{A}$ line (red) and 0.24R$_{A}$ line (gray), respectively. The ratios are within a narrow range of 0.15-0.24R$_{A}$, which an average of R$_{A}$=0.22. These numbers indicate a 2.5% contribution of mantle derived ^{4}He and a 96% contribution of ^{3}He for all wells averaged. Whereas the mantle contribution is substantial, we do not see an increase of the mantle contribution in the direction of the fault. This is different from the previously discussed Groß-Gerau case (Figure 5.20) where a ratio of 0.41R$_{A}$ and a ^{4}He mantle contribution of 5.2% were estimated in combination with substantially upconing of salinized water in the near vicinity of the fault.

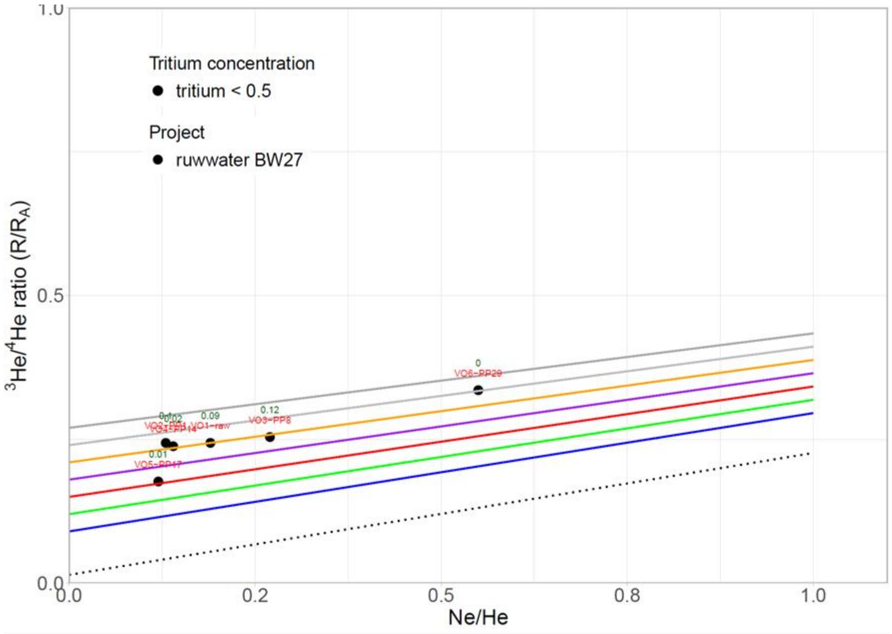

Figure 5.23 Three-isotope plot for the BW27 raw water and individual pumping wells. Lines indicate different values of the ^{3}He/^{4}He ratio, relative to atmospheric ration R_A.

Methane and methane isotopes

The other tracers that we applied to potentially reveal a deep component in the waters from BW27 also failed to give evidence of a connection between the deeper subsurface to the pumped aquifer. The pumping well VO2-PP1 that shows the oldest water is lowest in methane (4 mg/l) and has a $\delta^{13}C_{CH4}$ value of -88.6‰. The $\delta^{13}C_{CH4}$ value is indicative for a biogenic source of methane, which is probably located in the pumped aquifer itself. Dutch aquifers are typically rich in organic matter contents and methanogenesis in deeper aquifers is a common feature (Griffioen et al. 2013, Yu et al. 2018). The value of -88.6‰ of PP1 is within the relatively small range of values observed in the other wells (-89.2 - -84.1‰). The δ^2H_{CH4} values confirm the biogenic nature of the methane and the limited range of values (-280 - -269‰). An extra argument against a deep source of methane stems from the fact that the pumping well that has the largest contribution of Holocene water (VO3-PP8) shows the highest methane concentrations (7.7 mg/l).

5.3.2.7 Discussion and conclusions for the gases and isotopes in the Veghel pilot

The study at the Veghel well field BW27 reveals clear differences in the age distributions of the 5 individual pumping wells. Pumping well 1 (“VO2-PP1”) pumps the olders water, with a large contribution from the age class 10,000-25,000 years. The chloride concentrations are related to the age of the water, indicating that the wells with higher chloride pump water from deeper parts of the subsurface, which is also visible from the eleveated ^{4}He concentrations. Overall, we conclude that there is no thermogenic deep source of methane and a significant but limited contribution of 2.5% mantle derived ^{4}He which leads to elevated ^{3}He concentrations. There are no indications that concentrations of the tracers change in the direction of the fault, and no indications that the fault itself acts as a permeable path connecting the deeper and shallower subsurface through transport of gas and fluids.

The position of the Veghel well field close to a secondary fault of the Peel Boundary fault on the northeastern edge of the Roer Valley Graben probably causes pumping wells 14 (“VO4-PP14”) and 1 (“VO2-PP1”) to draw more water from the deeper subsurface, leading to elevated chloride concentrations (see conceptual model of Figure 5.24). For VO2-PP1, this could be confirmed by a complete set of tracers that indicate a very high proportion of water from the age class 10,000-25,000 years (85%). Unfortunately, no $^{14}C_{DIC}$ activity is available for VO4-PP14 which limited the age distribution assessment.

Figure 5.24 Conceptual model of the flow around the Veghel well field BW27. Lateral inflow from the east is limited to assumed sealing in the fault zone. Given their position in the center of the overall well field, the wells PP1 and PP14 are forced to pump a larger proportion of their water from deeper parts of the subsurface, whereas the pumping wells that are more at the fringe of the well field (PP8 and PP29) have easier access to water from the pumped aquifer and above.

5.3.3 Connections between deep and shallow: area with regional groundwater discharge near the city of 's-Hertogenbosch

Groundwater from a regional groundwater discharge area in the Northern part of the Roer Valley Graben has been also analysed for influences from the deep subsurface. Samples have been taken from a monitoring well near the city of 's-Hertogenbosch (Figure 5.25 and Figure 5.1). The multi-level well is located in the low-lying Bossche Broek, a wet nature reserve that is also used for water storage to prevent flooding. It lies near the confluence of three small rivers: the Aa, the Dommel and the Esschestroom, which drain different parts of the Roer Valley Graben. The water flows into the river Meuse north of the city of 's-Hertogenbosch. The area was chosen for a number of reasons:

- The Bossche Broek is known to be a regional discharge area where we may expect older water to discharge from deeper aquifers into the river system;
- The presence of paleowater in a nearby well was suggested by high ^4He concentrations that resemble ^4He concentrations in deeper groundwater (Broers & de Weert 2015, see also section 5.3.1);

- The baseline study of section 5.3.1 gave indications for the presence of thermogenic methane, as we derived from the elevated $\delta^{13}C_{CH4}$ values;
- A deep multi-level observation well is available, which is part of the provincial groundwater quality monitoring network of the province of Noord-Brabant, for which the well construction was made according to high standards, including bentonite seals at the depth of the main aquitards which prevent downward or upward flow around the observation well.

The questions that we addressed in the study were:

1. Is there indeed deep old water which discharges at the location?
2. Does the discharging water originate from deeper aquifers below the main aquitard of the upper Waalre Formation?
3. Does the methane have a thermogenic origin, which could indicate a connection between the deep and shallow subsurface?

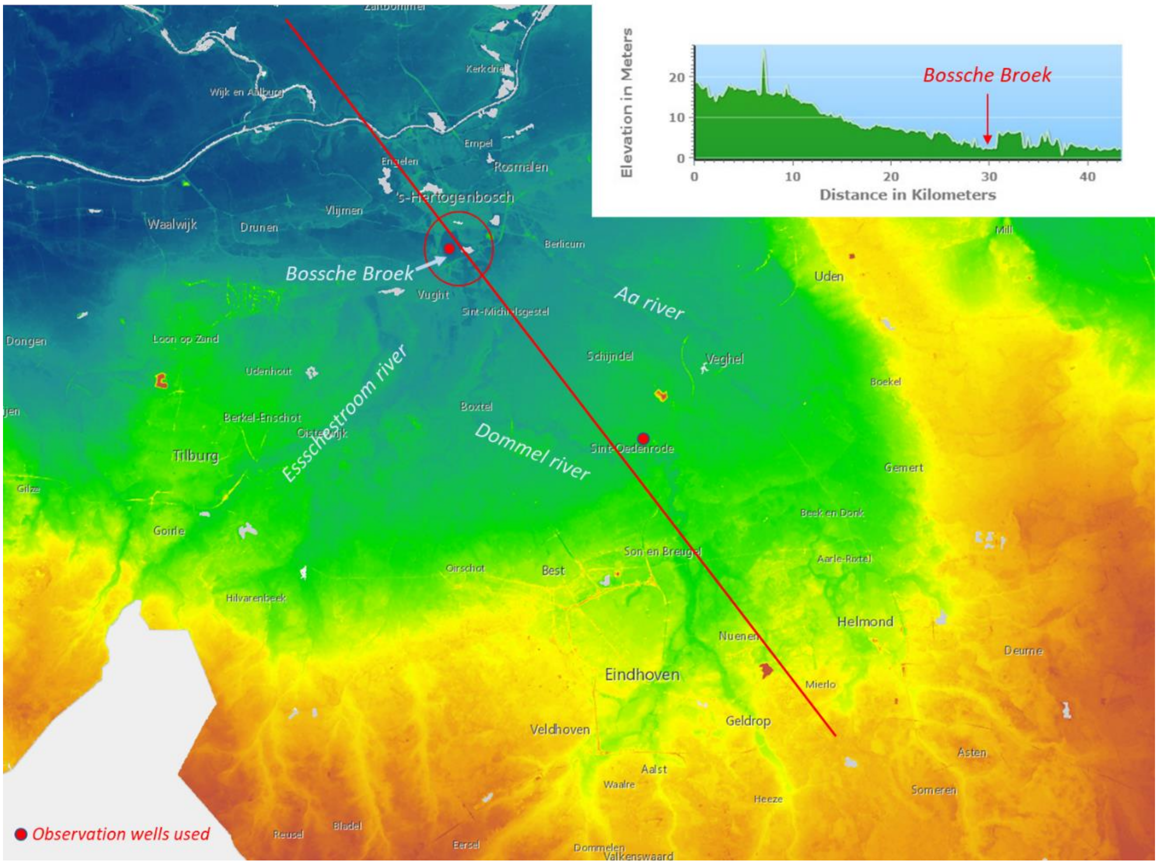

Figure 5.25 Location of the deep multi-level observation well at the Bossche Broek, south of the city of 's-Hertogenbosch in relation to the altitude of the terrain. The red line indicates the position of the altitude profile. Red points indicate the position of the observation well at the Boosche Broek and an additional observation well near St. Oedenrode that was used to identify groudwater level trends.

5.3.3.1 Hydrogeological setting

Figure 5.26 gives information about the well construction and shows the borehole description that belongs to the deep observation well. Figure 5.27 extends this borehole description to a hydrogeological cross section. From bottom to top; the following Formations are present:

- Boxtel Formation (yellow).

- Sterksel Formation (purple);
- Stramproy Formation (beige);
- Waalre Formation (ochre and orange; darker colors for aquitards);
- Kieseloolite Formation (brownish);
- Oosterhout Formation (olive green);

A description of these Formations is given in Section 5.2.

B45C0391
X-coordinaat: 149352.00
Y-coordinaat: 409917.00
Maaiveld: 2.68 m+NAP

Peilfilter	Diepte	⌀	Vervallen
1	13.08 m-mv	52 mm	-
2	33.08 m-mv	52 mm	-
3	78.08 m-mv	52 mm	14-05-2006
4	130.08 m-mv	52 mm	-
5	141.08 m-mv	52 mm	-
6	202.58 m-mv	52 mm	-
7	234.08 m-mv	52 mm	-

Identificatie: B45C0391
Coördinaten: 149352, 409917 (RD)
Maaiveld: 2.60 m t.o.v. NAP
Beschikbare informatie: Gescande documenten en Digitale opnamege
Beschrijfmethode: Standaard Boor Beschrijvingsmethode
Kwaliteit interpretatie: Gevalideerd in ondergrondmodel

Lithostratigrafie	Lithologie
BX	Leem
BXBS	Zand fijne categorie
ST	Zand midden categorie
SY	Zand grove categorie
WA	Grind
MS	Veen
KI	Gyttja
OO	Bruinkool

Figure 5.26 Borehole description, well construction and location of the observation well B45C0391, which contains 7 well screens of 52 mm diameter between 12 and 234 m depth.

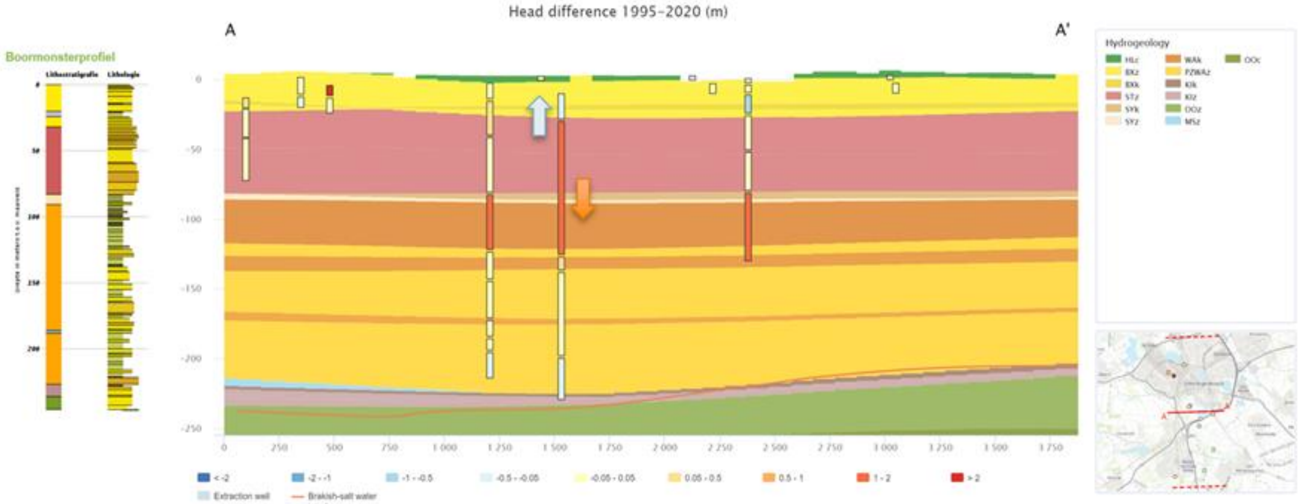

Figure 5.27 Hydrogeological cross-section over the Bossche Broek, indicating vertical head differences between different aquifers: positive difference in blue (potential upward flow), negative difference in red (potential downward flow).

Figure 5.27 gives information about groundwater head differences between the different monitoring screens, based on the tool that was developed under GeoERA RESOURCE in the H3O-PLUS work package (Broers et al., 2021c). In our cross section we observe a positive head difference between the Sterksel aquifer (purple) and the overlying Boxtel Formation (yellow) but a negative head difference between the Sterksel aquifer and the Waalre aquifer (ochre and orange) below. It means that the groundwater head is highest in the Sterksel with upward seepage. In the overlying layers, groundwater discharges to the surface water system. However, at deeper levels, the groundwater flow direction is opposite: potential downward flow over the Waalre top aquitard (ochre colour).

5.3.3.2 Data acquisition

In order to characterize the gas composition and assess the groundwater ages, We sampled the 7 observation screens in the 250 m deep multi-level observation well. The samples were analysed for major chemistry, methane, methane isotopes and ^{18}O. Furthermore, we collected samples for age dating, including ^{3}H, $^{14}C_{DIC}$, $^{13}C_{DIC.}$ A simple approach was used to age date the water using the approach also used in GeoERA HOVER deliverable 6.4 based on a method by Han and Plummer (Broers et al., 2021b). Figure 5.28 shows the samples in a Han-Plummer plot of $^{14}C_{DIC}$ vs $\delta^{13}C_{DIC}$, and lists the estimated ^{14}C apparent ages in years assuming that deep methanogenesis determined the $^{14}C_{DIC}$ activities and $\delta^{13}C_{DIC}$ values by dilution with decaying old organic matter in the aquifers. The resulting ^{14}C apparent ages were used to interpret the concentration-depth profiles of the other measured parameters. Additionally, the age was determined using the Discrete Travel Time Distribution Model (DTDDM; see Broers et al. (2021a). The DTDDM model ages differs from the ^{14}C apparent age because it also uses information provided by the $^{4}He_{rad}$, Noble Gas temperature (NGT) and ^{3}H measurements. The difference between the ^{14}C apparent age and DTDDM model age gives an indication of the uncertainty of the age determination (see Section 5.3.3.3).

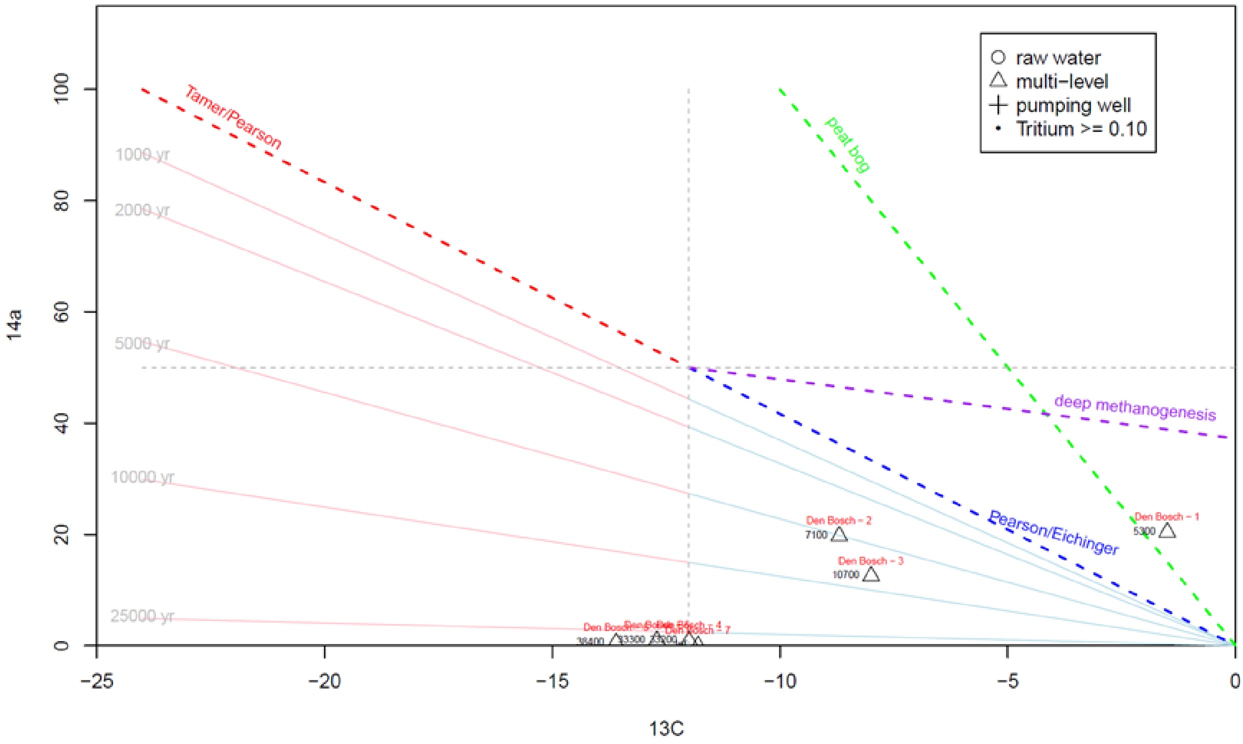

Figure 5.28 Han-Plummer plot for the samples from observation well B45C0391.

5.3.3.3 Results

The acquired data is illustrated in Figure 5.29 showing concentration-depth profiles for $^{14}C_{DIC}$, $^{4}He_{rad}$, noble gas temperature (NGT), $\delta^{18}O$, groundwater age, chloride, methane and $\delta^{13}C-CH_4$. For reference, the colours of the geological Formations comply with the cross-section of Figure 5.27, showing that the first monitoring screen is in the Boxtel Formation, the second and third ones in the Sterksel Formation, the fourth to sixth below the main Waalre aquitard in the Waalre Formation and the last one in the Kieseloolite Formation.

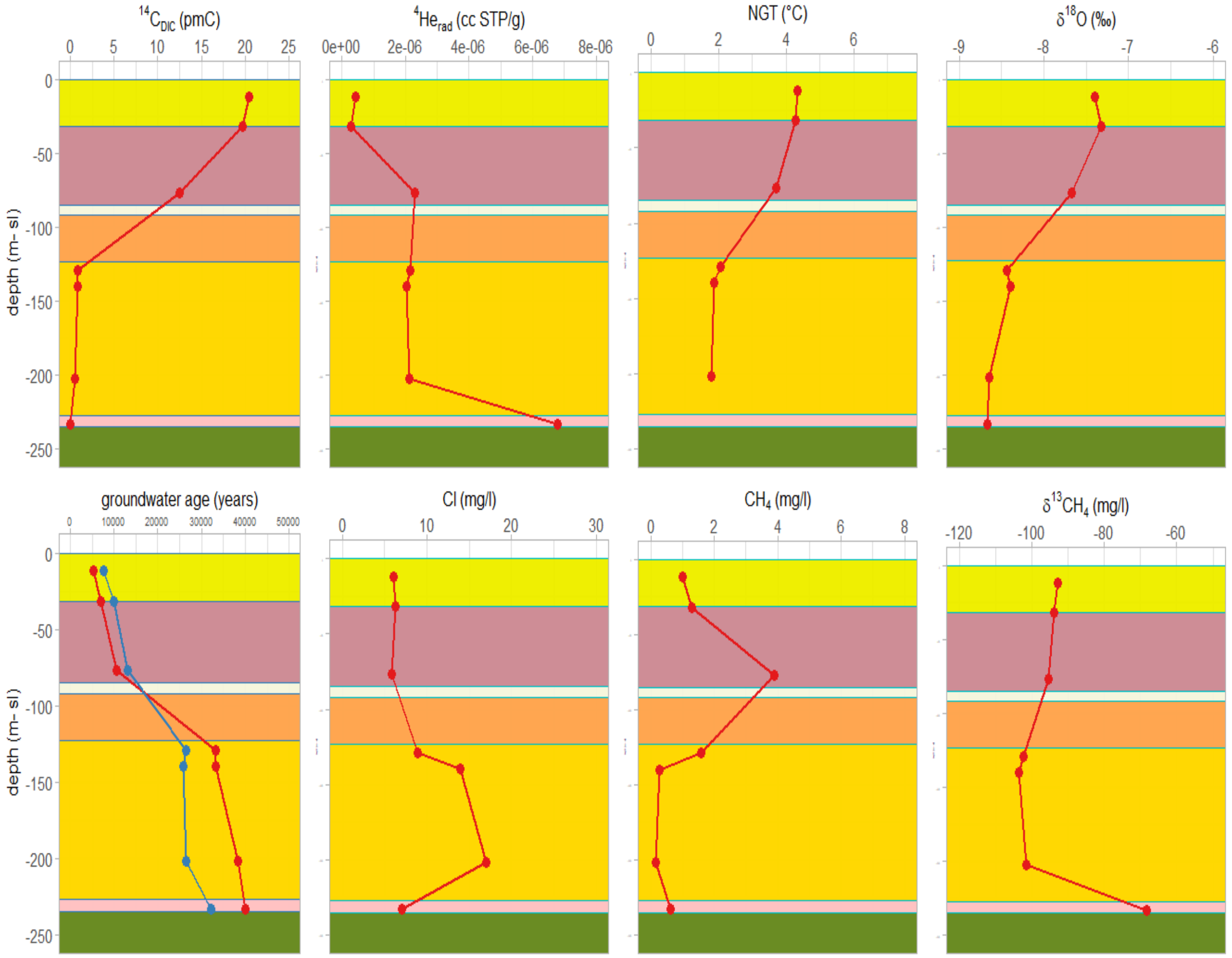

Figure 5.29 Concentration-depth profiles for the 250 m deep multi-level observation well near 's-Hertogenbosch. Groundwater age (figure bottom left): in blue the ^{14}C apparent age, in red the DTTDM model age.

The profiles show trends with depth:

- $^{14}C_{DIC}$ is much higher in the Sterksel Formation (12-20 pmC) than in the Waalre Formation (< 5 pmC);
- $^{4}He_{rad}$ increases with depth whereas the noble gas temperature (NGT) and $\delta^{18}O$ decrease with depth;
- Water is older with depth, with ages of 5000-10,000 years above the Waalre aquitard, and ages > 20,000 years below it;
- Chloride is very low in the Sterksel aquifer and Kieseloolite aquifer(5-6 mg/l) but higher in parts of the Waalre Formation;
- Methane is elevated in the lower part of the Sterksel Formation, but all water contains methane (and no sulphate) indicating strongly reduced methanogenic conditions over the whole profile;

- $\delta^{13}C_{CH4}$ varies between -105 and -90‰, except for the deepest sample from the Kieseloolite Formation which is ~-70‰;
- The values for the deepest screen in the Sterksel Formation (third screen) are between the samples from the shallower Sterksel (screens 1 and 2) and the samples from the Waalre Formation (screens 4-6) for all parameters, except for methane.

5.3.3.4 Hydrogeological interpretation

The concentration-depth profiles of Figure 5.29 confirm the presence of paleowater over the whole profile. Especially, the water in the Waalre aquifer is very old which is indicated by the low $^{14}C_{DIC}$, the high apparent age which is calculated from both carbon isotopes, but also by the elevated $^{4}He_{rad}$. The low NGT (~2°C) is indicative for cold recharge in or before the last glacial maximum when the land ice mass was close to the studied region. The depleted $\delta^{18}O$ signal confirms the hypothesis, as cold recharge produced depleted ^{18}O. When we compare the age distribution of the water with a previous regional study (Broers et al. 2021a) these signals comply with a grouping in either the MO and O groups with a large contribution of water aged between 10,000 years and 25,000 years. The paleowater shows close resemblance to water from other well fields in the province of Noord-Brabant (Broers et al., 2021a; see Figure 5.30). This is further illustrated in the three isotope plot of Figure 5.31, which shows that the Ne/He and $^{3}He/^{4}He$ ratios of the Waalre samples corresponds with those of the well fields belonging to the O age group.

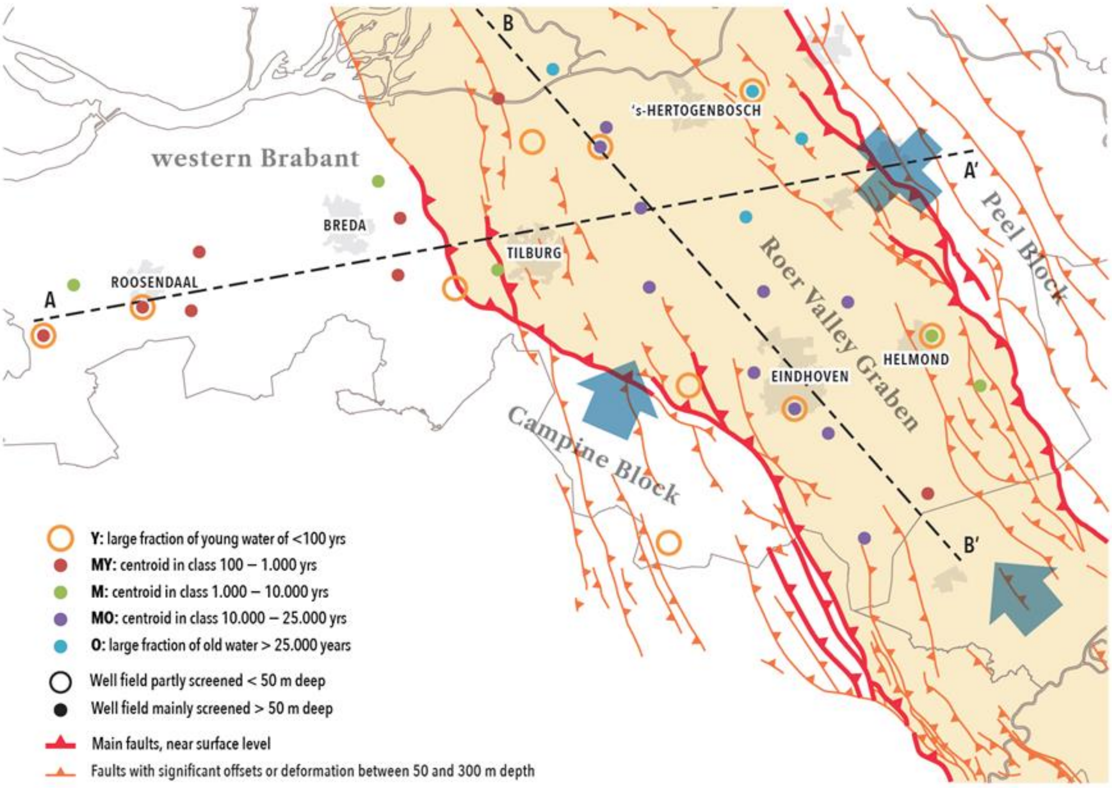

Figure 5.30 Age groups distinguished in the Roer Valley Graben (Figure from Broers et al. 2021a)

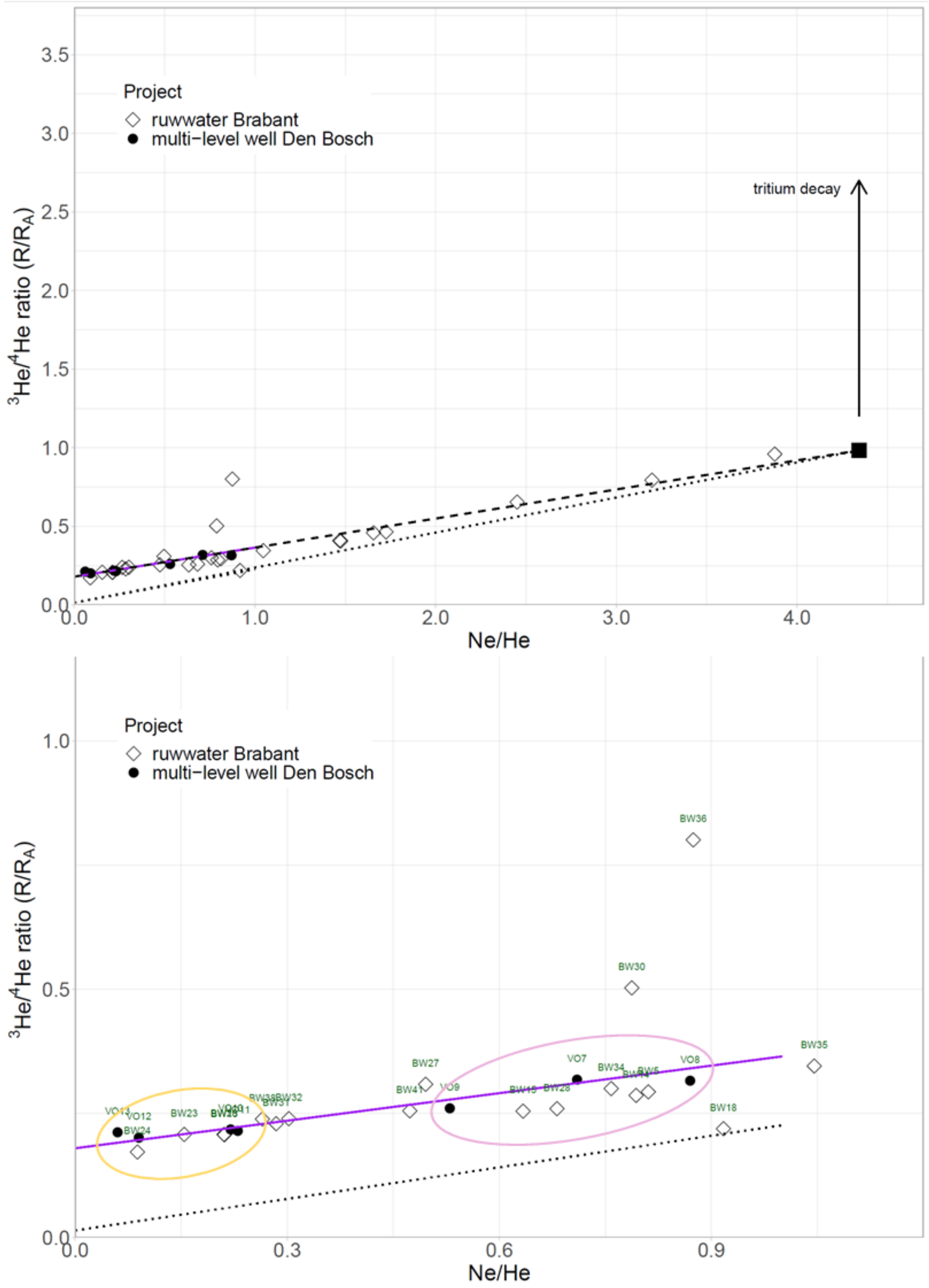

Figure 5.31 Three-isotope plot for the samples of the Broers et al. (2021) study for 39 well fields (open symbols) and the samples from observation well B45C0391 (closed symbols). Top: all samples of the BW series and well B45C0391. Bottom: zoom of the samples from B45C0391 and the older BW series well fields. Codes refer to the well fields in the Broers et al. (2021a) study.

The water in the Sterksel aquifer is old as well: the ^{14}C apparent age is between 5,000 and 10,000 years and the very low chloride concentrations suggest recharge around the period of the Last Glacial Maximum. Such old water is a exception in the Sterksel aquifer, which typically contains recently recharged water with even a large component of modern water aged less than 100 years old (Broers et al. 2021a). The Ne/He and $^3He/^4He$ ratios, however, plot close to well fields pumping from the deeper Waalre and Kieseloolite aquifers and part of the MO water group in Broers et al. (2021a). So, the age of the water should be related to deeper groundwater circulation, and the presence of this water in the Sterksel Formation is apparently the result of upward flow from these deeper aquifers into the Sterkel Formation. The surface water system receives seepage of more than 5000 years old.

5.3.3.5 The origin of the methane

The methane and $\delta^{13}C_{CH4}$ values in profile of Figure 5.29 indicate that strongly reduced methanogenic conditions are present over the complete depth profile. The presence of methane and the absence of recently introduced sulfate or chloride, confirms the discharge of groundwater at this location. Moreover, the $\delta^{13}C\text{-}CH_4$ values that were observed leave no doubts about the origin of the methane. The methane is clearly of biogenic origin and a thermogenic signal is totally absent. The enriched $\delta^{13}C_{CH4}$ values that were previously found in nearby observation wells (99-3 and 1868-4, see Section 5.3.1.2 must be related to the mixing of recent water that contains sulfate and a relict of old methanogenic water that was originally present. The high sulfate concentrations and the presence of tritium in those wells confirm the mixed nature and points to the process of anaerobic methane oxidation which leads to enriched $\delta^{13}C\text{-}CH_4$ (see Section 5.3.1.3). A deep thermogenic source of methane can therefore be excluded on the basis of the newly acquired data in this GeoERA Vogera project.

5.3.3.6 Conclusions of data from monitoring well near ‘s-Hertogenbosch

There is indeed old water discharging at the location, which originates from aquifers below the upper aquitard of the Waalre Formation. The methane in the groundwater is clearly of biogenic origin and gives no indication of a connection between the deep subsurface and the groundwater near ‘s-Hertogenbosch.

5.4 Discussion for province of Noord-Brabant

In this chapter, we analyzed patterns of gases and tracers to identify and evaluate potential contaminant migration pathways and controls on fluid flow/transport behaviour and to assess vulnerability of shallow aquifers in relation with possible connections with activities in the deeper subsurface.

A groundwater age-dating campaign made it possible to establish concentrations for dissolved gases in the shallow groundwater in the province of Noord-Brabant, that can be used as baseline for possible future energy-related activities in the deep subsurface. The gas composition and carbon and deuterium isotopes were measured to distinguish between biogenic and thermogenic methane. We conclude that the vast majority of detected methane is of biogenic origin, formed from methogenesis through the microorganism-mediated decomposition of organic matter. Enriched $\delta^{13}C\text{-}CH_4$ were found for a number of filters, but most of these enriched values are coupled with an absence of higher alkanes and a presence of high sulfate concentrations, pointing to anaerobic methane oxidation which is known to enrich $\delta^{13}C\text{-}CH_4$ values leading to a “pseudo-thermogenic” methane signal. In these cases there is most likely a mixing of biogenic methane from deeper layers with sulfate-rich groundwater from shallower layers, coming from agricultural or urban areas. We conclude that for the vast majority of samples no thermogenic methane was found, thus making natural pathways of deeper groundwater wich would transport thermogenic methane into the shallow subsurface unlikely.

However, quite a number of shallow wells carried an elevated ^4He which is an indication of influence from the deep subsurface. Near the city of ‘s-Hertogenbosch, we indeed confirmed that water of several thousands years old discharges in a local nature reserve. We argued that the discharging water originates from deeper aquifers below the main aquitard of the upper Waalre Formation, for which we found evidence based on the gas and tracer composition that resembled concentrations in deeper public water supply wells which pump from these deeper formations. The elevated ^4He in those water is also found near the discharge area and a low $^{14}C_{DIC}$ is indicative for the paleo character of the water. The methane of this water is of biogenic origin, so a thermogenic source of the gases in the deeper aquifers can be excluded.

We also studied the possible connections between the deep subsurface and shallow groundwater in the Veghel pilot. The Veghel public water supply well field BW27 is located around a secondary fault of the Peel Boundary Fault. We characterized the mixed water from 9 pumping wells and water from 5 individual pumping wells. We found a clear relation between the age distribution of the pumped water and the chloride concentrations, indicating that the wells with higher chloride pump older water from deeper parts of the subsurface. We did find elevated ^4He and ^3He concentrations pointing to a 2.5% mantle contribution for the ^4He and 96% for the ^3He, but found no relation of the $^3He/^4He$ ratio with the distance to the fault or with the age of the water. This signal for a deep connection between crustal and mantle helium concentrations was not reflected in the methane origins. All methane was of biogenic origin and the highest methane concentrations were found in the pumping wells with the youngest water on average. A deep thermogenic source of methane can thus be excluded. A fault displacement study in section 4.4.1 of this report indicates that the relay ramps are present in the fault indicating that the fault consists of multiple linked segments which could induce “linking damage”in the deeper subsurface. However, we did not find indications that concentrations of the tracers change in the direction of the fault, and no indications that the fault itself acts as a permeable path connecting the deeper and shallower subsurface through transport of gas and fluids.

Although we did not find concrete hotspots of fluid or gas transport from the deeper subsurface, such hotspots can have a very local influence. A recent study by Freundt (2017) found a clear ^{3}He hotspot indicating mantle connection in a comparable tectonic setting in the Lower Rhine Graben at Groß Gerau but many other locations lacked any indication for such a connection. In general, hotspots for preferential fluid and gas flow along faults are not uncommon (see e.g. Gumm et al. 2016, Banks et al. 2019). Furthermore, the 3D seismic analysis done in section 4.4.4 shows that linking damage zones are abundant in sections of faults near Tilburg and the overall presence of elevated ^{3}He concentrations in the paleowater in the Roer Valley Graben (Broers et al. 2021a) may provide a signal that these kind of connections exist or have existed in the Roer Valley Graben tectonic setting as well. However, we did not find any credible signal for methane gas of a thermogenic origin seeping upward in either the shallow groundwater between 10-25 m depth or in any of the well fields studied here or in a previous study (Broers et al. 2015).

6 Pilot Rauw Fault, Belgium

6.1 Introduction of Rauw fault pilot

Faults play an important role in flow and transport in regional groundwater systems (Bense et al., 2013; Lapperre et al., 2019). The inclusion of faults during the conceptualization of regional groundwater systems and their incorporation during the construction of groundwater models is crucial, e.g. for performance assessments of radioactive waste repositories, as well as risk assessment for other deep subsurface activities. Faults can act as: i) barriers slowing down groundwater flow, ii) conduits speeding up groundwater flow, or iii) a combination of both (Raiber et al., 2015; Walraevens et al., 2015; Battle-Aguilar et al., 2017; Verbeeck et al., 2017; Oiro et al., 2018; Bense et al., 2013; Gumm et al., 2016). Determining flow and transport behaviors across these structures is challenging since they are rarely exposed on the surface and their hydraulic behavior varies spatially (Ladevèze et al., 2019; Lapperre et al., 2019). Environmental tracers may provide valuable information potentially useful to determine flow pathways, travel times, and groundwater age. If the latter are affected by the presence of fault zones, they can yield useful information for the parameterization of faults in groundwater models (Read et al., 2013; Banks et al., 2019).

The specific scope of this study is to investigate potential horizontal flow across and vertical flow along the Rauw fault. The first phenomenon has never been incorporated in the Neogene aquifer model (NAM) in this region (Gedeon et al., 2007), and hence its impact on groundwater flow is not known yet. The latter phenomenon may be of importance as it may connect potential geothermal reservoirs with the shallow Neogene aquifer. The current hypothesis is that there is no connection between the deep subsurface and the upper aquifer. Hence, the objective is to show that the investigated tracer concentrations and spatial patterns can be explained by groundwater dynamics in the upper aquifer above the Boom Clay, without the need for such connection. The investigated tracers are: heat, major ion geochemistry, stable isotopes, radiocarbon, helium and tritium.

6.2 Geology and hydrogeology of the Rauw fault area

The Rauw fault is one of the westernmost border faults of the Roer Valley Graben, a tectonic structure that became more or less permanently active from the Oligocene onwards (Geluk et al., 1994; compare sections 4.1 and 4.2). This structure runs in a southeast-northwest direction from the outcropping Rhenohercynian Massif in Germany down to the southern North Sea Basin (Figure 6.1a). In a NW European context, the Campine Basin is a subsiding structure, sandwiched in between the Brabant Massif in the south and the Roer Valley Graben in the northeast.

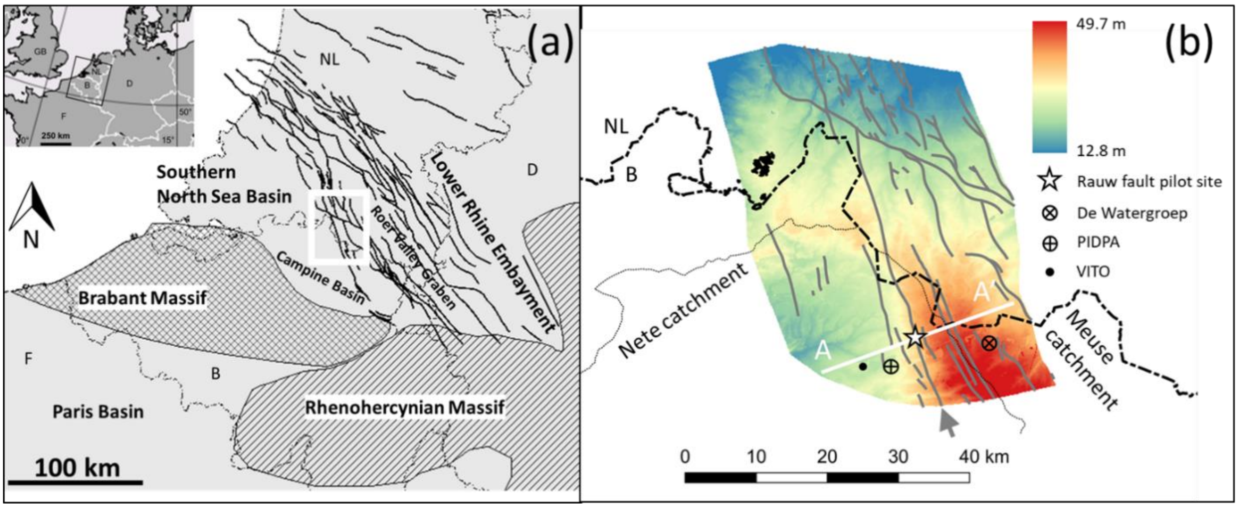

Figure 6.1 (a) Structural setting of the Rauw fault pilot site in a northwestern European context. White rectangle refers to the area depicted in (b). Relevant references for the compilation of this figure can be found in Beerten et al. (2013). (b) Topography of the H3O-De Kempen model area (Vernes et al., 2018). Grey lines indicate faults that are visible in the base of the Boom Formation. Rauw fault is indicated by grey arrow. Thin black line is the outline of the Nete catchment. The profile line A-A' refers to the cross-section in Figure 6.2. Circles indicate the location of major groundwater abstraction.

Recently, the cross-border (hydro)stratigraphy of the region has been modelled in de H3O-De Kempen project (Vernes et al., 2018). The model area is outlined in Figure 6.1b. The Rauw fault can be identified as a major fault (grey arrow), running through the entire model area. The shallow geological cross-section (Figure 6.2) shows an offset of about 50-100 m along the fault, the eastern part being downthrown, as might be expected for a synthetic normal fault. The amount of displacement decreases towards the surface. Palaeoseismological investigations identified that the fault has not been active for the last 500 ka (Verbeeck et al., 2017). It is (almost) reaching the surface due to the fact that overlying sediment has been removed by subsequent erosion. There are several minor faults east and west of the Rauw fault. Overall, the geological formations dip towards the Roer Valley Graben due to tectonic tilting. Several km to the east of the Rauw fault, the water divide between the Meuse and Nete catchments marks the highest topographical point in the profile. The water flow direction in the aquifers has a strong component towards the west, up-dip (Gedeon et al., 2007; Vandersteen et al., 2014). Modelling of both the shallow and deep aquifers has identified that there is only a very weak downward hydraulic gradient over the Boom Clay, due to the pressure gradient, as the site is located in the upper part of the Nete catchment. However, these models never treated the hydraulic role of the Rauw fault explicitly. Moreover, potential contact or decreased hydraulic resistance between the two aquifers was not considered up to now. The aquifer of interest in this cross-section is the so-called Neogene aquifer, which comprises all the dominantly sandy (hydro)geological units above the Boom Clay (BM; Figure 6.2). Below the Boom Clay, an alternation of Formations with dominantly aquitard properties and dominantly aquifer properties can be seen. Among the aquitards we mention the clayey Maldegem (MG) and Kortrijk (KO) Formations. The other formations are dominantly sandy, ranging from slightly clayey fine sand to medium-coarse sand. The top of the Cretaceous (mainly chalk) corresponds with the top of the dark grey mass in Figure 6.2, and is up to 200-300 m thick (Bos and Laenen, 2017). From the base of the Cretaceous to the top of the Carboniferous Limestone Group, a thick sequence of alternating claystone, sandstone and coal is present, which belongs to the Belgian Coal Measures Group (Figure 6.3; Bos and Laenen, 2017). From ca. 3200 m depth onwards (at the location of production well MOL-GT-0S1), Dinantian limestones of the Loenhout Formation are present – these are currently being targetted for geothermal energy.

In the region around the Rauw fault there is limited deep subsurface activity. There is one deep geothermal doublet (see Figure 6.3 and Figure 6.1), and two drinking water wells. The geothermal production well at the Ballmat site near VITO ends in the Lower Carboniferous Limestone Group at a true vertical depth of approximately 3600 m. The two drinking water wells are pumping the Miocene aquifer (Diest Formation) at a depth of ca. 100 and 200 m (De Watergroep and PIDPA).

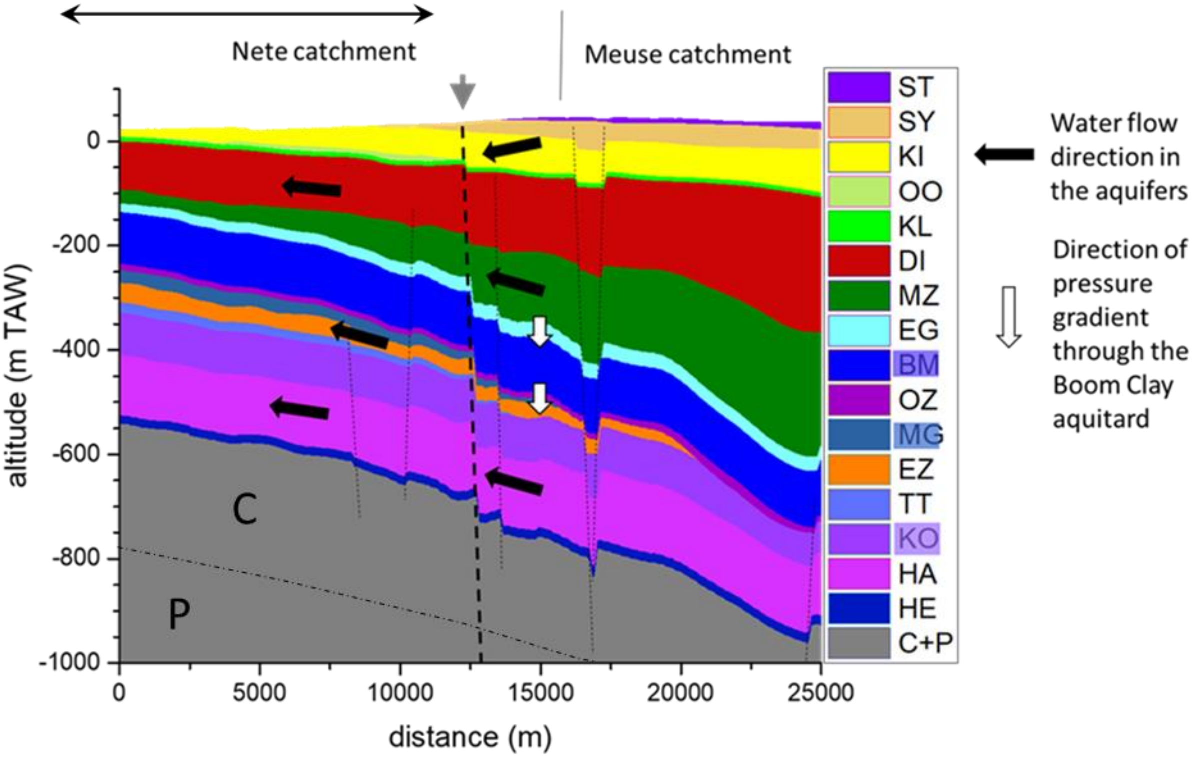

Figure 6.2 Shallow geological cross-section according to profile line A-A' in Figure 1b. The Rauw fault is indicated with grey arrow and thick dashed line, minor faults are indicated by thin dashed lines. Water divide between the Nete and Meuse catchment is given, as well as the direction of water flow in the aquifers, and leakage through the Boom Clay. ST = Sterksel Formation, SY = Stramproy Formation, KI = Kiezelooliet Formation, OO = Oosterhout Formation, KL = Kasterlee Formation, DI = Diest Formation, MZ = Late Oligocene to Middle Miocene sands, EG = Eigenbilzen Formation, BM = Boom Formation, OZ = Early Oligocene sands, MG = Maldegem Formation, EZ = Early to Late Eocene sands, TT = Tielt Formation, KO = Kortrijk Formation, HA = Hannut Formation, HE = Heers Formation, C = Mesozoic, P = Palaeozoic. Formations with dominant aquitard properties are shaded in the legend. The double arrow on top of the figure indicates the horizontal extent of the profile shown in Figure 6.3.

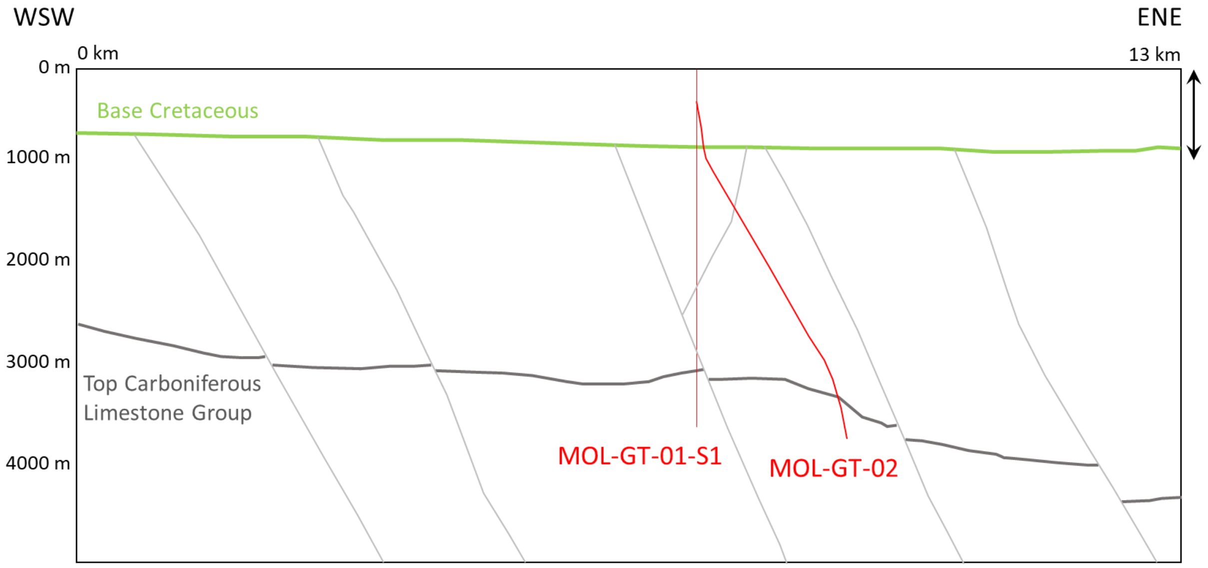

Figure 6.3 Deep cross-section of the profile indicated by the double arrow in Figure 6.2. The base of the Cretaceous and the top of the Carboniferous Limestone Group is shown. Note that the Rauw fault itself falls outside this cross-section. Other faults are indicated as terminating at the base of the Cretaceous. Production well MOL-GT-01-S1 and injection well MOL-GT-02 are indicated in red. The double arrow at the top right indicates the vertical extent of the cross-section shown in Figure 6.2. Redrawn from Bos and Laenen (2017).

6.2.1 Modelling groundwaterflow and heat transport

For the current work, the Neogene aquifer model (NAM), a steady-state groundwater flow model has been constructed by Casillas-Trasvina et al. (submitted), and a heat-transport model by Rogiers et al. (2015) has been updated by Casillas-Trasvina et al. (in prep. a) and used for simulations. See Casillas-Trasvina et al. (submitted) and Casillas-Trasvina et al. (in prep. a) for an extended description of the methods and results for both groundwater flow and transport models. Here a brief summary is presented.

The NAM, which covers the Nete catchment (Figure 6.4), is updated from Gedeon (2008) including finer vertical discretization, an updated stratigraphy (Deckers et al., 2019a) and various normal faults as horizontal flow boundaries. It uses the MODFLOW-2005 simulation program (Harbaugh, 2005). The NAM by Casillas-Trasvina et al. (submitted) assumes 9 hydrostratigraphic units: non-tabular Quaternary, Weelde, Malle, Merksplas, Mol, Lillo, Kasterlee, Diest, and Berchem and Voort (Figure 6.5). The model domain is discretized in 49 vertical layers thinning out closer to the surface to ensure smaller modelling cells close to surface hydrological features were groundwater gradients are the highest. The modelled area was discretized into a regular model grid of 96 rows and 146 columns resulting in cells with dimensions of 400 m × 400 m. A total of 23 faults were simulated with the horizontal flow barrier (HFB) package (Harbaugh, 2005) starting from the top of the second numerical layer (from around 12 to 18 meters below surface) to the bottom of the modelled domain, given that the faults do not present a clear surface expression (Verbeeck et al., 2017). Rivers, lakes, canals and abstraction wells are defined in the groundwater flow model. The groundwater abstractions range from a few m^3/d to more than 300 m^3/d. Data from several sources was used to define these parameters including the Flemish hydrographic atlas (“Vlaamse Hydrografische Atlas”) and the IGN/NGI dataset. Spatially distributed recharge is implemented with values obtained from DiCiacca (2020) which are derived from vegetation cover, soil texture and depth to the groundwater table spatial input layers. A scaling factor (a multiplier layer) was used during the model inversion for the calibration of the recharge initial value. A total of 1393 averaged hydraulic head observations are used in the NAM. These observations are obtained from the SCK CEN piezometric network (maintained for ONDRAF/NIRAS) and from the subsurface database for Flanders (Databank Ondergrond Vlaanderen; DOV). Automatic parameter optimization was implemented as technique for model inversion.

Backward particle tracking was performed using MODPATH 7 (Pollock 2016). MODPATH is a particle-tracking model that simulates advective transport, designed to work with the flow output from MODFLOW (Pollock 2015). Here we use it to determine the main flow patterns across the horizontal flow barriers (HFB) at different depths and test the potential for the faults to act as horizontal barriers or vertical conduits.

Building on previous work, a version of the heat-transport model built by Rogiers et al. (2015) has been updated from MT3DMS (Zheng 2010) to MT3D-USGS (Bedekar et al., 2016) following the new hydrostratigraphy and grid discretization used for the updated NAM groundwater flow model by Casillas-Trasvina et al. (submitted). The latest heat transport model development is explained in detail in Casillas-Trasvina et al. (in prep. a). The heat transport model is finally calibrated against temperature-depth profiles (TD’s) measured in various piezometers. Model runs are performed for the full Holocene, accounting for recent temperature variations using land surface temperature data and geothermal heat flux, as top and bottom boundary conditions, respectively.

Temperature logs have been collected within the framework of various projects and campaigns. Historical data was compiled by Rogiers (2015) from previous campaigns. The quality of the logs taken from 1988 to 1997 is unknown since sensor resolution and accuracy are not known together with the performed logging speed (up to four logs per day), potentially inducing considerable bias in the obtained temperatures. The location of these logs is presented in Figure 6.5.

Five temperature logs reported by Rogiers et al. (2014) were the only data for which type and characteristics of sensor, logging speed are known up to that date. For these wells a correction was applied to the raw data to account for the logging error. For a more detailed description of this temperature data, refer to Rogiers et al. (2014). Another five temperature logs were taken in a second campaign presented by the Rogiers (2015). A different temperature logger was used. The stop-go measurement method by Harris and Chapman (2007) was followed similarly to the previous campaign. The temperature probe used for the new campaign is the Star-Oddi’s DST-mili TD, which is typically used in temperature-depth logging by tagging fish in migration and behavior studies. A first temperature measurement campaign on the same (8) previously sampled wells (Figure 6.5), including wells R-54d and R-54e, was carried out. Additionally, 15 groundwater wells were measured, to extend the number of observations spread across the Nete catchment.

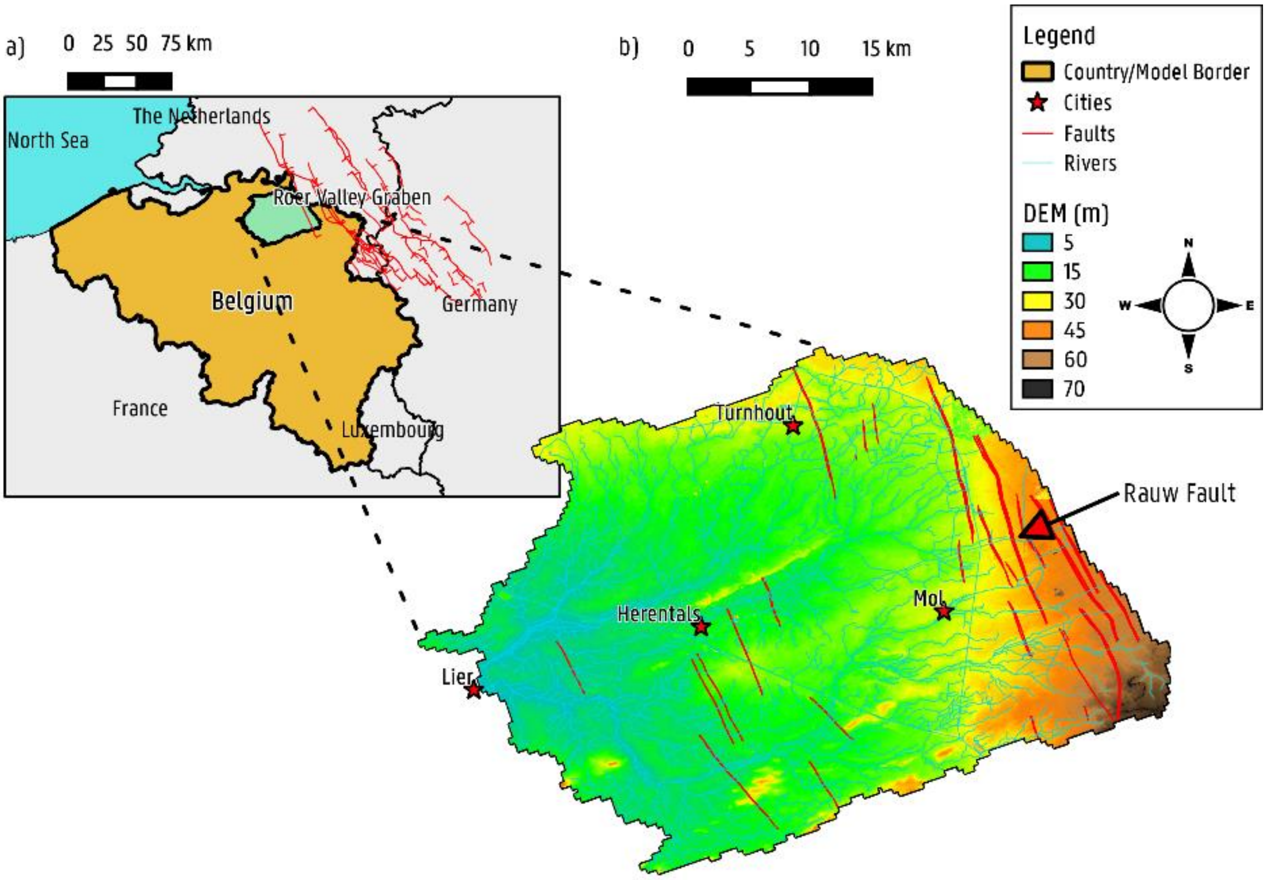

Figure 6.4 – (a) Location of the Nete catchment, which defines the no-flow boundary of the Neogene Aquifer Model (NAM), its position within Belgium and with respect to the Roer Valley Graben faults. (b) Digital Elevation Model (DEM) of the Nete catchment, including the location of faults and the drainage network (incl. canals). From Casillas-Trasvina et al. (submitted).

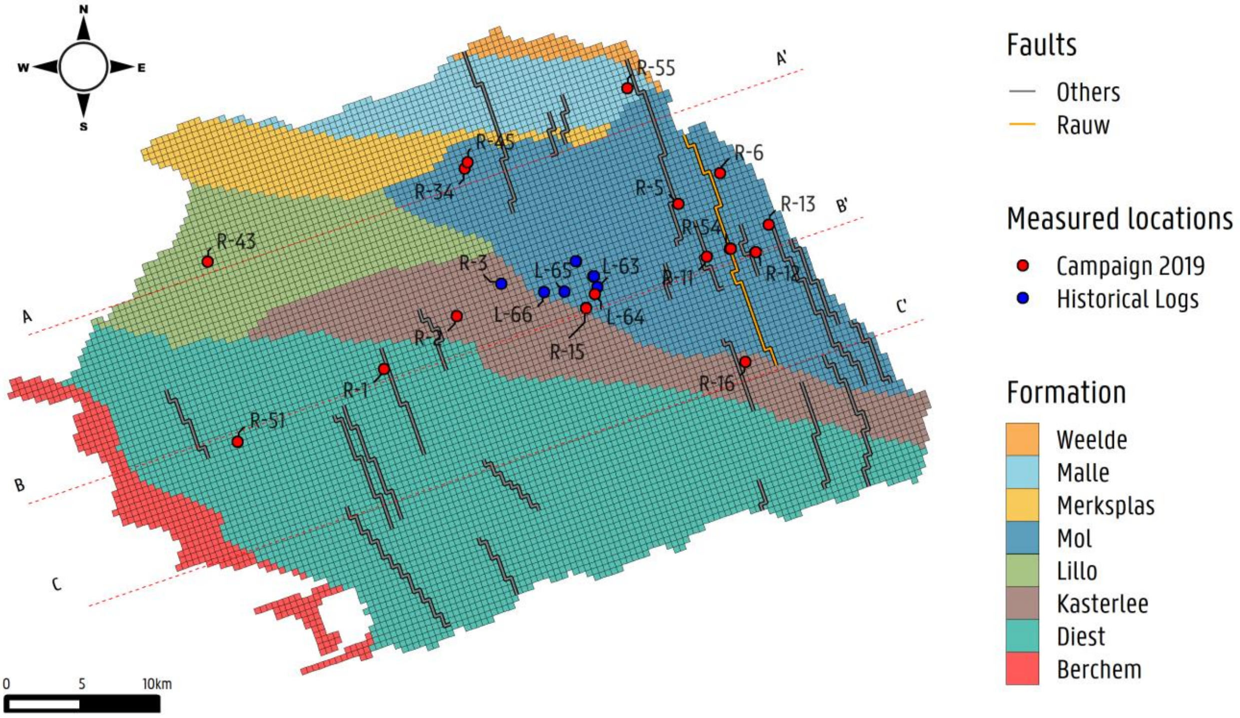

Figure 6.5 – Non-tabular Quaternary subcrop geological map with indication of faults and measured temperature locations. From Casillas-Trasvina et al. (in prep. a).

6.2.2 Hydrochemistry, stable isotopes, radiocarbon and helium

The sampling strategy was focused on getting a complete data set which includes chemical composition (major and minor ions and trace elements), isotopic data, radiocarbon ages and helium and tritium concentrations at each sampling site. Groundwater was sampled at 8 locations (Figure 6.6) within the Neogene aquifer, from a total of 22 piezometers that are being monitored by SCK CEN. Some additional data from previous sampling campaigns will also be used. Further details in applied methods and derived results from hydrochemistry and aforementioned tracers are presented by Casillas-Trasvina et al. (in prep. b).

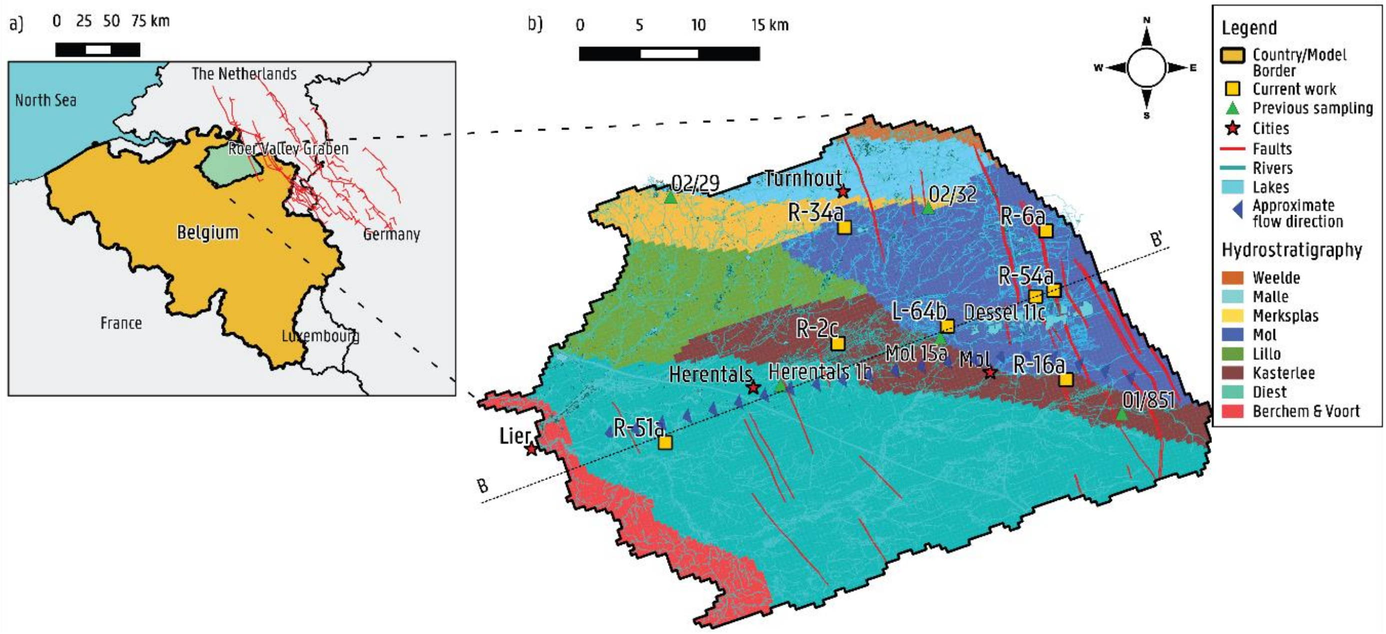

Figure 6.6 – (a) Location of the Nete catchment (NAM model) in Belgium. (b) Geological map of the Nete catchment, with faults, drainage network, sampling locations of current (orange rectangles) and previous (green triangles) work, and the approximate direction of groundwater flow. From Casillas-Trasvina et al. (in prep. b).

Two different submergible pumps were used: the Geotech SS Geosub pump and the Grundfos MP1 pump. Both allow controlling the flow down to rates as low as 100 ml/min. Before any sampling, the wellbores were purged at least 3 casing volumes, when possible, and until the pH, temperature and EC had stabilized. This was done to obtain representative samples of in-situ groundwater with minimum disturbance of the flow system and the collected sample.

Different sampling bottles were used depending on the hydrochemical analysis to be carried out: transparent polyethylene (PE), brown glass and green glass bottles; some bottles were acidified with 1 ml of H_2SO_4. The SCK CEN procedure for noble gas sampling of groundwater using cupper tubes was followed. This procedure is based on the provided guidelines by HELIS (see Vandersteen et al., 2017). For ^{3}H and δ^{13}C and ^{14}C, two 1 liter PE bottles were air-tight filled with groundwater. All samples were stored in a refrigerator until the submission to their respective laboratories for analyses. The parameters measured on-site include pH, EC, Eh and dissolved oxygen with the use of portable probes and a flow-through cell.

For hydrochemical analyses, the following techniques were used by Eurofins: titrimetry for acidity and alkalinity; ICP-MS for Al, Ca, K, Mg, Mn, and Na; spectrometry for Cl^- and SO_4^{2-}; potentiometry for pH. For isotopic analyses, the following techniques were used by Isotoptech Zrt: Gasbench-IRMS for δ^{18}O, ^{2}H and δ^{13}C; accelerator mass spectrometry (AMS) for ^{14}C (radiocarbon). Radiocarbon ages were corrected following the Coetsiers and Walraevens (2009) ^{14}C correction model which was developed for the Neogene aquifer. For noble gas analyses, the following techniques were used by HELIS Univ. Bremen: quadrupol mass spectrometer (QMS) for ^{4}He and Ne; sector field mass spectrometer (MAP 215-50) for ^{3}He, ^{4}He, ^{3}H (tritium).

6.3 Results for the Rauw fault

6.3.1 Groundwater flow and heat transport modelling results

Figure 6.7 shows results from the groundwater flow model: a) the hydraulic head distribution over the Nete catchment; b) the scatter plot of simulated equivalent vs observed hydraulic head observations. The model performance of the NAM model had a RMSE of 0.70 meters accounting for a total head loss of 46.5 meters. A forward particle tracking model run was performed to observe the advective travel flow paths from a location at the eastern side of the Rauw fault at several depths along the entire vertical model domain, as shown in Figure 6.8. Particles located in the Diest and younger formations travel in a downward direction crossing through the easternmost fault. When arriving in the block between that fault and the Rauw fault they start to travel upwards and along the fault due to the difference in hydraulic conductivity (lower across the fault) versus the formation they are located in. Particles that begin in the upper parts of the aquifer flow above the Rauw fault then travel downwards once they are at the western side of it; others flow through it and then continue their travel downwards similarly. Afterwards, particles begin traveling upwards most likely following the natural local groundwater system circulation being driven by the surface water networks, since there is no indication of other faults having a clear effect on the groundwater flow pattern. On the other hand, the flow of particles located in the Berchem formation does not appear to be strongly influenced by the Rauw fault, or any other fault, flowing close to the Boom Clay to be later discharged vertically in a more downstream location. The overall flow pattern is indicative that the Neogene aquifer consists of several local and intermediate flow systems conforming the general regional system.

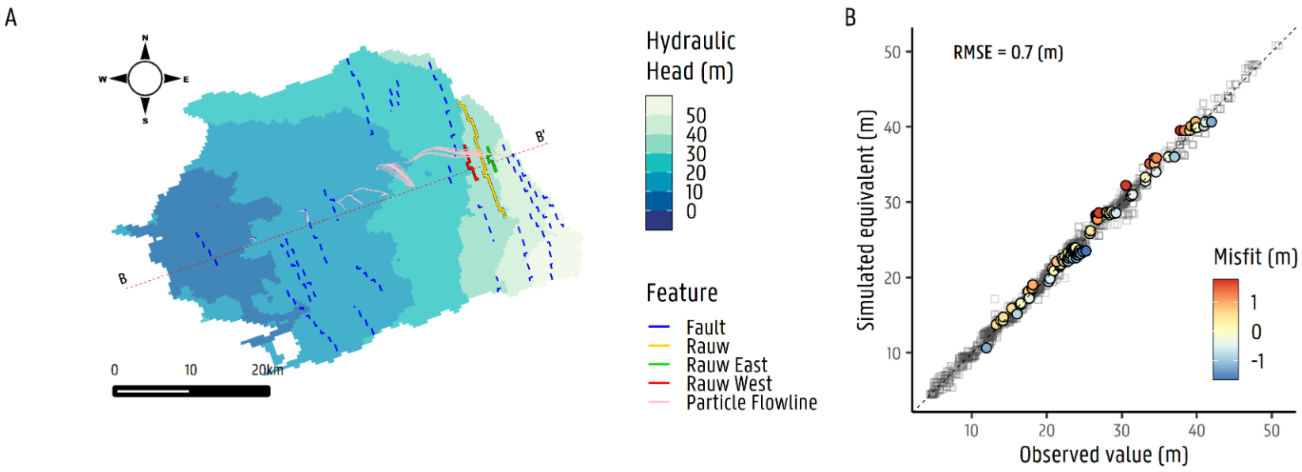

Figure 6.7 – (a) The hydraulic head distribution over the Nete catchment. (b) Scatter plot of observed hydraulic heads and simulated equivalents. Modified from Casillas-Trasvina et al. (in prep. a).

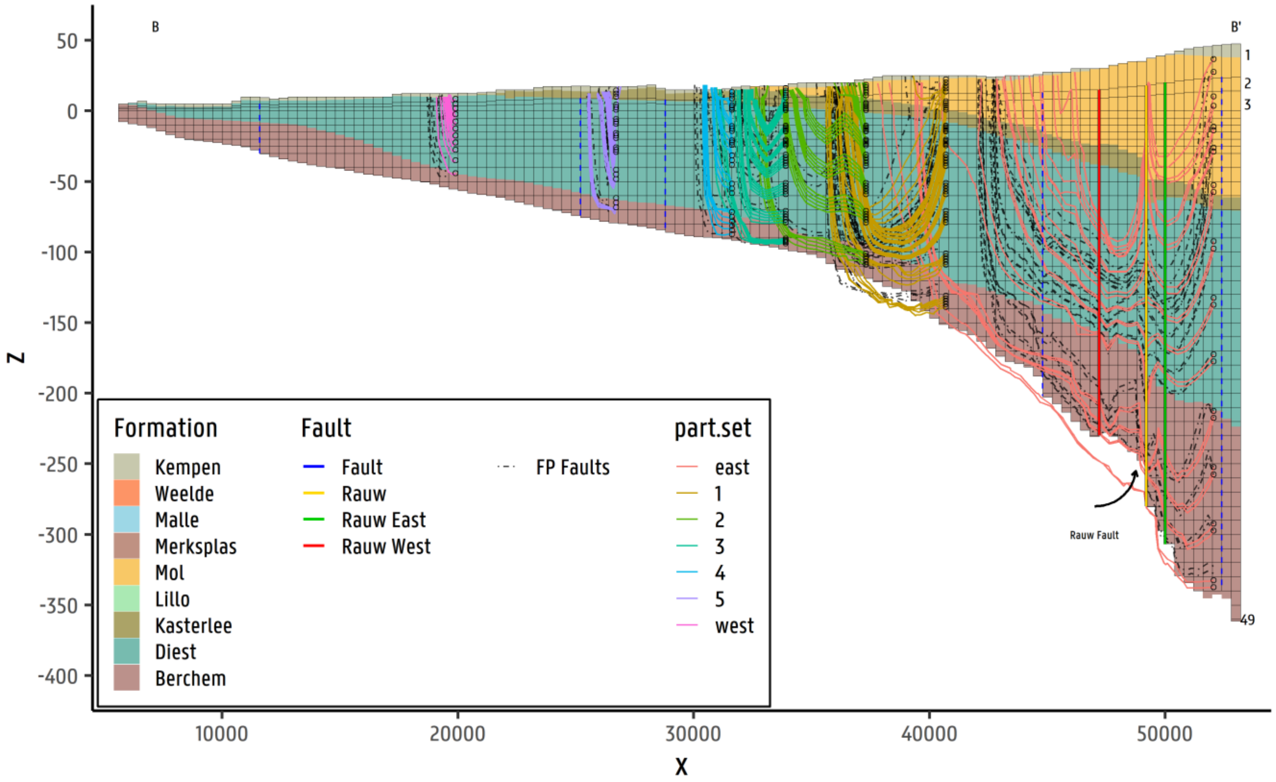

Figure 6.8 – Forward particle tracking using MODPATH. See text for detailed explanation. From Casillas-Trasvina et al. (submitted).

The groundwater flow and heat transport parameter composite scaled sensitivities (CSS) show that the flow parameters have a much larger effect on the model results than the temperature parameters implying their relevance to the produced results. Recharge and river conductance show the largest sensitivity, followed by saturated hydraulic conductivity of Diest, Mol, Quaternary, Kasterlee Clay (and vertical anisotropy) and Lillo Formations. The next most sensitive parameter is the hydraulic characteristic (d^{-1}) of the Rauw fault, confirming its role as a flow boundary. In terms of temperature, the Diest Formation thermal conductivity presents the highest sensitivity, given that most of the temperature profiles were taken at these depths. On the contrary, the Berchem Formation (Berchem & Voort), not having a large number of observations, presents relatively high sensitivity as well. Given that at these depths the magnitude of groundwater flow is very low (around $1x10^{-7}$- $1x10^{-5}$ m/d), the transport of heat is less advective, and more driven by thermal conduction.

The temperature distribution results from the heat-transport model are shown in Figure 6.9. In (a), a cross-section B-B' is shown, indicated in Figure 6.9b. Both figures are showing the spatial temperature distribution at the last transport step (i.e. October 2019) at the last stress period (i.e. monthly for the years 2001 to 2019) for the paleo-temperature heat-transport model. Figure 6.9a shows a distribution that closely relates to groundwater flow as seen in Figure 6.8, indicating the influence of advection. At the east of the Rauw fault colder water infiltrates, travels downwards and mixes with warmer groundwater from the bottom of the aquifer. Groundwater with a slightly higher temperature is transported upwards before penetrating the Rauw fault, however with most groundwater flowing across the fault (z = ca. -150 m a.s.l.). Then, adjacent to the Rauw fault, a portion of the groundwater flowing upwards overflows above it to then continue its flow direction downwards mixing again with colder infiltrated water at the west of the Rauw fault. Groundwater to the west of the Rauw fault then gets mixed with colder and younger infiltrated water reducing its temperature along the approximate flow direction (i.e. to the west) until the end of the fault block, to then continue flowing laterally to the west merging with another local flow system. This can be seen from Figure 6.9b, which displays the model layer 10, where groundwater temperature to the west of the Rauw fault zone is higher than to the east, given that it has already traveled from deeper in the aquifer and has already crossed the Rauw fault. Groundwater is being driven by groundwater abstraction, recharge and the surface water network into more local groundwater flow systems.

In the shallower parts of the aquifer ($z < -100$ m a.s.l.; Figure 6.9b) ‘spots’ with lower temperatures can be identified in the vicinity of other faults (i.e. from east to west: ‘HFB_094’, ‘HFB_089’, ‘HFB_129’; represented as blue dashed lines). These ‘spots’ correspond to the groundwater flow distribution producing local flow systems in the area formed by the relatively large density of rivers and canals. Even though the faults in the vicinity have a relatively low sensitivity (not shown), these might still have an effect on the distribution of temperature. In their review, Irvine et al. (2012) mention that although thermal properties might have low variations, as stated by Saar (2011), these variations might have a reasonable effect in the overall temperature distribution in sedimentary environments (Constantz et al., 2003; Hidalgo et al., 2009), such as the Neogene aquifer. On the other hand, in the deeper parts of the aquifer (near the bottom of the aquifer, Figure 6.9a) higher temperatures are present (close to the main source of heat to the aquifer). At these depths, groundwater flow magnitudes are low (~$1x10^{-7}$ m/d), which would indicate that the heat transport here would be most likely advection-driven. Although in some areas, surface water seems to have a strong influence driving deeper groundwater to the surface in combination with deep groundwater withdrawals.

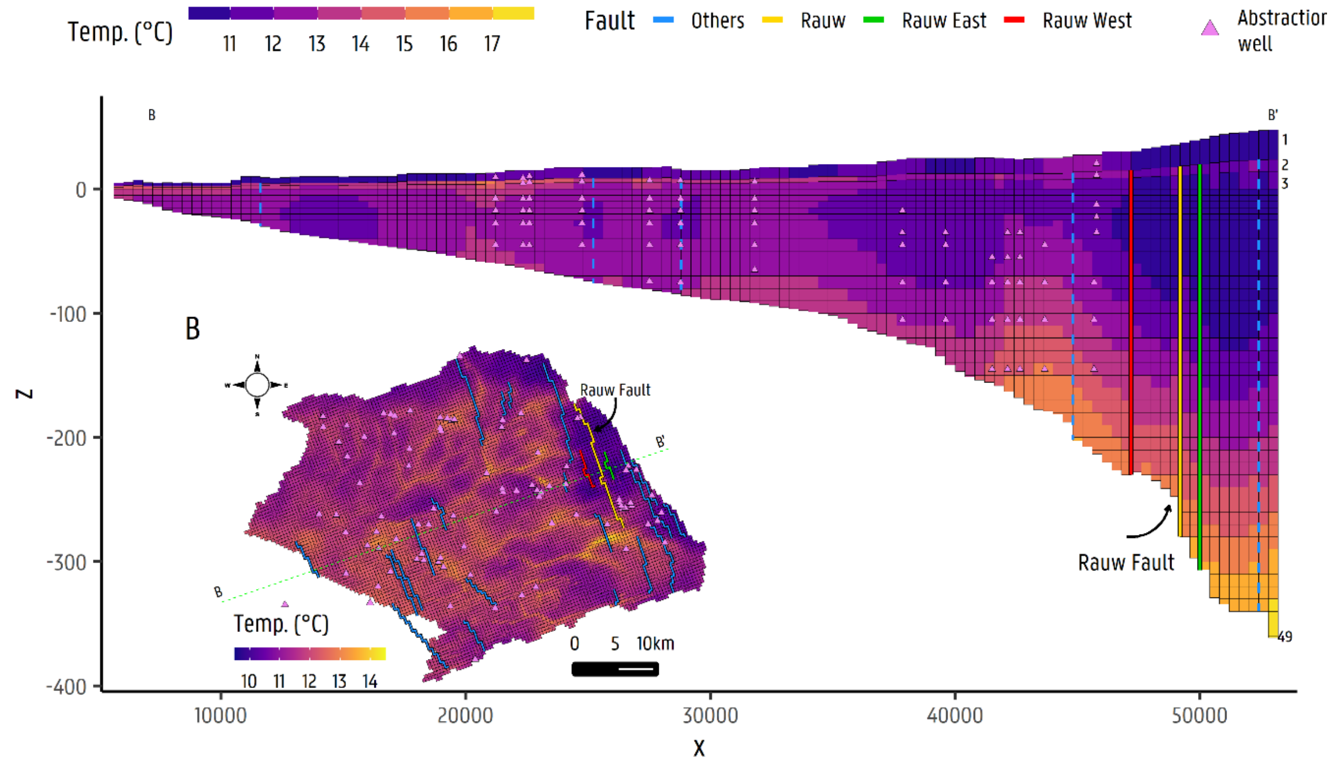

Figure 6.9 – Temperature distribution at the last transport step for the transport model in (a) cross section and (b) plan view from model layer 10. Modified from Casillas-Trasvina et al. (in prep. a).

6.3.2 Hydrochemistry, stable isotopes, radiocarbon and helium

6.3.2.1 Hydrochemistry

The well, screen depth, date, pH and EC values are shown in Table 6.1. For most of the samples, the error on the ionic balance was smaller than 5%, and in some cases even smaller than 2%. However, in some cases (denoted with * in the table) the error was higher than 5%, and up to 11%. For these cases, the $\Sigma c + \Sigma a < 5$meq/l (sum of anions + sum of cations), indicating that these are very weakly mineralized waters and this error may be acceptable (Walraevens, 2000). For 2 cases (denoted with ** in the table), the $\Sigma c + \Sigma a > 5$meq/l, and the error amounts 10%. The Stuyfzand (1986) classification was applied to the chemical data, included in Table 6.1. All the groundwater samples in the Neogene aquifer have Cl < 150 mg/l, indicating fresh/fresh-oligohaline waters (Codes F and g, respectively) and very soft to hard (* to 2). The groundwater sample taken from below the Boom Clay (R-54e), on the other hand, presents a value of 1790 mg Cl/l, and is classified as a brackish-salt water type (Code b).

Table 6.1 – Well ID, depth, geological formation, sampling date, pH, EC and water type for the various groundwater samples.

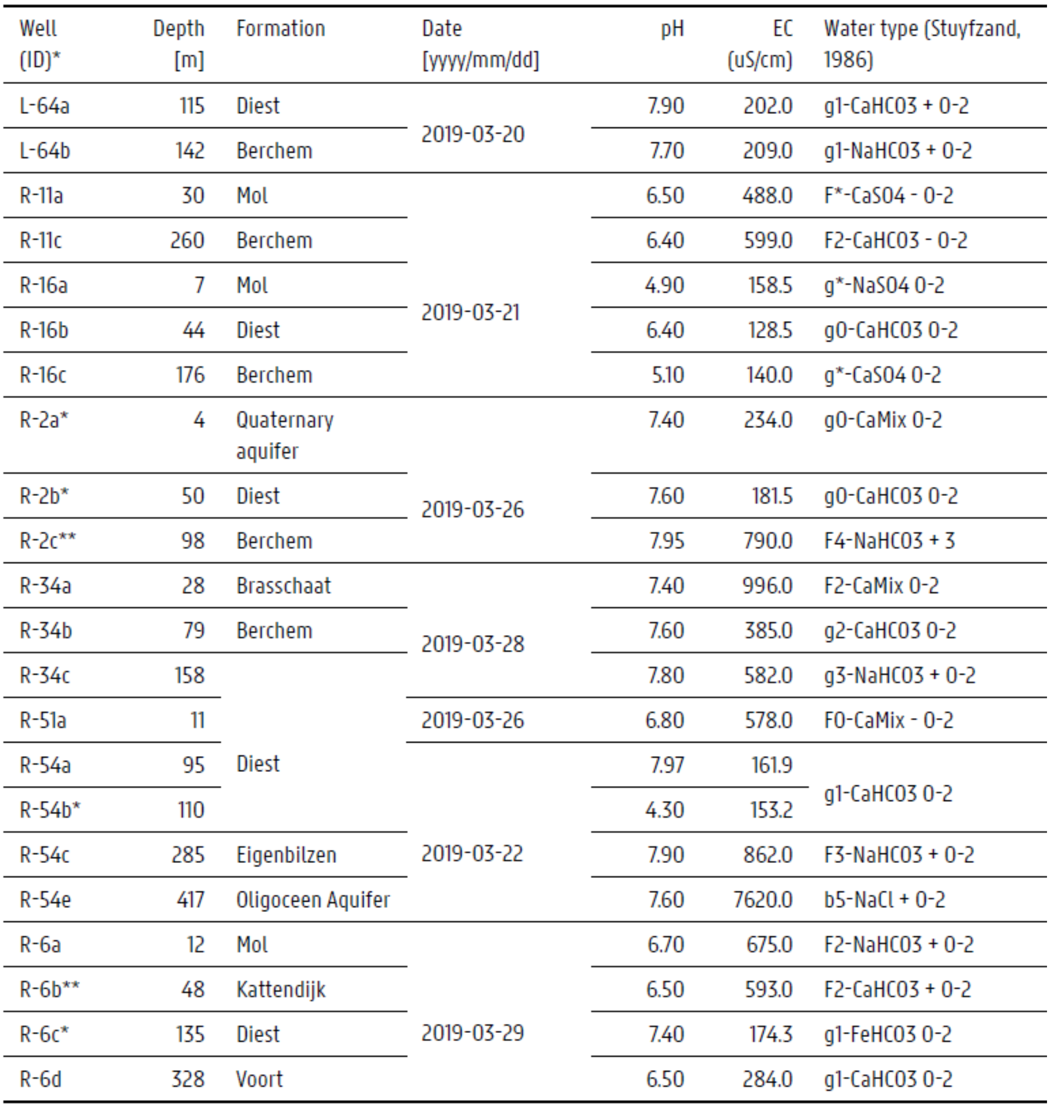

Well (ID)*	Depth [m]	Formation	Date [yyyy/mm/dd]	pH	EC (uS/cm)	Water type (Stuyfzand, 1986)
L-64a	115	Diest	2019-03-20	7.90	202.0	g1-CaHC03 + 0-2
L-64b	142	Berchem		7.70	209.0	g1-NaHC03 + 0-2
R-11a	30	Mol	2019-03-21	6.50	488.0	F*-CaS04 - 0-2
R-11c	260	Berchem		6.40	599.0	F2-CaHC03 - 0-2
R-16a	7	Mol		4.90	158.5	g*-NaS04 0-2
R-16b	44	Diest		6.40	128.5	g0-CaHC03 0-2
R-16c	176	Berchem		5.10	140.0	g*-CaS04 0-2
R-2a*	4	Quaternary aquifer	2019-03-26	7.40	234.0	g0-CaMix 0-2
R-2b*	50	Diest		7.60	181.5	g0-CaHC03 0-2
R-2c**	98	Berchem		7.95	790.0	F4-NaHC03 + 3
R-34a	28	Brasschaat	2019-03-28	7.40	996.0	F2-CaMix 0-2
R-34b	79	Berchem		7.60	385.0	g2-CaHC03 0-2
R-34c	158	Diest		7.80	582.0	g3-NaHC03 + 0-2
R-51a	11		2019-03-26	6.80	578.0	F0-CaMix - 0-2
R-54a	95		2019-03-22	7.97	161.9	g1-CaHC03 0-2
R-54b*	110			4.30	153.2	
R-54c	285	Eigenbilzen		7.90	862.0	F3-NaHC03 + 0-2
R-54e	417	Oligoceen Aquifer		7.60	7620.0	b5-NaCl + 0-2
R-6a	12	Mol	2019-03-29	6.70	675.0	F2-NaHC03 + 0-2
R-6b**	48	Kattendijk		6.50	593.0	F2-CaHC03 + 0-2
R-6c*	135	Diest		7.40	174.3	g1-FeHC03 0-2
R-6d	328	Voort		6.50	284.0	g1-CaHC03 0-2

The obtained results are in accordance with the published results of Coetsiers and Walraevens (2006) for the region. Groundwater sampled in shallow wells is mostly a CaMix or $CaSO_4^{2-}$ water type. According to Coetsiers and Walraevens (2006), pyrite oxidation in the unsaturated zone is responsible for the occurrence of these water types since calcite is not present here. The oxidation of pyrite plays an important role in the formation of acid sulfate soils resulting from drainage of lowlands (Appelo and Postma 2005). Next, the oxidation of organic matter increases the HCO_3^- content, leading to the occurrence of HCO3 water types. These become $CaHCO_3^-$ (still very soft) and then $NaHCO_3^-$ deeper in the aquifer, indicating the existence of cation exchange as a result of freshening. Most of this groundwater type indicates a positive cation exchange code which is mostly related to freshening conditions (Coetsiers et al., 2004). This evolution is presented in a Piper diagram in Figure 6.10. In the lower-left and central section of the Piper diagram, the evolution from $CaHCO_3^-$ to $NaHCO_3^-$ (from left to right, and up to down then right) indicates cation exchange as major freshening process. From the same figure we can see that the water below the Boom Clay has a different composition and is much more mineralised, with up to 10-50 times higher EC values (Table 6.1). In turn, the degree of mineralisation of the geothermal water is again much higher than the one from below the Boom Clay, with Cl-concentrations of up to 1x10^5 mg/l (Bos and Laenen, 2017). The geothermal water is also much more acid, with a pH value of around 5.4-5.5, as can also be observed from the very low alkalinity (Figure 6.10). Redox zones and water types are also shown in cross-section along the approximate flow direction in Figure 6.11.

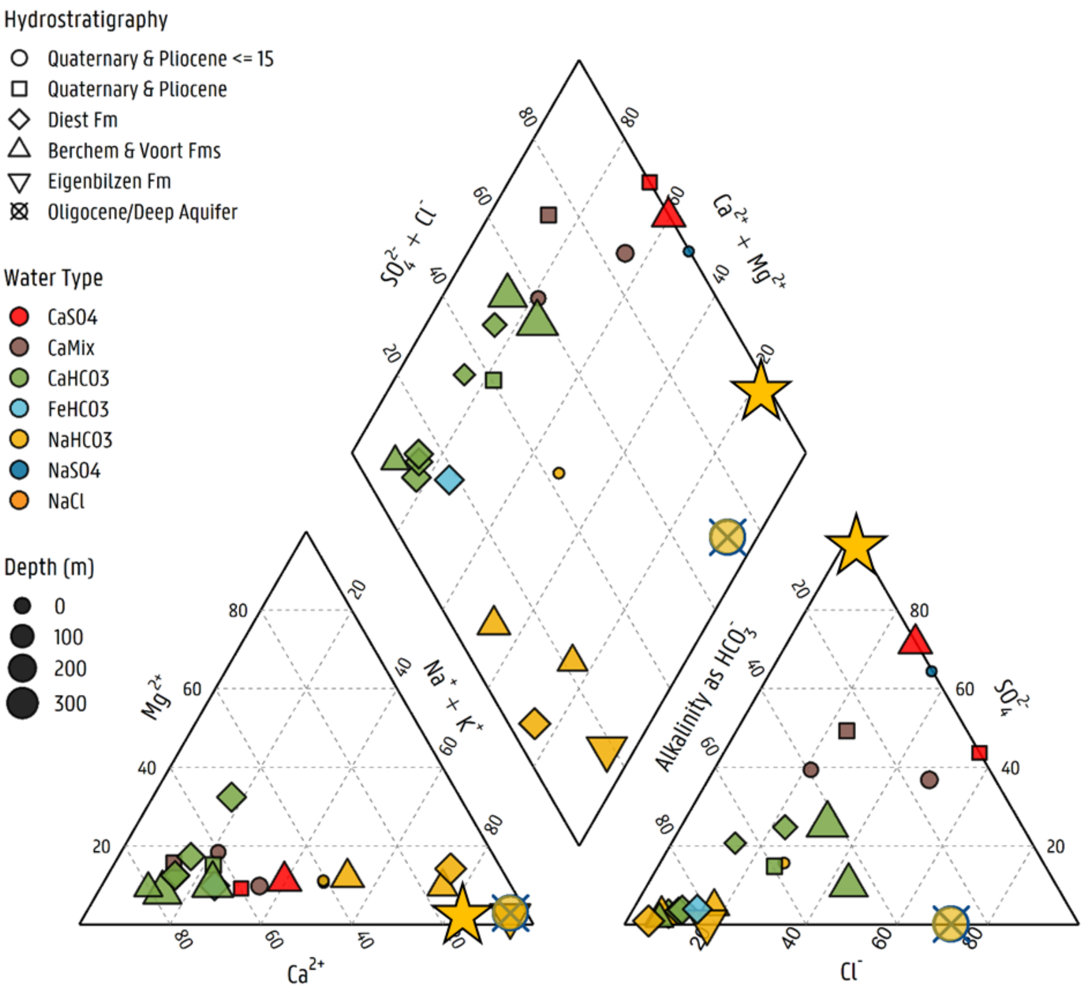

Figure 6.10 – Piper diagram indicating water type (major ions) for each groundwater well from 22 samples. The yellow star indicates the geothermal water. Freshening process is indicated by cyan arrow. Modified from Casillas-Trasvina et al. (in prep. b).

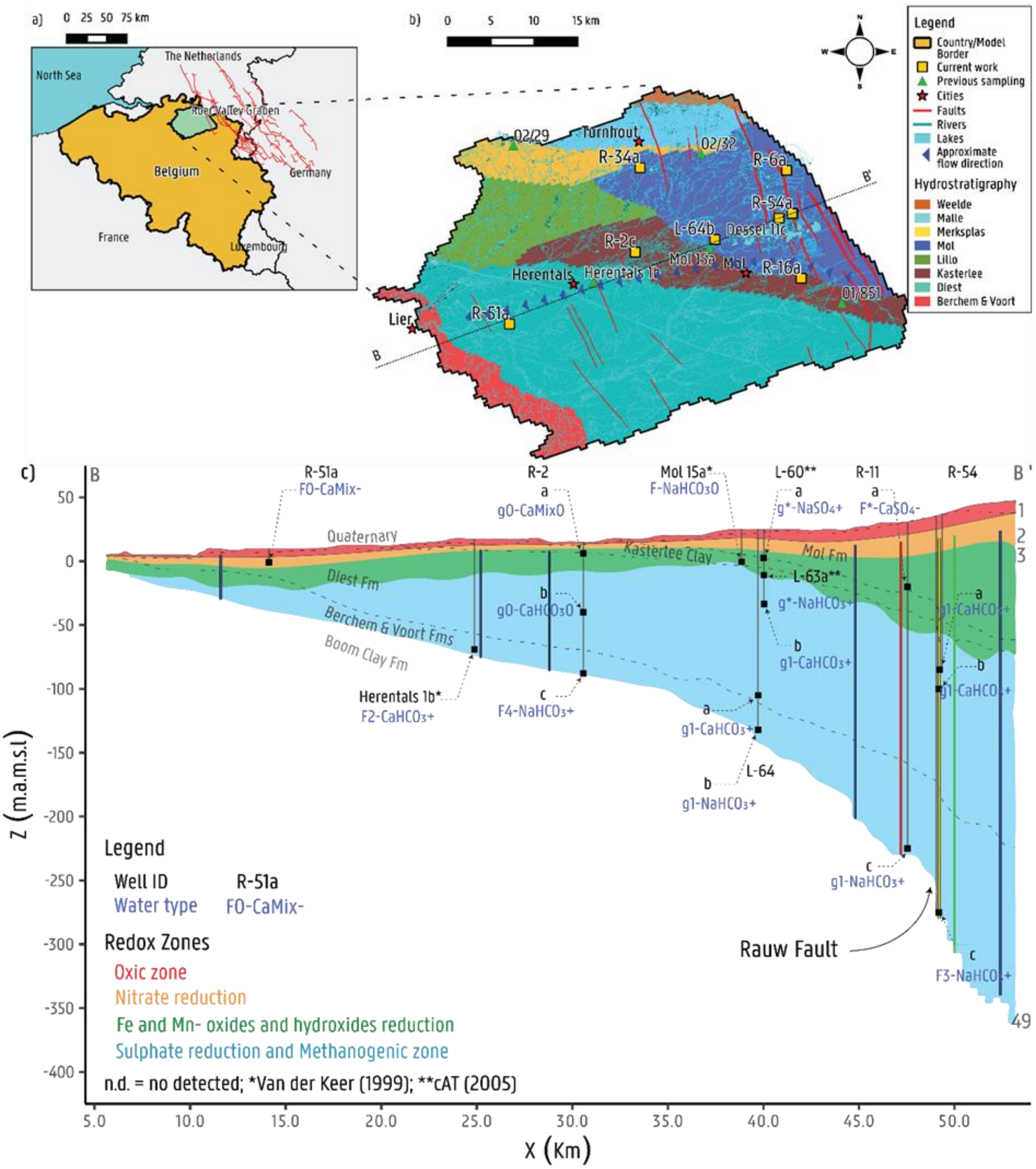

Figure 6.11 – (a) Location of the Nete catchment. (b) Geological map of the Nete catchment including sampling locations. (c) Cross-section along line B-B' in (b), showing the various stratigraphical units, faults, wells, water types and redox zones. From Casillas-Trasvina et al. (in prep. b).

6.3.2.2 Stable isotopes

Monthly data from the Global Network of Isotopes in Precipitation (GNIP) was retrieved from the International Atomic Energy Agency (IAEA)[2] website from 1980 to 1990, in order to have a reference isotope set for precipitation to compare the groundwater samples with. The data was collected from three stations: Beek, Liege and Gilzen-Rijen, being the closest stations to the study area. The GNIP data was used to construct the Local Meteoric Water Line (LMWL) providing the average relationship between hydrogen and oxygen stable isotopic compositions in precipitation.

A scatter plot of δ^{18}O and δ^{2}H of the groundwater samples (shown in Figure 6.12) is used to develop a groundwater isotopic regression line for the study area following $\delta D = 6.158 * \delta^{18}O - 2.72‰$ (R^2 = 0.76). The clustering of a large number of groundwater samples around the LMWL indicates that local modern meteoric water is a significant source of groundwater recharge (Coplen et al., 2011; Porowski, 2014). However, some of the samples fall slightly below both the GMWL and the LMWL showing lighter isotopes though still within the range measured from precipitation waters in GNIP stations. This might be attributed to the proximity of the evaporation source, the North Sea, ensuring that precipitation and recharge isotopes are characterized by these isotopes (Oiro et al., 2018). The groundwater isotopic regression line (GWL), which presents a lower slope than the GMWL and a negative intercept (intercept = -2.72, slope = 6.158), can explain this suggesting the effect of evaporative enrichment on groundwater (Wassenaar et al., 2011; Joshi et al., 2018). Additionally, the evaporative enrichment may be indicative of irrigation return flow which may infiltrate the groundwater in some areas (Coplen et al., 2011; Han and Zheng, 2018). Piezometers presenting more negative values than those on surface waters (from the same well, with shallower filters), i.e. R-34c, R-2c, R-16b, might be indicative of wells recharged with older ground waters (than modern/actual precipitation waters, from colder climatic conditions) with some mixing of younger with older groundwater inputs (still within the range of modern precipitation) (Clark and Fritz, 1997; Wassenaar et al., 2011). The Online Isotopes in Precipitation Calculator (OPIC) predicts average (based on interpolation of the isotopic composition of modern meteoric precipitation) values of -47‰ and -7.1‰ for δ^{2}H and δ^{18}O for the region, respectively, both in accordance with the analyzed values. The isotopic more positive/heavier values from piezometer R-34b could be associated to temperature effects on isotope fractionation and change in seasonality, being recharged from warmer local modern meteoric waters, (Clark and Fritz, 1997; Bäumle et al., 2019). On sample R-2b, to the left (or above) the meteoric water line, isotope exchange reactions, which occurred during the saline water evolution (in relation to perhaps R-2c, deeper), either caused δ^{18}O depletion, δ^{2}H enrichment, or both. Fritz and Frape (1982) in their works attributed enrichment in δ^{2}H to water participation in the process of hydration of primary silicates under closed-system conditions. However, if only depletion of δ^{18}O occurred, it could be explained if a large scale equilibrium between primary silicates and fluids occurred (Fritz and Frape, 1982). More observations might however be necessary to confirm this.

---

[2] https://www.iaea.org/services/networks/gnip

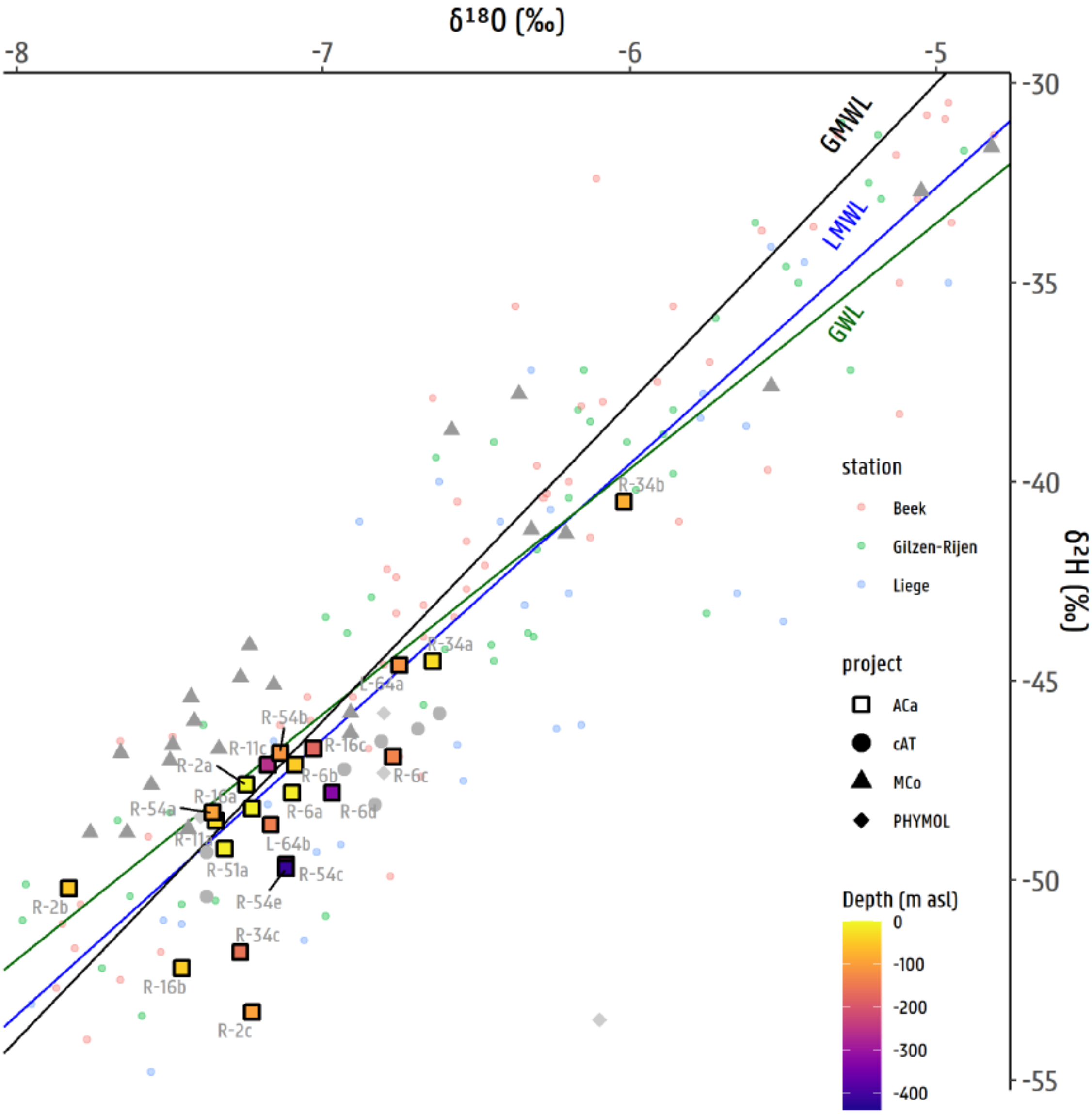

Figure 6.12 – Relation d2H and d18O in groundwater samples. The Global meteoric water line (GMWL, black line), groundwater line (GWL, green line), and local meteoric water line (LMWL, blue line) are indicated. Precipitation data are given by the small coloured dots (see legend for station name), as well as isotope data previously published for (parts of) the Neogene aquifer Modified from Casillas-Trasvina et al. (in prep. b).

6.3.2.3 Helium and radiocarbon

The results of the radiocarbon and helium analyses are shown in Figure 6.13. The ^{14}C ages are corrected ages according to the model from Coetsiers and Walraevens (2009). The helium data represent the fration that is due to the accumulation of radiogenic ^{4}He ($^{4}He_{rad}$) in groundwater. The plausibility of the corrected ^{14}C ages can be evaluated by analysing them in relation to the accumulation of the $^{4}He_{rad}$ concentration. This relation is shown in Figure 6.13. The $^{4}He_{rad}$ values generally agree with findings derived from corrected ^{14}C ages. Groundwaters with a NaHCO3 signature seem to have a larger accumulation of $^{4}He_{rad}$ (10^{-5} to 10^{-3} ccSTP/kg) indicating a longer residence time, which agrees with the older ^{14}C ages. Samples with this water type are found near the bottom of the Neogene aquifer, in the Berchem & Voort Sands or in the deepest parts of the Diest Sands where the groundwater velocities are considerably slower, in relation to the rest of the aquifer Casillas-Trasvina et al. (submitted). Unexpectedly, a similar ^{14}C age and similar $^{4}He_{rad}$ concentration is found for the NaCl water type in sample R-54e, which is situated in the Oligocene aquifer below the Boom Clay. As this water seems to be less diluted we would have expected a slightly older age and higher $^{4}He_{rad}$ concentration.

In the CaHCO3, CaMix, CaSO4 water types the $^{4}He_{rad}$ concentration is significantly lower, from 10^{-6} to 10^{-5} ccSTP/kg, which agrees with their ^{14}C model ages younger than 10 ka. In several samples, $^{4}He_{rad}$ could not be detected, most notably those near the surface with shallow filters located in Quaternary and Pliocene formations, or in the shallow parts of the Diest Sands. This may be due to the flux velocity at these depths where $^{4}He_{rad}$ concentrations get diluted (Jean-Baptiste et al., 2009). However, for samples L-64a, R-16c, R-2b, R-34b, R-51a, and R-54c, $^{4}He_{rad}$ concentrations were detected, together with the presence of ^{3}H (Figure 6.14; Casillas-Trasvina et al., in prep. b). Samples R-16c and R-51a both have large activities of ^{14}C (91 and 100 pMC, respectively) and ^{3}H (6.3 and 4.9 TU, respectively), very likely due to a significant component of modern recharge water. Given the depth at which R-16c is located (137 m) in the Berchem & Voort Sands, the occurrence of $^{4}He_{rad}$ ($1.9x10^{-6}$ ccSTP/kg) is expected given its proximity to the main He source in the Boom Clay at the bottom of the aquifer. However, for R-51a with a filter at 11 meters depth an accumulation of $7.2x10^{-6}$ ccSTP/kg of $^{4}He_{rad}$ was detected. This well is in the Diest Sands at the westernmost side of the study area (Figure 6.11b). Here, the Neogene aquifer thins to a thickness of 60 meters, leaving the filter of the well just a couple tens of meters above the Boom Clay. Samples L-64a, R-2b, R-34b, and R-54c have all ^{14}C values below 55 pMC and ^{3}H below 0.1 TU, indicating that a large portion of these waters were derived from tritium-free groundwater of the pre-bomb era with possibly a low fraction of post-bomb recharged groundwater (Mayer et al., 2014). The presence of $^{4}He_{rad}$ here restates the mixing of young and old groundwater occurring in this part of the Neogene aquifer. The accumulation of $^{4}He_{rad}$ increases with distance along the approximate flow direction: groundwater at R-54c in the easternmost location, the deepest filter within the Neogene aquifer, flows in a sub-regional, deep flow system, towards the direction of L-64b potentially receiving inputs from more recently infiltrated groundwater. This also agrees with the old ^{14}C age for this well (Figure 6.13).

The highest total ^{4}He concentration, which was measured in sample R-2c, is $3.3x10^{-3}$ ccSTP/kg, of which $3.2x10^{-3}$ ccSTP/kg is radiogenic $^{4}He_{rad}$. Even though this value is ca. 2 orders of magnitude larger than what is to be expected from solubility equilibrium with the atmosphere, it is still 2 orders of magnitude lower than the concentration measured in a shallow unconsolidated sedimentary aquifer in the Lower Rhine Embayment (LRE), Germany, close to a known fault (Bornheim Fault). There, concentrations of up to $1.7x10^{-1}$ ccSTP/kg were measured (total ^{4}He), and attributed to the upwelling of deep circulating fluids along sub-vertical faults. In the case of the Neogene aquifer in the Nete catchment, such high concentrations have not been observed yet.

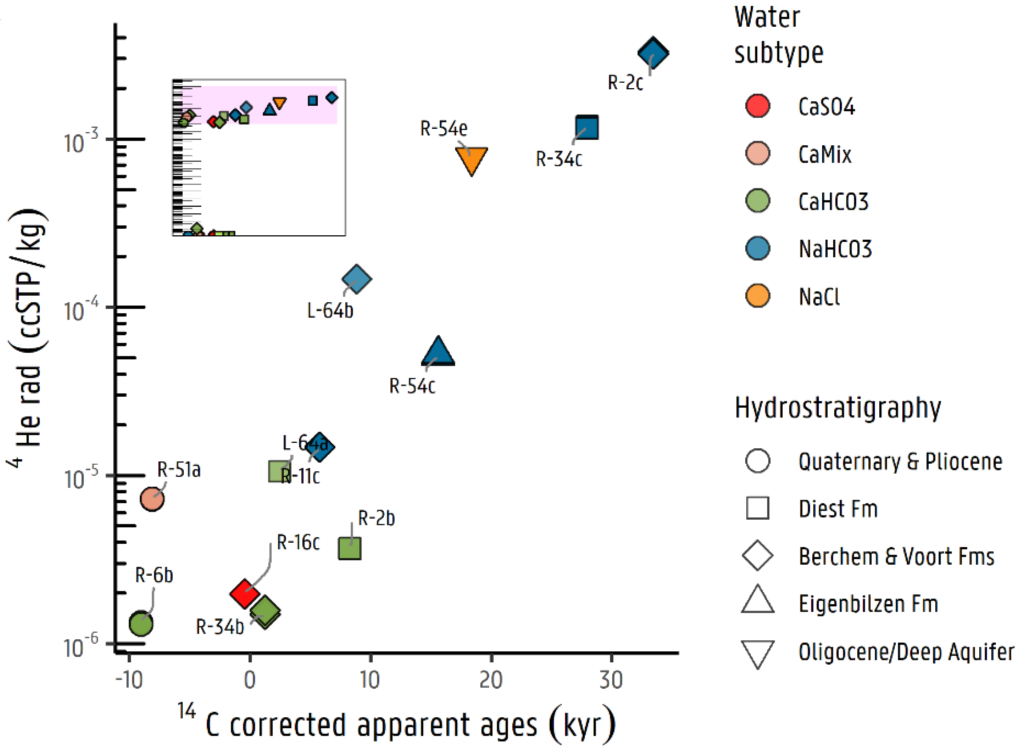

Figure 6.13 – Corrected radiocarbon ages (kyr) versus radiogenic ^{4}He concentrations for various samples. Water subtypes (Stuyfzand, 1986) and hydrostratigraphic formation are given. From Casillas-Trasvina et al. (in prep. b).

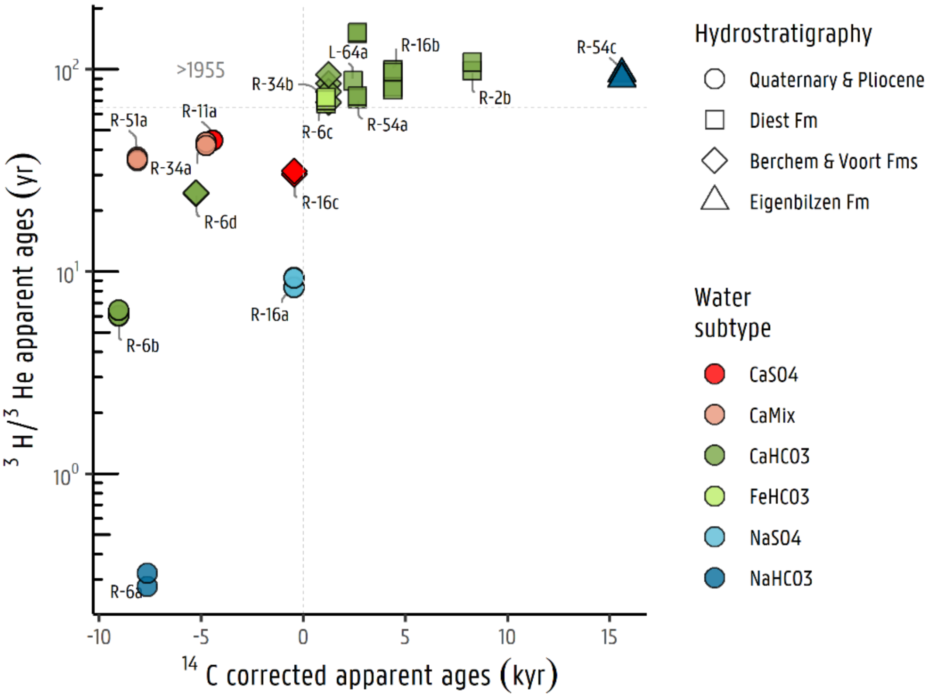

Figure 6.14 – Apparent ages of corrected ^{14}C vs ^{3}H/^{3}He indicating water subtypes following Stuyfzand (1986), and their hydrostratigraphic formation. From Casillas-Trasvina et al. (in prep. b).

6.3.3 Integration of results: hydraulic behaviour of the Rauw fault

The principal research questions for this case study were: i) if there is evidence of a no-flow behavior across and along the Rauw fault, and ii) if there indications of horizontal and/or vertical preferential flow patterns. With respect to the first sub question, whether the Rauw fault acts as a horizontal barrier or conduit for flow, the answer is rather straightforward. The flow model and heat transport model clearly show that the Rauw fault acts as a horizontal flow boundary, and even promotes the upwelling of deeper groundwater in the upper aquifer above the Boom Clay, east of the Rauw fault, up-gradient. This causes the typical expression of higher groundwater heads east of the fault, and (local) upwelling of warmer water where it is not expected, e.g., on the basis of the local drainage network. The quantitative assessment of the horizontal flow boundary properties of the Rauw fault is treated in the RESOURCE project, WP H3O-PLUS, Deliverable 3.2 (Vernes et al., 2021).

Concerning the second sub question, whether the Rauw fault may act as a vertical conduit for upward groundwater flow, there are no clear indications that would allow for a straightforward positive conclusion. Firstly, the overall major ion hydrogeochemistry suggests a simple freshening process from the top of the upper aquifer, leading to a stratification of groundwater types, where the water below the Boom Clay still has a NaCl water type signature and the shallow groundwater is a CaSO4 water type due to cation exchange and oxidation of pyrite. Compared to the waters above and below the Boom Clay, the geothermal water from the Balmatt site is an acid brine, and there are no indications for the existence of plumes of this water in the aquifers above and below the Boom Clay. As can be seen in the stable isotope data (^{18}O and ^{2}H), all waters have a strong meteoric signature, with indications for some samples to contain water that was recharged during a colder climate. The radiocarbon, helium and tritium data suggest the presence of strong mixing in the upper aquifer above the Boom Clay, especially in the shallower parts where sub regional and local groundwater flow systems meet. The picture of various flowpaths interfering is furthermore complicated by the Rauw fault and local groundwater abstractions. ^{14}C model ages of more than 10 ka are found in the NaHCO3 water types in the deeper parts of the Neogene aquifer, as well as for the NaCl type of water directly below the Boom Clay (R-54e). The ^{4}He analysis shows the presence of radiogenic ^{4}He in a significant number of samples, which is to be expected with the Boom Clay as a major source for alpha fluxes. Not surprisingly, the samples with a NaCl and NaHCO3 water type signature show the oldest ^{14}C ages and the highest $^{4}He_{rad}$ concentrations. These waters are in close contact with the Boom Clay. If deep geothermal waters would be conducted upward along the Rauw fault, one would expect ^{4}He concentrations which are 2 orders of magnitudes larger than is observed today (Gumm et al., 2016).

6.4 Application of Tool to the Rauw fault

6.4.1 Introduction

The 3D Groundwater Vulnerability tool is subsequently being tested for the NAM (Neogene Aquifer Model) area, including the additional knowledge that was obtained for the Rauw fault pilot site. The outcome of this assessment exercise can be found in the corresponding Excel-file GWV3D.

In the worksheet ‘Site details’ the coordinates of the Rauw fault site are given, as well as the proposed activity that is going to be screened for, i.e., geothermal energy. As indicated above, the focus of this project is the role of the Rauw fault as a potential barrier/conduit for vertical and horizontal flow.

The geological setting was already outlined in one of the previous paragraphs, and illustrated in Figure 6.1 to Figure 6.3. For the assessment, several geological formations are grouped according to the HCOV classification system (Deckers et al., 2019b), leading to a set of 11 geological units (see worksheet ‘Geological sequence’), of which the lowermost is the target unit (i.e., Lower Carboniferous limestones). This is unit A1320 in Table 6.2.

Table 6.2 – Correlation table between HCOV codes and units used in indicated figures.

HCOV code	*Figure 6.1*	*Figure 6.3*	*Figure 6.8*
A0100+A0200	All units above BM	-	All units
A0300	BM	-	-
A0400	OZ	-	-
A0500	MG	-	-
A0600+A0800	EZ+TT	-	-
A0900	KO	-	-
A1010	HA	-	-
A1020	HA	-	-
A1030+A1100	HE+C	-	-
A1310	P	Between Base Cretaceous and Top Carboniferous Limestone Group	-
A1320	P	Below Top Carboniferous Limestone Group	-

6.4.2 *Potential receptors: classification*

Receptor classification is done according to the worksheet ‘Method notes’ in the Excel-file. Only the Neogene aquifer (HCOV A0100+A0200) , coinciding with the NAM, is classified as an A receptor, which means that is an aquifer of primary importance as a groundwater resource with high flow potential and used intensively. The Oligocene Aquifer System (A0400) and the Ledo-Paniselian Brusselian Aquifer System and Ypresian Aquifer System (A0600+A0800) are classified as a B receptor, which means that they are aquifers of secondary importance with medium flow potential. Finally, the Palaeocene and Cretaceous Aquifer Systems (A1010 and A1030+A1100) are classified as C receptors, which means that these are aquifers of minor importance only, with medium to low flow potential. The aquitards are not considered as a groundwater resource and thus receive a D label: the Boom Aquitard (A0300), Bartoon Aquitard System (A0500), Ypresian Aquitard System (A0900), the Landenian and Heersiaan Aquitard System (A1020) and the Upper Carboniferous (A1310).

6.4.3 Hazard

Hazard refers to the energy-related activity, which in the Rauw fault pilot case is geothermal energy. According to the ‘Method notes’ this activity receives a release mechanism hazard (H1) rating of 3, as it goes together with local permeability enhancement in the deep subsurface (worksheet ‘Hazard assessment’). However, there are no indications for flow driven by a head gradient from source (target) to any of the receptors. Therefore, all units receive an H2 hazard rating of 1, except for the Carboniferous units which receive a rating of 2 because the head gradient is unknown. The corresponding overall hazard scoring and confidence level is given in the last two columns in the corresponding worksheet, taking into account the weighting factors.

6.4.4 Intrinsic vulnerability

Intrinsic vulnerability describes properties that relate to vertical and horizontal distance between source and receptor, and the amount of clay/mudstone in intervening units. It also considers the type of flow (high flow potential to zero flow potential) in the intervening units, the presence of faults cross-cutting the intervening units and thus connecting source and receptor, solution features and anthropogenic features. The large thickness of the Upper Carboniferous strata, their impermeable nature, and the distance between the Balmatt geothermal plant and the Rauw fault determines the rather low values for the first part of the intrinsic vulnerability assessment scores (see box ‘Intervening Units’ in worksheet ‘Vulnerability assessment’). Indeed, the dimension of the Upper Carboniferous causes a very large separation between the source and all receptors, the distance being largest for the Neogene aquifer above the Boom Aquitard. This results in a rating of 1 for vertical separation. Given the fact that the Rauw fault site is more than 2 km away from the Balmatt site, the rating for lateral distance is zero. Finally, all receptors are underlain by intervening units with more than 250 m of clay and/or mudstone (cumulative), which results in a rating of 1 for this item. The Upper Carboniferous alone already accounts for ca. 1900 m of mudstone; this estimate is based on the descriptive litho-logs in Bos and Laenen (2017). For the uppermost aquifer (the Neogene aquifer), the cumulative thickness of intervening clay/mudstone is even larger, given the presence of, e.g., Ypresian and Rupelian clays.

For the box ‘Receptor and Intervening Units’, we see a rather high scoring for the Neogene aquifer as far as the flow mechanism is concerned. As has been clearly illustrated in the results section of the pilot study, the flow potential is indeed high. This is not a surprise given the dominance of sand in this aquifer. The groundwater flow mechanism subsequently changes from high to medium to low flow potential with depth. This trend is justified given the fact that hydraulic conductivities gradually decrease with depth, as can be seen from the K-value inventory for the Campine area that was produced in the H3O-PLUS work package (WP3) of the GeoERA RESOURCE project (see Vernes et al., 2021). For the item ‘Faults cutting intervening units and receptor’ the rating of 3 is rather high, but is due to the fact that the presence of faults, such as the Rauw fault, is proven. However, the rating is not as high as 4 because for now there are no indications for these faults to be transmissive. Note that the weighting factor for faults is rather large, such that the final scoring for this item is also large.

Finally, the ratings for solution features and presence of mines close to the site are set to zero, for obvious reasons. Also, the rating for presence of boreholes is set to zero because none of these penetrate to a distance of less than 600 m from the source (top of the target = Lower Carboniferous).

If we neglect the Upper Carboniferous because it is not a groundwater resource, the highest intrinsic vulnerability score is obtained for the Neogene aquifer (score = 28), with the underlying aquifers being given the second highest score.

6.4.5 Output Risk

Combining the Intrinsic Vulnerability Score and the Hazard Score yields the final Specific Vulnerability Score (Table 6.3). This is highest for the Upper Carboniferous (SpecV = 198), but, as indicated above, this is not considered to be a groundwater resource. The second highest SpecV is obtained for the Neogene aquifer (SpecV = 84), while the other aquifers show slightly lower scorings. However, because the Neogene aquifer qualifies as an A receptor, a groundwater resource of primary importance, even this small vulnerability score leads to a risk classification of Medium/Low. The risk classification for all other aquifers is Low, because these are groundwater resources of secondary or less importance only.

Table 6.3 Risk group for each geological unit considered in the Rauw fault pilot.

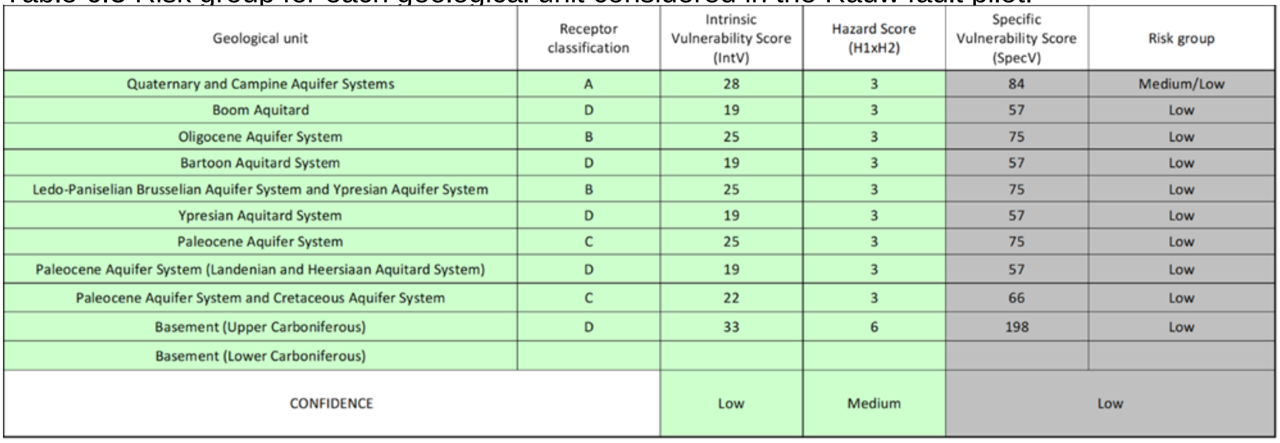

Geological unit	Receptor classification	Intrinsic Vulnerability Score (IntV)	Hazard Score (H1xH2)	Specific Vulnerability Score (SpecV)	Risk group
Quaternary and Campine Aquifer Systems	A	28	3	84	Medium/Low
Boom Aquitard	D	19	3	57	Low
Oligocene Aquifer System	B	25	3	75	Low
Bartoon Aquitard System	D	19	3	57	Low
Ledo-Paniselian Brusselian Aquifer System and Ypresian Aquifer System	B	25	3	75	Low
Ypresian Aquitard System	D	19	3	57	Low
Paleocene Aquifer System	C	25	3	75	Low
Paleocene Aquifer System (Landenian and Heersiaan Aquitard System)	D	19	3	57	Low
Paleocene Aquifer System and Cretaceous Aquifer System	C	22	3	66	Low
Basement (Upper Carboniferous)	D	33	6	198	Low
Basement (Lower Carboniferous)					
CONFIDENCE		Low	Medium	Low	

6.5 Discussion of the Rauw fault pilot

Application of the groundwater risk assessment tool suggests that geothermal activity at the Ballmat site near VITO (Figure 6.1) does not induce an increased risk for aquifer contamination from this type of activity, given the present configuration that was taken into account. We hypothesized that there was no increased potential for vertical flow of brines along the Rauw fault from the target units at more than 3000 m depth up to the various aquifers encountered in this part of the Campine Basin. The most vulnerable aquifer (an A receptor), i.e., the Quaternary and Campine Aquifer Systems (according to HCOV), also known as the Neogene aquifer (considered in the NAM model), shows a specific vulnerability score of 84, and thus ranks in the Medium/Low Risk group. The notion ‘Medium’ is added by default for type A-receptors. However, the threshold for the Medium/High Risk group is 250, which is three times higher than the current scoring. This low risk is primarily caused by the enormous vertical distance between the top of the target receptor (Lower Carboniferous), and the Neogene aquifer, i.e., more than 3000 m, and the large amount of intervening clay and mudstone layers, up to 2000 m. These properties of the geological sequence are fixed (together with flow potential), and will not change in an alternative assessment.

However, different scorings might be obtained for hazard assessment and intrinsic vulnerability, if values would be assigned differently. For instance, an alternative scenario can be explored with conservative parameterisation of the various fields in the assessment tool. If we assign a rating of 2 for head driven gradient in the hazard assessment, a rating of 4 for fault transmissivity (highest score), a rating of 3 for karst features in the subsoil (which is/might be the case for the Lower Carboniferous), a rating of 2 for known boreholes in the vicinity of the energy-related activity, the final Specific Vulnerability Score reaches 279 for the upper aquifer (Neogene aquifer/Quaternary and Campine Aquifer Systems), which is just above the threshold for Medium/High risk. All other aquifers would remain in the Low to Medium/Low Risk group. However, it has to be born in mind that this value (279) is the scoring based on a very conservative scenario, with the Rauw fault being included as transmissive feature. This assumption cannot be justified from the scientific basis set out in section 6.3.

7 Synthesis & outlook

The possible effects of deep energy related activities on groundwater resources have been studied for four pilot sites around Europe. The risks also have been assessed using the GWV 3D tools (Bianchi et al., 2021). Table 7.1 gives an overview of the pilots.

The Pannonian Basin is a large deep basin. It contains important aquifers for drinking water and thermal water. There also are hydrocarbon reservoirs and site for hydrothermal energy. The existing information in the Ölbö area has been integrated and based on this, the vulnerability of the groundwater resources for conventional oil and gas activities has been assessed in the GWV 3D tool. The outcome was that the groundwater resources in the Ölbö area have a Medium/low vulnerability for this type of deep energy related activity and the thermal waters a low vulnerability.

The Vale of Pickering pilot considers the potential extraction of shale gas from the Bowland Shale formation. The research conducted in response to proposals of shale gas exploration has been presented and the GWV 3D tool has been applied. The intrinsic vulnerability score for the primary aquifer is “Medium/high” and for the secondary aquifers “Medium/low”. The vertical separation from the target formation is large, but the presence of multiple faults within the area of interest increases the vulnerability of the shallow groundwater, especially in the worst-case scenario of vertical hydraulic gradients.

For the Dutch Pilot of Veghel, a characterization of the fault has been carried out which was limited by the fact that only 2D seismic data is available for this area. Furthermore, the water from the pumping wells of the Veghel well field has been sampled and analysed for chloride, methane, methane isotopes and gases. The flow pattern is influenced by the fault and this is reflected in differences in chloride concentration and groundwater age. We did find elevated ^{4}He and ^{3}He concentrations pointing to a 2.5% mantle contribution for the ^{4}He and 96% for the ^{3}He, but found no relation of the ^{3}He/^{4}He ratio with the distance to the fault or with the age of the water. This signal for a deep connection between crustal and mantle helium concentrations was not reflected in the methane origins.All methane was of biogenic origin and no indications exist for the upwelling of thermogenic methane from the deeper subsurface.
In addition to the Veghel pilot, work was done for two other Dutch pilots: Tilburg and Noord-Brabant. The Tilburg pilot shows the additional value of 3D seismic data for the analysis of faults resulting in locations of higher probability for hotspots with a connection with the deep subsurface, especially through the presence of linkage damage zones in the consolidated underlying Chalk formation. The groundwater sampling of the Noord-Brabant pilot for methane and helium can be used as a baseline for future activities. No evidence for thermogenic methane was found although elevated ^{4}He concentrations indicate the presence of the regional discharge of paleowater from deeper aquifers.

For the Rauw fault groundwater flow and transport modelling has been carried out to establish the hydraulic resistance of the fault for lateral flow. Groundwater samples have been taken and the hydrochemistry and stable isotopes have been analysed. The analysis gave no indication for vertical connection with the deep subsurface along the fault or elsewhere in the pilot area. The application of the GWV 3D tool resulted in the lowest risk class for all aquifers (see Table 7.1).

Table 7.1 Aspects of the VoGERA pilots and vulnerabilities from the application of the GWV 3D tool for the water resources of primary importance (receptor class A) and secondary importance (receptor class B).

Pilot	**Pannonian Basin**	**Vale of Pickering**	**Veghel fault**	**Rauw fault**
Aspect	**Hungary**	**United Kingdom**	**Netherlands**	**Belgium**
Existing groundwater use	Drinking, thermal	Drinking	Drinking, agriculture	Drinking
Existing energy activities	Geothermal, gas	Conventional gas	-	Geothermal
Faults present	yes	yes	yes	yes
Solution features	no	yes	unknown	unknown
GWV 3D				
Target	Conventional oil/gas	Shale gas	Geothermal	Geothermal
Max. vulnerability A receptor	Medium/low: 61	Medium/high: 328	Medium/low: 84	Medium/low: 84
Max. vulnerability B receptor	Low: 63	Medium: 336	Low: 66	Low: 75

The results of the research carried out for the pilots indicated that there is no direct evidence for pathways from the deep subsurface to the groundwater resources, that could lead to deterioration of these resources in case energy related activities would be started in the deep subsurface. However, hotspots with a direct connection to the deep subsurface have been reported in the literature (Groß Gerau, Australia) and in the Dutch pilot an elevated ^{3}He/^{4}He ratio in the groundwater of the tectonically active Roer Valley Graben indicates a mantle contribution of 2.5% for ^{4}He.

The pilot studies have focussed on the geological pathways and have not addressed anthropogenic pathways like:

- Well integrity;
- Abandoned boreholes that have not been sealed properly;
- Activities at the surface (e.g. spilling of fracking fluids during installation).

We alos did addresss the risks associated with induced seismicity. The hypothesis that the anthropogenic pathways pose higher risks than the natural geological pathways could not be verified for the pilots as we did not study the anthropogenic pathways or deduced effects. The results from the GWV3D tool indicate medium to low geological vulnerability for type A receptors for all of the pilot studies based on an assessment of the hydrogeological buildup of the pilot areas.

8 References

Al-Jubori, A., Johnston, S., Boyer, C., Lambert, S.W., Bustos, O.A., Pashin, J.C., Wray, A. (2009) Coalbed Methane: Clean Energy for the World, Oilfield Review, Volume 21, Number 2, Pages 4-13.

Allen, D. J., Brewerton, L. J., Coleby, L. M., Gibbs, B. R., Lewis, M. A., MacDonald, A. M., Wagstaff, S.J., Williams, A.T. (1997). The physical properties of major aquifers in England and Wales (Publication - Report). Retrieved from http://nora.nerc.ac.uk/id/eprint/13137/.

Aller, L., Bennett, T., Lehr, J.H., Petty, R.J. (1985) DRASTIC: A Standardized System for Evaluating Ground Water Pollution Potential Using Hydrogeologic Settings, EPA/600/2-85/018, United States Environmental Protection Agency, Robert S. Kerr Environmental Research Laboratory, Ada OK, USA.

Andrews, J. N., Burgess, W. G., Edmunds, W. M., Kay, R. L. F., Lee, D. J. (1982) The thermal springs of Bath, Nature, Volume 298, Pages 339-343.

Andrews, I. J. (2013). The Carboniferous Bowland Shale gas study: geology and resource estimation.

Appelo, C.A.J., Postma, D. (2005) Geochemistry, groundwater and pollution. In: Petroleum review, 2nd edn. A.A. Balkema Publishers, LeidenRotterdam, Netherlands.

Assonov, S., Fajgelj, A., Hélie, J.F., Allison, C., Gröning, C. (2020) Characterisation of new reference materials IAEA-610, IAEA-611 and IAEA-612 aimed at the VPDB δ13C scale realisationwith small uncertainty. Rapid Communications Mass Spectrometry, 35, e9014, https://doi.org/10.1002/rcm.9014

Banks, E.W., Hatch, M., Smith, S., Underschultz, J., Lamontagne, S., Suckow, A., Mallants, D. (2019) Multi-tracer and hydrogeophysical investigation of the hydraulic connectivity between coal seam gas formations , shallow groundwater and stream network in a faulted sedimentary basin. Journal of Hydrology 578: 124132. https://doi.org/10.1016/j.jhydrol.2019.124132.

Battle-Aguilar, J., Banks, E.W., Batelaan, O., Kipfer, R., Brennwald, M.S., Cook, P.G. (2017) Groundwater residence time and aquifer recharge in multilayered, semi-confined and faulted aquifer systems using environmental tracers. Journal of Hydrology 546: 150–165. https://doi.org/10.1016/j.jhydrol.2016.12.036

Bäumle, R., Himmelsbach, T., Noell, U. (2019) Hydrogeology and geochemistry of a tectonically controlled, deep-seated and semi-fossil aquifer in the Zambezi Region (Namibia). Hydrogeology Journal 27:885–914. https://doi.org/10.1007/s10040-018-1896-x.

Barker, J.F., Fritz, P. (1981). Carbon isotope fractionation during microbial methane oxidation. Nature 293, 289-291.

Bearcock, J.B., Smedley, P.L., Milne, C.J (2015) Baseline groundwater chemistry: the Corallian of the Vale of Pickering, Yorkshire. BGS Open Report, OR/15/048. Retrieved September 17, 2018, from http://nora.nerc.ac.uk/id/eprint/511547/.

Bedekar, V., Morway, E., Langevin, C., Tonkin, M. (2016) MT3D-USGS version 1: A U.S. Geological Survey release of MT3DMS updated with new and expanded transport capabilities for use with MODFLOW. Tech Methods 84. doi: 10.3133/tm6A53.

Beerten, K., De Craen, M., Wouters, L. (2013) Patterns and estimates of post-Rupelian burial and erosion in the Campine area, north-eastern Belgium. Physics and Chemistry of the Earth 64, 12–20.

Bell, R.A., Darling, W.G., Manamsa, K., Dochartaigh. B. É. Ó. (2016) The Baseline Concentrations of Methane in Great British Groundwater - the National Methane Baseline Survey. British Geological Survey Open Report, OR/15/071. 45pp. Retrieved September 17, 2018, from http://nora.nerc.ac.uk/id/eprint/514557/.

Bell, R. A., Darling, W. G., Ward, R. S., Basava-Reddi, L., Halwa, L., Manamsa, K., Dochartaigh, B.E.Ó. (2017). A baseline survey of dissolved methane in aquifers of Great Britain. Science of The Total Environment, 601–602, 1803–1813. https://doi.org/10.1016/j.scitotenv.2017.05.191.

Bense, V.F., van Balen, R.T., de Vries, J.J. (2003) The impact of faults on the hydrogeological conditions in the Roer Valley Rift System: an overview, Netherlands Journal of Geosciences, Vol. 82, No. 1, Pages 41-54.

Bense, V., Gleeson, T., Loveless, S., Bour, O., Scibek, J. (2013) Fault zone hydrogeology, Earth-Science Reviews, Vol. 127, Pages 171-192. https://doi.org/10.1016/j.earscirev.2013.09.008

Bense, V. F., & Person, M. A. (2006). Faults as conduit-barrier systems to fluid flow in siliciclastic sedimentary aquifers. Water Resources Research, 42(5).

Bhutto, A.W., Bazmi, A.A., Zahedi, Gholam, r. (2013) Underground coal gasification: From fundamentals to applications, Progress in Energy and Combustion Science Vol. 39, Pages: 189-214.

Bianchi, M., Zaadnoordijk, W.J., Szalkai, Á., Slenter, C., Beerten, K. (2021) Technical report on the common methodology for characterizing the vulnerability of shallow groundwater to deep industrial activities and methodology evaluation, GeoERA Groundwater project #4 VoGERA, deliverable D4.2.

Birdsell, D. T., Rajaram, H., Dempsey, D., Viswanathan, H. S. (2015) Hydraulic fracturing fluid migration in the subsurface: A review and expanded modeling results, Water Resources Research, Volume 51, Pages 7159–7188, doi:10.1002/2015WR017810.

Blinderman, M.S., Jones, R.M. (2002) The Chinchilla IGCC Project to Date: UCG and Environment, 2002 Gasification Technologies Conference, San Francisco, USA, October 27-30, 2002.

Bos, S., Laenen, B. (2017) Development of the first deep geothermal doublet in the Campine Basin of Belgium. European Geologist 43, 16-20.

Broers, H.P. and J. de Weert (2015). Dating for drinking water production: isotopes and noble gases in the mixed water of Brabant water (In Dutch). Deltares report 1208195-000.

Broers, H.P., J. Sültenfuß, W. Aeschbach, A. Kersting, A.Menkovich, J. de Weert and J. Castelijns (2021a). Paleoclimate signals and groundwater age distributions from 39 public water works in the Netherlands, insights from noble gases and carbon, hydrogen and oxygen isotope tracers. Water Resources Research, doi:10.1029/2020WR029058.

Broers, H.P., Kivits, T., Hinsby, K. (2021b). Investigation of age distributions in water supply wells with long screens and recommendations for application of tracers and models mainly for estimating groundwater ages between 100 and 1000 years. Deliverable 6.4, GeoERA HOVER.

Broers, H.P., Zaadnoordijk, W.J., Berendrecht, W.L. (2021c) Introducing the GeoERA Groundwater Measurements Viewer: analyzing groundwater depletion signals in the Roer Valley Graben. Deliverable 3.7, GeoERA RESOURCE.

Buma, J., Reindersma, R. (2021). Deliverable 3.4, Harmonisation of volumes, water balances and recharge and discharge fluxes. GeoERA RESOURCE.

Burton, E., Friedmann, J., Upadhye, R. (2007) Best Practices in Underground Coal Gasification. Lawrence Livermore National Laboratory, Livermore CA, USA.

Carey, M. A., Chadha, D. (1998). Modelling the hydraulic relationship between the River Derwent and the Corallian Limestone aquifer. Quarterly Journal of Engineering Geology and Hydrogeology, 31(1), 63–72. https://doi.org/10.1144/GSL.QJEG.1998.031.P1.06.

Casillas-Trasvina, A. (2019) Joint inversion of physical and chemical state variable data within a multi-model subsurface hydrology framework. PhD Research Plan. Universiteit Gent, 21 pp.

Casillas-Trasvina, A., Rogiers B., Beerten, K., Wouters, L., Walraevens, K. (submitted) Exploring the hydrological effects of normal faults at the boundary of the Roer Valley Graben in Belgium using a catchment-scale groundwater flow model.

Casillas-Trasvina, A., Rogiers B., Beerten, K., Wouters, L., Walraevens, K. (in prep a) Characterizing groundwater heat-transport in a complex Low Land aquifer using paleo-temperature reconstruction, satellite data, temperature-depth profiles, and numerical models.

Casillas-Trasvina, A., Rogiers B., Beerten, K., Wouters, L., Walraevens, K. (in prep b) Using noble gases, tritium, carbon-14 and other hydrogeochemical evidence to evaluate the groundwater age distribution: the case of the Neogene aquifer, Belgium.

Clark, I., Fritz, P. (1997) Environmental Isotopes in Hydrogeology. Lewis Publishers, New York, USA.

Coetsiers, M. (2007) Onderzoek naar de hydrogeologische en hydrochemische toestand van de Neogene Aquifer in Vlaanderen met behulp van modellering en isotopen hydrochemie. PhD thesis, Ghent University, Ghent, Belgium.

Coetsiers, M., Van Camp, M., Walraevens, K. (2004) Influence of the former marine conditions on groundwater quality in the Neogene phreatic aquifer, Flanders. Proceedings 18th Sea Water Intrusion Meeting (SWIM), Cartagena (Spain) 499–509

Coetsiers, M., Walraevens, K. (2006) Chemical characterization of the Neogene Aquifer, Belgium. Hydrogeology Journal 14:1556–1568. https://doi.org/10.1007/s10040-006-0053-0

Coetsiers, M., Walraevens, K. (2009) A new correction model for14C ages in aquifers with complex geochemistry - Application to the Neogene Aquifer, Belgium. Applied Geochemistry 24:768–776. https://doi.org/10.1016/j.apgeochem.2009.01.003

Constantz, J., Cox, M.H., Su, G.W. (2003) Comparison of Heat and Bromide as Ground Water Tracers Near Streams. Ground Water 41:647–656. doi: 10.1111/j.1745-6584.2003.tb02403.x

Coplen, T.B., Herczeg, A.L., Barnes, C. (2011) Isotope Engineering—Using Stable Isotopes of the Water Molecule to Solve Practical Problems. Environmental Tracers in Subsurface Hydrology 79–110. https://doi.org/10.1007/978-1-4615-4557-6_3.

Council of Canadian Academies (2014) Environmental Impacts of Shale Gas Extraction in Canada. Ottawa (ON): The Expert Panel on Harnessing Science and Technology to Understand the Environmental Impacts of Shale Gas Extraction, Council of Canadian Academies, Ottawa, Canada.

Davies, Richard J., Almond, Sam, Ward, Robert S., Jackson, Robert B., Adams, Charlotte, Worrall, Fred, Herringshaw, Liam G., Gluyas, Jon G., Whitehead, Mark A. (2014) Oil and gas wells and their integrity: Implications for shale and unconventional resource exploitation, Marine and Petroleum Geology, Volume 56, Pages 239-254, http://dx.doi.org/10.1016/j.marpetgeo.2014.03.001.

Davies, R.J., Almond, S., Ward, R.S., Jackson, R.B., Adams, C., Worrall, F., Herringshaw, L.G., Gluyas, J.G., Whitehead, M.A. (2015) Reply: “Oil and gas wells and their integrity: Implications for shale and unconventional resource exploitation”, Marine and Petroleum Geology, Volume 59, Pages 674-675, http://dx.doi.org/10.1016/j.marpetgeo.2014.07.014.

Deckers, J., De Koninck, R., Bos, S., Broothaers, M., Dirix, K., Hambsch, L., Lagrou, D., Lanckacker, T., Matthijs, J., Rombaut, B., Van Baelen, K., Van Haren, T. (2019a) Geologisch (g3dv3) en hydrogeologisch (h3d) 3D-lagenmodel van Vlaanderen. Studie uitgevoerd in opdracht van: Vlaams planbureau voor omgeving (departement omgeving) en vlaamse milieumaatschappij.

Deckers, J., De Koninck, R., Rombaut, B. (2019b) Update Hydrogeologische Codering van Vlaanderen: HCOV-versie 2. Studie uitgevoerd in opdracht van: Vlaamse Milieumaatschappij 2019/RMA/R/1899, 21p. + bijlagen.

De Ridder, N.A., Hondius, P., Hellings, A.J. (1967) Hydrogeological Investigations of the Peel Region and Its Environs, Technical Bulletin 48, Institute for Land and Water Management Research, Wageningen, the Netherlands.

DiCiacca, A. (2020) Spatially distributed recharge and groundwater – surface water interactions in groundwater models : from the field to the catchment scale. KU Leuven.

DiGulio, Dominic C., Jackson, Robert B. (2016) Impact to Underground Sources of Drinking Water and Domestic Wells from Production Well Stimulation and Completion Practices in the Pavillion, Wyoming, Field, Environmental Science & Technology, Volume 50, Number 8, Pages 4524-4536, https://doi.org/10.1021/acs.est.5b04970.

Environment Agency, n.d. 2017. Aquifer Designations [Online]. http://apps.environment-agency.gov.uk/wiyby/117020.aspx. Accessed (11/12/18).

Evans, D. J., Bateman, M.D., Roberts, D.H., Medialdea, A. , Hayes, L. , Duller, G.A., Fabel, D., Clark, C.D. (2017), Glacial Lake Pickering: stratigraphy and chronology of a proglacial lake dammed by the North Sea Lobe of the British–Irish Ice Sheet. J. Quaternary Sci., 32: 295-310. doi:10.1002/jqs.2833.

Fairley, J., Heffner, J., Hinds, J. (2003) Geostatistical evaluation of permeability in an active fault zone, Geophysical Research Letters, Volume 30, Number 18, 1962, doi:10.1029/2003GL018064.

Finkenrath M, Pazzi S, D'Ercole M. (2009) Status and technical challenges of advanced Compressed Air Energy Storage (CAES) technology. In: Int. workshop on environment and alternative energy, 2009.

Fisher, Kevin, Warpinski, Norm (2011) Hydraulic Fracture-Height Growth: Real Data, SPE 145949, Society of Petroleum Engineers Annual Technical Conference and Exhibition, Denver, Colorado, USA, 30 October–2 November 2011.

Flewelling, S.A., Sharma, M. (2014) Constraints on upward migration of hydraulic fracturing fluid and brine. Groundwater, Volume 52, Number 1, Pages 9–19, DOI:10.1111/gwat.12095.

Foley, A., Cachandt, G., Franklin, J., Willmore, F., Atkinson, T. (2012) Tracer tests and the structure of permeability in the Corallian limestone aquifer of northern England, UK. Hydrogeology Journal, 20(3), 483–498. https://doi.org/10.1007/s10040-012-0830-x.

Ford, J.R., Hughes, L., Burke, H.F., Lee, J.R. (2015) The Vale of Pickering: an initial summary of the Quaternary/superficial geology and data holdings. BGS Open Report, OR/15/064. Retrieved September 17, 2018, from http://nora.nerc.ac.uk/id/eprint/512437/.

Fossen, H., Rotevatn, A. (2016) Fault linkage and relay structures in extensional settings—A review. Earth-Science Reviews, 154, 14–28. doi:10.1016/j.earscirev.2015.11.014.

Freundt, F. (2017). Application of Helium Isotopes in Shallow Groundwaters for Geothermal Energy Exploration in the Upper Rhine Graben. Dissertation submitted to the Combined Faculties for the Natural Sciences and for Mathematics of the Ruperto-Carola University of Heidelberg, Germany for the degree of Doctor of Natural Sciences

Friedmann, S. J., Upadhye, R., Kong, F-M (2009) Prospects for underground coal gasification in carbon-constrained world, Energy Procedia, Volume 1, Pages 4551-4557, doi:10.1016/j.egypro.2009.02.274.

Fritz, P., Frape, S.K. (1982) Saline groundwaters in the Canadian Shield - A first overview. Chemical Geology 36:179–190. https://doi.org/10.1016/0009-2541(82)90045-6.

Fülöp, J. 1990: Magyarország geológiája. Paleozoikum I. (Geology of Hungary. Palezoicum I., In Hungarian), Magyar Állami Földtani Intézet, 325 p. Budapest, Hungary

Gallagher, D., McGee, E.J., Kalin, R.M., Mitchell, P.I. (2000) Performance of Models for Radiocarbon Dating of Groundwater: An appraisal using selected Irish aquifers. Arizona Board of Regents on behalf of the University of Arizona 42:235–248.

Gardner, W. P., Harrington, G. A., Solomon, D. K., & Cook, P. G. (2011). Using terrigenic 4He to identify and quantify regional groundwater discharge to streams. Water Resources Research, 47(6).

Gass, T.E., Lehr, J.H., Heiss Jr., H.W. (1977) Impact of abandoned wells on ground water, EPA-600/3-77-095, Robert S. Kerr environmental research laboratory, U.S. Environmental Protection Agency, Ada OK, USA, August 1977.

Gedeon, M. (2008) Neogene Aquifer Model. Institute for Environment, Health, Safety, Belgian Nuclear Research Centre (SCK CEN), Boeretang 200, 2400 Mol, Belgium.

Gedeon, M., Wemaere, I., Marivoet, J. (2007) Regional groundwater model of north-east Belgium. Journal of Hydrology 335, 133-139.

Geluk, M.C., Duin, E.J.T., Dusar, M., Rijkers, M.H.B., van den Berg, M.W., van Rooijen, P. (1994) Stratigraphy and tectonics of the Roer Valley Graben. Geologie en Mijnbouw 73, 129–141.

GeoERA (2017) Call Announcement and Scientific Scope: Stage Two – Project Proposals, Joint call document no.9, available at: http://geoera.eu/wp-content/uploads/2016/11/GeoERA-Call-Document-No.-9-SRTs-20171017.pdf, accessed at 27 May 2019.

Goetzl, G., Zekiri, F., Lenkey, L., Rajver, D., Svasta, J. (2012) Geothermal Models at Supra-regional Scale, Summary report. Transenergy Project. (http://transenergy eu.geologie.ac.at).

Grasby, S.E., Ferguson, G., Brady, A., Sharp, C., Dunfield, P., McMechan, M. (2016) Deep groundwater circulation and associated methane leakage in the northern Canadian Rocky Mountains, Applied Geochemistry Volume 68, Pages 10-18.

Griffioen, J., Vermooten, S., and Janssen, G. (2013). Geochemical and palaeohydrological controls on the composition of shallow groundwater in the Netherlands. Applied geochemistry, 39, 129-149.

GS Noord-Brabant (2012). Besluit Beslissing van Gedeputeerde Staten van Noord-Brabant op grond van artikel 7.16. van de Wet Milieubeheer. Energieopslag Paleiskwartier te ’s-Hertogenbosch (Decision Environmental management law energy storage Paleiskwartier in ’s-Hertogenbosch, in Dutch). Gedeputeerde Staten van Noord-Brabant, ’s-Hertogenbosch, Netherlands.

Gumm, L.P., Bense, V.F., Dennis, P.F., Hiscock, K.M., Cremer, N., Simon, S. (2016) Dissolved noble gases and stable isotopes as tracers of preferential fluid flow along faults in the Lower Rhine Embayment, Germany. Hydrogeology Journal 24:99–108. https://doi.org/10.1007/s10040-015-1321-7.

Haas, J., Götz, A.E., & Pálfy, J. (2010). Late Triassic to Early Jurassic palaeogeography and eustatic history in the NW Tethyan realm: New insights from sedimentary and organic facies of the Csővár Basin (Hungary). Palaeogeography, Palaeoclimatology, Palaeoecology, 291, 456-468.

Haas, J., Budai, T., Raucsik, B. (2012) Climatic controls on sedimentary environments in the Triassic of the Transdanubian Range (Western Hungary), Palaeogeography, Palaeoclimatology, Palaeoecology, Volumes 353–355, 31-44, https://doi.org/10.1016/j.palaeo.2012.06.031

Haas, J., Budai, T. 2014: Geology of the pre-Cenozoic basement of Hungary. Explanatory notes for “Pre-Cenozoic geological map of Hungary” (1:500 000). Geological and Geophysical Institute of Hungary, Budapest, p. 73.

Hammack, R., Harbert, W., Sharma, S., Stewart, B., Capo, R., Wall, A., Wells, A., Diehl, R., Blaushild, D., Sams, J., Veloski, G. (2014) An Evaluation of Fracture Growth and Gas/Fluid Migration as Horizontal Marcellus Shale Gas Wells are Hydraulically Fractured in Greene County, Pennsylvania, NETL-TRS-3-2014, EPAct Technical Report Series, U.S. Department of Energy, National Energy Technology Laboratory: Pittsburgh, PA, USA.

Han, F., Zheng, Y. (2018) Joint analysis of input and parametric uncertainties in watershed water quality modeling: A formal Bayesian approach. Advances in Water Resources 116:77–94. https://doi.org/10.1016/j.advwatres.2018.04.006

Harbaugh, A.W. (2005) MODFLOW-2005, The U.S. Geological Survey Ground-water Model, Ground-water Flow Process. USGS: Techniques and Methods 6-A16 1–253. https://doi.org/https://doi.org/10.3133/tm6A16

Harris, R.N., Chapman, D.S. (2007) Stop-go temperature logging for precision applications. Geophysics 72:E119–E123. doi: 10.1190/1.2734382.

Harrison, D., Haarhoff, M., Heath-Clarke, M., Hodgson, W., Hughes, F., Ware, D., Mortimer, A. (2020). The Vale of Pickering gas fields: Kirby Misperton, Malton, Marishes and Pickering, North Yorkshire, UK Onshore. Geological Society, London, Memoirs, 52(1), 82–93. https://doi.org/10.1144/M52-2017-33.

Hidalgo, J.J., Carrera, J., Dentz, M. (2009) Steady state heat transport in 3D heterogeneous porous media. Advances Water Resources 32: 1206–1212. doi: 10.1016/j.advwatres.2009.04.003.

House of Commons Energy and Climate Change Committee (2011) Shale Gas - Fifth Report of Session 2010–12. HC 795, Stationary Office Limited, London UK.

Houtgast, R. F., and Van Balen, R. T. (2000). Neotectonics of the Roer Valley rift system, the Netherlands. Global and Planetary Change, 27(1-4), 131-146.

Humez, P. Osselin, F., Kloppmann, W. and Mayer, B. (2019). A geochemical and multi-isotope modelling approach to determine sources and fate of methane in shallow groundwater above unconventional hydrocarbon reservoirs. Journal of Contaminant Hydrology 226.

Ingraffea, A.R., Wells, M.T., Santoro, R.L., Shonkoffd, S.B.C. (2014) Assessment and risk analysis of casing and cement impairment in oil and gas wells in Pennsylvania, 2000–2012, PNAS, Volume 111, Number 30, Pages 10955-10960, https://doi.org/10.1073/pnas.1323422111.

Irvine, D.J., Brunner, P., Franssen, H.H., Simmons, C.T. (2012) Heterogeneous or homogeneous ? Implications of simplifying heterogeneous streambeds in models of losing streams. Journal of Hydrology 424–425:16–23. doi: 10.1016/j.jhydrol.2011.11.051.

Jackson, R.E., Gorody, A.W., Mayer, B., Roy, J.W., Ryan, M.C., Van Stempvoort, D.R. (2013) Groundwater Protection and Unconventional Gas Extraction: The Critical Need for Field-Based Hydrogeological Research, Issue Paper, Groundwater, Volume 51, Number 4, Pages 488-510, doi: 10.1111/gwat.12074.

Jackson, R.B., Vengosh, A., Darrah, T.H., Warner, N.R., Down, A., Poreda, R. J., Osborn, S.G., Zhao, K. and Karr, J.D. (2013). Increased stray gas abundance in a subset of drinking water wells near Marcellus shale gas extraction. Proceedings of the National Academy of Sciences of the United States of America PNAS 110(28), 11250-11255.

Joshi, S.K., Rai, S.P., Sinha, R., Gupta, S., Densmore, A.L., Rawat, Y.S., Shekhar, S. (2018) Tracing groundwater recharge sources in the northwestern Indian alluvial aquifer using water isotopes (δ18O, δ2H and 3H). Journal of Hydrology 559: 835–847. https://doi.org/10.1016/j.jhydrol.2018.02.056.

Kallesøe, A.J. & Vangkilde-Pedersen, T. (eds). 2019: Underground Thermal Energy Storage (UTES) – state-of-the-art, example cases and lessons learned. HEATSTORE project report, GEOTHERMICA – ERA NET Cofund Geothermal.

Kim, Y.-S., Peacock, D. C., Sanderson, D. J. (2004) Fault damage zones. Journal of Structural Geology, 26, 503–517. doi:10.1016/j.jsg.2003.08.002.

Kim, Y.-S., Sanderson, D. J. (2005) The relationship between displacement and length of faults: a review. Earth-Science Reviews, 68, 317–334. doi:10.1016/j.earscirev.2004.06.003.

King, G.E., Valencia, R.L. (2014) Environmental Risk and Well Integrity of Plugged and Abandoned Wells, SPE-170949-MS, SPE Annual Technical Conference and Exhibition, Amsterdam, the Netherlands, 27-29 October 2014.

Kivits T., Broers H.P., & Van Vliet M.E. (2019). Dateren grondwater van het Provinciaal Meetnet Grondwaterkwaliteit Noord-Brabant. Inzicht in de toestand en trends van 12 indicatoren van de grondwaterkwaliteit. TNO-rapport 2019 R11094.

Koornneef, J., Ramírez, A., Turkenburg, W., Faaij, A.(2011) The environmental impact and risk assessment of CO2 capture, transport and storage -an evaluation of the knowledge base using the DPSIR framework, Energy Procedia, Volume 4, Pages 2293-2300, doi:10.1016/j.egypro.2011.02.119.

Ladevèze, P., Rivard, C., Lavoie, D., Séjourné, S., Lefebvre, R., Bordeleau, G., (2019) Fault and natural fracture control on upward fluid migration: insights from a shale gas play in the St. Lawrence Platform, Canada, Hydrogeology Journal 27:121–143, https://doi.org/10.1007/s10040-018-1856-5.

Lapperre, R.E., Kasse, C., Bense, V.F., Woolderink, H.A.G., Van Balen, R.T. (2019) An overview of fault zone permeabilities and groundwater level steps in the Roer Valley Rift System. Netherlands Journal of Geosciences 98:e5. https://doi.org/10.1017/njg.2019.4

Levebvre, René (2017) Mechanisms leading to potential impacts of shale gas development on groundwater quality, WIREs Water 2017, 4:e1188. doi: 10.1002/wat2.1188.

Loveless, S., Lewis, M.A., Bloomfield, J.P., Terrington, R., Stuart, M.E., WARD, R S. (2018) 3D Groundwater Vulnerability, Internal Report OR/18/12, British Geological Survey, 201pp.

Loveless, S., Mallin-Martin, D., Szalkai, Á., Zaadnoordijk, W.J., Slenter, C., Beerten, K, Ward, R.S. (2019) Expanded diagrams of conceptual models identifying potential pathways for energy activity in the deep sub-surface and shallow groundwater vulnerability, VoGERA Report 1, WP 4.

Luo, Xing, Wang, Jihong, Dooner, Mark, Clarke, Jonathan (2015) Overview of current development in electrical energy storage technologies and the application potential in power system operation, Applied Energy, Volume 137, Pages 511–536, http://dx.doi.org/10.1016/j.apenergy.2014.09.081.

Machiwal, Deepesh, Jha, Madan Kumar, Singh, Vijay P., Mohan, Chinchu (2018) Assessment and mapping of groundwater vulnerability to pollution: Current status and challenges, Earth-Science Reviews, Volume 185, Pages 901–927.

Maros, G., Albert, G., Szeiler, R.B., Fodor, L., Gyalog, L., Jocha-Edelényi, E., Kercsmár, Z., Magyari, Á., Maigut, V., Maros, G., Nádor, A., Orosz, L., Palotás, K., Selmeczi, I., Uhrin, A., Vikor, Z., Atzenhofer, B., Berka, R., Bottig, M., Brüstle, A., Hörfarter, C., Schubert, G., Weilbold, J., Baráth, I., Fordinál, K., Kronome, B., Maglay, J., Nagy, A., Jelen, B., Lapanje, A., Rifelj, H., Rižnar, I., Trajanova, M. (2012) Summary Report of Geological Models, Transenergy Project. pp. 189. (http://transenergy-eu.geologie.ac.at/Downloads/outputs/Summary%20report%20 of%20geological%20models/Summary%20report%20of%20geological%20models.pdf).

Molofsky, Lisa J., Connor, John A., Wylie, Albert S., Wagner, Tom, Farhat, Shahla K. (2013) Evaluation of Methane Sources in Groundwater in Northeastern Pennsylvania, Groundwater, Volume 51, Number 3, Pages 333–349, doi: 10.1111/gwat.12056.

Moritz, Anja, Hélie, Jean-Francois, Pinti, Daniele L., Larocque, Marie, Barnetche, Diogo, Retailleau, Sophie, Lefebvre, René, Gélinas, Yves (2015) Methane Baseline Concentrations and Sources in Shallow Aquifers from the Shale Gas-Prone Region of the St. Lawrence Lowlands (Quebec, Canada), Environmental Science & Technology, Volume 49, Pages 4765-4771.

Newell, A.J., Ward, R.S., Fellgett, M.W. (2015) A preliminary 3D model of post-Permian bedrock geology in the Vale of Pickering, North Yorkshire, UK. Nottingham, UK, British Geological Survey, 23pp. (OR/15/068). Available at: http://nora.nerc.ac.uk/id/eprint/520795/, accessed 27 May 2019.

Nicol, A., Seebeck, H., Field, B., McNamara, D., Childs, C., Craig, J., Rolland, A. (2017) Fault permeability and CO2 storage, Energy Procedia, Volume 114, pages 3229-3236.

Ortiz, J.P., Person, M.A. , Mozley, P.S. , Evans, J.P., Bilek, S.L. (2019) The Role of Fault-Zone Architectural Elements on Pore Pressure Propagation and Induced Seismicity, Groundwater , Vol. 57, No. 3, pages 465–478.

Oil and Gas Authority (n.d.). Interactive Map Viewer [Online]. https://ogauthority.maps.arcgis.com/apps/webappviewer/index.html?id=29c31fa4b00248418e545d222e57ddaa. Accessed (10/12/18).

Oiro, S., Comte, J.C., Soulsby, C., Walraevens, K. (2018) Using stable water isotopes to identify spatio-temporal controls on groundwater recharge in two contrasting East African aquifer systems. Hydrological Sciences Journal 63:862–877. https://doi.org/10.1080/02626667.2018.1459625.

Perkins, Greg (2018) Underground coal gasification – Part I: Field demonstrations and process performance, Progress in Energy and Combustion Science, Volume 67, pages 158-187

Pinson, S., Malcuit, E., Gourcy, L., Ascott, M., Broers, H.P., van Vliet, M., Hinsby, K., Thorling, L., Rosenbom, A. and Christophi, C. (2020). Assessment of attenuation patterns for a number of relevant European settings. Deliverable 5.4, GeoERA HOVER.

Pollock, D.W. (2015) Extending the MODPATH algorithm to rectangular unstructured grids. Groundwater 54: 121–125. https://doi.org/10.1111/gwat.12328

Pollock, D.W. (2016) User guide for MODPATH version 7A particle-tracking model for MODFLOW.

Porowski, A. (2014) Isotope hydrogeology. Handbook of Engineering Hydrology: Fundamentals and Applications 345–378. https://doi.org/10.1201/b15625.

Powell, J. H., Cooper, A. H., Benfield, A. C. (1992). Geology of the country around Thirsk. London: HMSO.

Pyle, D.M. (1993) Graphical analysis of rare gas mixing systematics in geothermal systems. In: Geochemical Journal 49 (3,,5), p. 347–34, 42, 43 .

Raiber, M., Webb, J.A., Cendón, D.I., White, P.A., Jacobsen, G.E. (2015) Environmental isotopes meet 3D geological modelling: Conceptualising recharge and structurally-controlled aquifer connectivity in the basalt plains of south-western Victoria, Australia. Journal of Hydrology 527:262–280. https://doi.org/10.1016/j.jhydrol.2015.04.053.

Read, T., Bour, O., Bense, V., Le Borgne, T., Goderniaux, P., Klepikova, M.V., Hochreutener, R., Lavenant, N., Boschero, V. (2013) Characterizing groundwater flow and heat transport in fractured rock using fiber-optic distributed temperature sensing. Geophysical Research Letters 40:2055–2059. https://doi.org/10.1002/grl.50397.

Reagan, M. T., Moridis, G. J., Keen, N. D., Johnson, J. N. (2015) Numerical simulation of the environmental impact of hydraulic fracturing of tight/shale gas reservoirs on near-surface groundwater: Background, base cases, shallow reservoirs, short-term gas, and water transport, Water Resources Research, Volume 51, Pages 2543–2573, doi:10.1002/2014WR016086.

Recasens, M., Garcia, S., Mackay, E., Delgado, J., Maroto-Valer, M.M. (2017) Experimental study of wellbore integrity for CO2 geological storage. Energy Procedia 114, 5249 – 5255.

Reeves, M. J., Parry, E. L., Richardson, G. (1978). Preliminary evaluation of the groundwater resources of the western part of the Vale of Pickering. Quarterly Journal of Engineering Geology and Hydrogeology, 11(3), 253–262. https://doi.org/10.1144/GSL.QJEG.1978.011.03.05.

Rinaldi, A.P., Rutqvist, J., Cappa, F. (2014) Geomechanical effects on CO2 leakage through fault zones during large-scale underground injection, International Journal of Greenhouse Gas Control, Volume 20, Pages 117-131, DOI: 10.1016/j.ijggc.2013.11.001.

Rogiers, B. (2015) Groundwater flow and solute transport modelling from within R: The RMODFLOW and RMT3DMS packages. In: MODFLOW and more 2015: Modeling a complex world. Golden CO, USA.

Rogiers, B., Beerten, K., Smeekens, T., Mallants, D., Gedeon, M., Huysmans, M., Batelaan, O., Dassargues, A. (2014) The usefulness of outcrop analogue air permeameter measurements for analyzing aquifer heterogeneity: Quantifying outcrop hydraulic conductivity and its spatial variability. Hydrological Processes 28:5176–5188. https://doi.org/10.1002/hyp.10007.

Rogiers, B., Labat, S., Gedeon, M. (2015) An assessment of dilution tests and ambient temperature logging for quantifying groundwater flow in the Neogene aquifer. SCK•CEN External Report ER-276, 103 p.

Rosen, M.A., Reddy, B.V., Self, S.J. (2018) Underground coal gasification (UCG) modeling and analysis, in: Underground Coal Gasification and Combustion, Elsevier, https://doi.org/10.1016/B978-0-08-100313-8.00011-6

Rotár-Szalkai, Á., Tóth, G., Gáspár, E., Kerékgyártó, T., Kovács, A., Maros, G., Goetzl, G., Schubert, G., Fatime, Z., Bottig, M., Cernak, R., Svasta, J., Rajver, D., Lapanje, A., Fuks, T., Janža, M., Šram, D. (2013) Summary report of the steady-state modeling. Report of the TRANSENERGY project (http://transenergy-eu.geologie.ac.at/Downloads/outputs/Summary%20report%20of%20the%20supra-regional%20hydrogeological%20model/WP5/2CE124P3_6PR_WP5A_%20Steady_state_model_report.pdf).

Rotár-Szalkai, Á., Nádora, A., Szöcs, T., Maros, G., Goetzl, G., Zekiri, F. (2017) Outline and joint characterization of transboundary geothermal reservoirs at the western part of the Pannonian basin. Geothermics 70., 1-16.

Rotár-Szalkai, Á., Csizmeg, J., Vetó, I., Király, C.S. (2018) Oil Accumulation, Regional Groundwater Flow and Inert Gas Risk In The Southern Danube Basin, Hungary. Interpretation 6 (1), pp. 1-35.

Rutqvist, J., Rinaldi, A.P., Cappa, F., Jeanne, P., Mazzoldi, A., Urpi, L., Guglielmi, Y., Vilarras, V. (2016) Fault activation and induced seismicity in geological carbon storage - Lessons learned from recent modeling studies, Journal of Rock Mechanics and Geotechnical Engineering, Volume 8, Pages 789-804.

Saar, M.O. (2011) Review: Geothermal heat as a tracer of large-scale groundwater flow and as a means to determine permeability fields. Hydrogeology Journal 19: 31–52. doi: 10.1007/s10040-010-0657-2.

Schloemer, S., Oest, J., Illing, C.J., Elbracht, J. and Blumenberg, M. (2018). Spatial distribution and temporal variation of methane, ethane and propane background levels in shallow aquifers – A case study from Lower Saxony (Germany). Journal of Hydrology: Regional Studies 19, 57-79.

Slenter, C. (2021) Overview of groundwater management strategies on different sides of common borders. Deliverable D3.6 RESOURCE, GeoERA.

Self, S.J., Reddy, B.V., Rosen, M.A. (2012) Review of underground coal gasification technologies and carbon capture, International Journal of Energy and Environmental Engineering, Volume 3, Number 1, Article 16, http://www.journal-ijeee.com/content/3/1/16.

Shafirovich, E., Varma, A. (2009) Underground Coal Gasification: A Brief Review of Current Status, Industrial & Engineering Chemistry Research, Volume 48, Pages 7865–7875.

Sherwood, O. A., Rogers, J. D., Lackey, G., Burke, T. L., Osborn, S. G., Ryan, J. N. (2016) Groundwater methane in relation to oil and gas development and shallow coal seams in the Denver-Julesburg Basin of Colorado. Proceedings of the National Academy of Sciences of the United States of America, 113(30), 8391–8396. doi:10.1073/pnas.1523267113.

Smedley, P.L., Ward, R.S., Allen, G., Baptie, B., Daraktchieva, Z., Jones, D.G., Jordan, C.J., Purvis, R.M., Cigna, F. (2015) Site selection strategy for environmental monitoring in connection with shale-gas exploration: Vale of Pickering, Yorkshire and Fylde, Lancashire. BGS Open Report, OR/15/067. Retrieved January 3, 2020, from http://nora.nerc.ac.uk/id/eprint/512628/.

Smedley, P. L., Ward, R. S., Bearcock, J. M., Bowes, M. J. (2017). Establishing the baseline in groundwater chemistry in connection with shale-gas exploration: Vale of Pickering, UK. Procedia Earth and Planetary Science, 17, 678–681. https://doi.org/10.1016/j.proeps.2016.12.143.

SODM (2017) Staat van de Sector Geothermie (status of the geothermics sector, in Dutch), Dutch regulatory agency for activities in the deep subsurface, The Hague, available at: https://www.sodm.nl/onderwerpen/aardwarmte/documenten/rapporten/2017/07/13/staat-van-de-sector-geothermie, accessed 4 June 2019.

SODM (2019a) Eindrapport de integriteit van de onshore putten in Nederland (Integity of onshore wells in the Netherlands), Dutch regulatory agency for activities in the deep subsurface, The Hague, available at: https://www.sodm.nl/documenten/rapporten/2019/02/07/de-integriteit-van-onshore-putten-in-nederland, accessed 4 June 2019.

SODM (2019b) Dutch regulatory agency for activities in the deep subsurface, https://www.sodm.nl/sitemap, accessed 4 April 2019.

Stuyfzand, P. (1986) A newhydrochemical classification of watertypes: principles and application to the coastal dunes aquifer system of the Netherlands. Proceedings of the Nineth Salt Water Intrusion Meeting 641–655.

Taherdangkoo, R., Tatomir, A., Taylor, R., Sauter, M. (2017) Numerical investigations of upward migration of fracking fluid along a fault zone during and after stimulation, Energy Procedia, Volume 125, Pages 126-135.

Tari, G., Horváth, F. (2010) Eo-Alpine evolution of the Transdanubian Range in the nappe system of the Eastern Alps: revival of a 15 years old tectonic model. Földtani Közlöny, 140/4, pp.483–510.

Thorogood, J.L., Younger, P.L. (2015) Discussion of “Oil and gas wells and their integrity: Implications for shale and unconventional resource exploitation” by R.J. Davies, S. Almond, R.S., Ward, R.B. Jackson, C. Adams, F. Worrall, L.G. Herringshaw, J.G. Gluyas and M.A. Whitehead. (Marine and Petroleum Geology 2014), Marine and Petroleum Geology, Volume 59, Pages 671-673.

Tóth G., Rotár-Szalkai Á., Kerékgyártó T., Szőcs T., Gáspár E., Lapanje A., Rman N., Cernak R., Remsik, A. G. Schubert, Summary report of the supra-regional hydrogeological model, TRANSENERGY project, MFGI, GeoZS, GBA, ŠGÚDŠ, Budapest, Vienna, Ljubljana, Bratislava (2012).

Tóth, G., Rman, N., Rotár-Szalkai, Á., Kerékgyártó, T., Szöcs, T., Lapanje, A., Černák, R., Remsík, A., Schubert, G., Nádor, A. (2016) Transboundary fresh and thermal groundwater flows in the west part of the Pannonian Basin. Renew. Sustain. Energy Rev. 57, 439–454.

US EPA (2016) Hydraulic Fracturing for Oil and Gas: Impacts from the Hydraulic Fracturing Water Cycle on Drinking Water Resources in the United States (Final Report). U.S. Environmental Protection Agency, Washington, DC, EPA/600/R-16/236F.

Van Baar, M., Beekman, W, and Caljé, R.J. (2013). Prognosos chloride concentration in mixed raw water at the well fields Nuland, Loosbroek and Veghel. Artesia, Schoonhoven, the Netherlands.

van den Berg, M., Vanneste, K., Dost, B., Lokhorst, A., van Eijk, M., Verbeeck, K. (2002) Paleoseismic investigations along the Peel Boundary Fault: geological setting, site selection and trenching results, Netherlands Journal of Geosciences, 81 (1) pp.39-60.

Vandersteen, K., Gedeon, M., Marivoet, J., Wouters, L. (2014) Regional groundwater flow modelling of the confined aquifers below the Boom Clay in NE Belgium. Geological Society, London, Special Publications 400, 163-177.

Vandersteen, K., Rogiers, B., Labat, S., Beerten, K. (2017) Sampling procedure for CFCs / SF-6 and H-3 / He. Institute for Environment, Health, Safety, Belgian Nuclear Research Centre (SCKCEN), Boeretang 200, 2400 Mol, Belgium.

Vandersteen, K., Gedeon, M., Marivoet, J., Wouters, L. (2014) Regional groundwater flow modelling of the confined aquifers below the Boom Clay in NE Belgium. Geological Society, London, Special Publications 400, 163-177.

Van Gessel, S., van Ede, R., Doornenbal, H., ten Veen, J., & Hintersberger, E. (2021). A European Fault Database as a stepping stone towards improved subsurface evaluation of hazards and resources. In EGU General Assembly Conference Abstracts (pp. EGU21-16232).

Van Keer, I., Marivoet, J., Wemaere, I., et al (1999) A PalaeoHYdrogeological study of the MOL site.

Van Lopik, J.H., Hartog, N., Zaadnoordijk, W.J., Cirkel, D., Gijsbert, Raoof, A. (2015) Salinization in a stratified aquifer induced by heat transfer from well casings, Advances in Water Resources, Volume 86, Part A, Pages 32-45, https://doi.org/10.1016/j.advwatres.2015.09.025.

Van Uum, R. , K. Kasse & D. Edelman. (2003). De Gilze-Rijen breuk bij Tilburg. Grondboor & Hamer, 57(5), 81–85

Van Vliet, Marielle, Hans Peter Broers, Cis Slenter, Koen Beerten en Bernd Linder, 3D visualisation of groundwater composition and age, Deliverable 3.3, GeoERA RESOURCE.

Verbeeck, K., Wouters, L., Vanneste, K., Camelbeeck, T., Vandenberghe, D., Beerten, K., Rogiers, B., Schiltz, M., Burow, C., Mees, P., De Grave, J., Vandenberghe, N. (2017) Episodic activity of a dormant fault in tectonically stable Europe : the Rauw fault (NE Belgium). Tectonophysics 699, 146-163.

Vernes, R.W., Deckers, J., Bakker, M.A.J., Bogemans, F., De Ceukelaire, M., Doornenbal, J.C., den Dulk, M., Dusar, M., Van Haren, T.F.M., Heyvaert, V.M.A., Kiden, P., Kruisselbrink, A.F., Lanckacker, T., Menkovic, A., Meyvis, B., Munsterman, D.K., Reindersma, R., ten Veen, J.H., van de Ven, T.J.M., Walstra, J., Witmans, N. (2018) Geologisch en hydrogeologisch 3D model van het Cenozoïcum van de Belgisch-Nederlandse grensstreek van Midden-Brabant / De Kempen (H3O – De Kempen). Studie uitgevoerd door VITO, TNO-Geologische Dienst Nederland en de Belgische Geologische Dienst in opdracht van Vlaams Planbureau voor Omgeving, Vlaamse Milieumaatschappij, TNO, Geologische Dienst Nederland, Nederlandse Provincie Noord-Brabant, Brabant Water, Programmabureau KRW/DHZ Maasregio.

Vernes, R., Beerten, K., Linder, B., Casillas-Trasvina, A., Kruisselbrink, A., Reindersma, R., Rogiers, B., Slenter, C. (2021) RESOURCE Deliverable 3.2: Report with associated database of hydraulic properties of prime aquifers and aquitards and fault zones. WP3 H3O-PLUS. European Commission.

Visser, A., Broers, H.P. and Bierkens, M.F.P. (2007). Dating degassed groundwater with 3H/3He. Water Resources Research 43(10)

Walraevens, K. (2000) Quality of Groundwater Resources. In: Syllabus: Groundwater quality course in university of Ghent. p 136.

Ward, R.S., Smedley, P.L., Allen, G., Baptie, B.J., Daraktchieva, Z., Horleston, A., Jones, D.G., Jordan, C.J., Lewis, A., Lowry, D., Purvis, R.M., Rivett, M.O. (2017) Environmental Baseline Monitoring Project. Phase II, final report. British Geological Survey, 163pp. (OR/17/049). Retrieved December 6, 2018, from http://nora.nerc.ac.uk/id/eprint/517889/.

Ward, R. S., Smedley, P. L., Allen, G., Baptie, B. J., Cave, M. R., Daraktchieva, Z., , Fisher, R., Hawthorn, D., Jones, D.G., Lewis, A., Lowry, D., Luckett, R., Marchant, B.P., Purvis, R.M., Wilde, S. (2018) Environmental baseline monitoring: Phase III final report (2017-2018) [Publication - Report]. Retrieved January 3, 2020, from http://nora.nerc.ac.uk/id/eprint/521380/.

Warner, N.R., Jackson, R.B., Darrah, T.H., Osborn, S.G., Down, A., Zhao, K., White, A., Vengosh, A. (2012) Geochemical evidence for possible natural migration of Marcellus Formation brine to shallow aquifers in Pennsylvania, PNAS, Volume 109, Number 30, Pages 11961-11966, doi:10.1073/pnas.1121181109.

Wassenaar, L.I., Athanasopoulos, P., Hendry, M.J. (2011) Isotope hydrology of precipitation, surface and ground waters in the Okanagan Valley, British Columbia, Canada. Journal of Hydrology 411:37–48. https://doi.org/10.1016/j.jhydrol.2011.09.032.

Waters, C. N., Terrington, R. L., Cooper, M. R., Raine, R. J., Thorpe, S. (2016). The construction of a bedrock geology model for the UK: UK3D_v2015 [Publication - Report]. Retrieved March 28, 2019, from http://nora.nerc.ac.uk/id/eprint/512904/.

Wei, W., Aeschbach-Hertig, W. and Chen, Z. (2015). Identification of He sources and estimation of He ages in groundwater of the North China Plain. Applied Geochemistry, 63, 182-189.

Younger, P.L. (2016) How can we be sure fracking will not pollute aquifers? Lessons from a major longwall coal mining analogue (Selby, Yorkshire, UK), Earth and Environmental Science Transactions of the Royal Society of Edinburgh, Volume 106, Pages 89–113.

Yu, L., Rozemeijer, J., Van Breukelen, B. M., Ouboter, M., Van Der Vlugt, C. and Broers, H. P. (2018). Groundwater impacts on surface water quality and nutrient loads in lowland polder catchments: monitoring the greater Amsterdam area. Hydrology and Earth System Sciences, 22(1).

Zaadnoordijk, W.J., Szalkai, Ágnes, Beerten, Koen, Mallin Martin, Dan, Ward, Rob, Bowes, M., Newell, A., Smedley, P., Broers, Hans Peter, Slenter, Cis, Loveless, Sian (2019) Scope – Terms and definitions – Literature review on pathways – Pilot areas and data collection plans, VoGERA delevirable D3.1, VoGERA, Work Package 3, Technical Report 1, GeoERA.

Zaadnoordijk, W.J., Buma, J., Vernes, R., Beerten, K., Rogiers, B., Slenter, C., Jaritz, R., Linder, B. and Broers, H.P. (2021). Deliverable 3.5, 3D visualization of cross-border patterns of groundwater depletion. GeoERA RESOURCE.

Zang, A., Oye, V., Jousset, P., Deichmann, N., Gritto, R., McGarr, A., Majer, E., Bruhn, D. (2014) Analysis of induced seismicity in geothermal reservoirs – An overview, Geothermics, Volume 52, Pages 6-21, https://doi.org/10.1016/j.geothermics.2014.06.005.

Zheng, C. (2010) MT3DMS v5.3 Supplemental User's Guide. University of Alabama, Tuscaloosa AL, USA, 56 pp. Available at: https://hydro.geo.ua.edu/mt3d/mt3dms_v5_supplemental.pdf

Zhonglan, T., Lin, S., Lei, Q. (2015) Problems in the wellbore integrity of a shale gas horizontal well and corresponding countermeasures, Natural Gas Industry B, Volume 2, Pages 522-529, http://dx.doi.org/10.1016/j.ngib.2015.12.006.